THE EFFECTS OF STRUCTURAL MODIFICATIONS ON THE ELECTRICAL AND ELECTROCHEMICAL PROPERTIES OF STANNUM BASED NASICON STRUCTURED SOLID ELECTROLYTES

NUR AMALINA MUSTAFFA

INSTITUTE OF GRADUATE STUDIES
UNIVERSITY OF MALAYA
KUALA LUMPUR

2017

THE EFFECTS OF STRUCTURAL MODIFICATIONS ON THE ELECTRICAL AND ELECTROCHEMICAL PROPERTIES OF STANNUM BASED NASICON STRUCTURED SOLID ELECTROLYTES

NUR AMALINA MUSTAFFA

THESIS SUBMITTED IN FULFILMENT OF THE REQUIREMENTS FOR THE DEGREE OF DOCTOR OF PHILOSOPHY

INSTITUTE OF GRADUATE STUDIES
UNIVERSITY OF MALAYA
KUALA LUMPUR

2017

UNIVERSITY OF MALAYA

ORIGINAL LITERARY WORK DECLARATION

Name of Candidate : **NUR AMALINA BINTI MUSTAFFA**

Registration/Matric No : **HHC 130005**

Name of Degree : **DOCTOR OF PHILOSOPHY**

Title of Project Paper/Research Report/Dissertation/Thesis ("this Work"):

THE EFFECTS OF STURUCTURAL MODIFICATIONS ON THE ELECTRICAL AND ELECTROCHEMICAL PROPERTIES OF STANNUM BASED NASICON STRUCTURED SOLID ELECTROLYTES

Field of Study : **APPLIED SCIENCE (ADVANCED MATERIALS)**

I do solemnly and sincerely declare that:

(1) I am the sole author/writer of this Work;
(2) This Work is original;
(3) Any use of any work in which copyright exists was done by way of fair dealing and for permitted purposes and any excerpt or extract from, or reference to or reproduction of any copyright work has been disclosed expressly and sufficiently and the title of the Work and its authorship have been acknowledged in this Work;
(4) I do not have any actual knowledge nor do I ought reasonably to know that the making of this work constitutes an infringement of any copyright work;
(5) I hereby assign all and every rights in the copyright to this Work to the University of Malaya ("UM"), who henceforth shall be owner of the copyright in this Work and that any reproduction or use in any form or by any means whatsoever is prohibited without the written consent of UM having been first had and obtained;
(6) I am fully aware that if in the course of making this Work I have infringed any copyright whether intentionally or otherwise, I may be subject to legal action or any other action as may be determined by UM.

Candidate‟s Signature Date:

Subscribed and solemnly declared before,

Witness‟s Signature Date:

Name:

Designation:

ABSTRACT

In this study, $LiSn_2P_3O_{12}$ parent compound was synthesized using water based sol-gel method and the parameters of sol-gel method have been optimized in obtaining minimize impurity of the NASICON compound. Then the effects of structural modifications by partial substitutions using trivalent (Cr^{3+}, Al^{3+}) and tetravalent (Zr^{4+}, Si^{4+}) ions at Sn^{4+} and P^{5+} sites on the conductivity and electrochemical properties of the modified NASICON compound were studied. The X-ray diffraction analysis showed that $LiSn_2P_3O_{12}$ compound can be indexed to rhomboherdral structure with space group ($R\bar{3}c$) for samples sintered for 24 and 48 hours. However, after the optimization of the sol-gel method, $LiSn_2P_3O_{12}$ compound sintered at 48 hours showed trace amount of SnO_2 compared to the sample sintered for 24 hours. The $LiSn_2P_3O_{12}$ compound sintered for 48 hours showed average bulk, grain boundary and total conductivity of 7.22×10^{-6} S cm^{-1}, 2.99×10^{-7} S cm^{-1} and 2.87×10^{-7} S cm^{-1} at room temperature. The total conductivity increased to 1.38×10^{-5} S cm^{-1} when the temperature was 500 °C. The frequency dependence of conductivity followed Jonscher"s universal power law. The plot of pre-exponent, *s* versus temperature suggested that Correlated Barrier Hopping Model was the conduction mechanism in the compound. The highest conducting sample was electrochemically stable up to 4.8 V. The impedance analysis showed that the conductivity of the parent compound increases with different substitutions of ions. The substitutions of smaller ionic radius of trivalent ions, Al^{3+} at Sn^{4+} site ($Li_{1.5}Al_{0.5}Sn_{1.5}P_3O_{12}$) enhanced the conductivity at room temperature. The value of bulk, grain boundary and total conductivity were 8.71×10^{-6} S cm^{-1}, 1.16×10^{-6} S cm^{-1} and 1.02×10^{-6} S cm^{-1} respectively. The total conductivity increased to 8.18×10^{-5} S cm^{-1} when the temperature was 500 °C. Linear sweep voltammetry analysis indicated that Al^{3+} substitution improved the electrolyte decomposition from 4.8 V in the parent

compound to 5.1 V. For tetravalent ion substitutions, (Zr^{4+}, Si^{4+}) ions were substituted at P^{5+} site. For Zr^{4+} substituted system, $Li_{1.5}Sn_2P_{2.5}Zr_{0.5}O_{12}$ compound displayed total conductivity values of 1.32×10^{-6} S cm^{-1} at room temperature and 5.77×10^{-5} S cm^{-1} at 500°C. The $Li_{1.5}Sn_2P_{2.5}Zr_{0.5}O_{12}$ compound was also electrochemically stable up to 5.2 V. Meanwhile in Si^{4+} substituted system, $Li_{1.5}Sn_2P_{2.5}Si_{0.5}O_{12}$ compound displayed total conductivity values of 1.05×10^{-6} S cm^{-1} at room temperature and 6.05×10^{-5} S cm^{-1} at 500°C. Linear sweep voltammetry analysis also showed that Si^{4+} substitution improved the electrolyte decomposition from 4.8 V in the parent compound to 5.1 V. The transference number value of all Al^{3+}, Zr^{4+} and Si^{4+} substituted samples were 0.99 suggesting that the majority of mobile charge carriers were ions and anticipated to be Li^{+}. Thus, the results of this study indicated that Al^{3+}, Zr^{4+} and Si^{4+} substitutions significantly enhanced the electrical and electrochemical properties of the $LiSn_2P_3O_{12}$ ceramic electrolytes.

ABSTRAK

Di dalam kajian ini, $Lin_2P_3O_{12}$ telah disediakan menggunakan kaedah sol-gel menggunakan air dan parameter kaedah sol-gel telah dioptimumkan bagi mendapatkan bahan NASICON yang mengandungi kurang bendasing. Seterusnya, kesan pengubahsuaian struktur bagi penggantian separa menggunakan trivalen ion (Cr^{3+}, Al^{3+}) dan tetravalen (Si^{4+}, Zr^{4+}) ion di kedudukan Sn^{4+} and P^{5+} kepada kekonduksian dan elektrokimia bagi bahan NASICON yang telah diubahsuai telah dikaji. Keputusan dari belauan sinar-x menunjukkan bahan $LiSn_2P_3O_{12}$ boleh diindeks kepada struktur rhombohedra dalam ruang kumpulan ($R\bar{3}c$) bagi sampel yang telah dipanaskan pada suhu tinggi selama 24 dan 48 jam. Walaubagaimanapun, bahan yang telah dipanaskan selama 48 jam mempunyai jumlah bendasing SnO_2 yang kurang berbanding dengan sampel yang dipanaskan selama 24 jam. Maka , bahan $LiSn_2P_3O_{12}$ yang dipanaskan pada suhu tinggi selama 48 jam menunjukkan nilai paling tinggi untuk kekonduksian pukal, kekonduksian sempadan butiran dan kekonduksian jumlah sebatian pada suhu bilik adalah 7.22×10^{-6} S cm^{-1}, 2.99×10^{-7} S cm^{-1} dan 2.87×10^{-7} S cm^{-1}. Kekonduksian jumlah sebatian meningkat kepada 1.38×10^{-5} S cm^{-1} apabila suhu dinaikkan kepada 500 °C. Kebergantungan kekonduksian pada frekeunsi adalah mematuhi undang-undang sejagat Jonscher‟s. Plot pra- pelopor *s* melawan suhu menunjukkan bahawa mekanisme pengaliran dalam bahan boleh diterangkan dengan menggunakan model korelasi halangan loncat. Sampel yang mempunyai kekonduksian tertinggi stabil sehingga 4.8 V. Analisis spektroskopi impedans menunjukkan bahawa kekonduksian bahan induk meningkat dengan penggantian separa. Penggantian ion trivalen, Al^{3+} ke Sn^{4+} ($Li_{1.5}Al_{0.5}Sn_{1.5}P_3O_{12}$) ke bahan induk telah meningkatkan kekonduksian pada suhu bilik. Nilai kekonduksian pukal, sempadan butiran dan jumlah kekonduksian adalah masing-masing 8.71×10^{-6} S cm^{-1}, 1.16×10^{-6} S cm^{-1} dan 1.02×10^{-6} S cm^{-1}. Kesan ini adalah

disebabkan oleh ion celahan tambahan dan peningkatan kekonduksian sempadan butiran. Kekonduksian jumlah sebatian meningkat kepada 8.18 $\times 10^{-5}$ S cm^{-1} apabila suhu dinaikkan kepada 500 °C. Voltammetri sapuan linear menunjukkan sampel yang penggantian separa Al^{3+} juga telah meningkatkan kestabilan bahan kepada 5.1 V berbanding 4.8 V bagi bahan induk. Bagi sampel penggantian tetravalen, (Zr^{4+}, Si^{4+}) telah digantikan separa pada kedudukan P^{5+}. Bagi sampel penggantian separa menggunakan Zr^{4+}, sampel $Li_{1.5}Sn_2P_{2.5}Zr_{0.5}O_{12}$ menujukkan jumlah kekonduksian 1.32 $\times$ 10^{-6} S cm^{-1} pada suhu bilik dan 5.77 $\times$ 10^{-5} S cm^{-1} pada 500 °C. Bahan $Li_{1.5}Sn_2P_{2.5}Zr_{0.5}O_{12}$ juga adalah stabil sehingga 5.2 V jika dibandingkan dengan bahan induk. Sementara itu, bagi sampel dengan penggantian separa menggunakan Si^{4+}, $Li_{1.5}Sn_2P_{2.5}Si_{0.5}O_{12}$ menunjukkan jumlah kekonduksian 1.05 $\times$ 10^{-6} S cm^{-1} pada suhu bilik dan 6.05 $\times$ 10^{-5} S cm^{-1} pada suhu 500 °C. Voltammetri sapuan linear menunjukkan sampel yang penggantian separa Si^{4+} juga telah meningkatkan kestabilan bahan kepada 5.1 V berbanding hanya 4.8 V bagi bahan induk. Nombor pemindahan bagi semua penggantian separa Al^{3+}, Zr^{4+} and Si^{4+} adalah 0.99 di mana ia menujukkan bahawa majoriti pembawa cas adalah ion dan merupakan ion Li^{+}. Oleh itu, hasil kajian ini menunjukkan penggantian separa menggunakan Al^{3+}, Zr^{4+} dan Si^{4+} meningkatkan sifat-sifat elektrik dan elektrokimia elektrolit seramik $LiSn_2P_3O_{12}$.

ACKNOWLEDGEMENTS

First and foremost, I would like to extend my praise to Allah s.w.t for giving me the strength, determination, patience and courage to produce this doctoral thesis.

I would like to express my special gratitude to Professor Dr. Nor Sabirin Mohamed from Centre of Foundation Studies in Science, University of Malaya for all she has done for me as a research supervisor and advisor. Without her assistance, guidance, ideas, supervision and encouragement, I would not be able to complete my graduate studies at University of Malaya. I would also like to express my gratitude to all the research members including lecturers and postgraduate students of Electrochemical Materials and Devices (EMD) group, Centre of Foundation Studies in Science, University of Malaya for providing the research facilities and for all their help and cooperation given throughout my study.

I gratefully acknowledge Ministry of Higher Education Malaysia through Fundamental Research Grant Scheme, FP006-2013B and University of Malaya through Postgraduate Research Fund (PPP), PG015-2014A for the financial support. A highly gratitude goes to Universiti Teknologi Mara and Ministry of Higher Education Malaysia for the scholarship under SLAI that allows me to complete this work.

My sincere thanks to all my friends who have directly or indirectly contributed towards the success of this study. Last but not least, to my beloved husband, Naguib and my daughter, Nadra, parents, mother in law, siblings and relatives, I would like to extend my special thanks for their love, understanding, support, patience and encouragement. Without all of them, the path to this thesis will be a lonely endeavor. Your love and belief have given me the strength to walk through difficulties to achieve success.

TABLE OF CONTENTS

LIST OF FIGURES

LIST OF TABLES

LIST OF ABBREVIATIONS

AC	:	Alternating current
Ag^+	:	Silver ion
AgBr	:	Silver bromide
AgCl	:	Silver chloride
AgI	:	Silver iodide
Al	:	Aluminium
Al_2O_3	:	Aluminium oxide
Al^{3+}	:	Aluminium ion
ATR	:	Attenuated Total Reflectance
$C_{14}H_{23}Cr_3O_{16}$	:	Chromium (III) acetate
$C_2H_6O_2$	:	Poly ethylene glycol
$C_6H_{10}ZrO_7$	:	Zirconium (IV) acetate hydroxide
$C_6H_8O_7$	:	Citric acid
$C_6H_9AlO_6$	:	Aluminium (III) acetate
Ca	:	Calcium
CBH	:	Correlated Barrier Hopping
CH_3COOLi	:	Lithium acetate
CPE	:	Constant Phase Element
Cr	:	Chromium
Cr^{3+}	:	Chromium ion
Cu^+	:	Copper ion
CuI	:	Copper iodide
DC	:	Direct current
EDX	:	Energy Dispersive X-Ray Spectroscopy

F^-	:	Flouride ion
Fe	:	Ferum
Fe_2O_3	:	Iron (III) oxide
FTIR	:	Fourier Transform Infrared Spectroscopy
Ge	:	Germanium
H^+	:	Hydrogen ion
$H_{12}N_3O_4P$	:	Ammonium phosphate
Hf	:	Hafnium
IS	:	Impedance Spectroscopy
KCl	:	Potassium chloride
La	:	Lanthanum
Li^+	:	Lithium ion
LiI	:	Lithium iodide
LISICON	:	Lithium Super Ionic Conductor
LSV	:	Linear Sweep Voltammetry
Mg	:	Magnesium
Mg^{2+}	:	Magnesium ion
Mn	:	Manganese
Na / S	:	Sodium / Sulphur
Na^+	:	Sodium ion
NASICON	:	Sodium Super Ionic Conductor
Na-β-alumina	:	Sodium – beta - alumina
Nb	:	Niobium
NH_4O_4	:	Ammonium hydroxide
Ni	:	Nickel
P^{5+}	:	Phosphorus ion

QMT	:	Quantum Mechanical Tunneling
SEM	:	Scanning Electron Microscopy
Si	:	Silicon
Si^{4+}	:	Silicon ion
SiO_2	:	Silicon dioxide
Sn	:	Stannum / Tin
Sn^{2+}	:	Stannum / Tin ion
$SnCl_4.5H_2O$	:	Stannum (IV) chloride pentahydrate
SnO_2	:	Stannum / Tin dioxide
SPEs	:	Solid Polymers Electrolytes
Ta	:	Tantalum
TGA	:	Thermogravimetric Analysis
Ti	:	Titanium
V	:	Vanadium
XRD	:	X-Ray Diffraction
Y	:	Yttrium
Zr	:	Zirconium
Zr^{4+}	:	Zirconium ion
ZrO_2	:	Zirconium dioxide

LIST OF SYMBOLS

μ	:	Mobility of ion
A	:	Cross sectional area
Å	:	Angstrom
b	:	Bulk
C	:	Capacitor
D	:	Diffusion coefficient
e	:	Electron
Ea	:	Activation energy
f	:	Frequency
gb	:	Grain boundary
k	:	Boltzmann constant
K	:	Magnitude of charge carrier concentration
n	:	Concentration of ion
R	:	Resistance
R_b	:	Bulk resistance
R_{gb}	:	Grain boundary resistance
s	:	Frequency exponent
T	:	Temperature
t_{ion}	:	Ionic transference number
W_m	:	Binding energy
Z	:	Impedance
γ	:	Correlation factor
ε‟	:	Dielectric constant
ε”	:	Dielectric loss

ε_0	:	Permittivity of free space
θ	:	Bragg angle
λ	:	Wavelength
ζ	:	Conductivity
ζ_0	:	Pre-exponential factor of conductivity
ζ_{AC}	:	Alternating current conductivity
ζ_{DC}	:	Direct current conductivity
ω	:	Angular frequency
ω_p	:	Ionic hopping rate

CHAPTER 1: INTRODUCTION

1.1 Introduction

Increasing demands for high-energy-rechargeable batteries have developed battery technology. Many types of rechargeable batteries have been developed so far. Among them, the rechargeable lithium ion battery has been recognized as the most suitable battery for mobile information devices due to its high energy and power densities (Kotobuki & Koishi, 2013). Lithium ion batteries mainly consist of graphite negative electrode, organic liquid electrolyte, and lithium transition-metal oxide ($LiCoO_2$) positive electrode.

This type of batteries was firstly commercialized in 1991 and then such batteries have been widely spread out all over the world as a power source for mobile electronic devices such as cell phone, laptop and camcorder (Tatsumisago et al., 2013) . Figure 1.1 shows the examples of lithium battery applications and the form of cells used (Wang et al., 2015). The bulk size batteries are used in smart phones, laptops and even in electric vehicles. However, as the miniaturization trend dominates the market, microbatteries are used in medical devices, microelectronics and integrated circuits.

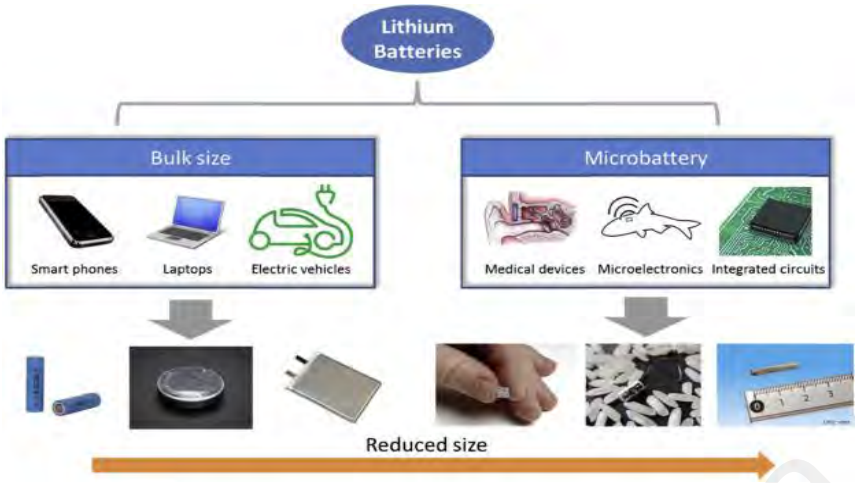

Figure 1.1: Examples of lithium battery applications and the form of cells used (Wang et al., 2015)

The liquid electrolytes used in the Li ion batteries, however, suffer several drawbacks compared to solid electrolytes. The drawbacks include limited temperature range of operation, device failure due to electrode corrosion by electrolyte solution, leakage and unsuitable shapes (Anantharamulu et al., 2011). So as an alternative, a suitable and ideal solid electrolyte with high ionic conductivity ($< 10^{-4}$ S cm^{-1}) at operating temperature, low electronic conductivity and also good electrochemical stability toward electrodes (> 4.5 V) is required to overcome these disadvantages.

Furthermore, solid electrolytes also are simple in design, can act as a natural seal, resistance to shock and vibration, resistance to pressure and temperature variations, possess a wider electrochemical stability and better safety (Park et al., 2010) . In addition, they also have thermal expansion compatible with that of electrodes and other construction materials, negligible volatilization of components, suitable mechanical properties and negligible interaction with electrode materials under operation conditions (Sarıboğa et al., 2013). Besides that, a negligibly small grain-boundary resistance is important in the case of when sing polycrystalline ceramic type materials. Finally, as in

all industrial developments, the solid electrolytes must be environmentally benign, non-toxic, non-hygroscopic, low cost materials and their preparation method should be easy (Knauth, 2009).

1.2 Background to research

Solid electrolytes are considered intermediate in structure and property between normal crystalline solid with regular three dimensional structures and immobile atoms or ions and liquid electrolytes which do not have regular structures but do have mobile ions (West, 1984). Based on their microstructure and physical properties, solid electrolytes are categorized into four categories: framework inorganic crystalline material (ceramics), amorphous glassy electrolyte, polymer electrolyte and composite electrolyte. In the search for new ion conducting crystalline materials, ceramic electrolytes form an important class of materials. This type of electrolytes presents advantages such as the high elastic moduli which makes them more suitable for rigid battery designs for example in thin-film-based devices. Furthermore, ceramics electrolytes also are more suitable for high temperature and aggressive environments (Fergus, 2012).

Another remarkable feature of solid electrolytes in addition to their contribution to the safety issue is their ion selectivity that is only Li^+ or Na^+ or Mg^{2+} ions are mobile in them. They do not accommodate any mobile species other than Li^+ or Na^+ or Mg^{2+} ions for example counter anions and molecules of the solvents as liquid or polymer electrolytes, which can diffuse to the surface of the electrodes and may cause side reactions. Therefore, side reactions hardly occur in solid-state systems. In other words,

the employment of solid electrolytes will solve the problems including capacity fading and self-discharge caused by the side reactions. In fact, solid state batteries showed remarkably long cycle life over 20000 cycles and self-discharge was very small even in the storage at elevated temperatures (Takada et al., 2004).

Among solid electrolytes, NASICON (Sodium Superionic Conductor) type ion conductors have been tested widely in energy applications for instance in batteries, electric vehicles, sensors and etc. (Vijayan & Govindaraj, 2012). According to Hong (1976), high ion conductivity and stability of phosphate units are advantages of NASICON over other electrolyte materials (Hong, 1976). Among the batteries, those based on lithium shows the best performance.

1.3 Problem Statements

Synthesis route plays an important role in determining chemical and physical properties of the materials. Normally, the most common method that is used to prepare NASICON materials is the conventional method of solid state method. However, the materials prepared by solid state method have certain drawbacks such as the use of high heating temperature (usually >1000°C), long heating time up to one or two days, contamination of impurities, volatilization and lack of control of microstructure and composition. The preparation method also produces materials that are not free of grain boundary resistance, thus resulting in low conductivity. Furthermore, the synthesis of NASICON compound of a pure phase without any second phases is very difficult, especially when performed by solid state reaction (Traversa et al., 2000). Recently, Norhaniza et al. (2010, 2011, 2012, 2013) has succeeded in obtaining stable pellets of

$LiSn_2P_3O_{12}$ via mechanical milling method but the prepared compound still contains impurity (Norhaniza et al., 2010, 2013; Norhaniza et al., 2012; Norhaniza et al., 2011). So, in this study, citric acid assisted sol-gel method is considered in order to overcome the problems. This simple method of sol-gel may yield homogenous and high purity materials leading to low grain boundary resistance. This method is also suitable for both small and large scale productions (Adnan et al., 2011).

Furthermore, in the NASICON family, Martinez-Juarez et al. (1997) and Lazarraga et al. (2004) have reported that $LiSn_2P_3O_{12}$ having low ionic conductivity (~ 10^{-10} S cm^{-1}) (Lazarraga et al., 2004; Martinez-Juarez et al., 1997). The studies were done by mixing the compound with teflon as a binder in order to improve the stability of the compound as it can be easily broken due to the phase change phenomena. This was due to the structure transition (monoclinic to rhombohedral structure) which yielded changes in the lattice volume leading to breakage of the sample pellets. Norhaniza et al. (2010; 2011; 2012; 2013) has succeeded in obtaining stable pellets of $LiSn_2P_3O_{12}$ via mechanical milling method without any use of binding agent but the ionic conductivity of the compound was ~10^{-7} Scm^{-1} at room temperature. Further enhancement in conductivity by one order of magnitude was also observed by partial substitution at P (V^{5+}) or Sn (Cr^{3+}) sites. Substitution at both P and Sn ($V^{5+,}$ Cr^{3+}) sites led to further enhancement of conductivity by two orders of magnitude. So, the low conductivity value can further be improved by modifications of lattice parameters, structure and bottle neck size via partial substitution. This may be effectively done by ions substitutions using trivalent (Cr^{3+}, Al^{3+}) and tetravalent (Si^{4+}, Zr^{4+}) ions at Sn^{4+} and P^{5+} site .

Previous study also only focused on structural properties of $LiSn_2P_3O_{12}$ based compound as reported by previous researchers (Iglesias et al., 1997; Martinez-Juarez et al., 1995; Martinez et al., 1994). Meanwhile in electrical studies, previous works also focused only on the DC conductivity of the stannum based compound (Lazarraga et al., 2004; Martinez-Juarez et al., 1997; Norhaniza et al., 2010, 2013; Norhaniza et al., 2012; Norhaniza et al., 2011). To date, other properties such as AC conductivity and electrochemical stability window have not yet been reported in literature. Furthermore, DC and AC conductivity of $LiSn_2P_3O_{12}$ parent and modified compounds prepared via sol-gel method also have not been reported so far. The study on both DC and AC conductivity are important in order to elucidate the ionic conduction such as charge carrier concentration, mobile ion concentration and ion hopping rate. Meanwhile, the study on electrochemical stability window is important in order to determine the suitable application for the $LiSn_2P_3O_{12}$ based compound.

1.4 Research Objectives

The main objectives of this research are summarized as follows:

1. To optimize the parameters of sol-gel method in obtaining NASICON-structured lithium stannum phosphate, $LiSn_2P_3O_{12}$ compound with minimum impurity.
2. To modify the structural properties of $LiSn_2P_3O_{12}$ compound by ion substitutions using trivalent (Cr^{3+}, Al^{3+}) and tetravalent (Si^{4+}, Zr^{4+}) ions at Sn^{4+} and P^{5+} sites .
3. To study the effects of ion substitutions to the electrical and electrochemical properties of the modified NASICON compound.

1.5 Scope of study

In this study, $LiSn_2P_3O_{12}$ parent compound was prepared via low temperature water based sol-gel method. The parameters of sol-gel method have been optimized by sintering at two different sintering times, 24 and 48 hours and different sintering temperature ranging from 500°C to 650°C in order to minimize impurity in the NASICON compound. The samples undergo various characterizations including X-Ray Diffraction (XRD), Fourier Transform Infrared spectroscopy (FTIR), Scanning Electron Microscopy (SEM), Energy Dispersive X-ray (EDX), particle size analysis and the optimum samples were characterized using Impedance Spectroscopy (IS), transference number measurement and Linear Sweep Voltammetry (LSV).

Then the effects of ion substitutions using smaller ionic radius, r_{ion} trivalent ions, Cr^{3+} (r_{ion} = 0.52 Å) and Al^{3+} (r_{ion} = 0.53 Å) at Sn^{4+} (r_{ion} = 0.69 Å) site to the structural properties of $LiSn_2P_3O_{12}$ compound were studied using X-ray diffraction. Besides that, the effects of ion substitutions using larger ionic radius, r_{ion} tetravalent ions, Zr^{4+} (r_{ion} = 0.72 Å) and Si^{4+} (r_{ion} = 0.40 Å) at P^{5+} (r_{ion} = 0.38 Å) site to the structural properties of $LiSn_2P_3O_{12}$ compound were also investigated.

Last but not least, the effects of ion substitutions; trivalent ions (Cr^{3+} and Al^{3+}) at Sn^{4+} site and tetravelant ions (Zr^{4+} and Si^{4+}) at P^{5+} site to the electrical and electrochemical properties of the modified NASICON compound were studied. Electrical properties measured include DC and AC conductivity analyses and transference number measurement while electrochemical properties were studied using linear sweep voltammetry.

1.6 Organization of thesis

This thesis is divided into seven chapters. General introduction is presented in Chapter 1. The overview of the NASICON-structured solid electrolytes is given in detail in Chapter 2. Meanwhile, Chapter 3 focuses on the experimental details including the synthesis method that is sol-gel method and also characterization techniques used.

Chapter 4 focuses on the results and discussions of $LiSn_2P_3O_{12}$ parent compound that consists of two system; System I ($LiSn_2P_3O_{12}$ sample sintered for 24 hours) and System II ($LiSn_2P_3O_{12}$ sample sintered for 48 hours). In this chapter the effects of different sintering times and temperatures on the structural, electrical and electrochemical properties are presented.

In Chapter 5, the effects of trivalent ions, Cr^{3+} and Al^{3+} substitutions at Sn^{4+} site on the structural, electrical and electrochemical properties of $LiSn_2P_3O_{12}$ are discussed. The substitutions of Cr^{3+} and Al^{3+} yielded compounds with the general formula of $Li_{1+x}Cr_xSn_{2-x}P_3O_{12}$ and $Li_{1+x}Al_xSn_{2-x}P_3O_{12}$ with x = 0.1, 0.3, 0.5, 0.7 and 0.9.

Chapter 6 presents the results and discussions of the effects of tetravalent ion substitutions (Zr^{4+} and Si^{4+}) at P^{5+} site on the structural, electrical and electrochemical behaviour of $LiSn_2P_3O_{12}$. The substitutions of Zr^{4+} and Si^{4+} yielded compounds with the general formula of $Li_{1+y}Sn_2P_{3-y}Zr_yO_{12}$ and $Li_{1+y}Sn_2P_{3-y}Si_yO_{12}$ with y = 0.1, 0.3, 0.5, 0.7 and 0.9.

Chapter 7 presents the conclusions of the present work as well as suggestions for further work.

CHAPTER 2: LITERATURE REVIEW

2.1 Electrolytes

Solid State Ionics (SSI) is about the properties associated with the motion of ions in solids (Kudo & Fueki, 1990) that represents the electrolytes. The electrolytes are the conducting medium in which the flow of current is accompanied by the movement of matter in the form of ions. The electrolytes material separates the cathode and anode in any of the electrochemical devices such as batteries, fuel cells, supercapacitors and sensors.

2.2 Solid electrolytes

The conventional rechargeable batteries supply high energy and power densities in various electronic devices. However, they contain hazardous and flammable organic liquid electrolytes, making them potentially unsafe (Notten et al., 2007; Thangadurai & Weppner, 2006) . The uses of solid electrolytes in the next generation lithium ion batteries provide numerous advantages, such as prevention of electrolyte leakage, improves the thermal and mechanical stability, no self-discharge and longer life cycle as well as increasing the possibility of miniaturization and integration. Hence, the development of new solid inorganic electrolytes to be applied in all-solid-state lithium ion batteries is currently the key issue of this technology (Scrosati, 2000). In the past few decades, research efforts were directed towards finding suitable solid electrolytes for lithium ion batteries with high lithium ion conductivity along with high electrochemical stability in contact with commonly used intercalation electrode materials for battery applications (Kamaya et al., 2011).

However, the ideal solid electrolytes to be employed in electrochemical devices should possess the following characteristics (Agrawal & Gupta, 1999; Robertson et al., 1997) :

i. High ionic conductivity at operating temperature ($10^{-1} – 10^{-4}$ S cm^{-1})
ii. Low or negligible electronic conductivity
iii. The absence of side reactions (chemical reactions) with the anode and cathode
iv. Non-hygroscopic
v. Low cost of fabrication
vi. Environmentally safe
vii. Wide electrochemical stability window
viii. The sole charge carriers should be only ions and ionic transference number value, $\eta_{ion} \approx 1$
ix. Low activation energy (> 0.3 eV)

2.3 Classification of solid electrolytes

Based on the microstructure and physical properties, solid electrolytes are categorized into four categories: polymer electrolytes, amorphous glassy electrolytes, composite electrolytes, and crystalline electrolytes.

2.3.1 Polymer electrolytes

Polymers are formed by an almost regular repetition (monomers) of units (atomic groups) connected by chemical bonds which form linear long chains or branched, or three-dimensional net (polymerization). Meanwhile, the polymer electrolytes consist of

polymers and salts or acids (Marcinek et al., 2015). These electrolytes possess several advantageous properties over other solid electrolytes such as non-volatility, shape flexibility, high mechanical integrity, mouldability, and flexible thin film which are formed by ensuing intimate electrode-electrolyte contacts during the fabrication of all-solid-state electrochemical devices (Armand, 1986; Marcinek et al., 2015) . Fenton et al. (1973) synthesized the first polymer electrolyte membranes by making complex alkali ion salts with a high molecular weight polar polymer i.e. polyethylene oxide (PEO) (Fenton et al., 1973).

Later on, based on poly (ethylene oxide) (PEO) - Li^+ - salt complex of solid polymer electrolyte (SPE) was demonstrated as a practical thin film battery for the first time by Armand et al. (1979) (Armand et al., 1979). This discovery attracted a widespread attention both in the academic and industrial sectors. As a result, a large number of polymer electrolytes involving different mobile ions (H^+, Li^+, Na^+, K^+, Ag^+, etc.) as principle charge carriers have been investigated during the last three and a half decades and explored their potential applicability as the electrolytes in a variety of all-solid-state electrochemical power sources, namely high power density rechargeable batteries, fuel cells, and supercapacitors.

On the basis of different preparation routes adopted during the casting of polymer electrolyte membranes as well as on their physical conditions, these materials were grouped into following broad categories:

- Conventional polymer salt complexes / dry SPEs
- Plasticized polymer-salt complexes and/or solvent swollen polymers
- Gel polymer electrolytes

• Rubbery polymer electrolytes

• Composite polymer electrolytes

The conduction mechanism in polymer electrolytes is associated with the local motion of polymer known as segmental motion in the vicinity of the ion (Armand, 1986). However, the main drawbacks that are limiting further development of polymer electrolytes are related to their very low conductivity value at room temperature (below 10^{-5} S cm^{-1}), and possessed low lithium transference number (ranging from 0.2 - 0.3) (Scrosati & Vincent, 2000).

2.3.2 Amorphous-glassy electrolytes

Fast ion conduction in amorphous-glassy solid electrolytes has attracted lots of attention in the later part of 1970. There are several advantages of these electrolytes from the viewpoint of ion conduction compared to the crystalline ones such as a wide range of selection compositions, isotropic properties, no grain boundaries, and easy film formation. Because of its so-called open structure, the ionic conductivity of amorphous materials is higher than that of the crystalline ones. In addition, a single ion conduction can be realized because of the glassy materials which belong to the decoupled systems where the mode of ion conduction relaxation is decoupled from the mode of structural relaxation (Minami et al., 2006).

Fast ion conduction in a melt-quenched glassy system known as AgI-Ag_2SeO_4 was reported for the first time in 1973 (Kunze & Van Gool, 1973). This glassy electrolyte exhibits very high Ag^+ ion conductivity (~ 10^{-2} S cm^{-1}) at room temperature. Since then,

a large number of superionic glasses involving different kinds of mobile ions such as Ag^+, Cu^+, Li^+, Na^+, F^- etc. have been reported (Minami, 1985; Tatsumisago et al., 1991). Among the variety of superionic glasses, Ag^+ ion conducting glassy electrolytes attracted relatively wider attentions as they exhibited relatively higher conductivity at room temperature and the materials handling and synthesis of glass are easier (Chandra et al., 2013; Souquet, 1981).

There are also several disadvantages concerning these amorphous – glassy electrolytes such as complicated synthesis technology, highly water reactive, and highly corrosive in silica containers. These difficulties limits their usage commercially.

2.3.3 Composite electrolytes

Composite solid electrolytes also referred as the dispersed solid electrolytes, are high ion conducting multiphase solid systems. These electrolytes have attracted great technological attentions after 1973 (Liang, 1973) as potential candidates for all solid state electrochemical device fabrication. They are mainly two - phases mixture, containing a moderately conducting ionic solid (AgI, CuI, etc.) as first – phase host salt and a second - phase material, may be either an inert insulating compound (Al_2O_3, SiO_2, ZrO_2, Fe_2O_3, etc.) or another low conducting ionic solid (AgBr, AgCl, KCl, etc.). As a consequence of dispersal of submicron sized particles of the second - phase in a small fraction into the first - phase host salt, a substantial improvement in various physical properties of the host is usually achieved without altering the structural/chemical nature of the constituent compounds. Both phases coexist together separately in the composite system. In two phases composite electrolytes, an enhancement of one to three orders of magnitudes could be obtained in the conductivity value at room temperature. For the

first time in 1973 , Liang reported a remarkable enhancement of Li^+ conductivity in a two - phase composite electrolyte system defined as LiI - Al_2O_3 (Liang, 1973). Since then, a large number of two - phase composite electrolytes involving different mobile ions such as Ag^+, Cu^+, Li^+, etc., has been investigated (Agrawal & Gupta, 1999; Chandra & Laskar, 1989; Liang et al., 1978; Wagner, 1980). The size of particles of second - phase dispersoid plays a significant role in improving the physical properties of the first - phase host salt especially the conductivity. Hence, the dispersal of nanosized particles would result in a substantial enhancement in the conductivity.

2.3.4 Crystalline electrolytes

The study on ionic conduction in solids was initiated in 1838 when Faraday discovered PbF_2 and Ag_2S as good conductors of electricity. In subsequent years, a variety of solids exhibiting appreciably high ion conductivity at their operating temperature was recognized. Silver ion conducting solids of the type, $RbAg_4I_5$, were discovered in the early sixties and were employed in the electrochemical cells (Bradley & Greene, 1967). The Na-β-alumina was successfully utilized in Na/S batteries in 1967 (Yao & Kummer, 1967). Hong (1976) and Goodenough et al. (1976) have reported a high ion conducting skeleton structure having polyhedral units popularly known as NASICON (Na Super Ionic Conductor) as can be seen in Figure 2.1 (Goodenough et al., 1976; Hong, 1976). The polyhedral skeleton structure consists of rigid (immobile) sub-array which provides a large number of three-dimensionally connected interstitial sites suitable for long range motion of monovalent cations. In contrast to the β-Al_2O_3, Na^+ ions move within three-dimensional channels of the structure in the NASICON compound. Analogous compounds, such as LISICON, were synthesized shortly after that (Goodenough et al., 1976; Hong, 1978). From 1970 onwards, several studies

focusing on the synthesis and characterization of lithium ion conductors were reported. The enhanced interest on lithium ion conductors was driven by the small ionic radii, lower weight, ease of handling and its potential use in high energy density batteries. Besides that, the Li_4SiO_4 as well as its non-stoichiometric solid solution of $Li_{4-3x}Al_3SiO_4$ ($0 \leq x \leq 0.5$) was also one of the promising Li^+ fast ionic conductors.

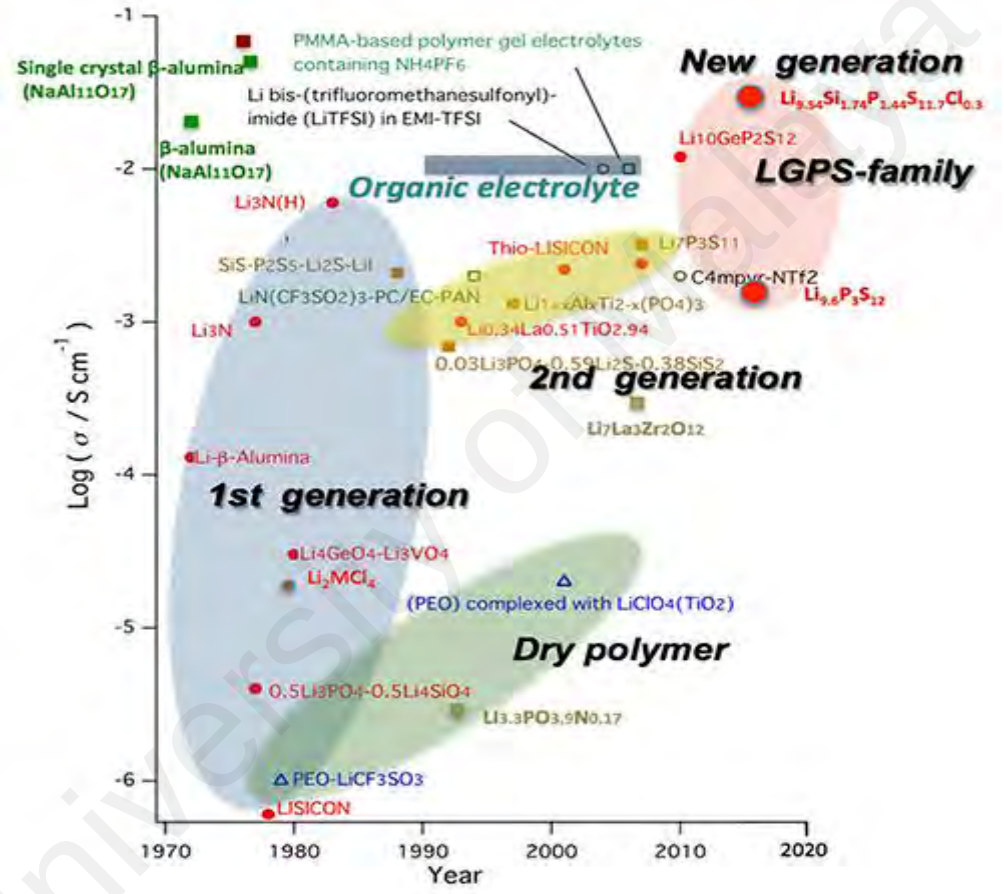

Figure 2.1: History of lithium superionic conductor (Kato et al., 2016)

2.3.4.1 Garnet-type

The garnet type compounds recieved significant attention in the field of materials science, due to their favorable magnetic, optical and electrical properties (Kahn et al., 1969). Garnet-type materials exhibit a general chemical formula of $A_3B_2(XO_4)_3$ (A = Ca, Mg, Y, La or rare earth; B = Al, Fe, Ga, Ge, Mn, Ni or V; X = Si, Ge, Al) where A, B and X are eight, six and four oxygen coordinated cation sites, which crystallize in a face centered cubic structure with the space group $Ia\bar{3}d$. Figure 2.2 shows the structure of ideal garnet-type metal oxides (Thangadurai et al., 2014). The compounds which exhibit useful technologically related physical and chemical properties become ideal materials for magnetic and optical devices. Another unique and perhaps the most important, but rather uncommon characteristic of Li ion excess garnet-type materials is the ionic conduction.

Commonly studied garnets typically contain five to seven Li atoms per formula unit, and are referred to as the Li-stuffed (Li-rich) garnets. It possesses more Li that can be accommodated at the tetrahedral sites, leaving excess Li at the octahedral sites in the garnet structure (Thangadurai et al., 2014). The first reported Li ion conducting Li-stuffed garnets are the $Li_5La_3M_2O_{12}$ (M = Nb, Ta), which were developed in 2003 (Thangadurai et al., 2003). The maximum lithium ionic conductivity of about 4×10^{-5} S cm^{-1} was obtained at room temperature for barium doped samples, $Li_6La_2BaTa_2O_{12}$ (Thangadurai & Weppner, 2005). The Ta^{5+} or Nb^{5+} ions were substituted by ions such as In^{3+}. The lithium ionic conductivity can reach 1.8×10^{-4} S cm^{-1} at 323 K in indium doped samples that is $Li_{5.5}La_3Nb_{1.75}In_{0.25}O_{12}$ (Knauth, 2009).

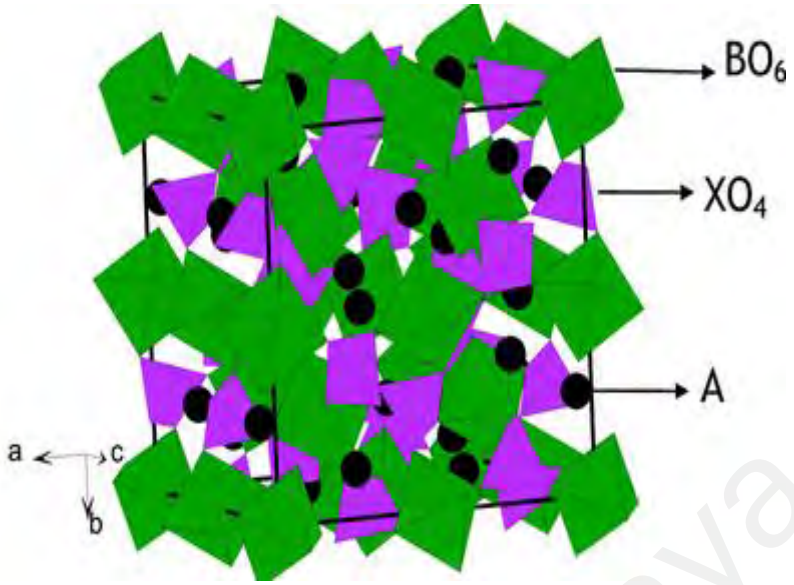

Figure 2.2: Idealized crystal structure of garnet – type materials (Thangadurai et al., 2014)

2.3.4.2 Perovskite-type

Perovskitese-type, ABX_3 with generally cubic crystal symmetry were extensively studied due to their functional properties such as electronic, magnetic, ferroelectric, ion conducting and optical properties (Galasso, 2013). The structure of perovskite is often depicted by corner-shared BX_6 octahedra enclosing 12 coordinated A-site ions as shown in Figure 2.3 (Zhang et al., 2011). Perovskites have different modifications, some have regular octahedra which are corner-shared in a straight line, but some others also have distorted structures accompanied by the distortion and tilting of the BX_6 octahedra and cation displacements. Their properties can easily be tuned due to the simple structure which tolerates various kinds of chemical substitution on A, B and X sites (Sebastian & Gopalakrishnan, 2003).

Latie et al. in 1984 reported the first lithium ion conducting perovskite by heterovalent substitution of La^{3+} by Li^{+} cations in the A-site deficient perovskite $La_2/_3TiO_3$ (Latie et al., 1984). Since then, $La_{2/3-x}Li_{3x}TiO_3$ (with optimum x ≈ 0.11) has stimulated a wide interest because of its high bulk lithium ion conductivity (10^{-3} S cm^{-1}). The high lithium ion conductivity in $La_{2/3-x}Li_{3x}TiO_3$ can be attributed to the presence of many equivalent sites which enable the lithium ions to move freely along A-site vacancies (Harada et al., 1999) that are affected by the charge carrier concentration, the degree of order on the A-site, and the bottleneck size.

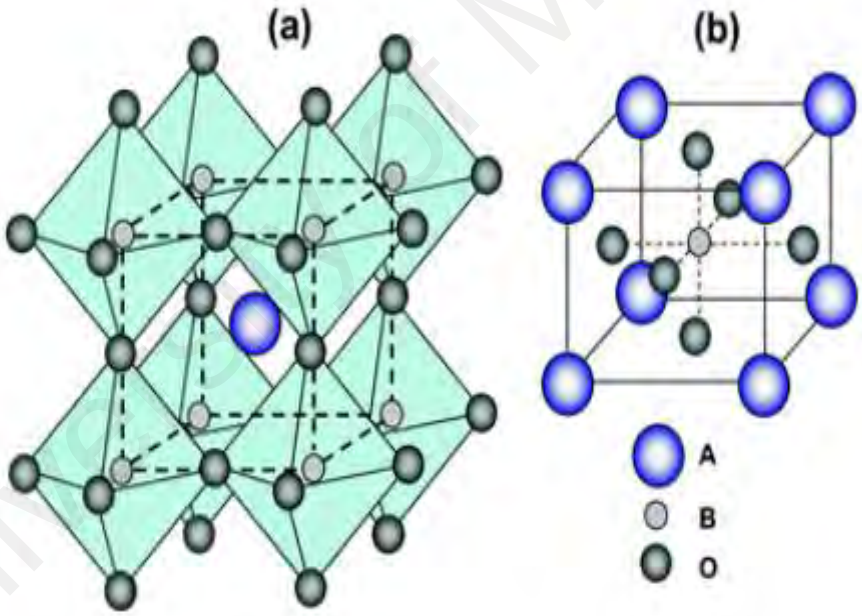

Figure 2.3: The structure of perovskite ABO_3, (a) corner-sharing (BO_6) octahedra with A ions located in 12-coordinated interstices, (b) B-site cation at the center of the cell (Zhang et al., 2011)

2.3.4.3 LISICON-type

LISICON (Lithium Super Ionic Conductor) compound firstly reported was $Li_{3.5}Zn_{0.25}GeO_4$ which is a member of the solid solutions of $Li_{2+2x}Zn_{1-x}GeO_4$ ($-0.36 < x < 0.87$) (Bruce & West, 1980; Hong, 1978). These solid solutions were based on stoichiometric and fully ordered Li_2ZnGeO_4, which is iso-structural with γ-Li_3PO_4 and can be derived by the double substitution of P^{5+} and Li^{+} by Ge^{4+} and Zn^{2+}, respectively.

The Li-rich solid solutions, including $Li_{3.5}Zn_{0.25}GeO_4$, crystallizes in the *Pnma* orthorombic space group as shown in Figure 2.4 and the LISICON network is formed by elements of $[Li_{2+x}Zn_{1-x}GeO_4]^{x-}$ and the remaining x amount of lithium (Li_x). The bottleneck size between these connected sites is large enough to fulfill the geometrical conditions for the fast lithium ion transport in two dimensions. The Zn rich compounds ($x < 0$) contain vacant Li^{+} in the tetrahedral sites (Abrahams et al., 1988).

The highest lithium ion conductivity measured is 0.12 S cm^{-1} at 300 °C but only 1×10^{-7} S cm^{-1} at room temperature can be reached with $Li_{3.5}Zn_{0.25}GeO_4$ stoichiometry ($x \approx 0.75$) (Bruce & West, 1982). A wide range of materials has been synthesized within the LISICON family, with the framework related to the γ-Li_3PO_4 structure and are formed by GeO_4, SiO_4, PO_4, ZnO_4 or VO_4 tetrahedra. From those possible compounds, $Li_{3.6}Ge_{0.6}V_{0.4}O_4$ showed the highest room temperature conductivity around 4×10^{-5} S cm^{-1} among the others (Kuwano & West, 1980) whereas the $Li_{3.4}Si_{0.4}V_{0.6}O_4$ was found to be stable in contact with lithium even above the 180 °C. The $Li_{3.4}Si_{0.4}V_{0.6}O_4$ has a slightly lower ionic conductivity of 1×10^{-5} S cm^{-1} at room temperature than germanium analogues (Khorassani & West, 1984). Recently, in the Li_4SiO_4 compound, partial substitution of Si^{4+} with Sn^{4+} considerably raises the

conductivity of the system with a maximum conductivity value of 3.07×10^{-5} S cm^{-1} at ambient temperature and 1.30×10^{-4} S cm^{-1} at 500 °C (Adnan & Mohamed, 2014).

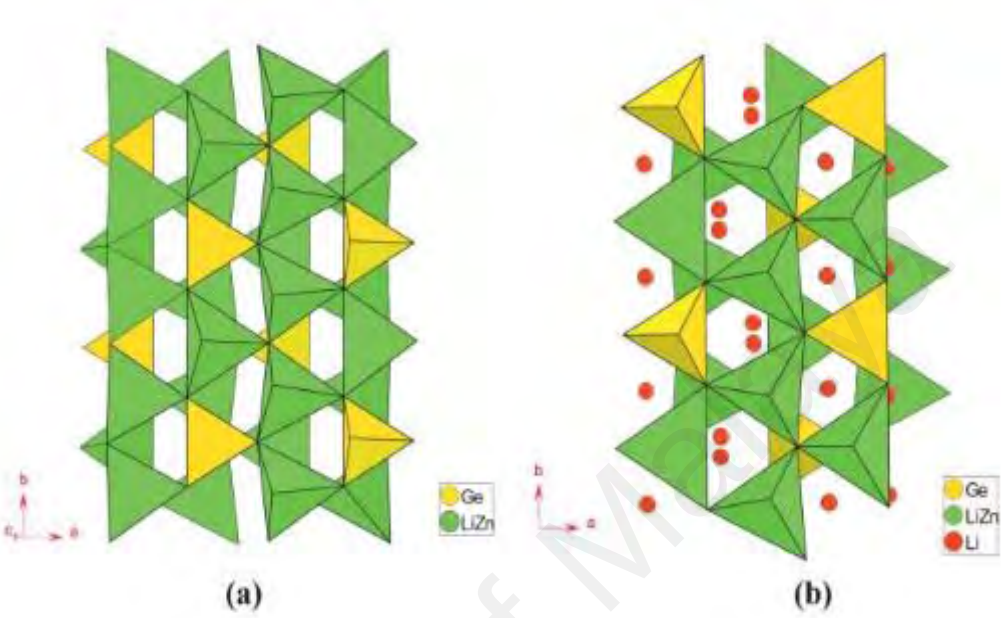

Figure 2.4: Structures of (a) Li_2ZnGeO_4 and (b) $Li_{3.5}Zn_{0.25}GeO_4$.In (b), the red circles within the channels denote interstitial Li^+ ions (Sebastian & Gopalakrishnan, 2003)

2.4 NASICON

NASICON (Sodium Superionic Conductor) type ion conductors were widely tested in energy applications of electric vehicles. High ionic conductivity and stability of phosphate units are the advantages of NASICON over other electrolyte materials. It was first discovered by Hong (1976) and Goodenough et al. (1976) with the general formula of $Na_{1+x}Zr_2Si_xP_3O_{12}$ (Goodenough et al., 1976; Hong, 1976).

2.4.1 Structure of $NaZr_2(PO_4)_3$

The basic structure of $Na_{1+x}Zr_2Si_xP_3O_{12}$ is rhombohedral which consists of a three-dimensional framework of corner-shared ZrO_6 octahedra and PO_4 tetrahedra. This $[Zr_2(PO_4)_3]^-$ framework is highly stable due to its covalent nature and shows high melting points (> 1650°C) (Kumar & Yashonath, 2006).Two ZrO_6 octahedra are separated by three $(Si,P)O_4$ tetrahedra that share corner oxygen atoms and two types of Na sites ($Na_1$and Na_2) (Song et al., 2014). The Na_1 site is located in between two octahedra along the *c* axis and other site, Na_2 is at the midway of two Na_1 sites along the *a* axis (Yadav & Bhatnagar, 2012). The two sodium sites, Na_1 and Na_2, inside the channels, are connected through triangular bottlenecks of oxygen atoms. The bottleneck between both sites of the rhombohedral symmetry is formed by three oxygen atoms whose centers make up an isosceles triangle. High ionic conductivity, due to the movement of sodium ions, depends on the size of the bottleneck, activation energy required for the movement of ions and lattice parameters whose value can be modified by changing compositions (Yadav & Bhatnagar, 2012).

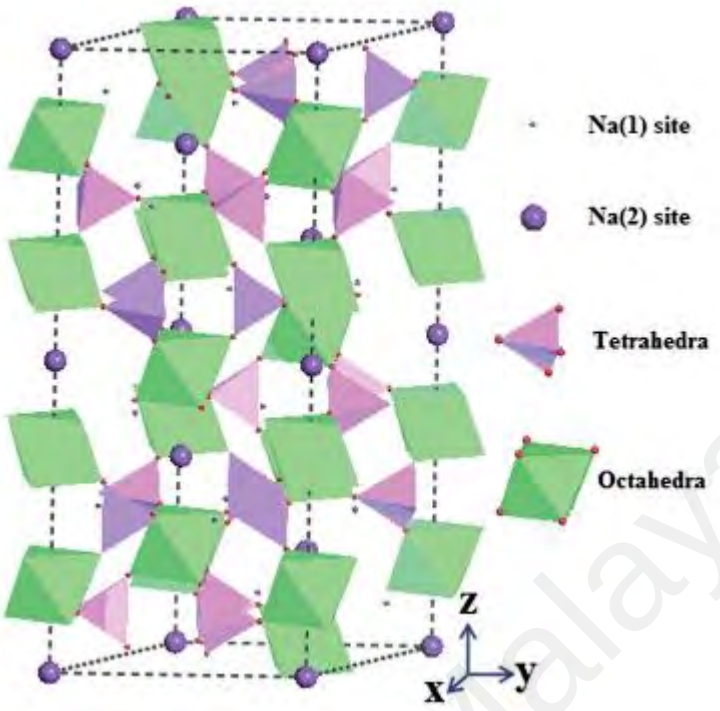

Figure 2.5: Schematic representation of $NaZr_2(PO_4)_3$ (Song et al., 2014)

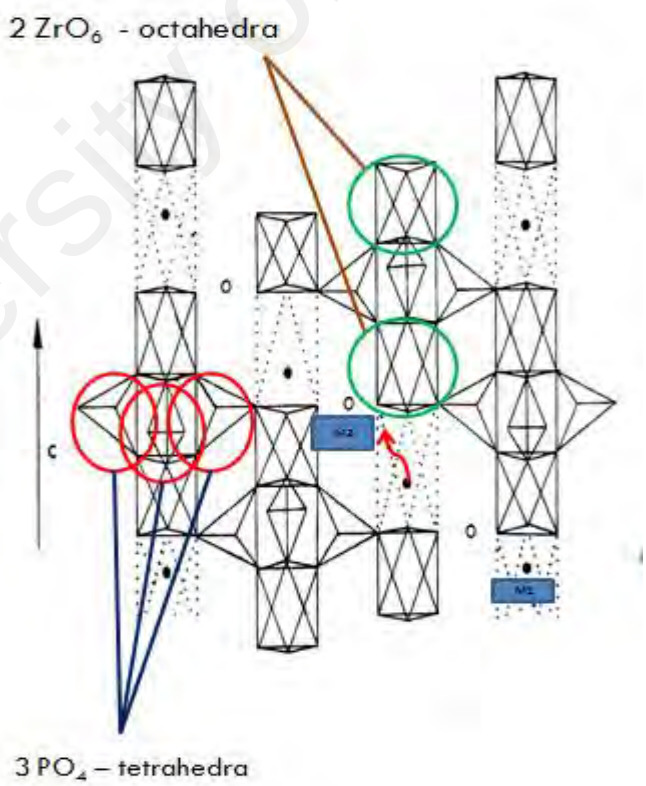

Figure 2.6: A view of the $NaZr_2(PO_4)_3$-structure parallel to the c axis. M(1), shown as filled circle (●), and M(2), shown as open circle (○). (Kumar & Yashonath, 2006)

Meanwhile, the Lithium Stannum Phosphate ($LiSn_2P_3O_{12}$) is a Li^+ ion conductor that shows NASICON type structure (Cui et al., 2012; Martinez et al., 1994; Martinez-juarez et al.,1996; Norhaniza et al., 2010).Two crystallographic phases have been reported for this compound (Iglesias et al., 1997; Martinez et al., 1994; Martinez-juarez et al., 1996); a high temperature phase with rhombohedral R3c symmetry and high ionic conductivity, a low-temperature phase with triclinic P_1 symmetry or monoclinic Cc symmetry and lower conductivity. Similar to the $Na_{1+x}Zr_2Si_xP_3O_{12}$, the $LiSn_2P_3O_{12}$ framework also consists of two types of sites that can be occupied by lithium ions: M_1 sites located between SnO_6 octahedral sites having six coordination with oxygens forming SnO_6 octahedra and; M_2 sites located between the ribbons of PO_4 tetrahedra possessing a distorted eight coordination with oxygens. Both sites are arranged in an alternating form of a 3D array along conduction channels, also known as the bottlenecks, which allow transportation of cations. The corner sharing bonding in this framework also allows rotation of the framework, while the modifications like partial substitution may be done to improve its properties (Arbi et al., 2007; Losilla et al., 1997). Besides, the stannum based compound are selected as they can be easily synthesized, less expensive, safe, thermodynamically stable and insensitive to the atmospheric surrounding.

2.4.2 Replacement of Cation

Since the discovery of NASICON by Hong (1976) and Goodenough et al. (1976), remarkable studies have been conducted to improve the ionic conductivity of the compound. As a result of corner sharing oxygens, NASICON structure has a flexible framework which allows the replacement of Na^+ ions by ions of different sizes (Table 2.1) such as Li^+, K^+, Mg^+ and Cs^+. The replacement causes the rotation in the skeleton

of the NASICON in order to accommodate the cation as shown in Figure 2.7. However, the rotation only modifies the lattice parameters but the NASICON structure is still maintained.

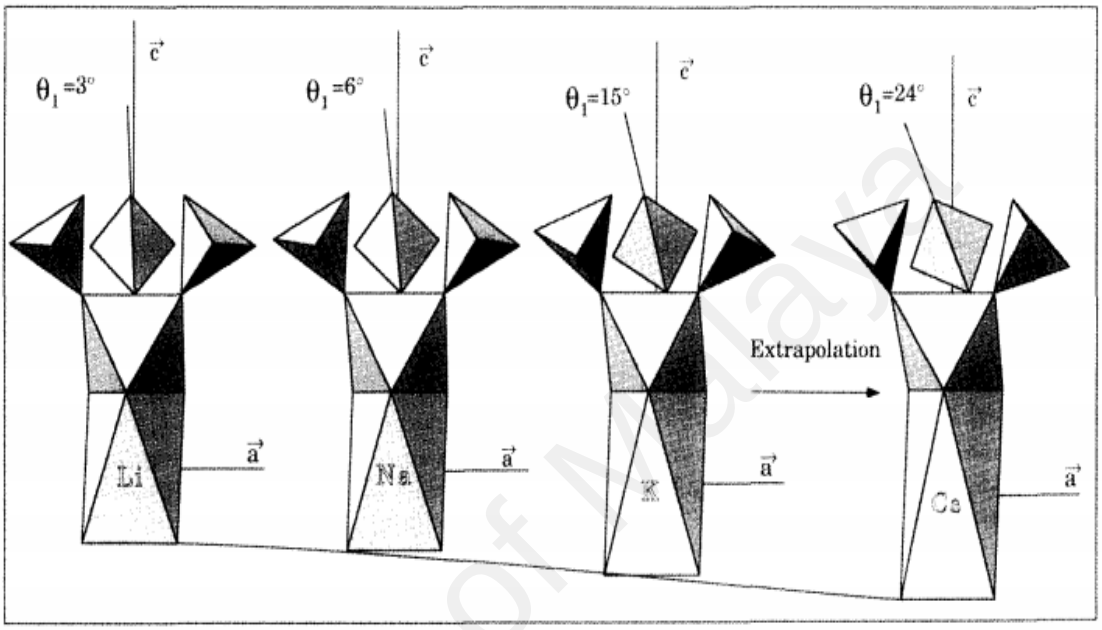

Figure 2.7: Different replacement of cation produces the rotation in PO_4 tetrahedra in the NASICON skeleton (Alamo, 1993)

In this study, Li^+ (r_{ion} = 0.76 Å) ions are chosen to replace Na^+ (r_{ion} = 1.02 Å) ions in the $Na_{1+x}Zr_2Si_xP_3O_{12}$. Replacement of smaller ionic radius of the ions will alter the conduction channels in the NASICON structure that will lead to the enhancement of the conductivity.

2.4.3 Partial Substitution

Apart from the replacement at the Na^+ site, partial substitutions can also be done at Zr^{4+} and P^{5+} sites. Kumar and Yashonath (2006) have listed the possible ions to be replaced at Na^+, Zr^{4+} and P^{5+} as in Table 2.1 (Kumar & Yashonath, 2006). According to

Knauth (2009), the strength of the NASICON framework increases when partial substitutions of ions with higher oxidations state at Zr^{4+} and P^{5+} sites (Knauth, 2009). Partial substitutions will cause changes in the value of *a* and *c* parameters resulting in a change of the size of the bottleneck channel. Partial substitutions are also normally carried to allow the optimization of the size of the bottleneck so that mobile ions can move easily in the structure and enhance the conductivity of the compound.

Table 2.1: List of ions for replacement and partial substitutions (Kumar & Yashonath, 2006)

Site	Replacement/ Substitutions
Na	Group I : H, Li, K, Rb, Cs, NH_4, Cu, Ag, Ti....
	Group II: Mg, Ca, Sr, Ba, Mn, Co, Zn, Pb, Fe....
Zr	Group II: Cu, Mg, Zn, Mn, Ni...
	Group III: Cr, Fe, Al, Co, Ga, In...
	Group IV: Sn, Ti, Ge, Th, U..
	Group V: Nb, V, Ta...
P	Group IV: Zr, Si..
	Group V: Nb, As, V...

(a) Types of partial substitutions

The lithium analogous NASICON structured have a general formula of $LiM_2P_3O_{12}$ where M = Ti, Hf, Zr, Ge, Sn and etc. Table 2.2 below shows the list of the previous research done by the partial substitution at M site.

Table 2.2: List of research done by partial substitution at M site in $LiM_2P_3O_{12}$ compound

M	Previous Research
Ti	Aono et al., 1990a, 1990b; Arbi et al., 2015; Best et al., 2000; Ding et al., 2012; Jackman & Cutler, 2013; Lin et al., 1988; Morimoto et al., 2013; Ortiz et al., 2014; Pérez-Estébanez et al., 2014; Pinus et al., 2012; Schroeder et al., 2011; Takada et al., 2001; Vijayan & Govindaraj, 2011; Wang et al., 2003; Wolfenstine et al., 2009; Yang et al., 2015; Zhang et al., 2015; Zhao et al., 2016
Hf	Aono et al., 1993; Chang et al., 2005; Kuwano et al., 1994; Losilla et al., 1997; Martínez-Juárez et al., 1997; Martínez-Juárez et al., 1996; París & Sanz, 2000
Zr	Alamo & Rodrigo, 1989; Arbi et al., 2002; Casciola et al., 1988; Catti & Stramare, 2000; Catti et al., 1999; Petit et al., 1986; Sanz et al., 1993; Sudreau et al., 1989
Ge	Alami et al., 1991; Arbi et al., 2015; Chung & Kang, 2014; Illbeigi et al., 2016; Inada et al., 2015; Kotobuki & Koishi, 2015; Yamamoto et al., 1997
Sn	Cui et al., 2012; Iglesias et al., 1997; Lazarraga et al., 2004; Martinez-Juarez et al., 1997; Martinez-Juarez et al., 1995; Martinez et al., 1994; Norhaniza et al., 2010; Norhaniza et al., 2011

However, the ionic conductivities of these systems are still lower than the $Na_{1+x}Zr_2Si_xP_3O_{12}$ system. So, the partial substitutions are normally done with the objectives:

i) Li^+ vacancies to form the structure with a general formula of $Li_{1-x}A_xM_{2-x}P_3O_{12}$ where $Li^+ + M^{4+} \rightarrow A^{5+}$.

(ii) Li^+ interstitials to form the structure with a general formula of $Li_{1+x}A_xM_{2-x}P_3O_{12}$ where $M^{4+} \rightarrow Li^+ + A^{3+}$.

Partial substitutions at the P site also have been reported by several researchers (Best et al., 1999; Chang et al., 2005; Geng et al., 2015; Norhaniza et al., 2011; Wong et al., 1998) with the following objectives:

(i) Substituted with the pentavalent ions to form the structure with a general formula of $LiM_{2-y}P_{3-y}N_yO_{12}$ where $P^{5+} \rightarrow N^{5+}$.

(ii) Li^+ interstitials to form the structure with a general formula of $Li_{1+y}M_2P_{3-y}R_yO_{12}$ where $P^{5+} \rightarrow Li^+ + R^{4+}$.

The partial substitutions at both M and P site have also been conducted and the choice of ions for M, A, R and Q sites are listed in Table 2.1. The highest conducting system that has been reported in the literature was the $Li_{1.3}Al_{0.3}Ti_{1.7}(PO_4)_3$ which showed the ionic conductivity of $\approx 3 \times 10^{-3}$ S cm^{-1} (Aono et al., 1990b; Arbi et al., 2005) at room temperature with low activation energy, E_a . The E_a for the system dropped from 0.35 eV to 0.20 eV at the temperatures above 200°C.

(b) Effects of partial substitutions on the conductivity

The conductivity enhancement in NASICON materials is related to the conduction channels or bottleneck size. Various works on the partial substitutions have been done since 1976 in order to optimize the conduction channels or bottleneck size for an optimum mobility of the ions. Aono et al. (1990) have prepared $Li_{1+x}Ti_{2-x}M_x(PO_4)_3$ (M = Al, Cr, Ga, Fe, Sc, In, Lu, Y, or La) and studied their conductivity. The enhancement of conductivity in M^{3+} substituted lithium NASICON was attributed to the densification of the sintered pellets (Aono et al., 1990b). These authors reported that enhancement of the

ionic conductivity observed in Al substituted compounds was due to an increase of the lithium content and a better connectivity of the grains caused by an increase of density associated with the segregated phases in the grain boundaries that acted as binders. This is probably the source of the high ionic conductivity of almost 10^{-3} S cm^{-1} at room temperature (Aono et al., 1991) for $Li_{1.3}Al_{0.3}Ti_{1.7}(PO_4)_3$.

Later on, this system was further investigated. Substitution of Al^{3+} into Ti^{4+} site, and M^{5+} (V, Nb) into the P^{5+} site in the series of $Li_{1+y}Al_yTi_{2-y}(PO_4)_3$ and $Li_{1+y}Al_yTi_{2-y}(PO_4)_{3-x}(MO_4)_x$ (M = V^{5+}, Nb^{5+}; y = 0.1, 0.3) gave several impurity phases such as TiO_2 (Rutile), $AlPO_4$-tridymite and TiP_2O_7 in addition to nonstoichiometric modified $LiTi_2P_3O_{12}$ (Wong et al., 1998). The increase in the conductivity is correlated to both the incorporation of Al and the presence of vacancies in the $LiTi_2P_3O_{12}$framework.

Besides that, an increase in conductivity was observed when $LiTi_2P_3O_{12}$ samples were partially substituted with Si^{4+} at P^{5+} site in $Li_{1+x+y}Al_xTi_{2-x}Si_yP_{3-y}O_{12}$ (Fu, 1997; Tan et al., 2012). Conductivity was enhanced significantly to 3×10^{-3} S cm^{-1} for this system at room temperature.

The effects of partial substitution using Cr^{3+} on the conductivity of NASICON structured materials were investigated by several researchers (Jiao et al., 2007; Pérez-Estébanez et al., 2013; Pérez-Estébanez et al., 2014) . Pérez-Estébanez et al. (2013, 2014) reported that room-temperature conductivity of $LiTi_2(PO_4)_3$ system substituted with Cr^{3+} with x = 0.1 was 1.4 x 10^{-4} S cm^{-1} and an activation energy of 0.31 eV. This was due to the ionic conductivity across grain boundaries correlated with the increased

density of the pellets that took place upon Cr addition (Pérez-Estébanez et al., 2013; Pérez-Estébanez et al., 2014). While Delmas et al, (1981) reported that the conductivity enhancement in Cr^{3+} substituted $NaZrP_3O_{12}$ was due to the increase in mobility of ions as reflected by the decrease in activation energy (Delmas et al., 1981).

Besides, several researchers such as Best et al. (1999), Geng et al. (2015), Norhaniza et al. (2011) and Wong et al (1998) also conducted the substitution at the P^{5+} site using V^{5+} that improved the sinterability and ionic conductivity of the compound (Best et al., 1999; Geng et al., 2015; Norhaniza et al., 2011; Wong et al., 1998).

2.4.4 Conduction mechanism in NASICON

The conductivity in crystalline framework materials is due to the phenomena of ion diffusion through lattice defects. There are two types of defects related to the context of ion mobility in crystals and they are the Schottky (vacancies) and Frenkel (interstitials) defects (Agrawal & Gupta, 1999). These defects belong to the class of „point defects" in crystals as shown in Figure 2.8. The Schottky defect refers to the crystal imperfection in which a pair of ions, one cation and an anion, disappears leaving their positions vacant. A single ion missing from its regular position and wandering in the interstitial sites resulted in the Frenkel defect. However, the interstitial sites have different environments regarding the number or type of their neighbours or its separation from the neighbours than the regular sites. Both the Frenkel and Schottky defects produce vacant sites in the crystal where any ion in the immediate vicinity can jump to one of the vacant sites. This jumping leaves the previous site of the ion as vacant which could be now hosted by

another ion. This process can lead to the transfer of ions across the solid giving rise to conductivity (Kumar & Yashonath, 2006).

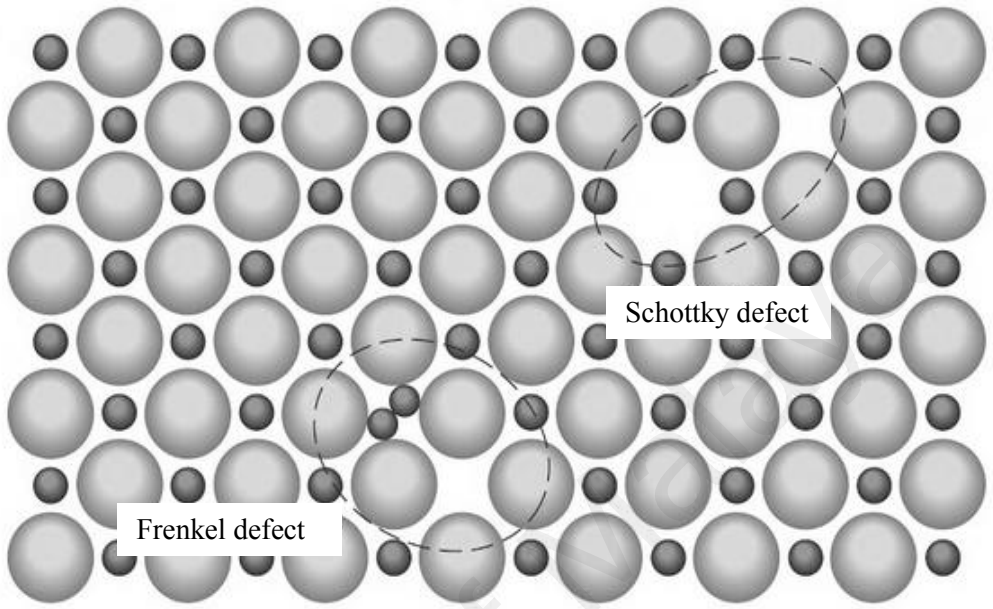

Figure 2.8: Schottky and Frenkel defects (Moffatt et al. , 1964)

However, the most important diffusion phenomena in the NASICON materials occurs in the form of hopping in the conduction channels known as bottlenecks (Guin & Tietz, 2015; Kumar & Yashonath, 2006). Three distinct conduction channels (pathways or hop path of ions) were proposed to exist in the rhombohedral $R\bar{3}c$ structure. The first conduction channel was between M(1) and M(2) sites while the second connects between neighbouring M(2) and M(2) sites as shown in Figure 2.9. The third path was most likely between M(1) to mid (M) and to M(2). The first path was the shortest path and was the most preferred path in NASICONs materials. However, it appears that M(1) to M(1) path does not exist.

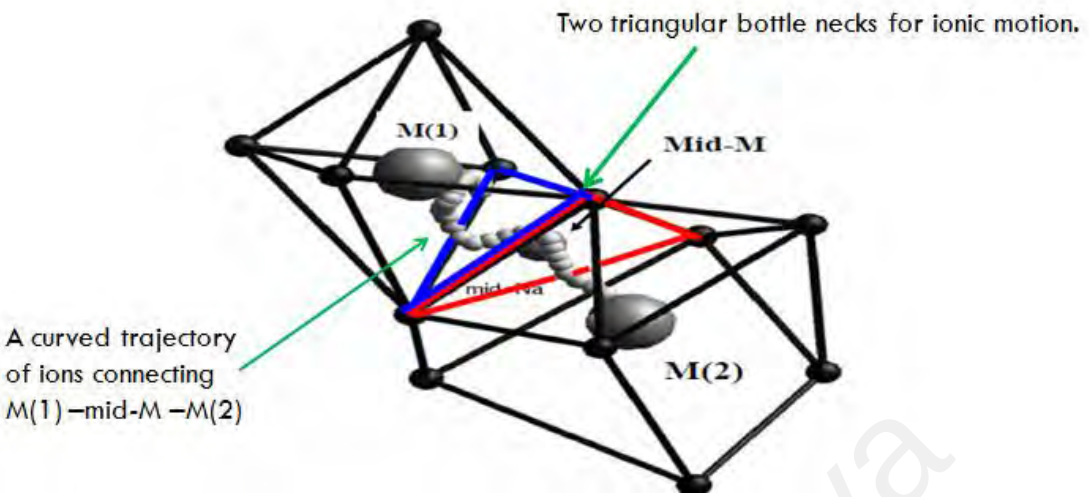

Figure 2.9: A typical trajectory showing ion hoping from M(1) to M(2) (Kumar & Yashonath, 2006)

Lithium ion DC conductivity, ζ of electrolytes is the possibility of electrolytes to bring the current density, $\vec{\imath}$ in the applied electric field, $\vec{E}$,

$$\sigma = \frac{\vec{\imath}}{\vec{E}} \tag{2.1}$$

Generally,

$$\sigma = Z_i \mu n \tag{2.2}$$

where Z_i is the charge of mobile ions, μ is the mobility while n is the concentration of the ions. The relation of σ and diffusion is given by the Nerst-Einstein relation,

$$\mu kT = Z_i D \tag{2.3}$$

where k is the Boltzman constant, T is the temperature and D is the diffusion coefficient.

Thus the Equation (2.2) becomes,

$$\sigma = \frac{nD(Z_i)^2}{kT} \tag{2.4}$$

Furthermore, the conductivity of NASICON materials is also temperature dependent as described by Arrhenius equation:

$$\sigma = \sigma_0 \, exp\left(\frac{-E_a}{kT}\right) \tag{2.5}$$

where the ζ, T, ζ_0, E_a, and k denote the conductivity, the absolute temperature, pre-exponential factor, activation energy for Li^+ ion migration, and Boltzmann's constant, respectively. The plot of log ζ versus $1/T$ yields a straight line with a gradient value of $\frac{-E_a}{kT}$. Besides that, AC conductivity was assessed from the dielectric data in accordance with the relation:

$$\sigma_{AC} = \omega\varepsilon_0\varepsilon" tan\delta \tag{2.6}$$

where ε_0 is the permittivity of the free space (8.854×10^{-14} F cm^{-1}), tan δ is the loss tangent factor and ε'' is the dielectric loss. The real and imaginary parts of permittivity and modulus are evaluated based on the calculation:

$$\varepsilon^* = \varepsilon' - j\varepsilon" \tag{2.7}$$

where;

$$\varepsilon' = \frac{Z"}{\omega C_0 (Z'^2 + Z"^2)} \tag{2.8}$$

$$\varepsilon'' = \frac{Z'}{\omega C_0 (Z''^2 + Z'^2)} \tag{2.9}$$

where angular frequency, $\omega = 2\pi f$ and C_o is acquired from Eq. (2.10):

$$C_0 = \frac{\varepsilon_0 A}{d} \tag{2.10}$$

In the above equation, A and d is the area and thickness of the sample respectively. In the above calculations, Z' and Z'' are the real and imaginary impedances acquired from impedance measurements.

Furthermore, according to Almond et al. (1983), the AC conductivity data can also be used to estimate the ionic hopping rate, ω_p (Almond et al., 1983). The hopping rate of an ion in a material is a valuable information to elucidate the ionic conduction of the samples. In this case, ω_p can be obtained from the graph of log ζ (ω) versus log ω by extrapolating at twice the value of DC conductivity from the vertical axis horizontally towards the graph and then extrapolating downwards vertically to the horizontal axis. The magnitude of the charge carrier concentration, K can be obtained using the equation as below (Adnan & Mohamed, 2012; Savitha et al., 2006; Teo et al., 2012; Vijayakumar et al., 2003)

$$K = \frac{\sigma T}{\omega_p} \tag{2.11}$$

where

$$K = ne^2 a^2 \gamma k^{-1} \tag{2.12}$$

In Equation 2.12, e is the electron charge, γ is the correlation factor which is set equal to 1, and a is the jump distance between two adjacent sites for the ions to hope which is assumed to be 3Å for all the samples (Adnan & Mohamed, 2012; Teo et al., 2012; Vijayakumar et al., 2003). The density of mobile ions (charge carrier) denotes as n which can be calculated using Equation 2.12 and k is the Boltzmann constant. The ionic mobility, μ can be calculated using equation:

$$\mu = \frac{\sigma_{dc}}{ne} \tag{2.13}$$

Furthermore, AC conductivity measurements are widely used for investigating the nature of defect centers assuming that they are responsible for this type of conduction. The general frequency behavior in this type of materials is of $A\omega^s$ – type of a wide frequency range where exponent s, is found to be temperature dependent and has a value ≤ 1. Various models were formulated to explain this behavior and the classical approach was used to consider AC and DC conduction separately. The theory of the classical hopping of carriers between localized states over a barrier, W was developed initially by Pike in 1972 to explain AC conduction in the scandium oxide films (Pike, 1972). In 1977, Elliot extended Pike"s theory of AC conduction, name as the Correlated Barrier Hopping (CBH) of charge carriers (Elliott, 1977) . According to this model, the conduction occurs via charge carriers hopping process where two charge carriers simultaneously hop over the potential barrier between two charged defects state (D^+ and D^-) and the barrier height is correlated with the intersite separation via a Coulumbic interaction.

In the CBH model, the charge carriers in charge defect states hop over the Coulombic barrier whose height, W, is given as

$$W = W_m - \left(\frac{ne^2}{\pi\varepsilon\varepsilon_0 R}\right) \tag{2.14}$$

where W_m is the maximum barrier height or binding energy as shown in Figure 2.10, ε is the bulk dielectric constant, ε_o is the permittivity of free space, R is the distance between hopping sites and n is the number of charge carriers involved in a hop.

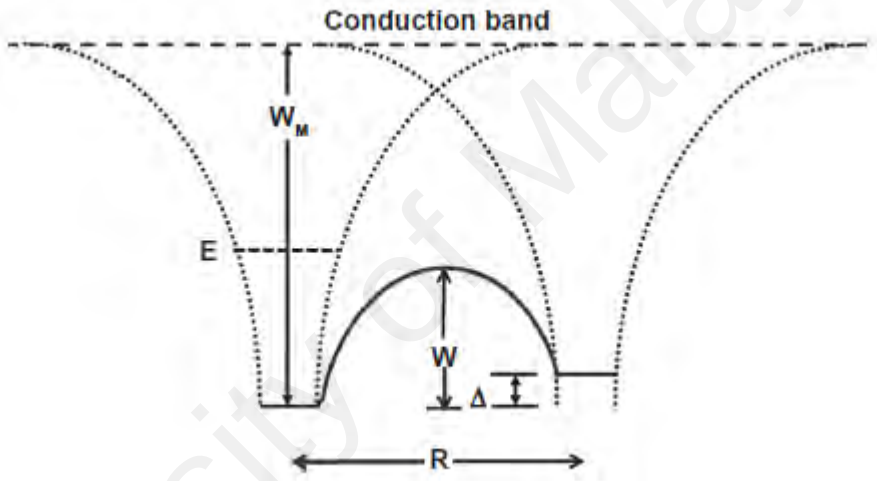

Figure 2.10: Model of overlapping Coulomb-type walls for charged centers (Murugavel & Upadhyay, 2012)

It has been reported in many crystalline materials that the AC conductivity varies with the frequency according to the following relation

$$\sigma'(\omega) = \sigma(0) + A\omega^s \tag{2.15}$$

where ζ (0) is the DC conductivity of the sample, A is the temperature reliant parameter and s is the frequency exponent with the value of $s \leq 1$.

The frequency exponent, *s* for CBH model is given by the expression (Elliott, 1977)

$$s = 1 - \frac{6k_B T}{W_m - k_B\, T ln\, (\frac{1}{\omega \tau_0})} \tag{2.16}$$

where k_B is the Boltzmann constant, T is the absolute temperature, W_m is the binding energy, ω is the angular frequency and η_0 is the characteristics relaxation time.

A first approximation of Equation 2.16 gives the simple expression (Taher et al., 2016)

$$s = 1 - \frac{6k_B T}{W_m} \tag{2.17}$$

From the above equation, the value of *s* can be predicted to be both temperature and frequency dependent (Elliott, 1977). It may be noted that for small values of (W_m / $K_B T$), *s* increases with increasing frequency, but for large values of (W_m / $K_B T$), the variation of *s* is so small that is independent of frequency. Therefore, the above equation predicts that *s* decreases with the increment of the temperature (Elliott, 1977, 1987).

CHAPTER 3: RESEARCH METHODOLOGY

3.1 Introduction

Most NASICON structured solid electrolytes reported in the literature were prepared by the conventional solid state reaction method. In this work, citric acid assisted sol-gel method was used. The synthesis of the samples using sol-gel method was divided into two stages. The first stage was to prepare the precursor materials followed by the second process that was heat treatment process known as sintering. The samples were then characterized using Thermogravimetric Analysis (TGA), X-Ray Diffraction (XRD), Fourier Transform Infrared Spectroscopy (FTIR), Laser Particle Sizer, Scanning Electron Microscopy (SEM), and Energy Dispersive X-Ray Spectroscopy (EDX) and Impedance Spectroscopy (IS), in order to investigate the thermal, structural and electrical properties of the samples. The voltage stability window of the samples was determined from Linear Sweep Volammetry (LSV) while the actual type charge carriers in the samples were carried out by using Transference Number Measurements.

3.2 Classification of the samples

The samples were divided into three main categories; $LiSn_2P_3O_{12}$ parent compound, partial substitution at Sn^{4+} site using trivalent ions ($Cr^{3+,}$ Al^{3+}) and partial substitution at P^{5+} site using tetravalent ions ($Zr^{4+,}$ Si^{4+}). Table 3.1 shows the categories of the samples based on their stoichiometric formula.

Table 3.1: Categories of the samples based on their stoichiometric formula

Samples	Stoichiometric formula
Parent compound	$LiSn_2P_3O_{12}$
Partial substitution at Sn^{4+} site using trivalent ions ($Cr^{3+,}$ Al^{3+})	$Li_{1+x}Cr_xSn_{2-x}P_3O_{12}$
	$Li_{1+x}Al_xSn_{2-x}P_3O_{12}$
Partial substitution at P^{5+} site using tetravalent ions ($Zr^{4+,}$ Si^{4+})	$Li_{1+y}Sn_2P_{3-y}Zr_yO_{12}$
	$Li_{1+y}Sn_2P_{3-y}Si_yO_{12}$

3.3 Synthesis of the samples

As mentioned earlier, all samples were prepared via citric-acid assisted sol-gel method. All the chemicals were of analytical grade and directly used as received without further purification. To prepare $LiSn_2P_3O_{12}$ samples, Lithium acetate (CH_3COOLi), stannum (IV) chloride pentahydrate ($SnCl_4.5H_2O$) and ammonium phosphate ($H_{12}N_3O_4P$) were used as the starting materials with citric acid ($C_6H_80_7$) as the chelating agent and distilled water as the solvent.

As the first step, CH_3COOLi, $SnCl_4.5H_2O$ and $H_{12}N_3O_4P$ of molar ratio 1:2:3 were dissolved in distilled water under magnetic stirring. Citric acid ($C_6H_8O_7$), poly ethylene glycol ($C_2H_6O_2$) and ammonium hydroxide (NH_4OH) were then mixed together with the previously prepared solution and was stirred continuously. $C_2H_6O_6$ and NH_4OH were then added to promote polyesterification and polycondensation reactions. The molar ratio of $C_2H_6O_6$:NH4OH was 1:1. The solution was then transferred into a reflux system and continuously stirred until a homogenous solution was formed. After stirring for 24 hours, the solution was taken out and vaporized for about 4 hours under magnetic

stirring at 80°C. The resulting gels formed was then dried in an oven at 150°C for 24 hours in order to remove water particles, resistance organic groups and also to avoid ceramics crack. The obtained precursor powder was then grounded for 30 minutes in order to obtain very fine powder. Then, the precursor powder was subjected to a sintering process at four different temperatures 500, 550, 600 and 650 °C for 24 hours. The final product was then grounded again for 30 minutes before the powder was pressed using Specac hydraulic press under a pressure of 5 tons to form pellets with a diameter of 13 mm and thickness of 1.00 - 3.00 mm respectively.

The same process was undertaken to prepare the second system that was $LiSn_2P_3O_{12}$ samples with minimum impurity. The only difference was the samples were sintered at 600 and 650 °C for 48 hours. For the substituted samples, again the same route was applied using Cr^{3+} and Al^{3+} for substitution at Sn^{4+} site as the third and fourth system. Additional chromium (III) acetate hydroxide ($C_{14}H_{23}Cr_30_{16}$) and aluminium (III) acetate ($C_6H_9AlO_6$) were used as the starting materials. For the fifth and sixth system, the same route was applied but using Si^{4+} and Zr^{4+} for substitution at P^{5+} site. To prepare these systems, additional zirconium (IV) acetate hydroxide ($C_6H_{10}ZrO_7$) and silicon dioxide (SiO_2) were used as the additional starting materials. All the prepared samples follow the stoichiometric formula of $Li_{1+x}Cr_xSn_{2-x}P_3O_{12}$, $Li_{1+x}Al_xSn_{2-x}P_3O_{12}$, $Li_{1+y}Sn_2P_{3-y}Zr_yO_{12}$ and $Li_{1+y}Sn_2P_{3-y}Si_yO_{12}$ where x and y = 0.1, 0.3, 0.5, 0.7 and 0.9. Figures 3.1 to 3.10 show the flow chart for sample preparation of each system.

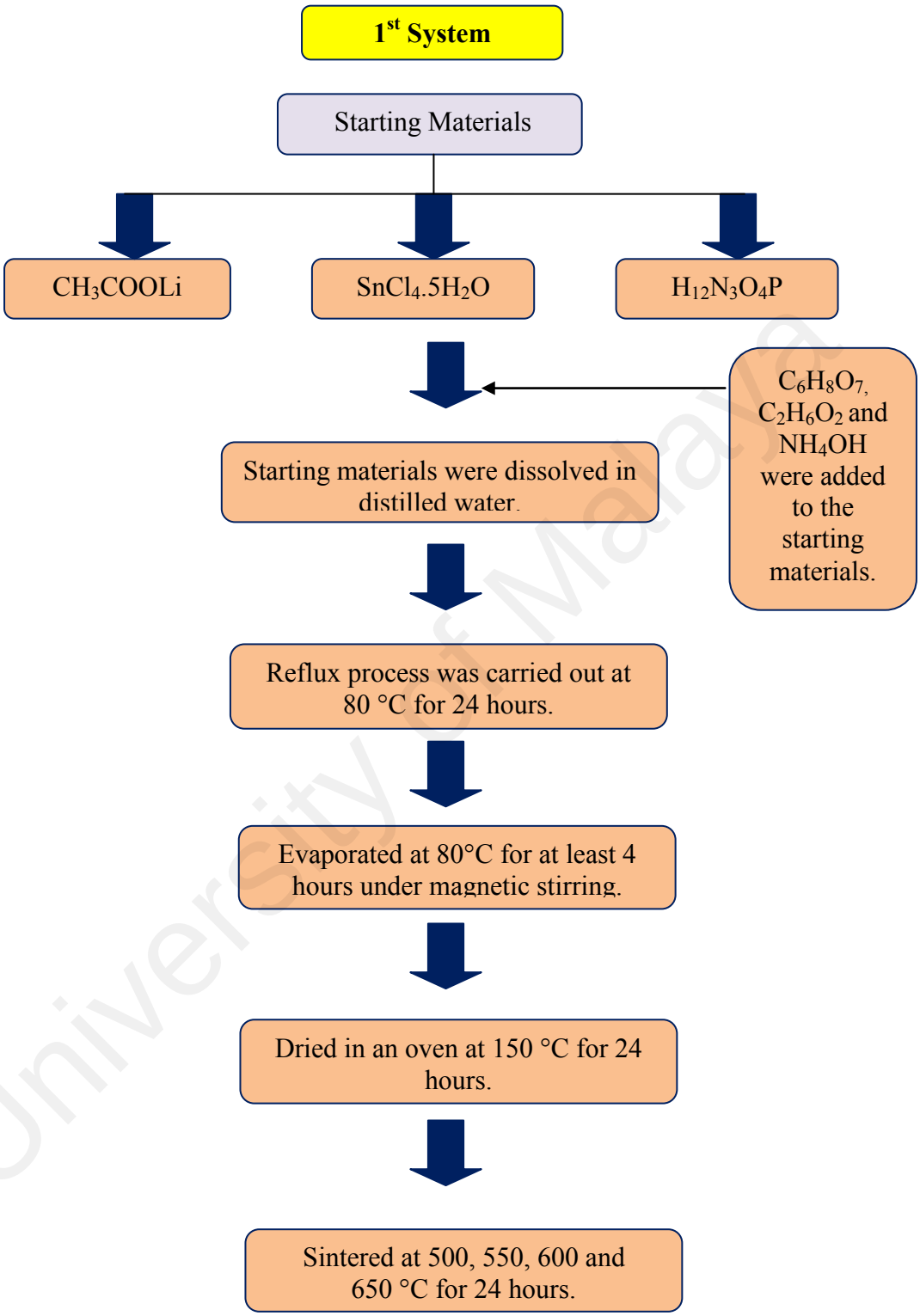

Figure 3.1: Flow chart of preparation of $LiSn_2P_3O_{12}$ system

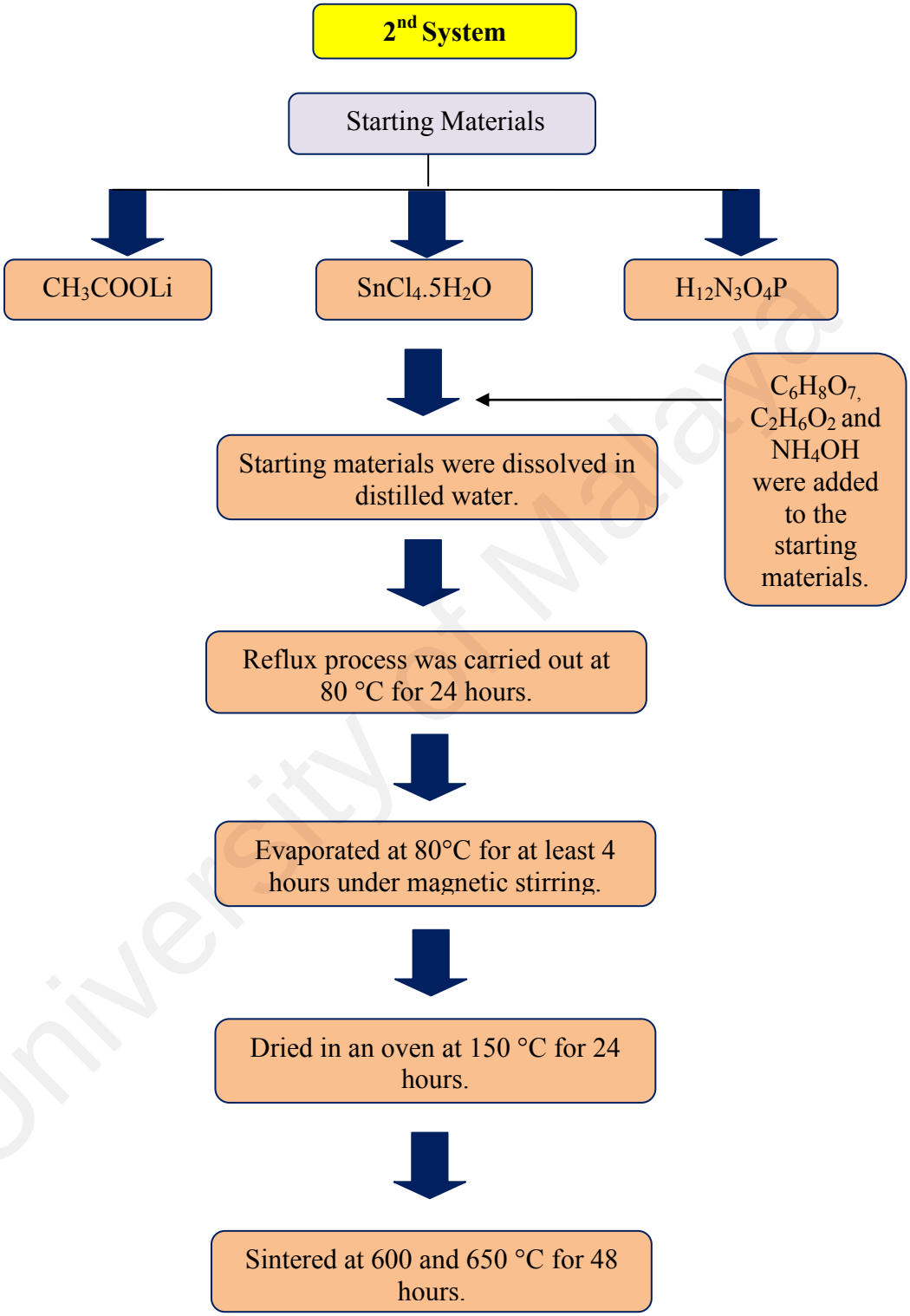

Figure 3.2: Flow chart of preparation of $LiSn_2P_3O_{12}$ system

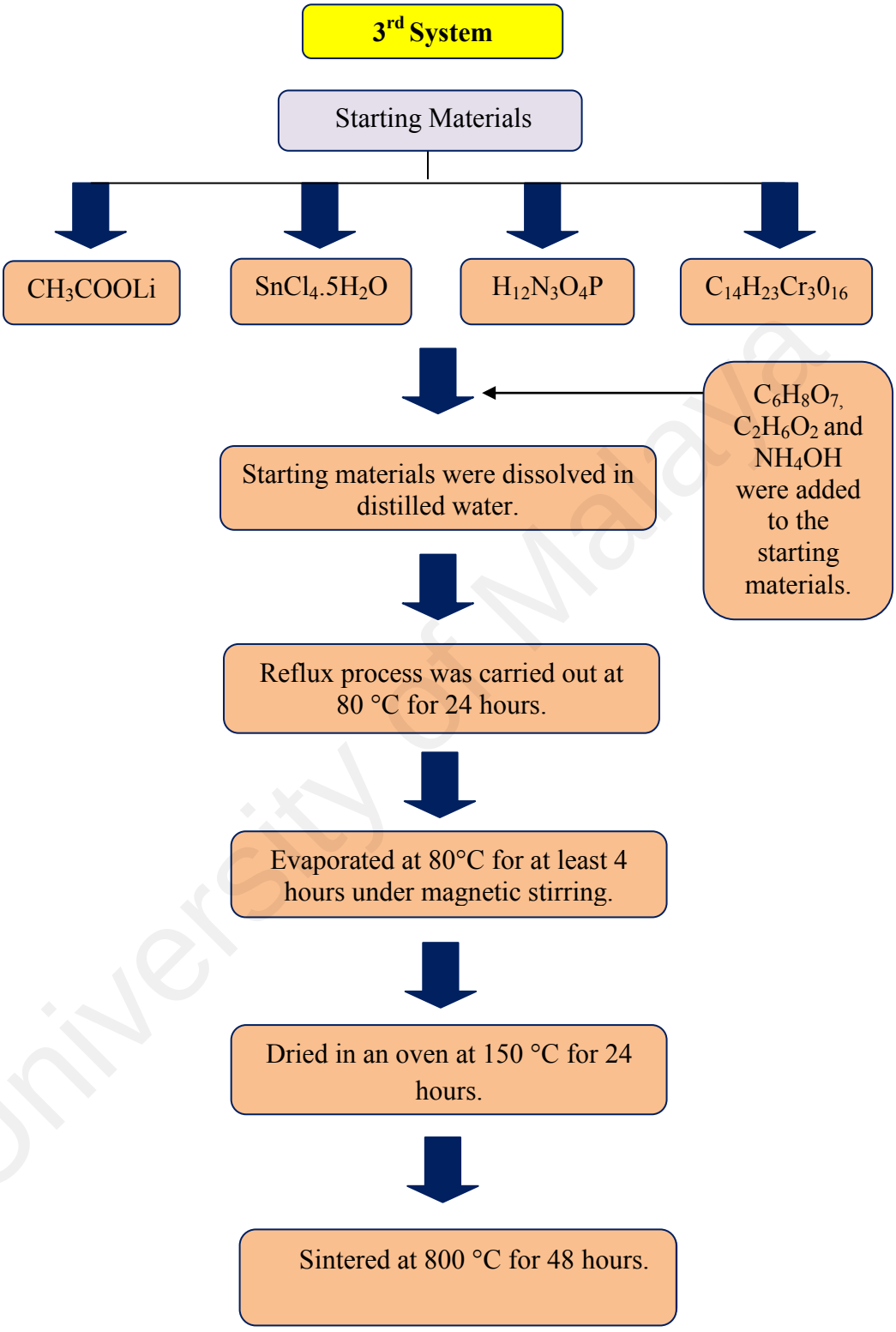

Figure 3.3: Flow chart of preparation of $Li_{1+x}Cr_xSn_{2-x}P_3O_{12}$ system

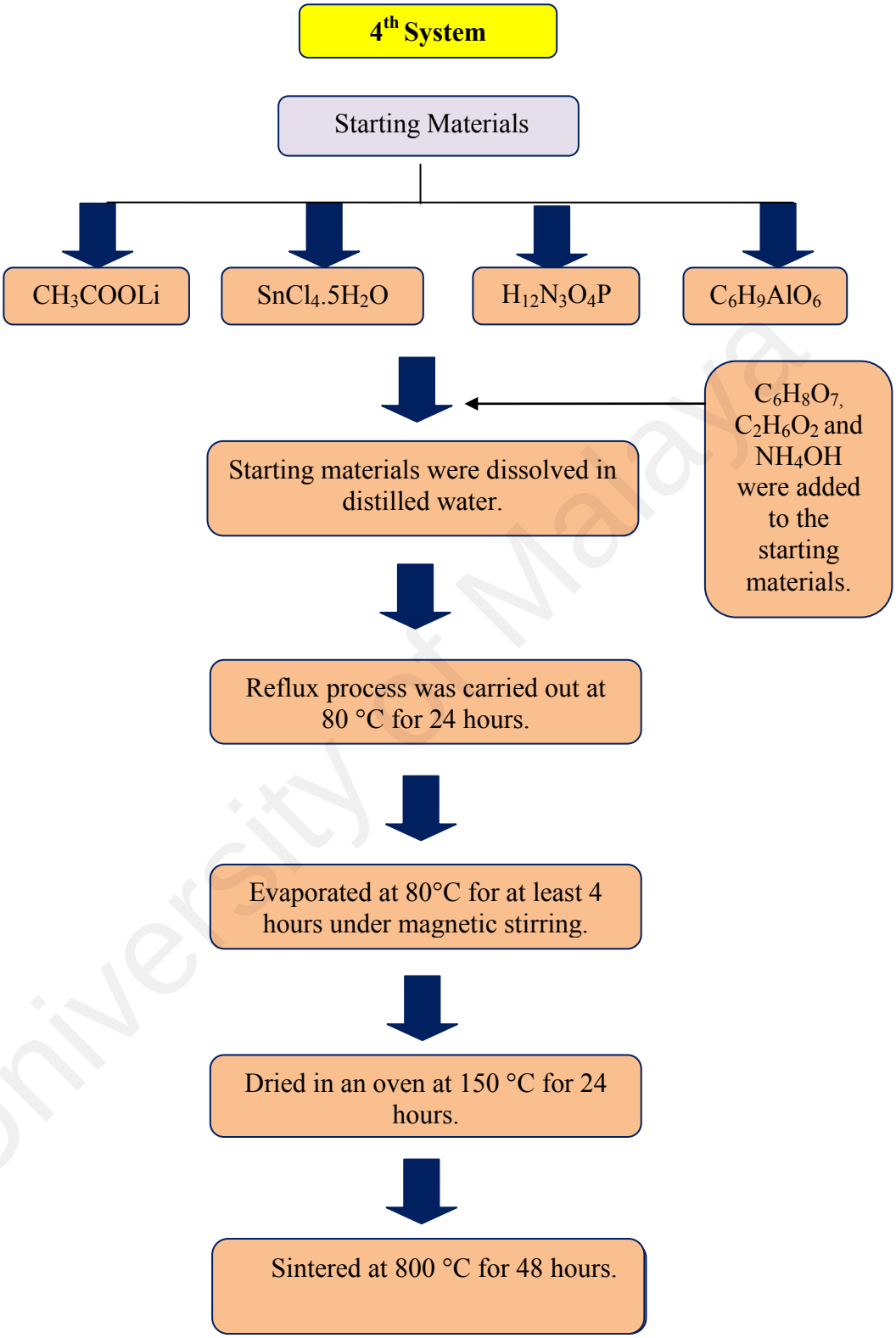

Figure 3.4: Flow chart of preparation of $Li_{1+x}Al_xSn_{2-x}P_3O_{12}$ system

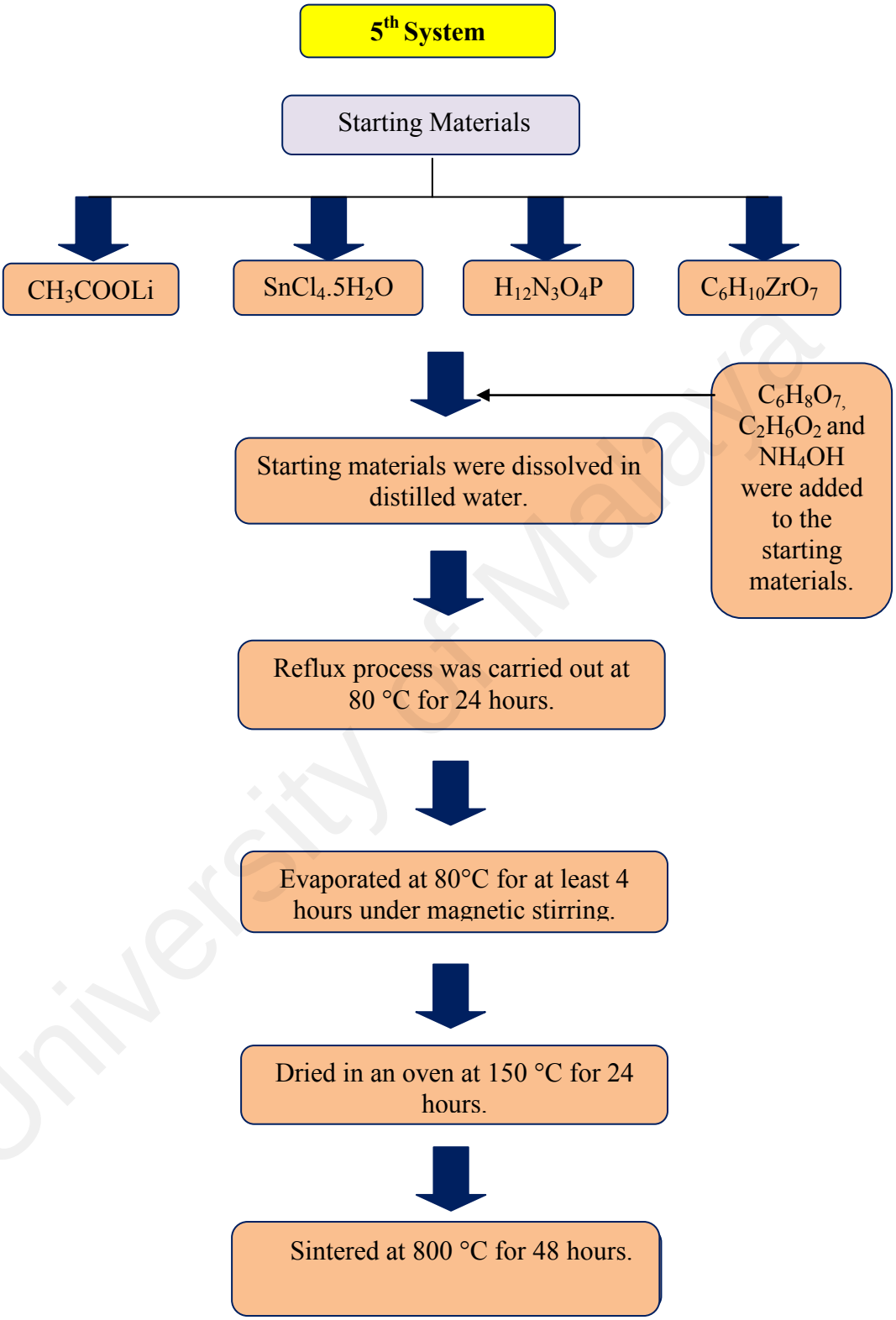

Figure 3.5: Flow chart of preparation of $Li_{1+y}Sn_2P_{3-y}Zr_yO_{12}$ system

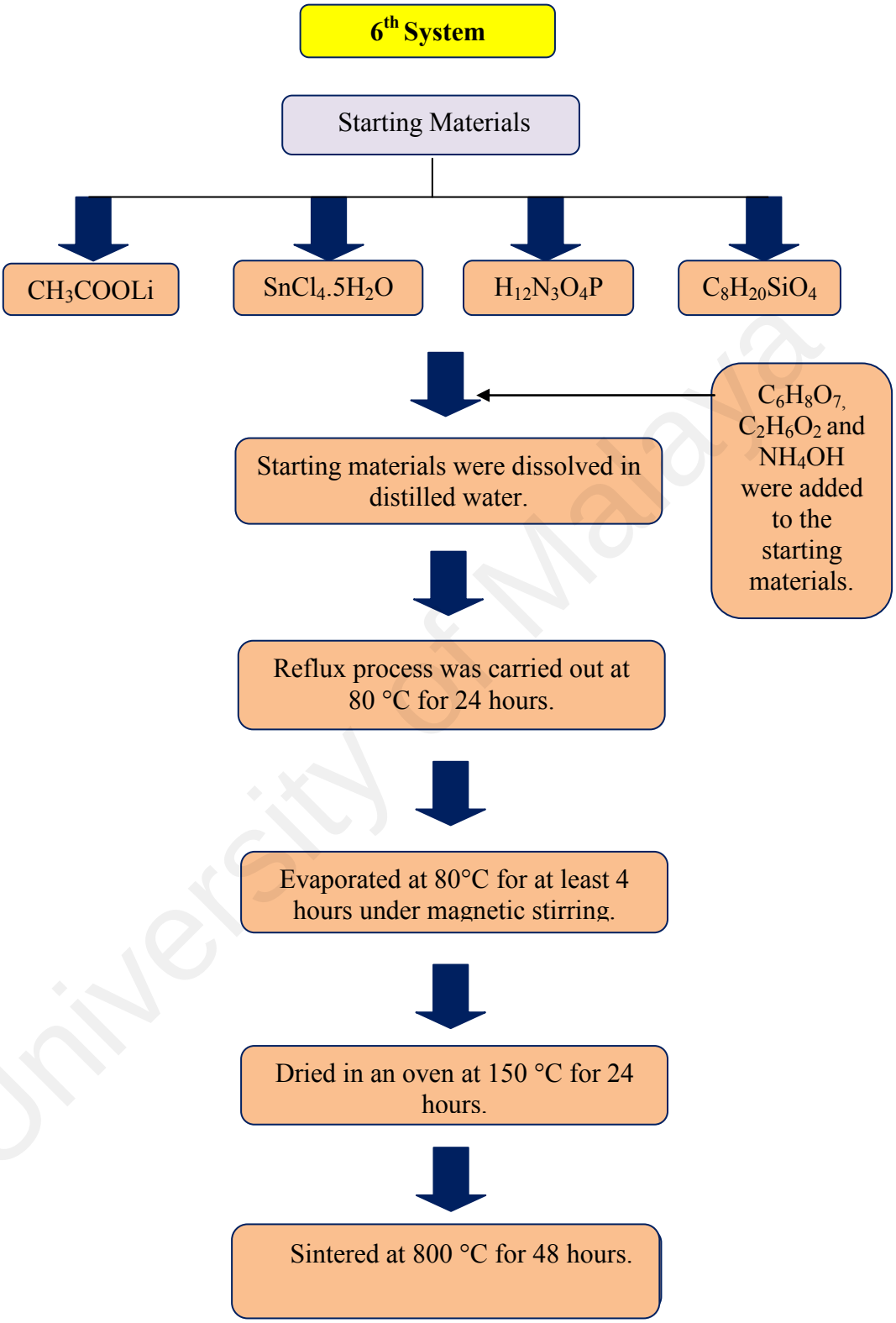

Figure 3.6: Flow chart of preparation of $Li_{1+y}Sn_2P_{3-y}Si_yO_{12}$ system

3.3 Characterizations

The prepared samples were subjected to various studies including, TGA, XRD, FTIR, laser particle sizer, SEM, EDX, IS, LSV and transference number measurements.

3.3.1 Thermogravimetric Analysis

TGA is an analytical technique used to determine the thermal stability of a material and its fraction of volatile components by monitoring the weight change that occurs as a specimen is heated. The measurement is normally carried out in air or in an inert atmosphere, such as in Helium or Argon, and the weight is recorded as a function of increasing temperature. Sometimes, the measurement is performed in a lean oxygen atmosphere (1 to 5% O_2 in N_2or He) to slow down oxidation. In this study, thermal behaviour of the samples was analyzed using Setaram Labsys Evo. The samples were carefully weighed to 15 ± 2 mg in an alumina crucible placed in the centre of the heating chamber. TGA scans were then carried out in nitrogen atmosphere at constant heating rate of 10 C min^{-1} in the temperature range from 30 to 1100°C. The data were then analyzed using Calisto software.

3.3.2 X-ray Diffraction

XRD is one of the most powerful techniques for qualitative and quantitative analysis of crystalline materials. The technique provides information including the types and nature of crystalline phases present, structural makeup of phases, degree of crystallinity, amount of amorphous content, microstrain and size and also orientation of crystallites (Suryanarayana & Norton, 2013).

When X-ray radiation is directed on a sample, the X-rays are scattered (diffracted) by the electrons present in the material. If the atoms in the material are arranged in a regular and crystalline structure, this scattering results in maxima and minima in the diffracted intensity. The signal maxima follow Bragg‟s law, $n\lambda = 2d\sin\theta$ (Pendry, 1990). Here n is an integer, λ is the X-ray wavelength, d is the distance between crystal lattice planes and θ is the diffraction angle. Thus, for each lattice spacing d, Bragg‟s law predicts a maximum at a characteristics diffraction angle θ. During an XRD measurement, the angles of incidence and detection are scanned. When the intensity of detected X-rays is plotted as a function of angle θ, an X-ray diffraction pattern is obtained, which is the characteristics for the materials (Suryanarayana & Norton, 2013).

The XRD analysis was carried out using using a PaNalytical – X‟pert^3 x-ray diffractometer with Cu-K_α radiation of wavelength of 1.5406 Å. The 2θ range was between 10 ° and 45 ° and 0.026 ° in step size. Then, the lattice parameters of the samples were calculated using the formulae that belongs to the rhombohedral crystal system with a hexagonal unit cell lattice (Jenkins, 2000; Jenkins & Snyder, 1996):

$$\frac{1}{d^2} = \frac{4}{3}\left(\frac{h^2+hk+k^2}{a^2}\right) + \frac{l^2}{c^2} \qquad (3.1)$$

Scherer equation was applied in order to determine the crystallite size (Jenkins, 2000; Jenkins & Snyder, 1996);

$$D = \frac{k\lambda}{\beta cos\theta} \qquad (3.2)$$

where k is the Scherer constant value (0.94), λ is the wavelength of the source (1.5406 $\dot{A}$), β is FWHM (in radians), and θ is the Bragg angle (in radians).

3.3.3 Fourier Transform Infrared Spectroscopy

FTIR is the preferred method of infrared spectroscopy. FTIR is a technique used to determine qualitative and quantitative features of IR-active molecules in organic or inorganic solid, liquid or gas samples (Schrader, 2008). It is a rapid and relatively inexpensive method for the analysis of solids that are crystalline, microcrystalline, amorphous, or films. In infrared spectroscopy, IR radiation is passed through a sample. Some of the infrared radiation is absorbed by the sample and some of it is passed through (transmitted). The resulting spectrum represents the molecular absorption and transmission, creating a molecular fingerprint of the sample (Stuart, 2005). Like a fingerprint no two unique molecular structures produce the same infrared spectrum.

Attenuated total reflection Fourier transform infrared (ATR-FTIR) was used to observe the functional group and chemical interaction in the samples prepared in this study. FTIR spectra were recorded by computer interfaced with Perkin-Elmer Frontier Spectrometer. The sample powder was placed onto ATR crystal and analyzed in the frequency range of 550 cm^{-1} to 1400 cm^{-1} with a scanning resolution of 2 cm^{-1} at room temperature.

3.3.4 Particle Size Analysis

Laser particle sizer is a measuring device for the determination of particle size distributions together with recognition of the particle shape in a single process (Allen, 2013). In principles, laser light falling on particles (powder, suspensions etc.) is diverted from its original direction by scattering. The angular distribution of the scattered light depends principally on the size of the particles, the laser wavelength and the refractive index (Syvitski, 2007). For particles that are smaller than about 1 μm, there are also important effects related to the polarisation of the laser: depending whether the plane of observation is perpendicular or parallel to the plane of polarisation, there are significant differences in the intensity distribution. Laser diffraction instruments measure the angular distribution of the light from a particle sample. Using special algorithms, the particle size distribution can be calculated from the results (Allen, 2013). The particle size information of the samples prepared in this study was obtained using FRITSCH-Analysette 22 NanoTec laser particle sizer at room temperature.

3.3.5 Scanning Electron Microscopy

SEM is a technique that uses electrons instead of light to form an image (Goldstein et al., 2012). The SEM has a large depth of field, which allows more of a specimen to be in focus at one time. The SEM also has much higher resolution, so closely spaced specimens can be magnified at much higher levels. Since the SEM uses electromagnets rather than lenses, the degree of magnification is controlled. A beam of electrons is produced at the top of the microscope by an electron gun. The electron beam follows a vertical path through the microscope, which is held within a vacuum (Goldstein et al., 2012). The beam travels through electromagnetic fields and lenses, which focus the

beam down toward the sample. Once the beam hits the sample, electrons and X-rays are ejected from the sample. In this study, the morphologies of the prepared sample powders were analyzed by scanning electron microscopy using Zeiss-Evo MA10 scanning electron microscope at 500 × magnification with 10 kV incident electron beam. The prepared powder samples were distributed onto the carbon tape and coated with gold using sputter coating machine for 90 s before the SEM analysis.

3.3.6 Energy Dispersive X-ray Spectroscopy

EDX is an analytical technique used for the elemental analysis or chemical characterization of a sample (Shindo & Oikawa, 2002; Van Grieken & Markowicz, 2001). It relies on the investigation of an interaction of some source of X-ray excitation with a sample. Its characterization capabilities are due in large part to the fundamental principle that each element has a unique atomic structure allowing unique set of peaks on its X-ray spectrum. To stimulate the emission of characteristic X-rays from a specimen, a high-energy beam of charged particles such as electrons or protons or a beam of X-rays, is focused into the sample being studied. At rest, an atom within the sample contains ground state (or unexcited) electrons in discrete energy levels or electron shells bound to the nucleus. The incident beam may excite an electron in an inner shell, ejecting it from the shell while creating an electron hole where the electron was. An electron from an outer, higher-energy shell then fills the hole, and the difference in energy between the higher-energy shell and the lower energy shell may be released in the form of an X-ray. The number and energy of the X-rays emitted from a specimen can be measured by an energy-dispersive spectrometer. As the energy of the X-rays is characteristic of the difference in energy between the two shells, and of the atomic structure of the element from which they were emitted, this allows the elemental

composition of the specimen to be measured. The elemental analysis of the samples for this study was analyzed using energy dispersive X-ray Oxford Aztec X-Act EDX spectrometer attached together with the Zeiss-Evo MA10 Scanning electron microscope.

3.3.7 Impedance Spectroscopy

The electrical properties of the prepared samples were investigated by electrochemical ac impedance spectroscopy using Solartron 1260 Impedance/ Gain-Phase Analyzer over a frequency range from 1 to 10^6 Hz. An applied voltage was fixed at 200 mV. All measurements were done at temperature range from 30 to 500°C. During analysis, a stimulus which was a sinusoidal voltage of known frequency ($\Delta E \sin(\omega t)$) was applied across the samples (Barsoukov & Macdonald, 2005). The samples will respond to this stimulus as an AC current signal containing the excitation frequency and its harmonic, $\Delta I\ (\omega t + \phi)$ through the sample (MacDonald, 1987). The Solartron analyzer recorded the transfer function relating the stimulus and response of the sample which was impedance, *Z* calculated using Ohm"s law as:

$$Z(\omega) = \frac{\Delta E\ (\omega)}{\Delta I\ (\omega)} \tag{3.3}$$

Impedance, *Z* is a measure of the ability of a sample to resist the flow of electric current. The resistances could be from the grain interior (bulk, *b*) or the intergranular grain (grain boundary, *gb*). The real part of the impedance is given by $Z^{'} = |Z| \cos \phi$ while the imaginary part is given by$Z^{"} = |Z| \sin \phi$. The plot of the imaginary part of

impedance, Z” versus the real part of the impedance, Z‟ gives a Cole-Cole plot or complex impedance plot as shown in Figure 3.7.

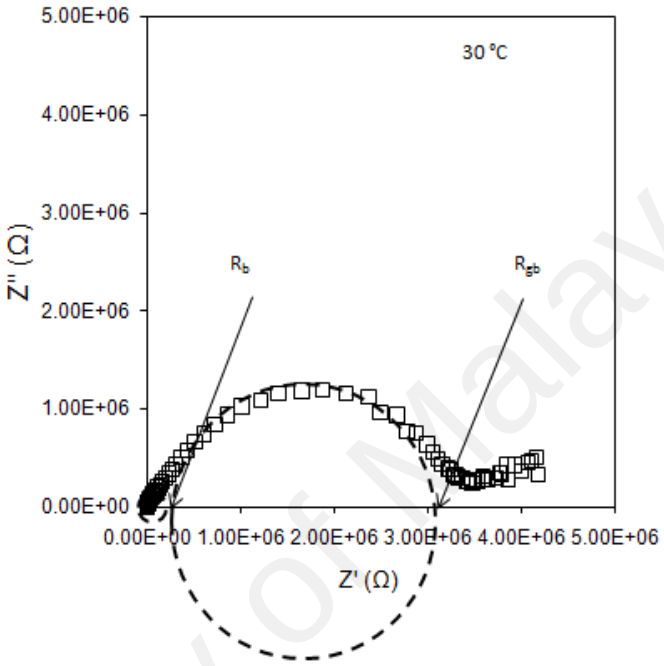

Figure 3.7: An example of impedance plot

Then, the bulk conductivity, ζ_b and grain boundary conductivity, ζ_{gb} which represent the DC conductivity in the samples were calculated using following equation:

$$\sigma_b = \frac{d}{AR_b} \text{ and } \sigma_{gb} = \frac{d}{AR_{gb}} \tag{3.4}$$

In these equations, d is the sample thickness, A is the cross- sectional area of sample, R_b is the bulk resistance and R_{gb} is the grain boundary resistance. Meanwhile, the total conductivity, ζ_t of the compound was evaluated using the following equation:

$$\frac{1}{\sigma_t} = \frac{1}{\sigma_b} + \frac{1}{\sigma_{gb}} \tag{3.5}$$

3.3.8 Linear Sweep Voltammetry

LSV is a voltammetric method where the current at a working electrode is measured while the potential between the working electrode and a reference electrode is swept linearly in time (Bard et al., 1980). Oxidation or reduction of species is registered as a peak or trough in the current signal at the potential at which the species begins to be oxidized or reduced (Wang, 2006).

The electrochemical stability window of the prepared sample was studied using Wonatech ZIVE MP2 multichannel electrochemical workstation. LSV measurement was carried out at a scan rate of 5 mV s^{-1}. Measurement was done at room temperature. The configuration of the cell was Li/Solid electrolytes/SS.

3.3.9 Transference Number Measurements

The ionic transference number measurement was evaluated by Wagner"s D.C polarization technique (Wagner & Wagner, 1957) using Wonatech ZIVE MP2 multichannel electrochemical workstation. The sample was sandwiched between two stainless steel blocking electrodes and polarized by applying a potential of 0.5 V and the current was monitored as a function of time until it reached a steady sate condition.

The ionic transference number was calculated from polarization current versus time plot using equation:

$$\tau_{ion} = \frac{I_{initial} - I_{final}}{I_{initial}} \quad (3.5)$$

where $I_{initial}$ is the initial current and I_{final} is the final residual current (constant current). If the solid electrolyte is purely ionic, then $\eta_{ion} = 1$, while mixed conductors, η_{ion} may ranging from 0 to 1 (Bhargav et al., 2007).

CHAPTER 4: $LiSn_2P_3O_{12}$ SYSTEM

4.1 Introduction

$LiSn_2P_3O_{12}$ system was synthesized using low temperature water based sol-gel method. Firstly, thermal analysis of the precursor sample was done using TGA in order to investigate the effect of the heat-treatment temperature and optimization of the sintering temperature. Therefore, based on the TGA analysis and in order to minimize impurity in the system, $LiSn_2P_3O_{12}$ samples were sintered at two different sintering times; 24 and 48 hours at different sintering temperatures. The samples in both systems; System I ($LiSn_2P_3O_{12}$ sample sintered for 24 hours) and System II ($LiSn_2P_3O_{12}$ sample sintered for 48 hours) were characterized using XRD, FTIR, SEM, EDX, particle size analysis, IS, LSV and transference number measurement.

4.2 Thermal analysis of the precursor of $LiSn_2P_3O_{12}$ system

TGA was carried out in order to investigate the effect of the heat-treatment temperature and optimize sintering temperature of $LiSn_2P_3O_{12}$ precursor sample. TGA curve for the precursor of $LiSn_2P_3O_{12}$ is presented in Figure 4.1. Three main weight losses are identified in the TG curve. The first soft slope is detected in between 30 and 120 °C with a total weight loss of 1.73 %, which is due to the evaporation of water. The second weight loss is a steep slope detected in the temperature range of 120 to 350 °C indicating the decomposition of ammonium and acetate group (Krok, 1987). The third weight loss is 3.70 % in the temperature range from 350 to 480 °C which is attributed to the chemical reaction during the formation of $LiSn_2P_3O_{12}$. At temperatures above 500 °C, there was no significant weight loss, which suggests that the gases (NH_3, CO_2 and

H_2O) are mainly produced below 500 °C and that the reaction at high temperature does not result in further weight loss (Cui et al., 2012). The plateau at temperature range 500 to 1100 °C suggests that all chemical reactions in the sample have been completed. So, based on the TGA result, four sintering temperatures have been chosen that were 500, 550, 600 and 650 °C. The samples were also sintered at two different sintering times; 24 and 48 hours. Table 4.1 shows the classification of the samples based on the sintering temperature and time.

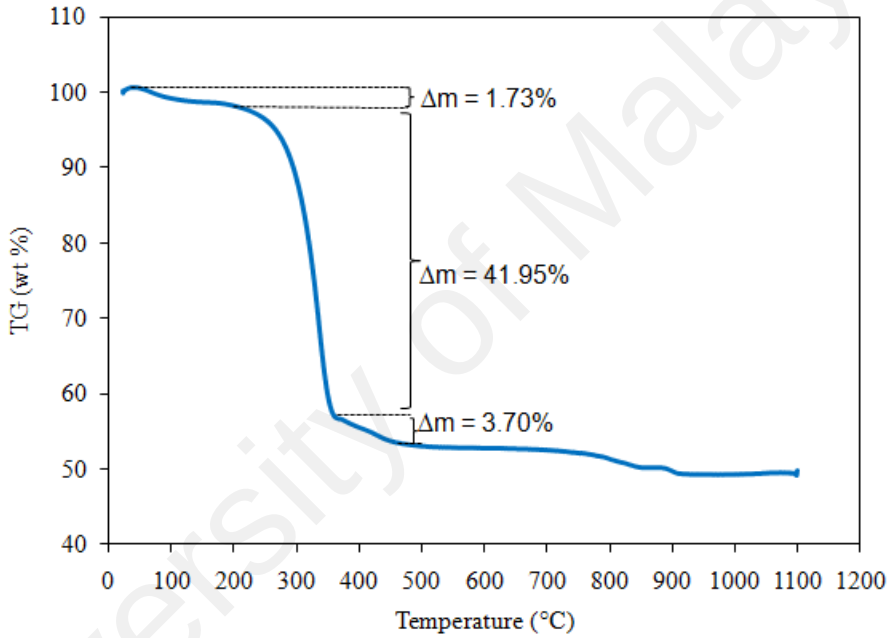

Figure 4.1: TGA curve of $LiSn_2P_3O_{12}$ precursor sample

Table 4.1: The classification of the $LiSn_2P_3O_{12}$ samples based on sintering temperature and time

System	Sample	Sintering temperature (°C)	Sintering time (Hours)
I	A1	500	24
	A2	550	
	A3	600	
	A4	650	
II	B1	600	48
	B2	50	

4.3 XRD analysis

The structural properties of $LiSn_2P_3O_{12}$ samples sintered at different temperatures and times, system I (sample A1 – A4) and system II (sample B1 – B2) were determined from XRD analysis. Figure 4.2 shows the XRD patterns of the $LiSn_2P_3O_{12}$ samples, A1 – A4, sintered for 24 hours. The figure shows that $LiSn_2P_3O_{12}$ samples started their crystallization around 600 °C to 650 °C. At lower sintering temperatures, mainly 500 °C and 550 °C, the low intensity of the main peaks indicates low crystallinity of the samples. Rhombohedral NASICON-type structure (Phase I) and ($R\bar{3}c$) *s*ymmetry along with minor traces of SnP_2O_7 impurity is successfully obtained upon sintering at 600 °C, denoted as sample A3. However, as the sintering temperature increases to 650 °C (sample A4), new peaks appeared at 19.9° and 20.9° that corresponds to the triclinic structure (Phase II) and ($P\bar{1}$) symmetry along with rhombohedral NASICON-type structure (Phase I) and ($R\bar{3}c$) symmetry exist together with minor traces of SnP_2O_7

impurity. It has previously been reported that the two phases of $LiSn_2P_3O_{12}$ coexist at temperatures below 700 °C (Cui et al., 2012), while in rhombohedral type structure (Phase I), this phase always coexisted with other substances such as phase II, SnO_2 and SnP_20_7 (Martinez-Juarez et al., 1995).

In order to further minimize the impurities in the $LiSn_2P_3O_{12}$ system, the sintering time was increased to 48 hours, system II. The sintering temperatures were fixed at 600 ^oC and 650 °C as the samples only started their crystallization at this temperatures instead of 500 and 550 °C. The XRD patterns of sample B1 and B2 are shown in Figure 4.3. A rhombohedral NASICON-type symmetrical structure ($R\bar{3}c$) is successfully obtained for samples B1 and B2 in the presence of only unreacted SnO_2 (Cui et al., 2012) compared to samples A3 and A4 where slight traces of SnP_2O_7 impurity peaks are still observed. This implies that SnP_2O_7 takes a longer time to decompose. Furthermore, the presence of only minor traces of impurity shows that the use of sol-gel method can minimizes the impurity compared to other methods, such as the mechanical milling method that was used by Norhaniza et al., (2010). Besides that, only rhombohedral phase ($R\bar{3}c$) is detected in sample B2 unlike sample A4 where both rhombohedral and triclinic phases are found to coexist.

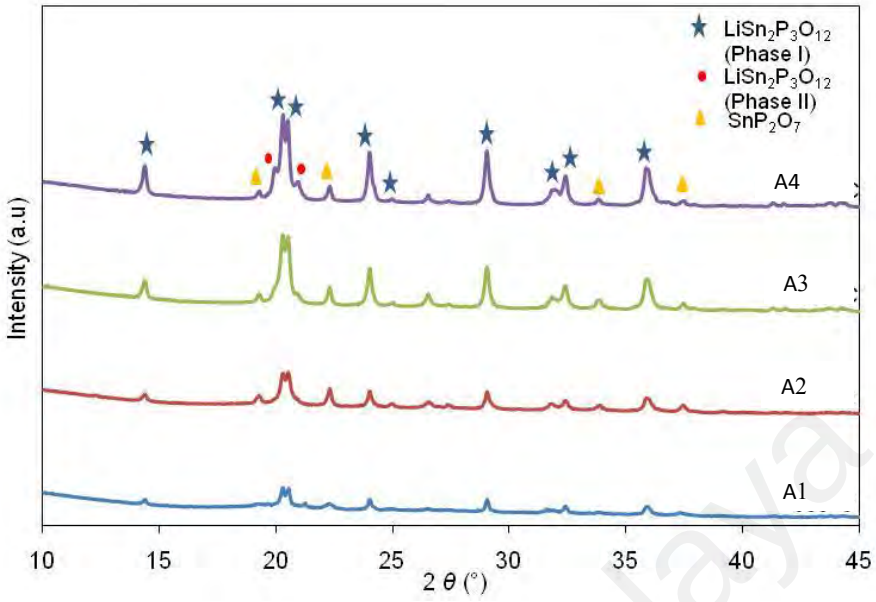

Figure 4.2: X-ray diffraction patterns of $LiSn_2P_3O_{12}$ samples (System I)

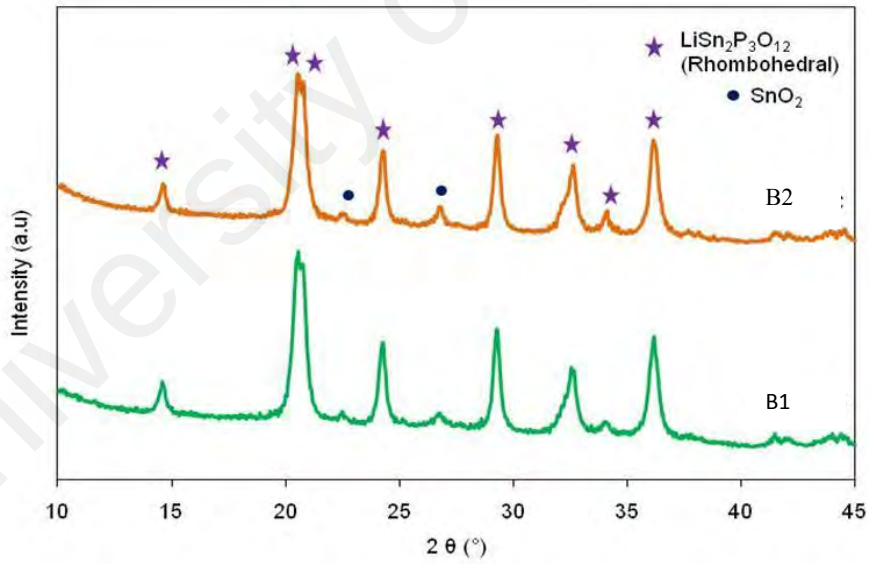

Figure 4.3: X-ray diffraction patterns of $LiSn_2P_3O_{12}$ samples (System II)

Meanwhile, the variations of the lattice parameters of samples A1 to A4 are listed in Table 4.2. Based on the table, the values of *a*, *c* and unit cell volume (*V)* increase with the increase of the sintering temperature. However, the crystallite size decreases as the sintering temperature increases. This observation illustrates that the increase in temperature leads to a decrease in defect concentration by decreasing the proportion of surface atoms (Gaber et al., 2014). Subsequently, this improves the degree of crystallization in $LiSn_2P_3O_{12}$ samples as proven in the XRD pattern in Figure 4.2.

For B1 and B2 samples, the lattice parameters and unit cell volume of both samples are listed in Table 4.3. From the table, it can be seen that the values of *a*, *c* and *V* for both samples increases with temperatures. At the same time, an increase in the sintering temperature from 600 to 650 ^{o}C is accompanied by an increase in the crystallite size, as evidenced by the narrowing of the peak, which indicates bigger grains (Narváez-Semanate & Rodrigues, 2010). For all samples, A1 to A4 and B1 to B2, the densities of all samples were more than 90 % of its theoretical density of 3.79 g cm^{-3}, with the highest density being that of sample A4 and B1, which is attributed to the compactness of the tiniest crystallites in the system.

Table 4.2: Lattice parameters and unit cell volume of $LiSn_2P_3O_{12}$ samples (System I)

Sample	Sintering temperature (°C)	*a* [Å]	*c* [Å]	*V* [Å]	Crystallite size [Å]
A1	500	8.6792	21.4286	1397.88	659.21
A2	550	8.6914	21.3768	1398.43	552.55
A3	600	8.7058	21.3836	1403.07	478.48
A4	650	8.7062	21.3850	1403.73	309.93

Table 4.3: Lattice parameters and unit cell volume of $LiSn_2P_3O_{12}$ samples (System II)

Sample	Sintering temperature (°C)	*a* [Å]	*c* [Å]	*V* [Å]	Crystallite size [Å]
B1	600	8.3880	22.0148	1341.38	137.4
B2	650	8.4071	21.9985	1346.50	138.3

4.4 FTIR analysis

Figures 4.4 and 4.5 display FTIR spectra of various functional groups in the $LiSn_2P_3O_{12}$ samples, System I (sample A1 to A4) and System II (sample B1 to B2) in the spectral region from 550 to 1400 cm^{-1}. From both figures, it can be observed that the entire region is dominated by the vibrations of PO_4 tetrahedral and these features are all the same in all the sintered samples. The bands in the region of 560 to 670 cm^{-1} as shown in Figure 4.4 and 4.5 are mainly caused by the asymmetric bending vibration of O-P-O units. Stretching vibrations of P-O-P are observed in the region of 700 to 800 cm^{-1}. Meanwhile, the bands in the region of 1000 to 1280 cm^{-1}, are assigned to the asymmetric stretching vibrations and bands in the region of 900 to 980 cm^{-1} correspond to the symmetric stretching vibrations of the PO_4^{3-} ions(Antony et al., 2011; Bohre et al., 2014; Bohre & Shrivastava, 2013; Ejehi et al., 2012; Kurazhkovskaya et al., 2010; Mariappan & Govindaraj, 2005).

For samples A1 to A4, comparing all the dominant absorption bands of O-P-O and PO_4^{3-}, as the sintering temperature increases, the two absorption bands are shifted to the lower wave number direction. This is due to the increase of the crystallinity of the sintered samples as also confirmed by the XRD analysis (Qiu et al., 2003). However, for samples B1 and B2, the bands are shifted to the higher wave number direction as the sintering temperature increases. This may be due to the decrease in crystallinity of the sintered samples. This observation is consistent with the XRD results discussed in the previous section.

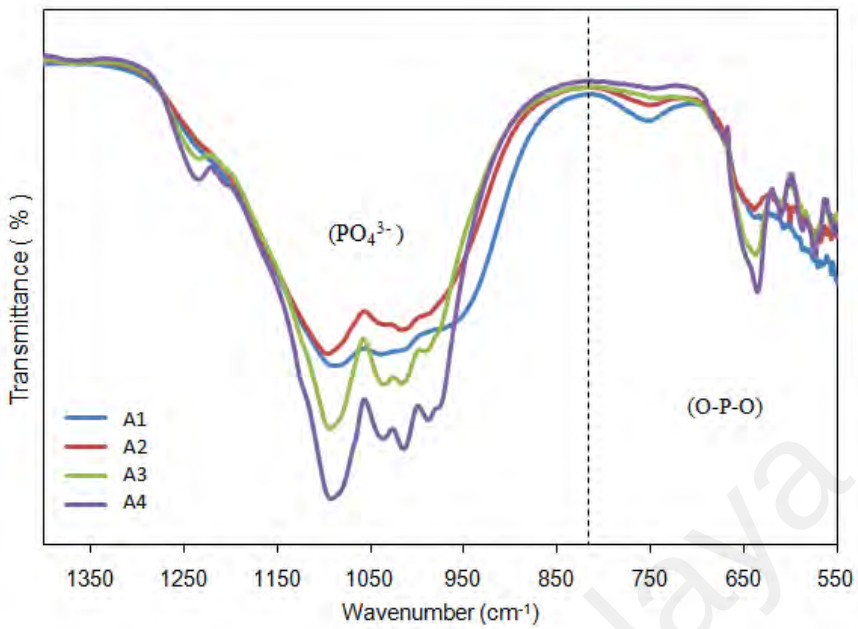

Figure 4.4: FTIR spectra of various functional groups in $LiSn_2P_3O_{12}$ samples (System I)

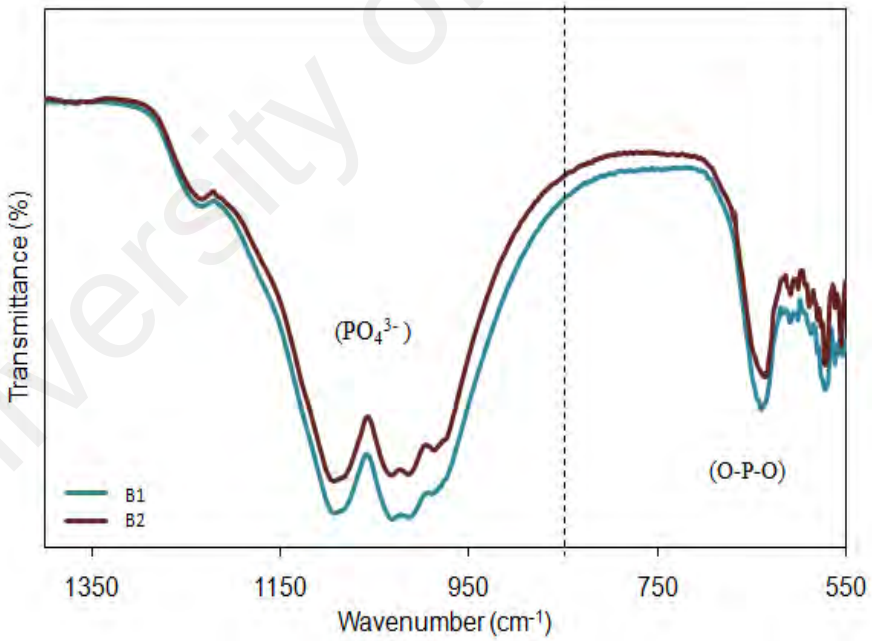

Figure 4.5: FTIR spectra of various functional groups in $LiSn_2P_3O_{12}$ samples (System II)

4.5 SEM, EDX and particle size distribution analyses

The cross-sectional SEM micrographs of $LiSn_2P_3O_{12}$ pellets and particle size distribution of samples A1 to A4 are presented in Figure 4.6. The SEM micrographs reveal that the particle size clearly decreases as the sintering temperature increases. This is confirmed by the analysis of the particle size distribution as displayed in Figure 4.7. The average particle size decreases from 10.01 μm to 5.58 μm as the sintering temperature increases from 500 °C to 650 °C. These results are in agreement with the XRD analysis which shows that the increase in sintering temperature improves the crystallinity of the prepared samples. Besides that, the smaller particles in $LiSn_2P_3O_{12}$ sintered samples are favourable as this may improve contact with electrode materials when it is used for device fabrication such as in electrochemical devices (Adnan & Mohamed, 2012).

Meanwhile, Figure 4.8 depicts the SEM micrographs and particle size distribution of B1 and B2 samples sintered at 600 and 650 °C. In SEM micrographs for both $LiSn_2P_3O_{12}$ samples, the powders are slightly agglomerated. The particle size of $LiSn_2P_3O_{12}$ electrolytes samples clearly increases with sintering temperature as confirmed by the particle size distribution analysis as displayed in Figure 4.9. The average particle size for the $LiSn_2P_3O_{12}$ sample increases from 22.8 μm to 26.8 μm as the sintering temperature increases from 600 °C to 650 °C. These results can be correlated with the X-ray diffraction analysis showing that increase of the sintering temperature increases the crystallite size and crystallinity of the prepared samples. The particle size for both samples B1 and B2 is slightly bigger compared to samples A1 to A4.

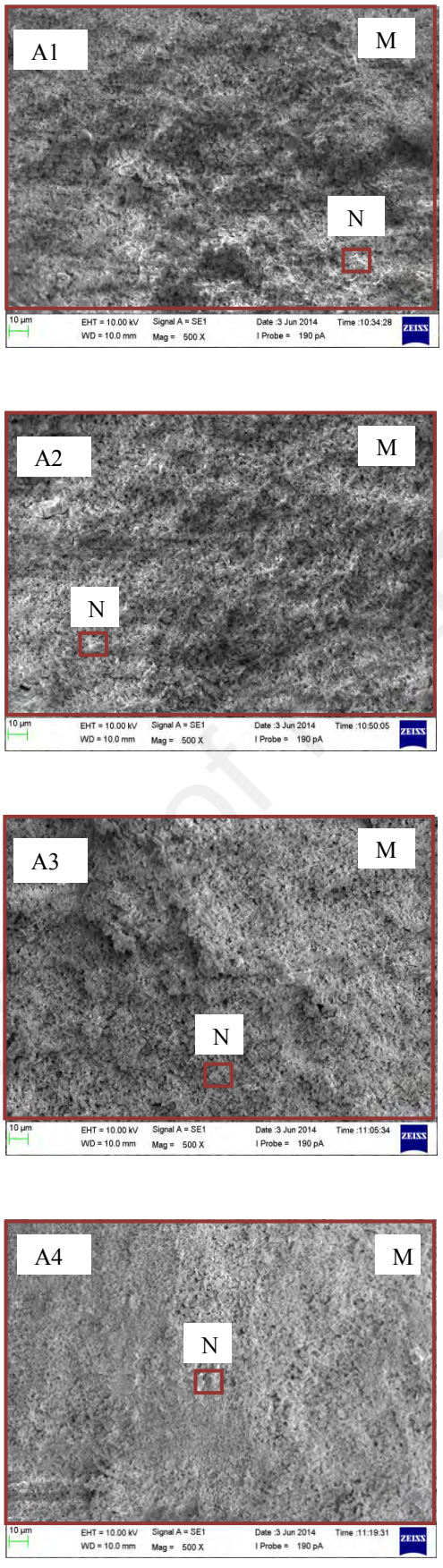

Figure 4.6: Cross-sectional SEM micrographs of $LiSn_2P_3O_{12}$ pellets (System I)

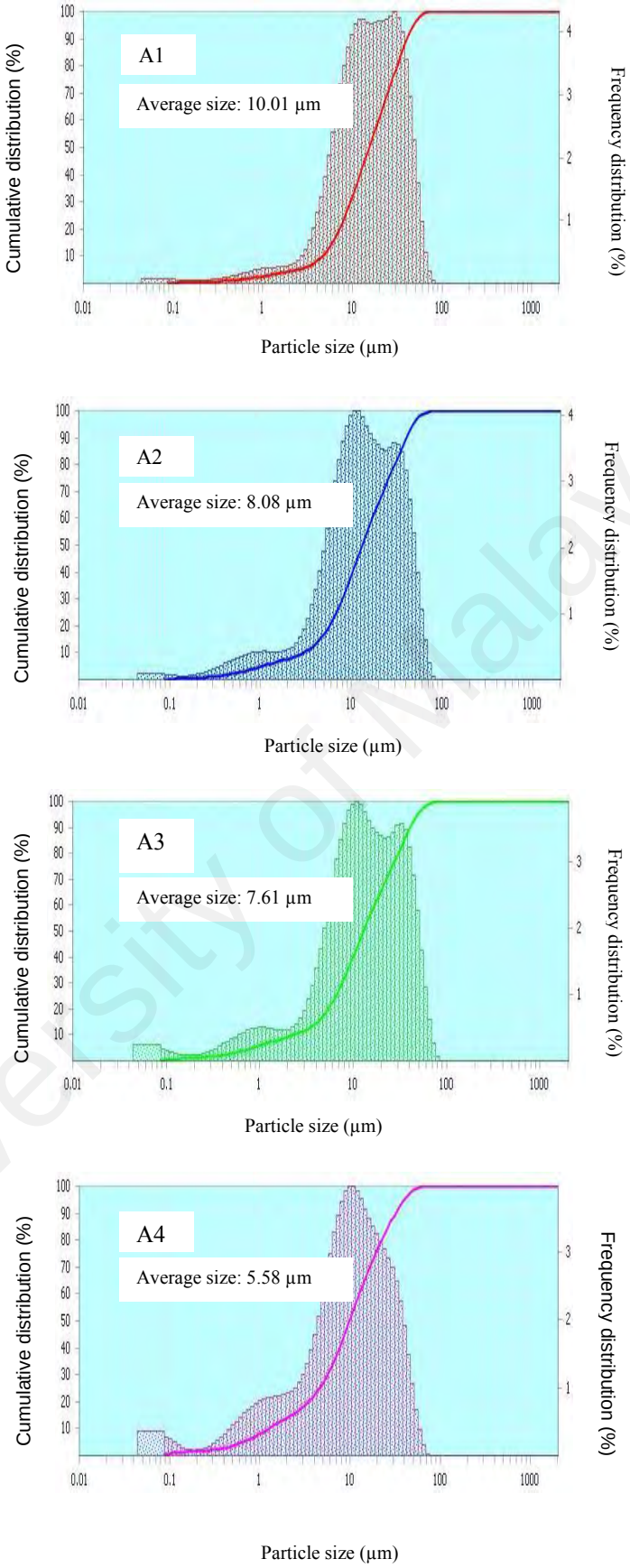

Figure 4.7: Particle size distributions of $LiSn_2P_3O_{12}$ samples (System I)

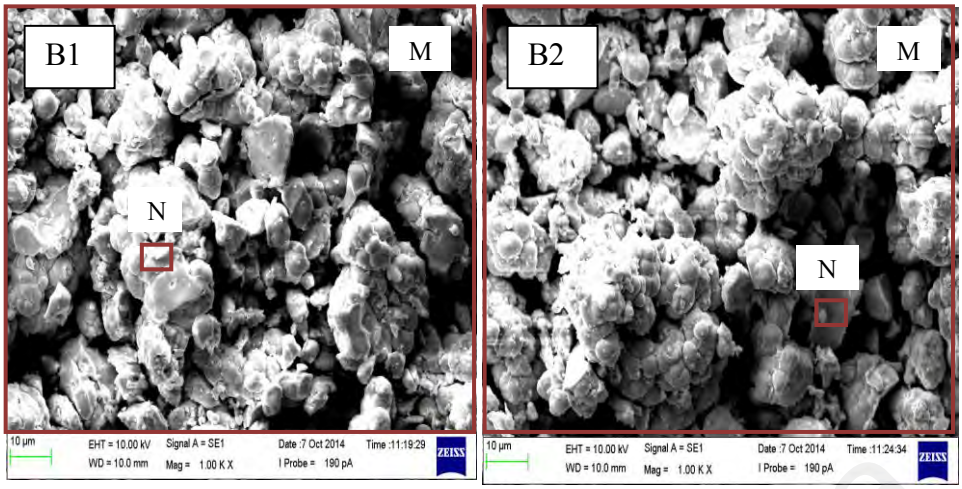

Figure 4.8: SEM micrographs of $LiSn_2P_3O_{12}$ samples (System II)

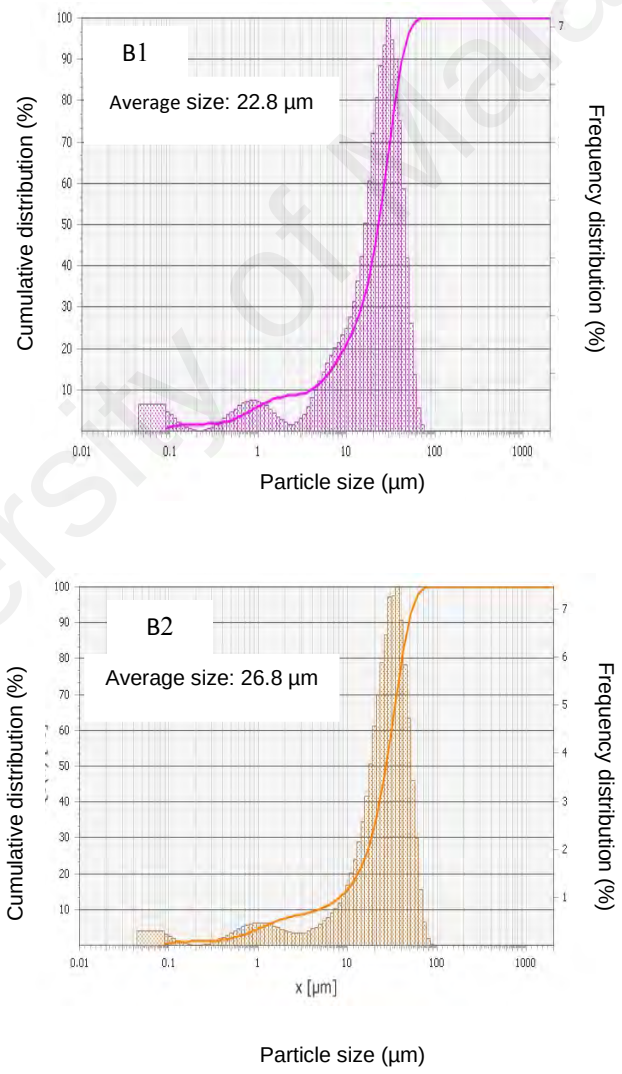

Figure 4.9: Particle size distribution of $LiSn_2P_3O_{12}$ samples (System II)

The EDX analyses of $LiSn_2P_3O_{12}$ samples, A1 to A4 and B1 and B2 are tabulated in Table 4.4 and 4.5. As lithium is not detectable by EDX due to its light atomic weight which does not permit the analysis of emitted radiations, the concept of charge neutrality is applied (Norhaniza et al., 2011). The analysis was carried out on a larger region (marked as M) in order to measure the average composition and smaller region (marked as N) in order to investigate whether the composition A is homogeneous on a relatively small scale.

In System I, it is found that the atomic ratio in region M for samples A3 and A4 are in good agreement with the stoichiometric ratio of the starting materials. However, on the small scale region marked as N, the SnP_2O_7 impurity found and also the coexistence of rhombohedral and triclinic phases in the system as shown in XRD analysis affected the stoichiometric ratio of the elements. Meanwhile, in System II, the results show that the atomic ratios in both region M and N for Sn: P: O are homogeneous and are in good agreement with the stoichiometric ratio of the starting materials for samples B1 and B2. Therefore, based on the EDX and XRD analysis, further investigation will only be done on samples B1 and B2.

Table 4.4: The EDX stoichiometric atomic ratio of $LiSn_2P_3O_{12}$ samples (System I)

Sample	Sintering temperature (°C)	Composition		Stoichiometric atomic ratio		
				Sn	P	O
		Starting mixture		2	3	12
A1	500	EDX analysis	M	2.0	2.9	11.5
			N	2.0	2.7	11.5
A2	550	EDX analysis	M	2.0	2.9	11.5
			N	2.0	2.7	11.5
A3	600	EDX analysis	M	2.0	2.9	12.0
			N	2.0	2.8	11.8
A4	650	EDX analysis	M	2.0	3.0	12.0
			N	2.0	2.8	11.9

Table 4.5: The EDX stoichiometric atomic ratio of $LiSn_2P_3O_{12}$ samples (System II)

Sample	Sintering temperature (°C)	Composition		Stoichiometric atomic ratio		
				Sn	P	O
		Starting mixture		2	3	12
B1	600	EDX analysis	M	2.0	3.0	12.0
			N	2.0	2.9	12.0
B2	650	EDX analysis	M	2.0	2.9	12.0
			N	2.0	2.9	12.0

4.6 Electrical properties of $LiSn_2P_3O_{12}$ system

4.6.1 DC conductivity of $LiSn_2P_3O_{12}$ system

DC ionic conductivity of solid electrolytes is a very important characteristic that can be determined using impedance spectroscopy. The complex impedance plots of samples B1 and B2 from System II are displayed in Figure 4.10, Figure 4.11 and Figure 4.13 respectively. From Figure 4.10, several important points are observed. Firstly, at 30°C for both systems, the plots seem to consist of two overlapping semicircles with an electrode spike at low frequency region.

The high frequency semicircle is assigned to bulk response with its intercept at the *x*-axis assigned to bulk resistance, R_b, while the middle frequency semicircle is assigned to grain boundary response with its intercept at the *x*-axis corresponds to grain boundary resistance, R_{gb}. The spike that can be clearly seen at the low frequency region of the sample B1 may indicate the effects of electrode polarization as a result of the accumulation of ions between the electrode and the sample (Mariappan & Govindaraj, 2005). When the temperature increases from 30 to 400°C for both samples, both bulk and grain boundary resistances, R_b and R_{gb} shifts towards lower value indicating an increase in conductivity as can be observed in Figure 4.11.

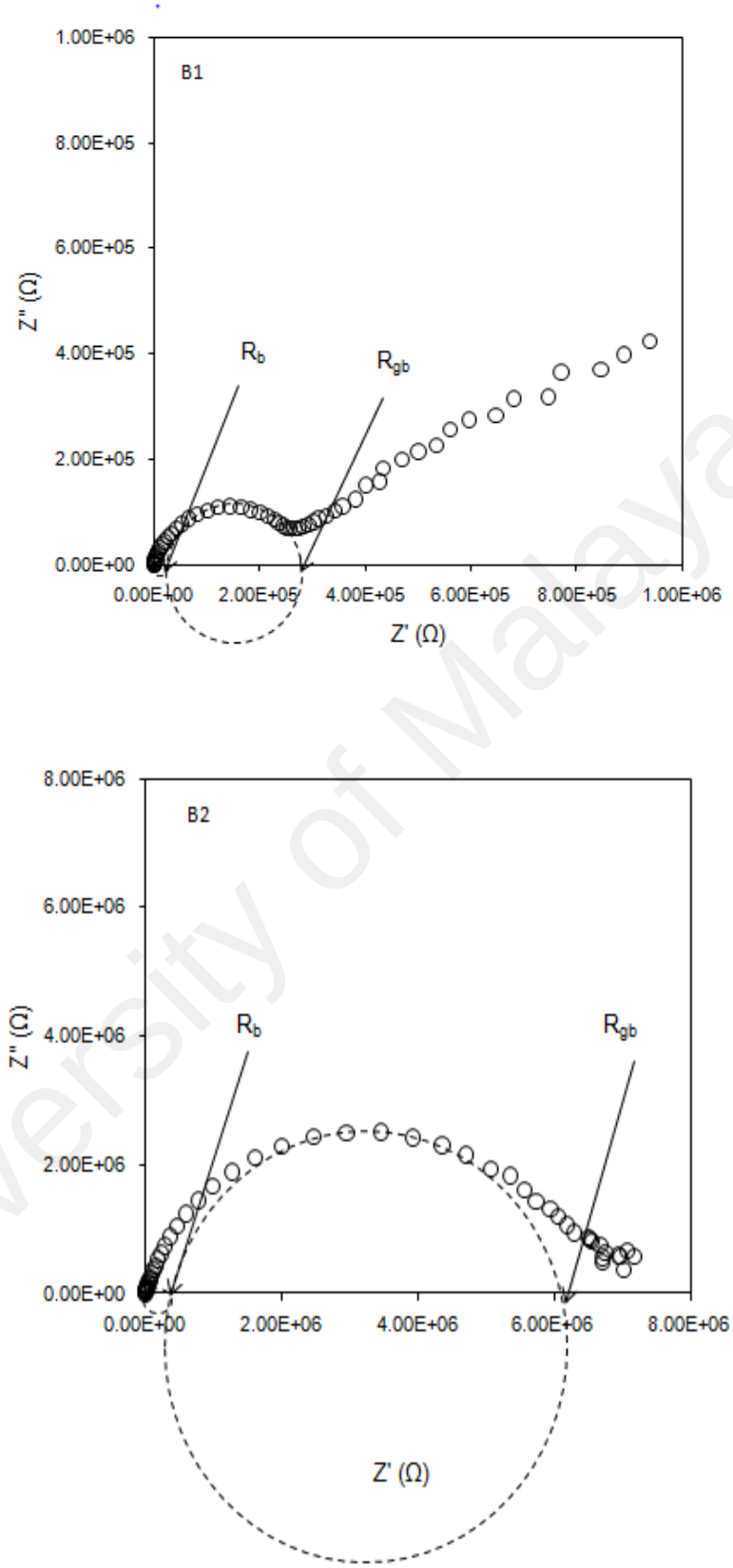

Figure 4.10: Complex impedance plot of $LiSn_2P_3O_{12}$ samples (System II) at room temperature

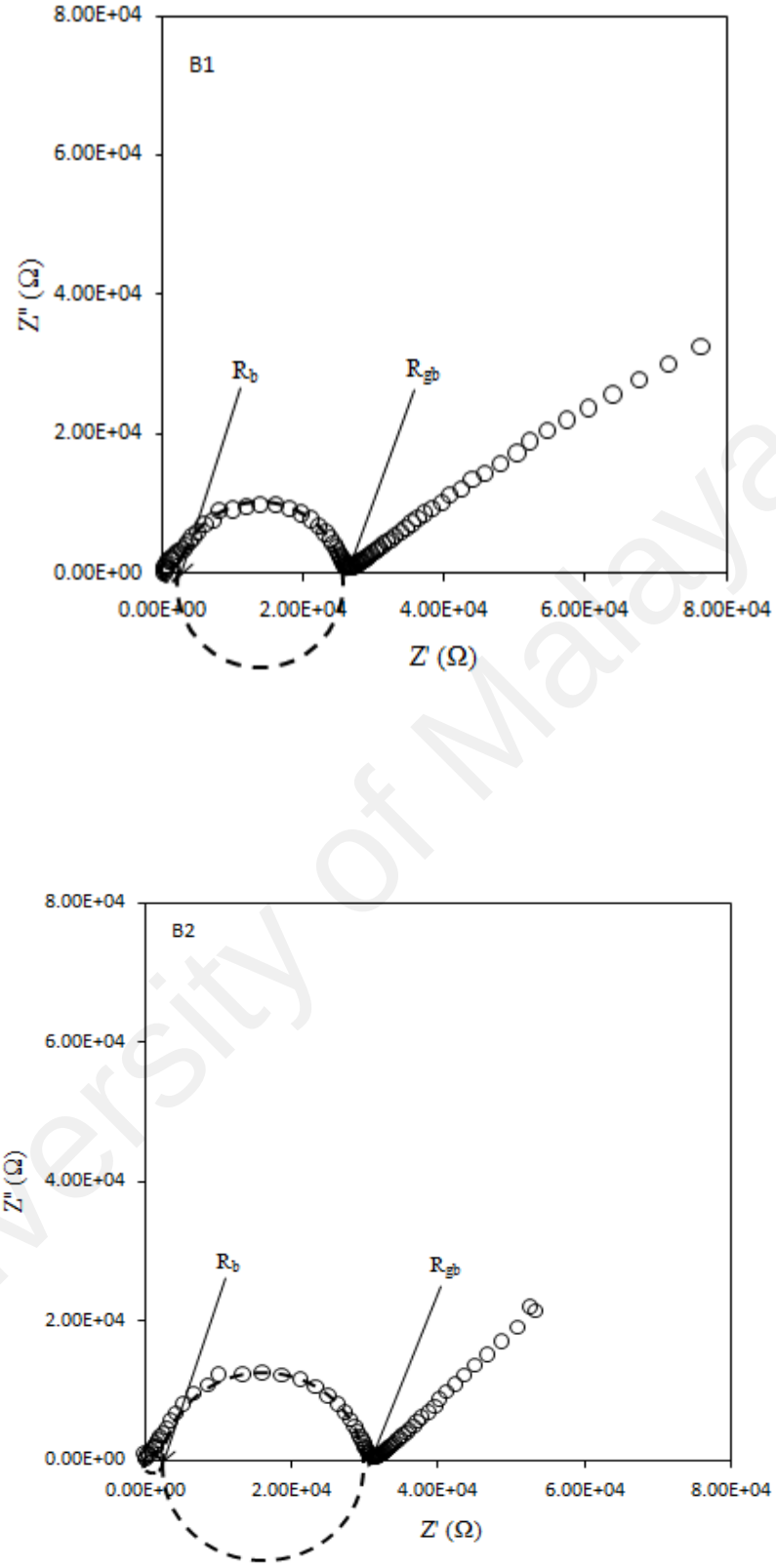

Figure 4.11: Complex impedance plot of $LiSn_2P_3O_{12}$ samples (System II) at 400 °C

Experimental complex impedance data may well be approximated by the impedance of an equivalent circuit composed of bulk and grain boundary resistance, R_b and R_{gb} and also bulk and grain boundary capacitance, C_b and C_{gb} with constant phase element (CPE) behaviour as depicted in Figure 4.12. The general expression of the CPE is (Almond et al., 1983; Zhou et al., 2009) :

$$Z_{CPE} = \frac{1}{C\,(j\omega)^n} \tag{4.1}$$

where C is the ideal capacitance when $n = 1$, $j = (-1)^{1/2}$, ω is the angular frequency and $\omega = 2\pi f$.

Therefore, the equivalent circuit for samples B1 and B2 at 30 °C and 400 °C now consists of parallel RC element and attached with series $CPE_{blocking\ electrode}$ with constant phase element (CPE). Parallel bulk and grain boundary resistance, R_b and R_{gb} and bulk and grain boundary capacitance, C_b (CPE), C_{gb} (CPE) are attached to series $CPE_{blocking\ electrode}$ with constant phase element (CPE) (Yadav & Bhatnagar, 2012).

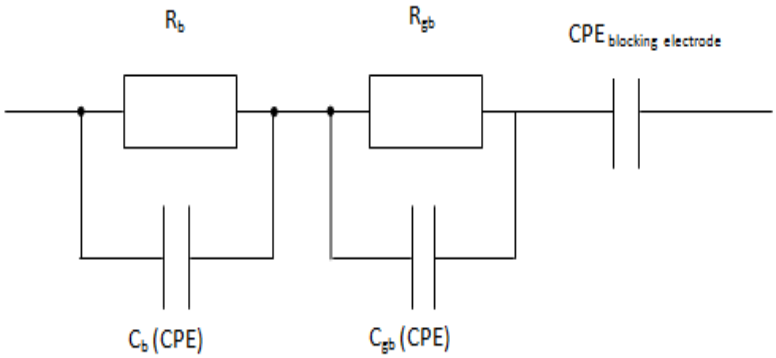

Figure 4.12: Equivalent circuit of $LiSn_2P_3O_{12}$ samples based on the impedance analysis at room temperature and 400 °C

As the temperature increases to 500°C, only one semicircle is found for both samples, sample B1 and B2 that correspond to bulk response with its intercept at the *x*-axis assigned to bulk resistance, R_b as depicted in Figure 4.13.

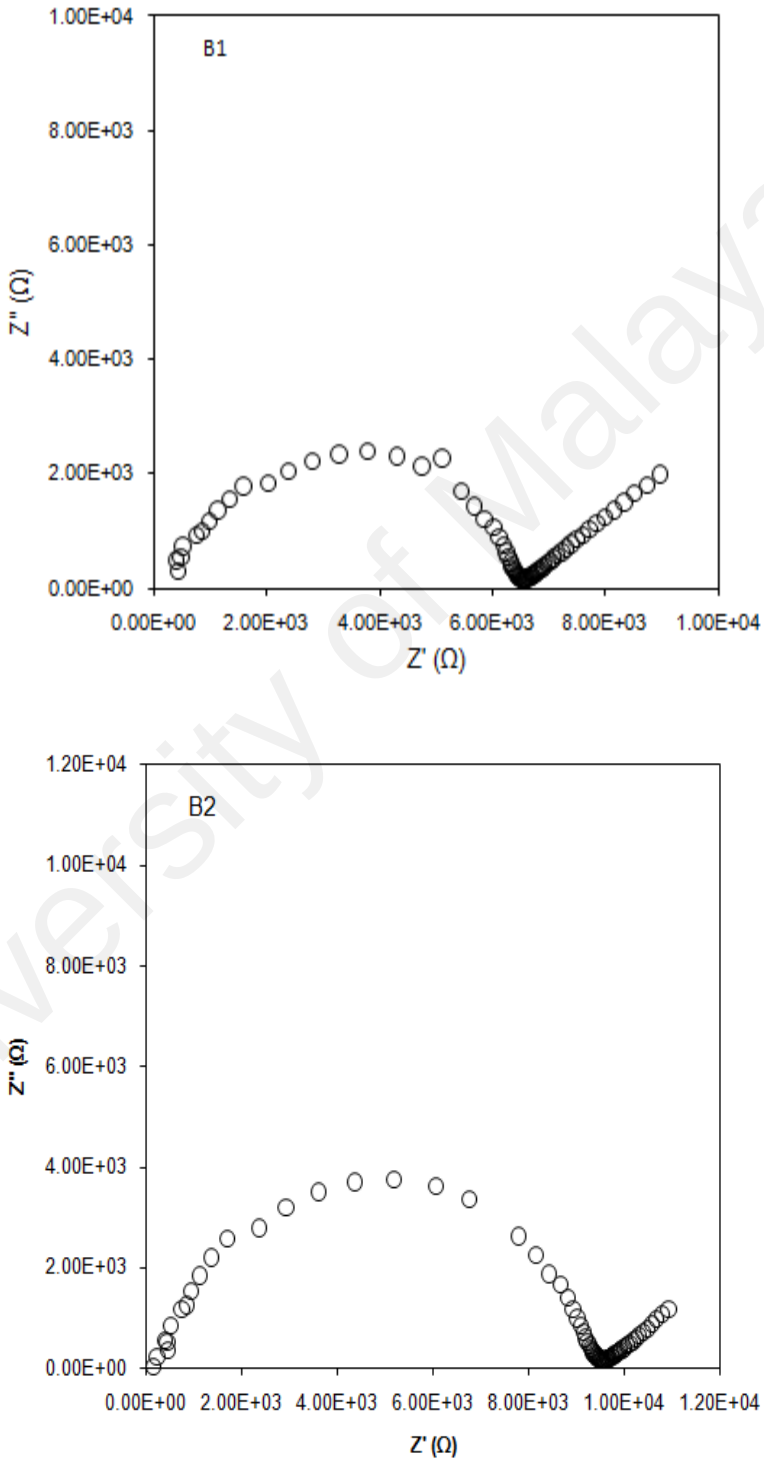

Figure 4.13: Complex impedance plot of $LiSn_2P_3O_{12}$ samples (System II) at 500 °C

Meanwhile, for samples B1 and B2 in System II at 500°C, experimental complex impedance data might now be approximated by a circuit only containing bulk resistance, R_b and bulk capacitance, C_b (CPE) and $CPE_{blocking\ electrode}$ with constant phase element (CPE) behaviour as in Figure 4.14.

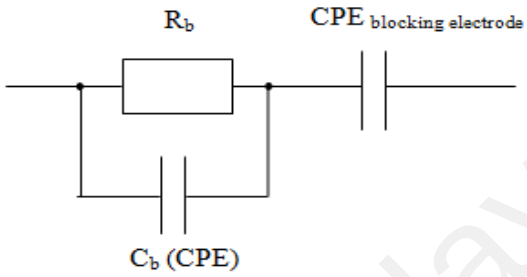

Figure 4.14: Equivalent circuit of $LiSn_2P_3O_{12}$ samples based on the impedance analysis at 500°C

Bulk and grain boundary conductivities, ζ_b and ζ_{gb} were then calculated using R_b and R_{gb} values determined from the impedance plots. It is observed that bulk, grain boundary and total conductivities for samples B1 and B2 in System II increase with temperature as listed in Table 4.6 and Table 4.7.

For $LiSn_2P_3O_{12}$ samples of System II, bulk conductivity, ζ_b increases from 7.22×10^{-6} S cm^{-1} at 30 °C to 1.38×10^{-5} S cm^{-1} at 500 °C for sample B1. On the other hand for sample B2, bulk conductivity, ζ_b at 30 °C and 500 °C are 3.28×10^{-6} S cm^{-1} and 1.03×10^{-5} S cm^{-1} respectively. The highest total conductivity, ζ_t found is 1.38×10^{-5} S cm^{-1} at 500 °C for sample B1 which is three orders of magnitude higher than that reported by Norhaniza et al, (2010). This may be due to only trace amount of unreacted SnO_2 impurity found in sample B1 compared to the sample prepared by Norhaniza et al. (2010) that contains impurities such as Li_3PO_4, SnP_2O_7 and SnO_2. The smaller grained powders of sample B1 can result in sintered pellet with high density,

small voids and grains, which lead to a high ionic conductivity compared to the other sample. Besides that, the volume, V (1341.38 Å) was found to be the suitable value for the ion conduction in sample B1. It is also known that the conductivity of NASICON increases with an decrease in the lattice constants because of the optimization of the tunnel or bottleneck size for Li^+ ion migration (Traversa et al., 2000). So, as sample B1 has smaller lattice constants as confirmed by XRD compared to sample B2, one should have expected higher conductivity for sample B1. The increment of conductivity with temperature also can be due to the increase in the thermal activated drift mobility of ions according to hopping conduction mechanism.

Table 4.6: Ionic conductivity values for $LiSn_2P_3O_{12}$ samples (System II) at 30 °C

Sample	$\zeta_{b,30}$ (S cm^{-1})	$\zeta_{gb,30}$ (S cm^{-1})	$\zeta_{t,30}$ (S cm^{-1})
B1	$(7.22 \pm 0.04) \times 10^{-6}$	$(2.99 \pm 0.06) \times 10^{-7}$	$(2.87 \pm 0.06) \times 10^{-7}$
B2	$(3.28 \pm 0.07) \times 10^{-6}$	$(1.79 \pm 0.08) \times 10^{-8}$	$(1.78 \pm 0.08) \times 10^{-8}$

Table 4.7: Ionic conductivity values for $LiSn_2P_3O_{12}$ samples (System II) at 500 °C

Sample	$\zeta_{b,500}$ (S cm^{-1})	$\zeta_{t,500}$ (S cm^{-1})
B1	$(1.38 \pm 0.03) \times 10^{-5}$	$(1.38 \pm 0.03) \times 10^{-5}$
B2	$(1.03 \pm 0.05) \times 10^{-5}$	$(1.03 \pm 0.05) \times 10^{-5}$

The activation energy for the Li^+ migration was determined from the Arrhenius equation:

$$\sigma = \sigma_0 \, exp\left(\frac{-E_a}{kT}\right) \tag{4.2}$$

where ζ, T, ζ_0, E_a, and k denote the conductivity, the absolute temperature, pre-exponential factor, activation energy for Li^+ ion migration, and Boltzmann‟s constant, respectively. The Arrhenius plots for System II are depicted in Figure 4.15. From the graph, it can be observed that the conductivity increases linearly with temperature implying that conduction is a thermally activated process. The regression value, R for all samples are found to be 0.9. Besides that, differences in slopes are evident as we can see two regions, region I associated with low temperature and region II associated with high temperature.

The values of bulk and grain boundary activation energies for both regions are displayed in Table 4.8. The bulk activation energy values for sample B1 and B2 for region I are 0.005 and 0.010 eV respectively. While for region II, the bulk activation energy values are 0.250 and 0.330 eV for the sample B1 and B2 respectively. Furthermore, the activation energy value reported for System II is much lower compared to those obtained by other researchers (Cui et al., 2012; Iglesias et al., 1997; Martinez-Juarez et al., 1997) . This low value of activation energy is characteristic of a fast ion conductor, and a result from the regularity of the diffusion channels in the NASICON structure (Narváez-Semanate & Rodrigues, 2010).

However, the activation energy values obtained at higher temperature is higher compared to that obtained at lower temperature. According to Chourashiya (2013), this may be due to at low temperatures; extrinsic vacancies are the most important parameters (Chourashiya, 2013). Furthermore, the concentrations of intrinsic vacancies are so small at low temperature that they may be ignored. The number of vacancies is essentially constant; m (slope) in the extrinsic region thus only depends on the mobility of mobile species due to the extrinsic defects. At higher temperature, the concentration of intrinsic defects has increased so that it is similar or greater than the concentration of extrinsic defects. Thus in this region, for a system with Schottky defects and with Frenkel defects a plot of log ζ versus 1000/T gives a larger value for the activation energy because it depends on both the activation energy for the cation to jump and the enthalpy of formation of a Schottky and Frenkel defect respectively.

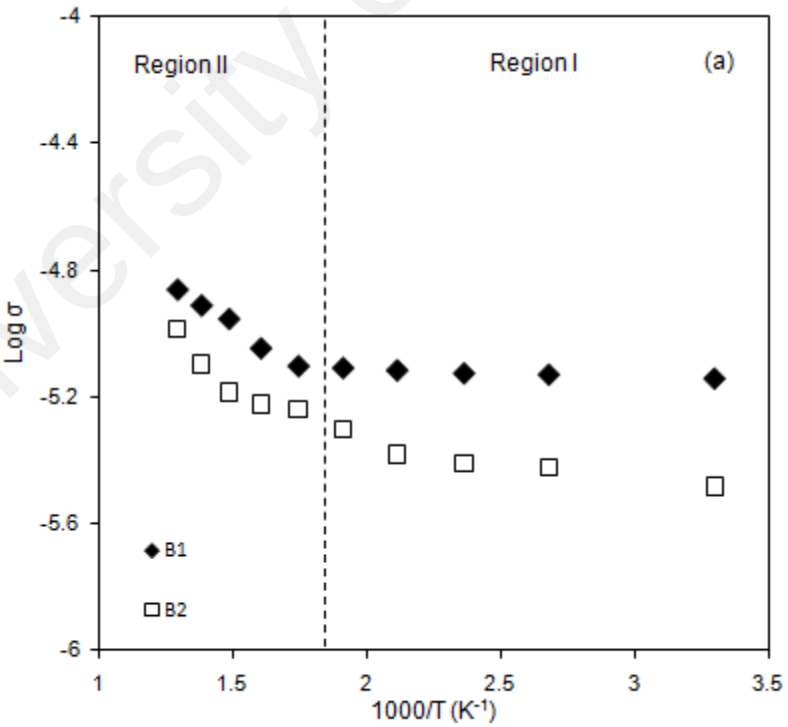

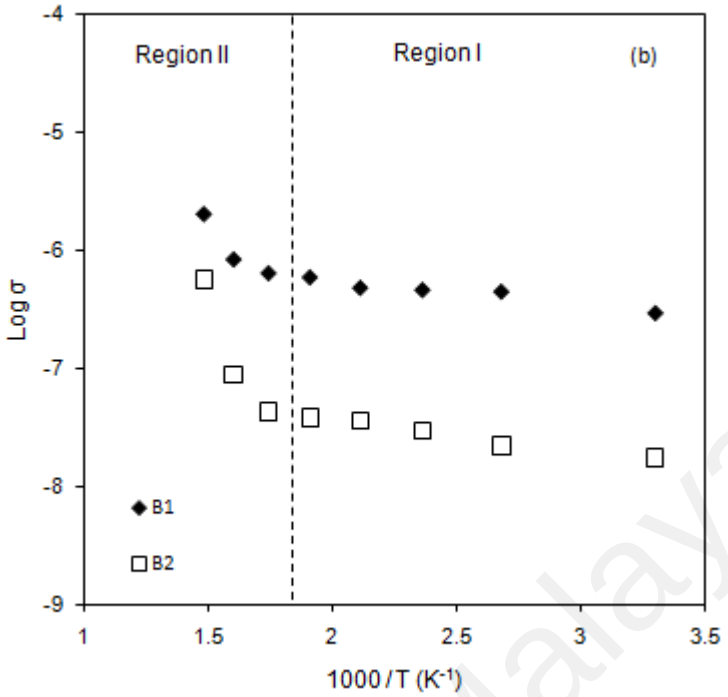

Figure 4.15: Log ζ versus 1000/T plots of (a) bulk and (b) grain boundary conductivity of $LiSn_2P_3O_{12}$ samples (System II)

Table 4.8: Bulk and grain boundary activation energies for $LiSn_2P_3O_{12}$ samples (System II)

Sample	$E_{a,b}$ (eV)		$E_{a,\ gb}$ (eV)	
	Region I (Low T)	Region II (High T)	Region I (Low T)	Region II (High T)
B1	0.005	0.250	0.018	0.380
B2	0.010	0.330	0.051	0.800

4.6.2 AC conductivity of $LiSn_2P_3O_{12}$ system

The AC conductivity spectra of log ζ_{ac} vs log ω plots of $LiSn_2P_3O_{12}$ samples for System II are illustrated in Figure 4.16. The plot consists of a plateau in the intermediate frequency region and high frequency dispersion. A spike in the low frequency region is also detected in the plots for temperatures from 303 to 573 K of sample B1. Meanwhile for sample B2, each plot consists of a plateau in intermediate frequency region and high frequency dispersion. The low frequency dispersion is due to electrode polarization effects which are related to blocking of ions between the electrode and samples (Mariappan & Govindaraj, 2005) and also observed in the complex impedance plots as discussed in previous section. Meanwhile, the intermediate frequency plateau is due to frequency independence of conductivity corresponding to DC conductivity. The transition from the DC plateau to AC conductivity dispersion region shifts towards higher frequency range when temperature increases.

At high frequencies, ζ_{ac} increases linearly with frequency obeying the empirical law of frequency dependence given by power law of the form (Jonscher, 1983) of:

$$\sigma'(\omega) = \sigma(0) + A\omega^s \tag{4.3}$$

where ζ (0) is the dc conductivity of the sample, A is the temperature dependent parameter and s is the frequency exponent.

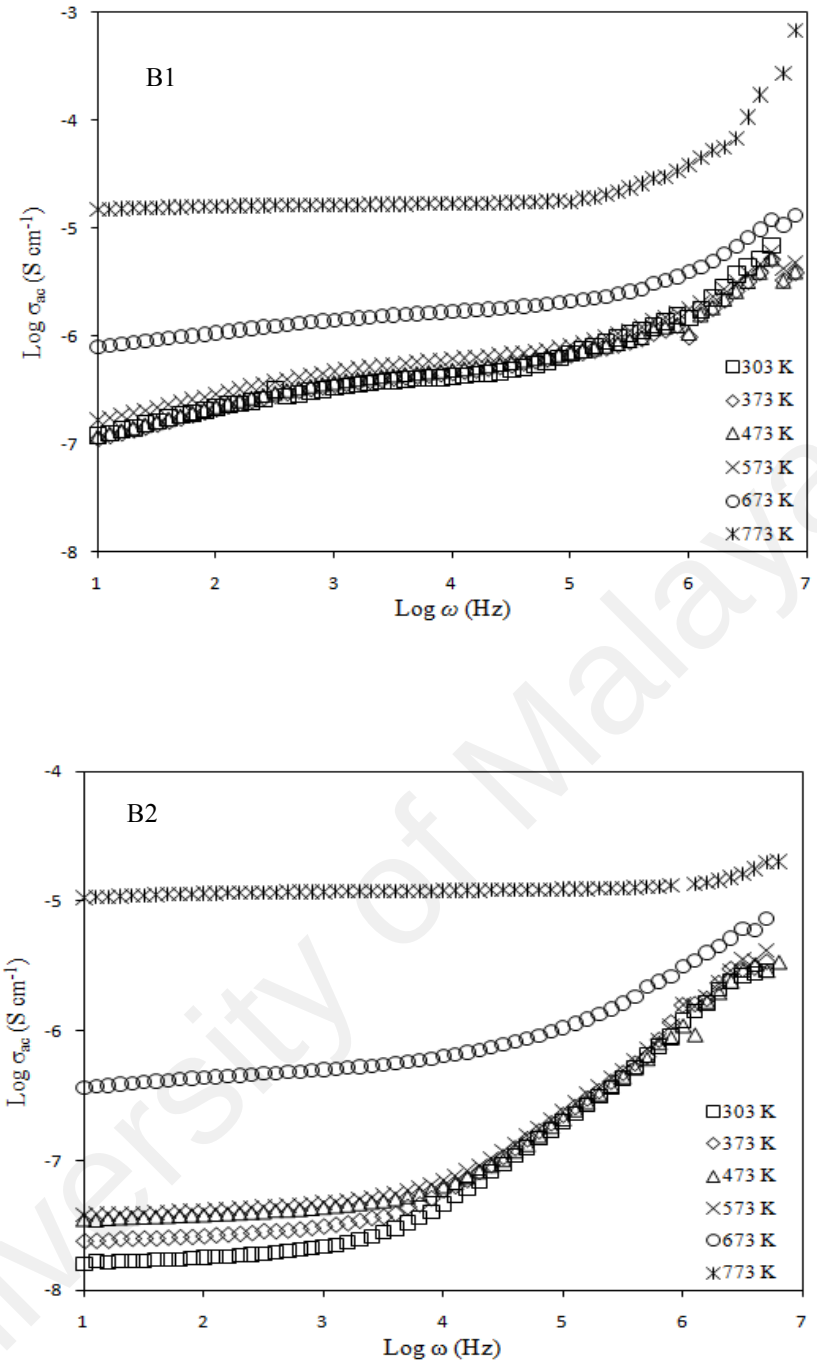

Figure 4.16: AC conductivity spectra of $LiSn_2P_3O_{12}$ samples (System II) at various temperatures

The value of ω_p, K, n,and μ, at all temperatures studied for $LiSn_2P_3O_{12}$ samples for System II are listed in Table 4.9. For both samples in System II, the values of ω_p, K, n, and μ, increase with the increase of temperature. As such the rise in conductivity in the samples can be attributed to the rise in ionic mobility as well as density of mobile ions (Teo et al., 2012; Vijayakumar et al., 2003) . The trend of μ value can be correlated with the outcomes from impedance analysis showing that the sample B1 exhibited the highest ionic conductivity value and also possessed the highest ionic mobility, μ that is 5.43×10^{-11} cm^2 V^{-1} s^{-1} and the highest density of mobile ions, n that is 1.99×10^{24} cm^{-3}.

Table 4.9: Parameters of ω_p, K, n and μ at various temperatures for $LiSn_2P_3O_{12}$ samples (System II)

Sample	T (K)	ω_p (Hz)	K (S cm^{-1} K Hz^{-1})	n (cm^{-3})	μ (cm^2 V^{-1} s^{-1})
B1	303	2.51×10^5	3.47×10^{-10}	1.30×10^{23}	1.38×10^{-11}
	373	3.16×10^5	3.48×10^{-10}	1.30×10^{23}	1.42×10^{-11}
	473	7.94×10^5	3.12×10^{-10}	1.17×10^{23}	2.81×10^{-11}
	573	1.26×10^6	3.37×10^{-10}	1.26×10^{23}	3.67×10^{-11}
	673	2.00×10^6	6.88×10^{-10}	2.00×10^{23}	4.95×10^{-11}
	773	2.51×10^6	5.32×10^{-9}	1.99×10^{24}	5.43×10^{-11}
B2	303	1.58×10^4	3.80×10^{-10}	1.42×10^{23}	8.74×10^{-13}
	373	2.51×10^4	4.28×10^{-10}	1.60×10^{23}	1.12×10^{-12}
	473	6.31×10^4	3.76×10^{-10}	1.41×10^{23}	2.23×10^{-12}
	573	1.00×10^5	3.62×10^{-10}	1.35×10^{23}	2.92×10^{-12}
	673	3.16×10^5	1.34×10^{-9}	5.02×10^{23}	7.85×10^{-12}
	773	2.24×10^6	4.32×10^{-9}	1.61×10^{24}	4.84×10^{-11}

Furthermore, the temperature dependence of *s* is very useful for determining the type of AC conduction mechanism in a material. In the literature, various theoretical models for AC conductivity have been proposed to explain the temperature dependence of *s*. In the Quantum Mechanical Tunnelling model (QMT) (Ghosh, 1990), the value of *s* increases slightly with increasing temperature while in the Correlated Barrier Hopping model (CBH) (Elliott, 1977) *s* is predicted to be frequency and temperature dependent with *s* increasing towards unity as temperature approaches 0 K with no minimum value for *s*.

Figure 4.17 exhibits the temperature dependence of the exponent *s* for $LiSn_2P_3O_{12}$ samples for System II calculated from the slopes of the linear part in the high frequency region of log ζ_{ac} versus log ω as shown in Figure 4.15. The value of *s* decreases from 0.94 to 0.59 for sample B1 while for sample B2, the value of *s* decreases from 0.64 to 0.29. The decreasing value of *s* with temperature suggests that CBH model is the predominant AC conduction mechanism in the samples. The model considers the hopping of carriers between two sites over a barrier separating them. The frequency exponent *s* in the CBH model can be expressed in relation (Elliott, 1977) as shown below:

$$s = 1 - \frac{6kT}{W_M} \tag{4.7}$$

where *k* is Boltzmann constant, *T* is temperature, W_M is maximum barrier height. From Equation 4.12 it can be deduced that *s* will become unity as temperature reaches 0 K. In system II, sample B1 is fitted to the equation $s = -0.0007T + 1.0998$ which suggests that $s = 1$ when $T \rightarrow 0$. Meanwhile, equation $s = -0.0006T + 0.8326$ can be fitted to the

plot of sample B2. This equation also suggests that $s = 1$ when $T \rightarrow 0$. These equations indicate again that CBH model is the appropriate model for $LiSn_2P_3O_{12}$ samples for System II.

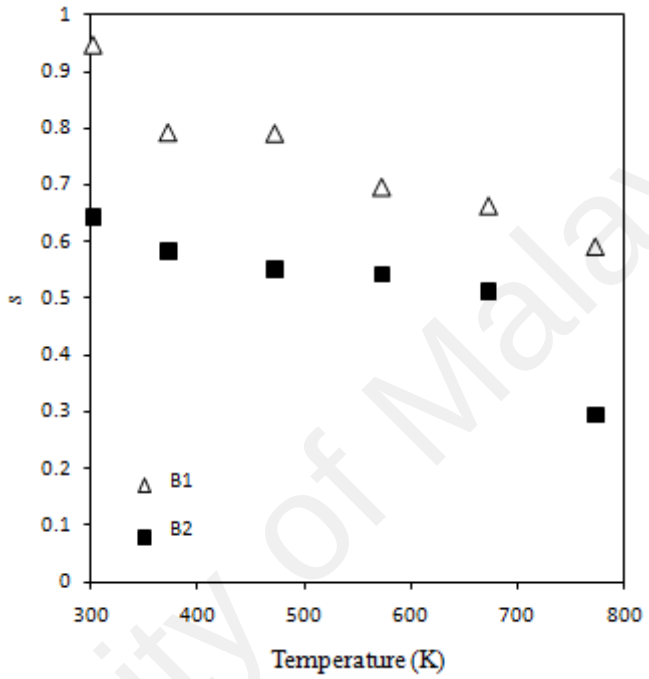

Figure 4.17: Variation of *s* with temperature for $LiSn_2P_3O_{12}$ samples (System II)

4.6.3 Transference number measurement analysis

The transference number corresponding to ionic (t_{ion}) for $LiSn_2P_3O_{12}$ system was evaluated using Wagner"s polarization method. In this method, the direct current, DC is monitored as a function of time of a fixed DC voltage of 0.5 V across SS/ $LiSn_2P_3O_{12}$ solid electrolytes/SS. After polarization, the graphs of normalized current versus time were plotted. Figure 4.18 presents a typical plot of normalized polarization current versus time for $LiSn_2P_3O_{12}$ samples in System II. From the plot, the polarization current for both samples, B1 and B2, the current saturated after about 500 s. Furthermore, both

samples show transference number value close to unity that is 0.99. This shows that the conductivity of the $LiSn_2P_3O_{12}$ samples was predominantly ionic and is expected to be that of Li^+ ions.

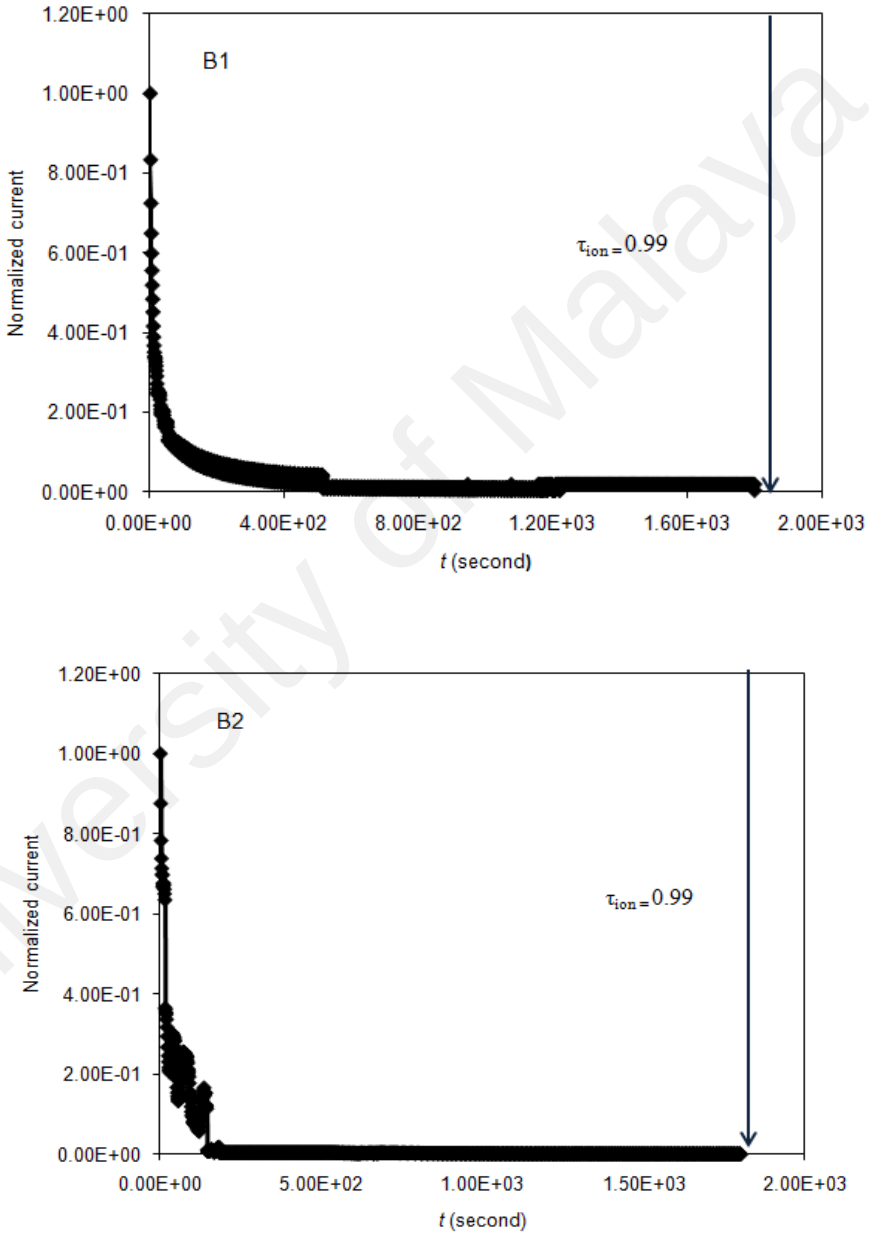

Figure 4.18: Typical plot of normalized polarisation current versus time for $LiSn_2P_3O_{12}$ samples (System II)

4.7 Electrochemical stability of $LiSn_2P_3O_{12}$ system

The electrochemical stability window of the samples was determined by LSV. The current-voltage responses obtained for System II samples, B1 and B2 are displayed in Figure 4.17. The voltage stability window of sample B1 at room temperature is up to 4.8 V. Meanwhile, for sample B2, the sample is stable up to 4.6 V at room temperature. This shows that the highest conducting sample, sample B1 have wider electrochemical stability window compared to sample B2. Thus, the result shows that $LiSn_2P_3O_{12}$ samples are electrochemically stable for applications as solid electrolytes in electrochemical devices such as lithium batteries.

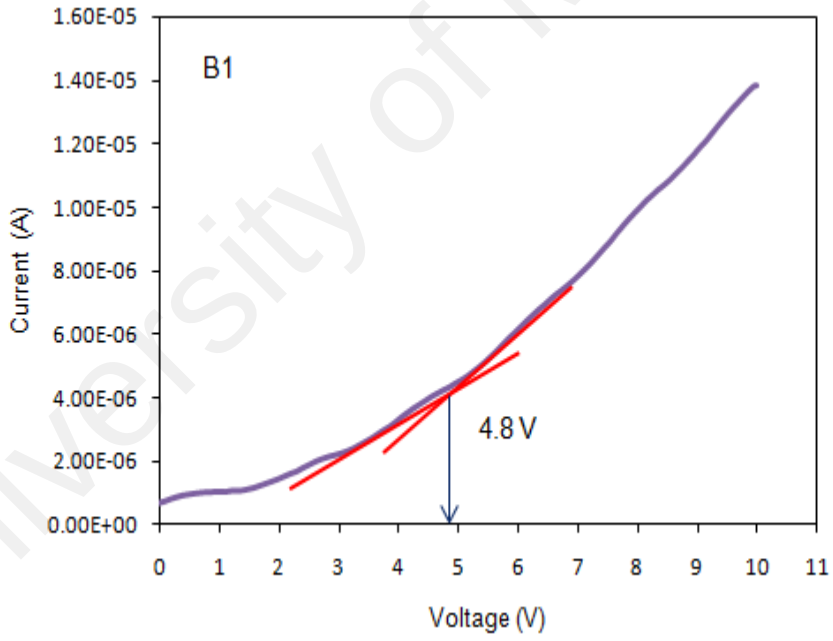

Figure 4.19, continued ….

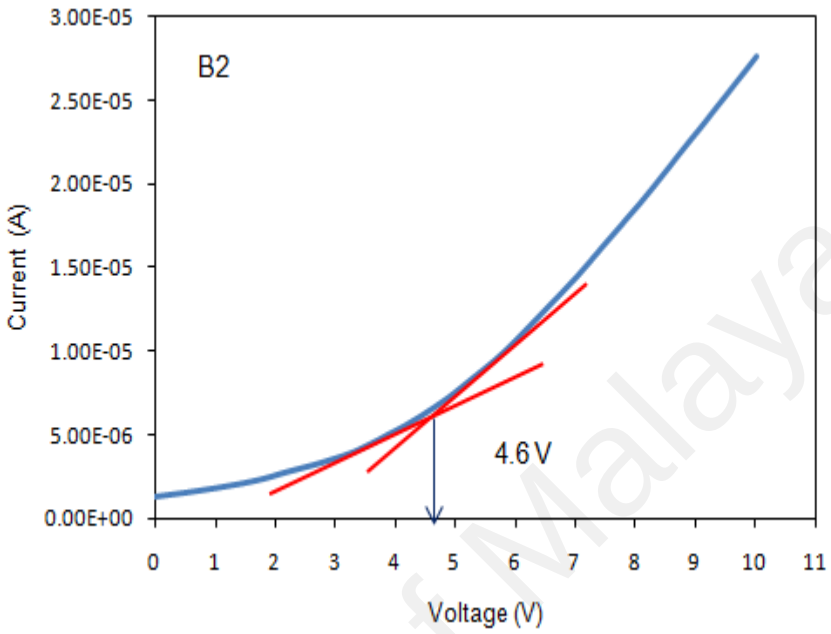

Figure 4.19: Linear sweep voltammogram of $LiSn_2P_3O_{12}$ samples (System II)

CHAPTER 5: TRIVALENT SUBTITUTION OF Cr^{3+} and Al^{3+} AT Sn^{4+} SITE: $Li_{1+x}Cr_xSn_{2-x}P_3O_{12}$ AND $Li_{1+x}Al_xSn_{2-x}P_3O_{12}$ SYSTEMS

5.1 Introduction

Generally, enhancement of ionic conductivity may be achieved by partial substitution at Sn^{4+} site with trivalent ions such as Al^{3+}, Cr^{3+} or Fe^{3+} into $LiSn_2P_3O_{12}$ parent compound as stated in Chapter 2. It was systematically shown for the first time by (Aono et al., 1990a), (Aono et al., 1990b) by using Al^{3+} in the system of $Li_{1.3}Al_{0.3}Ti_{1.7}(PO_4)_3$. In the present study, an effort to enhance the ionic conductivity of $LiSn_2P_3O_{12}$ parent compound was made by partially substituting Sn^{4+} (r_{ion} = 0.69 Å) site using smaller trivalent ion, Cr^{3+} (r_{ion}= 0.615 Å) with the goal of creating Li^+ interstitial ions where $Sn^{4+} \rightarrow Li^+ + Cr^{3+}$ as the third system. This substitution yielded compounds with the general formula of $Li_{1+x}Cr_xSn_{2-x}P_3O_{12}$ with x = 0.1, 0.3, 0.5, 0.7 and 0.9 . For the forth system, smaller trivalent ion, Al^{3+} (r_{ion} = 0.535 Å) was substituted at Sn^{4+} site with the same goal of creating Li^+ interstitial ions where $Sn^{4+} \rightarrow Li^+ + Al^{3+}$ producing compounds with general formula of $Li_{1+x}Al_xSn_{2-x}P_3O_{12}$ with x = 0.1, 0.3, 0.5, 0.7 and 0.9 . For both systems, the effects of Cr and Al substitution on the properties of $LiSn_2P_3O_{12}$ were then investigated using XRD, FTIR, SEM, laser particle sizer, impedance spectroscopy, LSV and transference number measurement.

5.2 Classification of the samples

As mentioned in section 5.1, this chapter consists of two systems, $Li_{1+x}Cr_xSn_{2-x}P_3O_{12}$ and $Li_{1+x}Al_xSn_{2-x}P_3O_{12}$ with x = 0.1, 0.3, 0.5, 0.7 and 0.9. Table 5.1 below summarizes the designation of the studied samples based on the value of x for both systems.

Table 5.1: The classification of the samples in $Li_{1+x}Cr_xSn_{2-x}P_3O_{12}$ and $Li_{1+x}Al_xSn_{2-x}P_3O_{12}$ systems

System	*x*	Sample
III $Li_{1+x}Cr_xSn_{2-x}P_3O_{12}$	0.1	CR1
	0.3	CR3
	0.5	CR5
	0.7	CR7
	0.9	CR9
IV $Li_{1+x}Al_xSn_{2-x}P_3O_{12}$	0.1	AL1
	0.3	AL3
	0.5	AL5
	0.7	AL7
	0.9	AL9

5.3 $Li_{1+x}Cr_xSn_{2-x}P_3O_{12}$ System

5.3.1 XRD analysis

In order to study the structural properties, XRD was done on the $Li_{1+x}Cr_xSn_{2-x}P_3O_{12}$ (x = 0.1, 0.3, 0.5, 0.7, 0.9) samples. XRD spectra of the samples are shown in Figure 5.1. The spectra clearly indicate the presence of rhombohedral ($R\bar{3}c$) $LiSn_2P_3O_{12}$ crystalline phase in all of the samples. All peaks are sharp and well defined; suggesting that the compounds are generally well crystallized. SnO_2 impurity is also observed in all samples indicating the presence of unreacted cassiterite SnO_2 (Cui et al., 2012).

In order to confirm that Cr^{3+} ion is in the $LiSn_2P_3O_{12}$structure, the peaks in 2θ range 24°- 25° were carefully analyzed for sample CR1, CR3 and CR5. Figure 5.2 shows the magnified XRD patterns in this 2θ range. As seen in this figure, the peak shifts to higher diffraction angle when Cr^{3+} ion is substituted into the parent structure indicating that Cr^{3+} ion is in the $LiSn_2P_3O_{12}$ structure rather than forming impurities. This suggests that there are more ions accommodated in the lattice structure. However, the SnO_2 impurity peaks observed in this system are quite high especially in sample CR7 and CR9. Therefore, further characterizations were not done on this system.

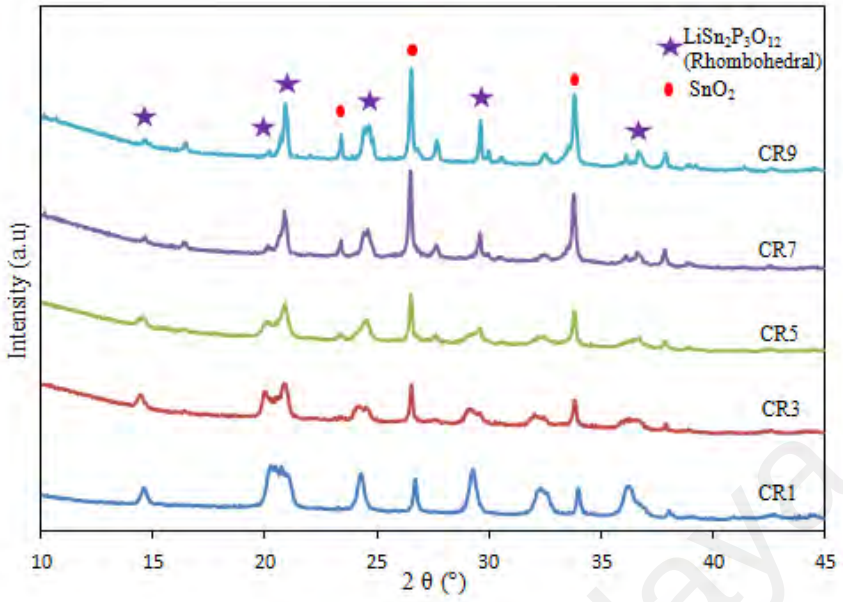

Figure 5.1: X-ray diffraction patterns of $Li_{1+x}Cr_xSn_{2-x}P_3O_{12}$ system

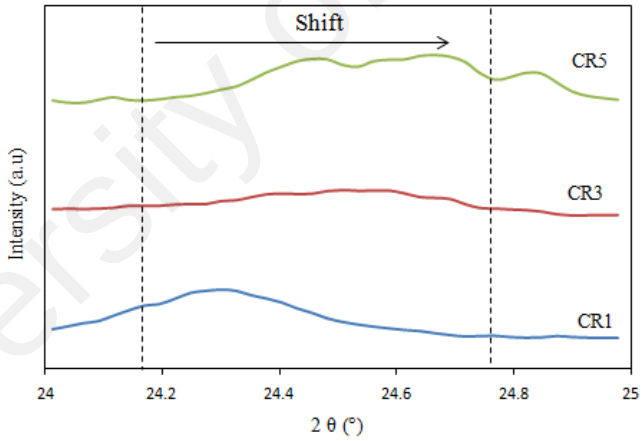

Figure 5.2: X-ray diffraction patterns of $Li_{1+x}Cr_xSn_{2-x}P_3O_{12}$ system in 2θ range from 24° to 25°

5.4 $Li_{1+x}Al_xSn_{2-x}P_3O_{12}$ System

5.4.1 XRD analysis

Figure 5.3 displayed the XRD spectra of the studied $Li_{1+x}Al_xSn_{2-x}P_3O_{12}$ system. The XRD spectra clearly points to the existence of rhombohedral ($R\bar{3}c$) $LiSn_2P_3O_{12}$ crystalline phase with the existence of unreacted cassiterite SnO_2 (Cui et al., 2012) . Nevertheless, no peak was attributed to aluminium, and the related compound was detected.

In order to confirm that Al^{3+} ion is in the $LiSn_2P_3O_{12}$structure, the peaks in 2θ range 23.5°- 25.0° were carefully analyzed for the sample AL1, AL3 and AL5 as the samples are well crystallized and contained no unknown peaks as samples A7 and A9. The magnified XRD patterns in this 2θ range are shown in Figure 5.4. When Al^{3+} was substituted into the parent structure, the peak shifts to higher diffraction angle suggesting that Al^{3+} ion is in the $LiSn_2P_3O_{12}$ structure rather than forming impurities. This indicates that there are more ions accommodated in the lattice structure. However, based on the analysis, the maximum value of *x* is only up to 0.5. When *x* exceeded 0.5, unknown peaks suddenly appeared. As such no further characterization was carried out on samples AL7 and AL9. Furthermore, all peaks are sharp and well defined for *x* up to 0.5 showing that the compound was generally well crystallized. This high crystallinity is thought to favour an improved connection between the channels in the NASICON structure through which ionic conduction occurs contributing to improving the material's ionic conductivity (Kubanska et al., 2014).

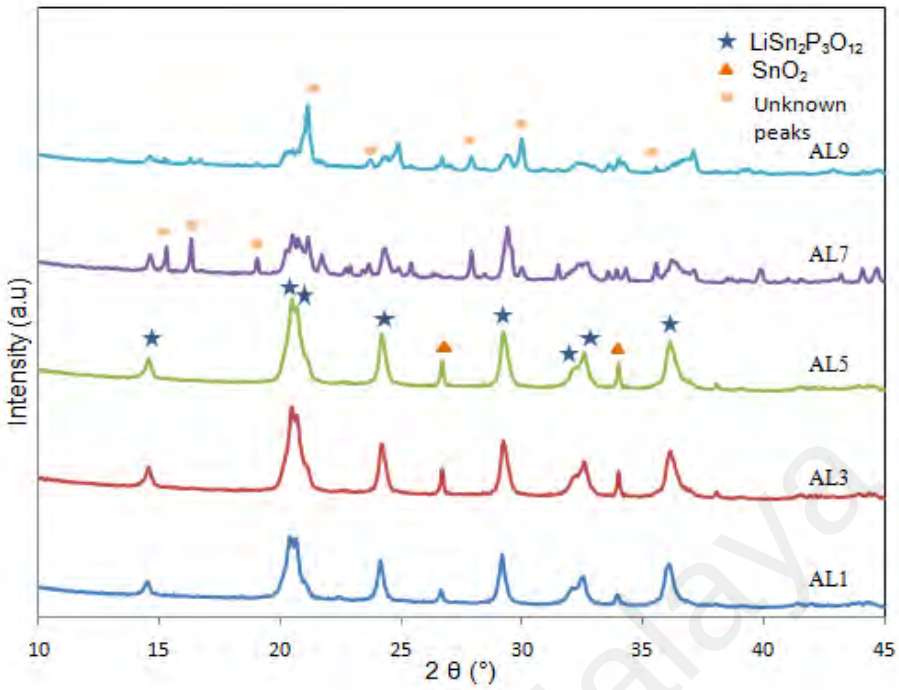

Figure 5.3: X-ray diffractograms of $Li_{1+x}Al_xSn_{2-x}P_3O_{12}$ system

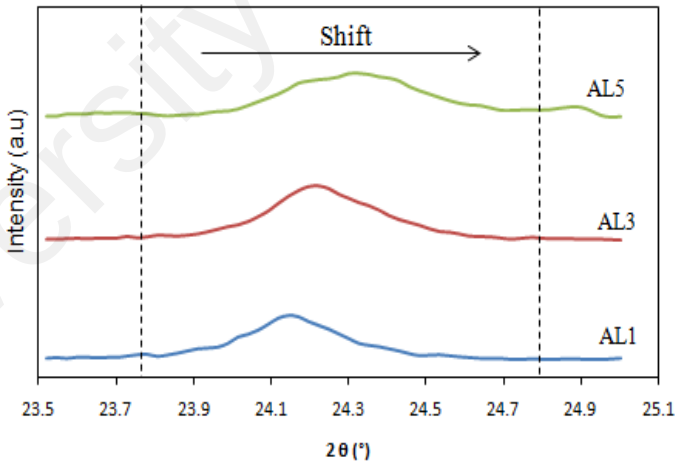

Figure 5.4: X-ray diffractograms of $Li_{1+x}Al_xSn_{2-x}P_3O_{12}$ system in 2θ range from 23.5 to 25.0°

The variations of the lattice parameters and crystallite size for the $Li_{1+x}Al_xSn_{2-x}P_3O_{12}$ system were then evaluated and the outcomes are itemised in Table 5.2. The table shows that the values of *a*, *c* and *V* in Al substituted samples decrease as the value of *x* increases. Nevertheless, the decrease in the unit cell volume compared to the unsubstituted parent compound is mostly related to the substitutions of smaller ionic radius of Al^{3+} ion (r_{ion} = 0.53 Å) compared to the Sn^{4+} ion (r_{ion} = 0.69 Å). However, the crystallite size of the system is found to increase as the value of *x* increases and was also found to be smaller than the parent compound that was 137.4 Å. Furthermore, the density of the prepared pellet was established from the physical dimensions and the weight of the pellet compared to the theoretical density of 3.79 g cm^{-3}. The density of the compound is 3.49 g cm^{-3} that is 92 % of the theoretical density.

Table 5.2: Lattice parameters and unit cell volume of $Li_{1+x}Al_xSn_{2-x}P_3O_{12}$ system

Sample	*a* [Å]	*c* [Å]	*V* [$Å^3$]	Crystallite size [Å]
AL1	8.5175	21.3200	1340.22	95.55
AL3	8.5061	21.2203	1329.63	95.93
AL5	8.4958	21.0054	1313.00	115.63

5.4.2 FTIR analysis

FTIR has been employed to identify the functional group in $Li_{1+x}Al_xSn_{2-x}P_3O_{12}$ system. Figure 5.5 shows the FTIR spectra of various functional groups in $Li_{1+x}Al_xSn_{2-x}P_3O_{12}$ system, respectively in the spectral region of 550 to 1400 cm^{-1}. All the samples investigated in this study show similar spectra and it is obviously dominated by the vibrations of PO_4 tetrahedral that range from 800 to 1300 cm^{-1} where the bands in the region of 1000 to 1300 cm^{-1} are attributed to the asymmetric stretching vibrations while bands in the region of 900 to 980 cm^{-1} are ascribed to the symmetric stretching vibrations of the PO_4^{3-} ions (Yadav & Bhatnagar, 2013; Yang et al., 2015). The bands in the region of 560 to 670 cm^{-1} are mainly due to the asymmetric bending vibration modes of O-P-O units (Vijayan & Govindaraj, 2011). The P-O-P stretching bands are observed in the region of 700 to 800 cm^{-1}(Schroeder et al., 2011).

For all samples, AL1, AL3 and AL5 comparing all the dominant absorption bands of O-P-O and PO_4^{3-}, as x increases, the two absorption bands are shifted to the lower wave number direction. The shifting is attributable to the presence of Al^{3+} ions in the compounds. The Al^{3+} ions may have modified the interaction forces between the O–P–O, O–Sn–O and O–Al–O bonds leading to considerable displacement of the transmission bands (Yadav & Bhatnagar, 2013).

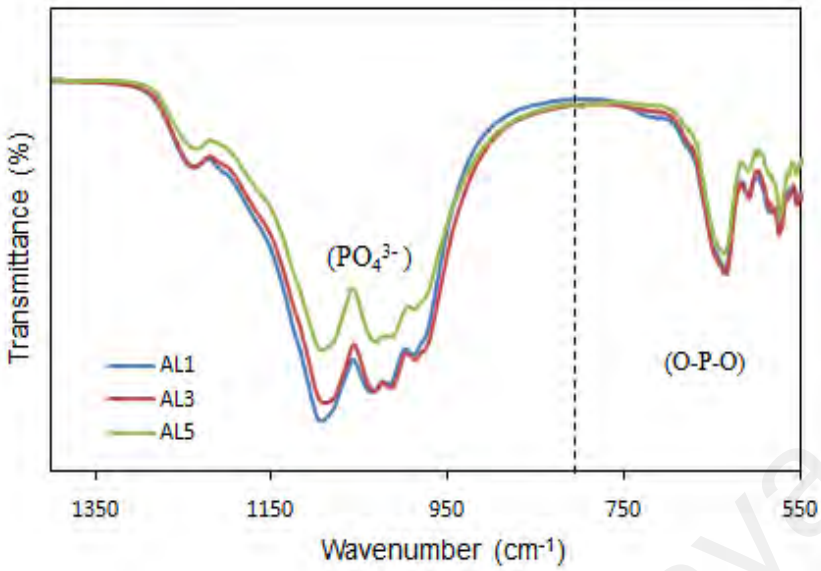

Figure 5.5: FTIR spectra of various functional groups in $Li_{1+x}Al_xSn_{2-x}P_3O_{12}$ system

5.4.3 SEM, EDX and particle size distribution analyses

The SEM micrographs of $Li_{1+x}Al_xSn_{2-x}P_3O_{12}$ samples are presented in Figure 5.6. It is observed that the particles in the compound appear to be agglomerated. Nevertheless, the particle"s sizes for $Li_{1+x}Al_xSn_{2-x}P_3O_{12}$ samples are slightly smaller than that of the unsubstituted parent compound. The particle size also increases as *x* increases. This is verified by the analysis of the particle size distribution as shown in Figure 5.7. The average particle size for AL5 compound is 19.70 µm compared to that of $LiSn_2P_3O_{12}$, which is 22.8 µm. This may have been due to the substitutions of smaller ionic radius of Al^{3+} ion (r_{ion} = 0.53 Å) compared to the Sn^{4+} ion (r_{ion} = 0.69 Å), which decreased the particle"s size in the Al subtituted compounds.

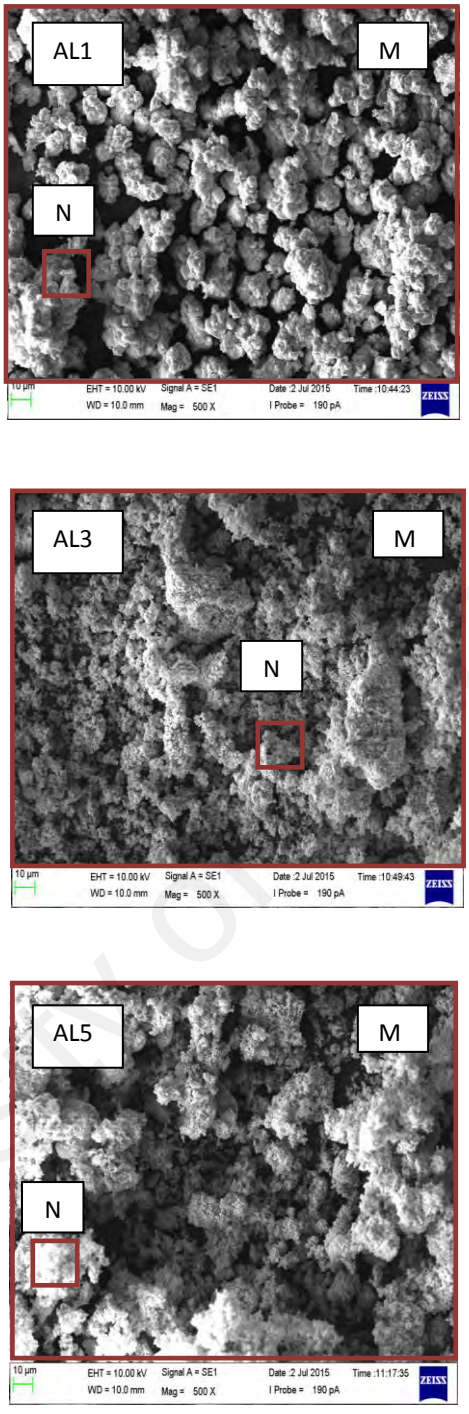

Figure 5.6: SEM micrographs of $Li_{1+x}Al_xSn_{2-x}P_3O_{12}$ system

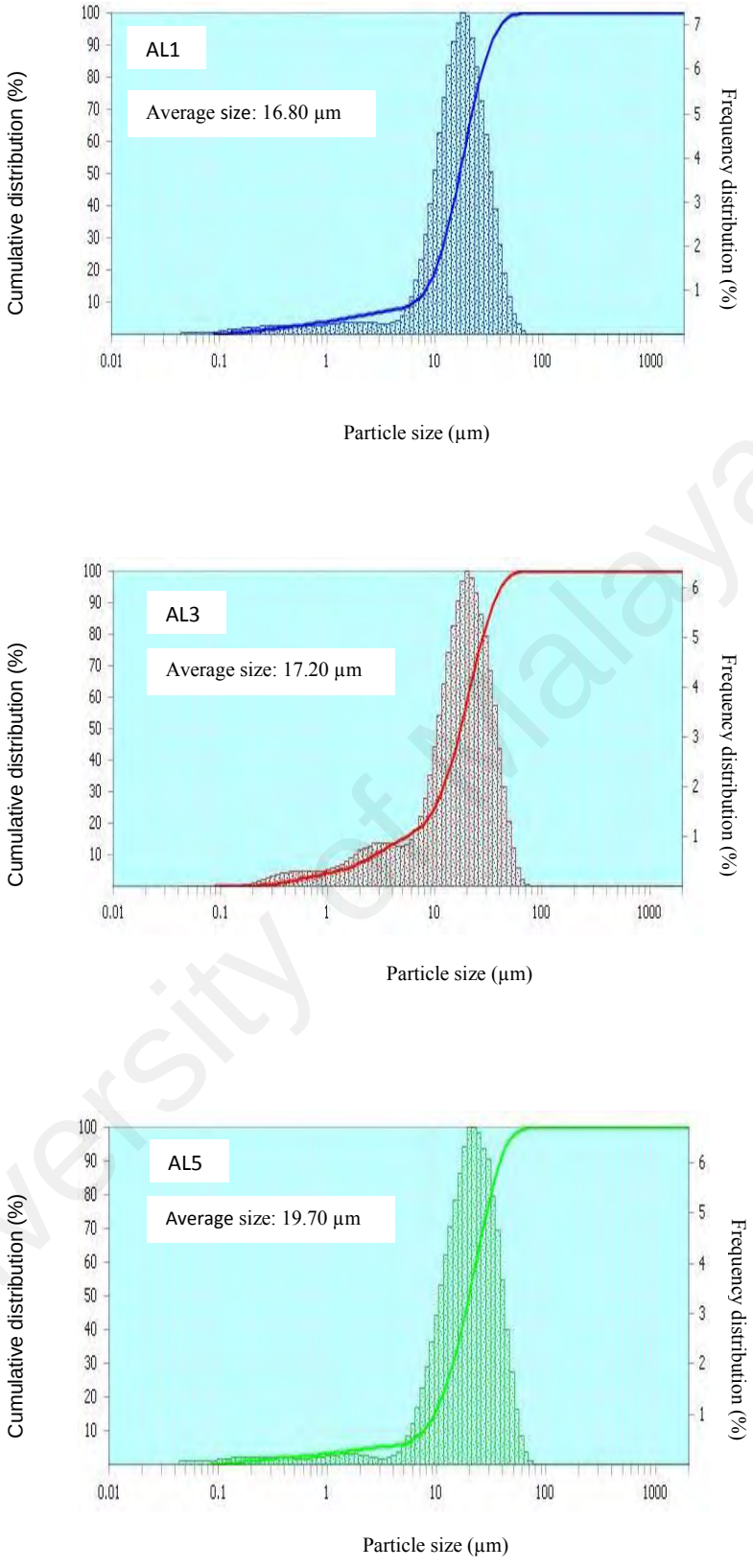

Figure 5.7: Particle size distribution of $Li_{1+x}Al_xSn_{2-x}P_3O_{12}$ system

Meanwhile, the elemental examination of the compounds was carried out by EDX examination and the results are tabulated in Table 5.3. The analysis was carried out on a larger region (marked as M) and also on smaller region (marked as N) in order to investigate the homogeneity of the elements at both regions. In both regions, M and N, the atomic ratios of the compounds are very near to the anticipated composition; thus verifying that the Al^{3+} was successfully inserted into the $LiSn_2P_3O_{12}$ structure leading to the formation of $Li_{1+x}Al_xSn_{2-x}P_3O_{12}$ **c**ompound. Nevertheless, the EDX of the sample could not show the existence of lithium due to its light atomic weight. Therefore, the concept of charge neutrality was applied for this case (Narváez-Semanate & Rodrigues, 2010; Norhaniza et al., 2011; Wu et al., 2009) .

Table 5.3: The EDX stoichiometric atomic ratio of $Li_{1+x}Al_xSn_{2-x}P_3O_{12}$ system

Sample	Composition		Stoichiometric atomic ratio			
			Sn	Al	P	O
AL1	Starting mixture		1.90	0.10	3.00	12.00
	EDX analysis	M	1.88	0.98	2.99	12.00
		N	1.88	0.99	2.99	12.00
AL3	Starting mixture		1.70	0.30	3.00	12.00
	EDX analysis	M	1.72	0.29	3.01	12.00
		N	1.70	0.29	3.00	12.00
AL5	Starting mixture		1.50	0.50	3.00	12.00
	EDX analysis	M	1.49	0.51	3.00	12.00
		N	1.50	0.50	3.00	12.00

5.4.4 Electrical properties of $Li_{1+x}Al_xSn_{2-x}P_3O_{12}$ system

5.4.4.1 DC conductivity of $Li_{1+x}Al_xSn_{2-x}P_3O_{12}$ system

The complex impedance plot of sample AL1, AL3 and AL5 at room temperature is shown in Figure 5.8. The impedance plots for all samples consist of two depressed semicircles in high and middle frequency area with an electrode spike at low frequency area. The high frequency semicircle corresponds to bulk response with its intercept at the *x*-axis allocated to bulk resistance, R_b, while the middle frequency semicircle is corresponds to grain boundary response and its intercept at the *x*-axis corresponds to grain boundary resistance, R_{gb}. In the Al^{3+} substituted system, as *x* increases from 0.1 to 0.5 at room temperature, both R_b and R_{gb} shifted to lower value indicating an increase in conductivity.

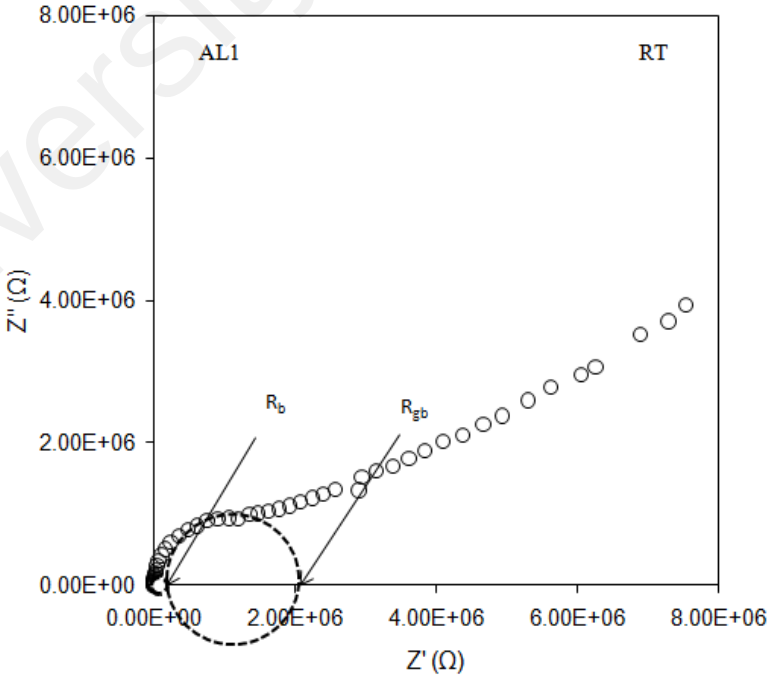

Figure 5.8, continued....

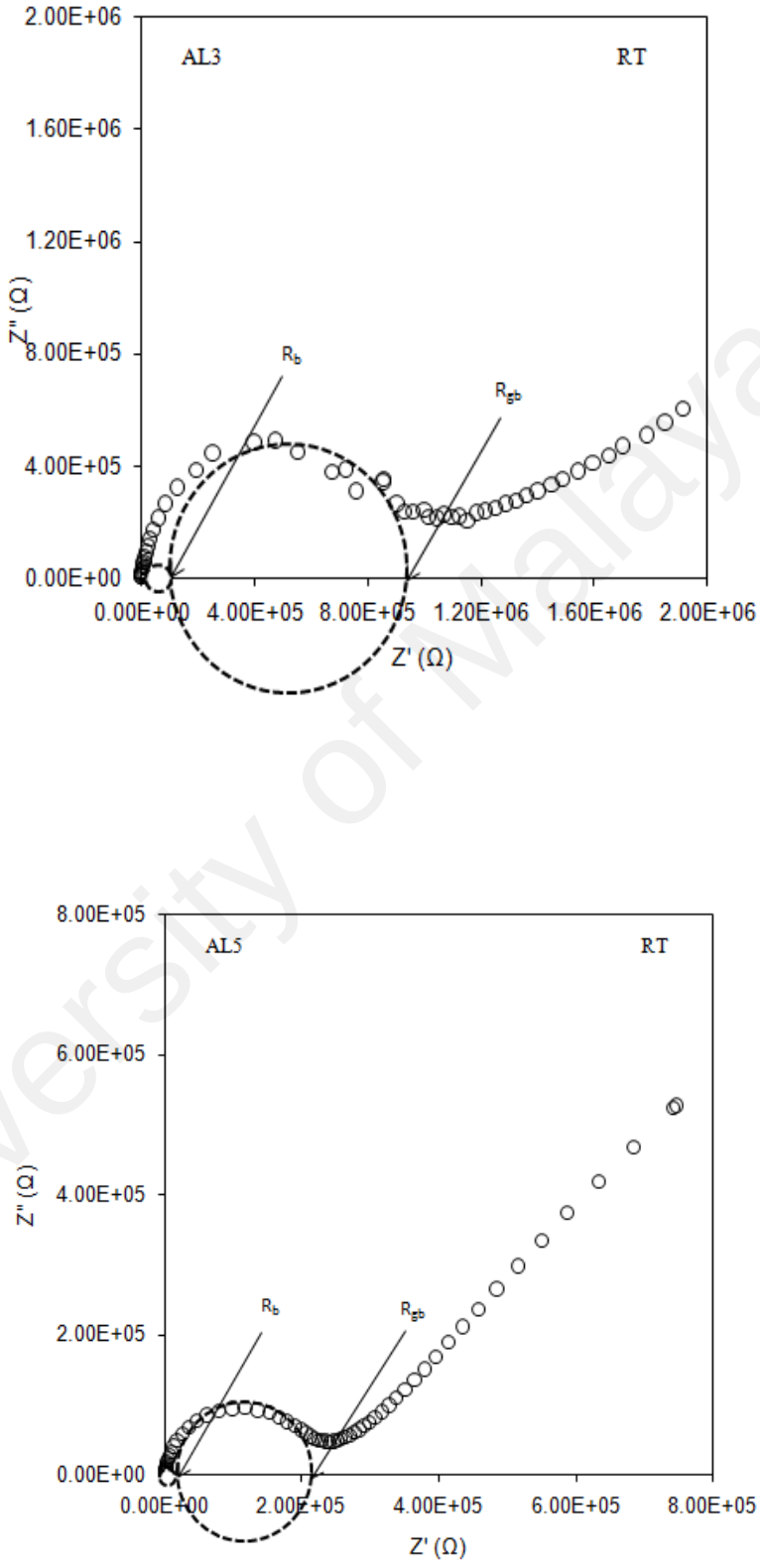

Figure 5.8: Complex impedance plots of $Li_{1+x}Al_xSn_{2-x}P_3O_{12}$ samples at room temperature

Experimental complex impedance data might well be approximated by the impedance of an equivalent circuit made up of bulk and grain boundary resistance, R_b and R_{gb} and bulk and grain boundary capacitance, C_b (CPE), C_{gb} (CPE) and $CPE_{blocking\ electrode}$ with constant phase element (CPE) behaviour as in Figure 5.9 (Kubanska et al., 2014).

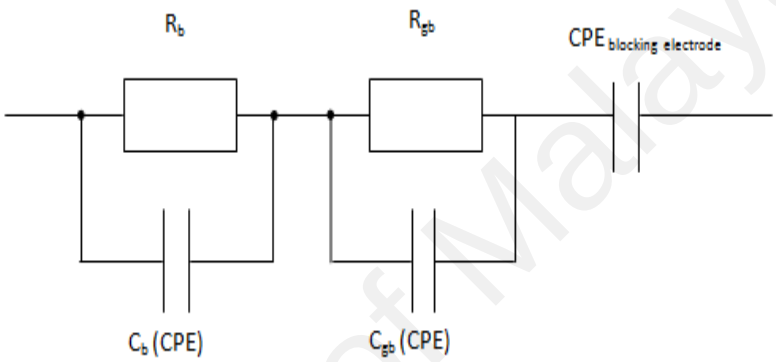

Figure 5.9: Equivalent circuit of $Li_{1+x}Al_xSn_{2-x}P_3O_{12}$ samples based on the impedance analysis at room temperature

However, at temperatures of 300 to 500 °C, only one semicircle is detected corresponding to bulk resistance, R_b together with a tilted spike at low frequency area as shown in Figure 5.10 and Figure 5.11 for sample AL1,AL3 and AL5. Experimental complex impedance data might now be approximated by a circuit only containing bulk resistance, R_b and bulk capacitance, C_b (CPE) and $CPE_{blocking\ electrode}$ with constant phase element (CPE) behaviour as shown in Figure 5.12.

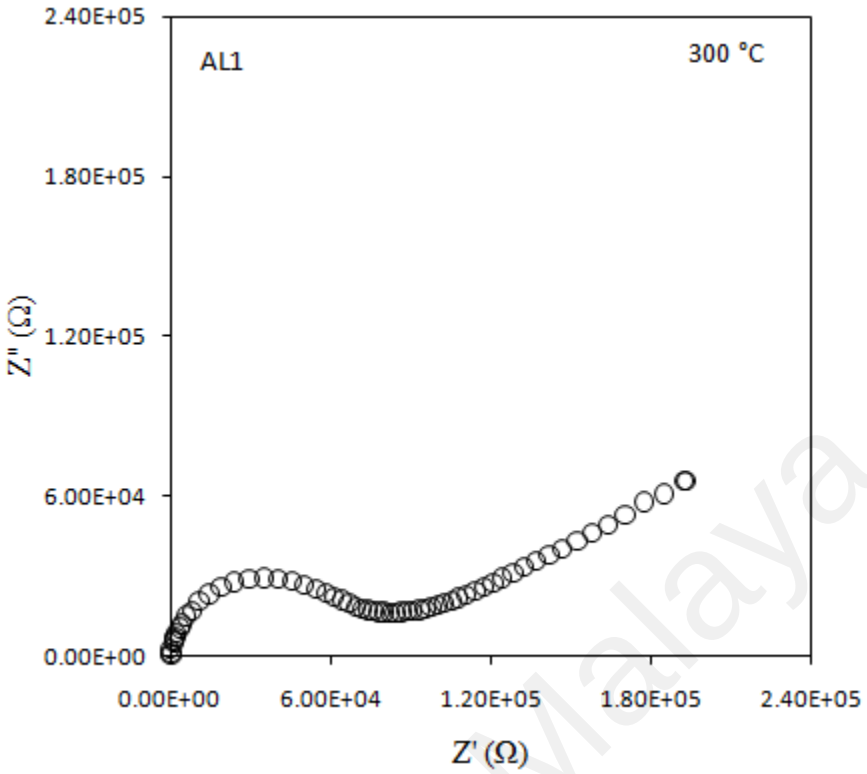

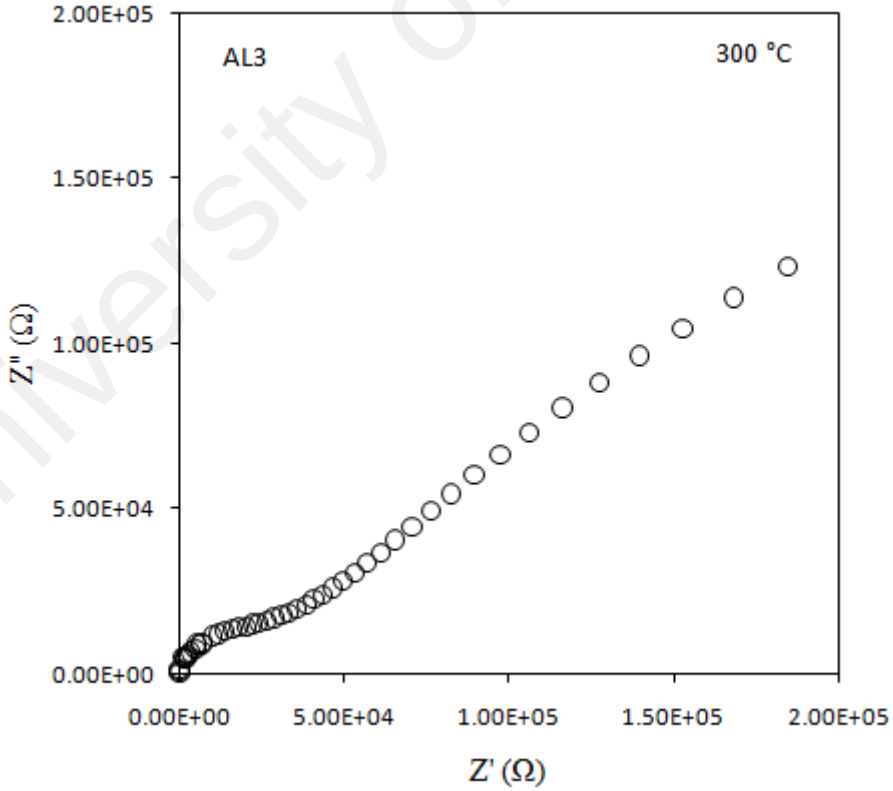

Figure 5.10, continued....

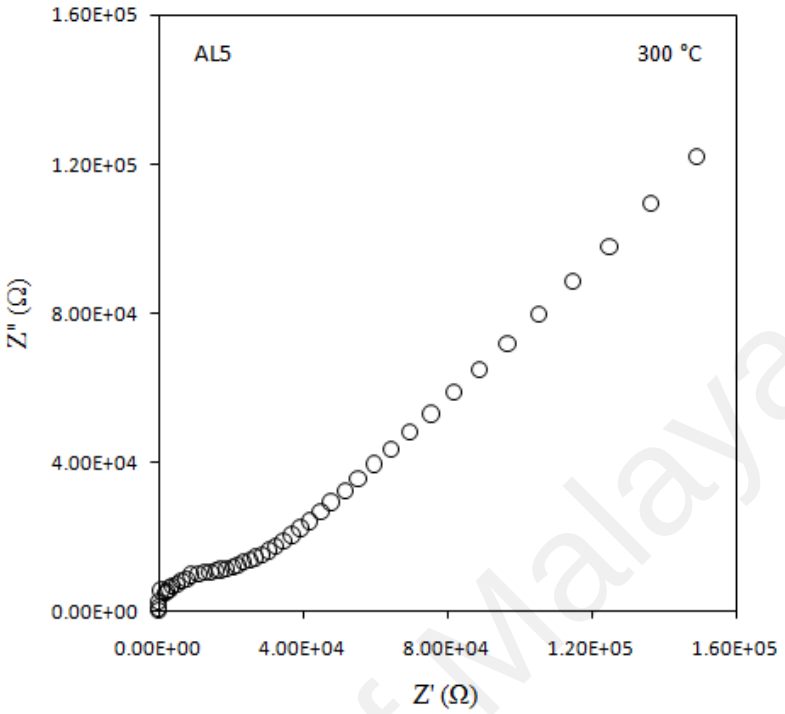

Figure 5.10: Complex impedance plots of $Li_{1+x}Al_xSn_{2-x}P_3O_{12}$ samples at 300 °C

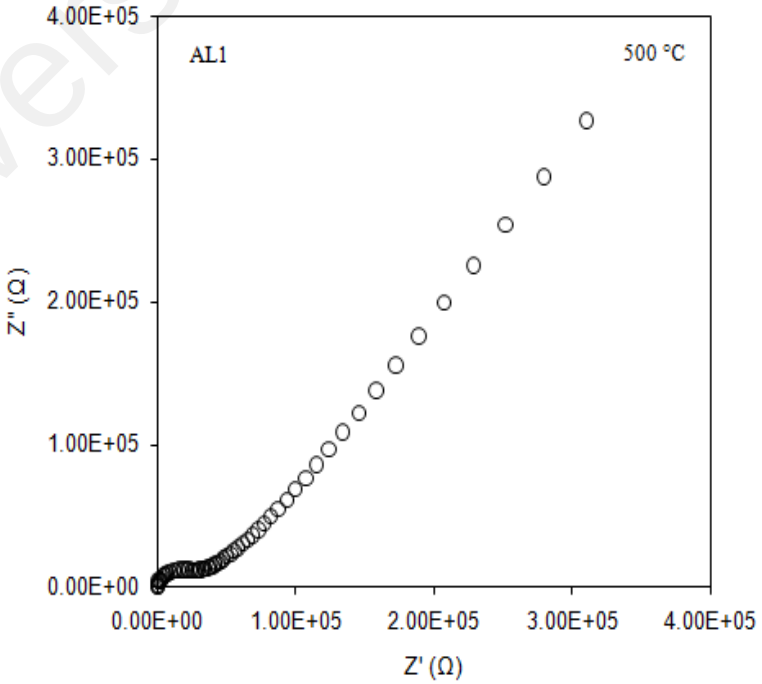

Figure 5.11, continued....

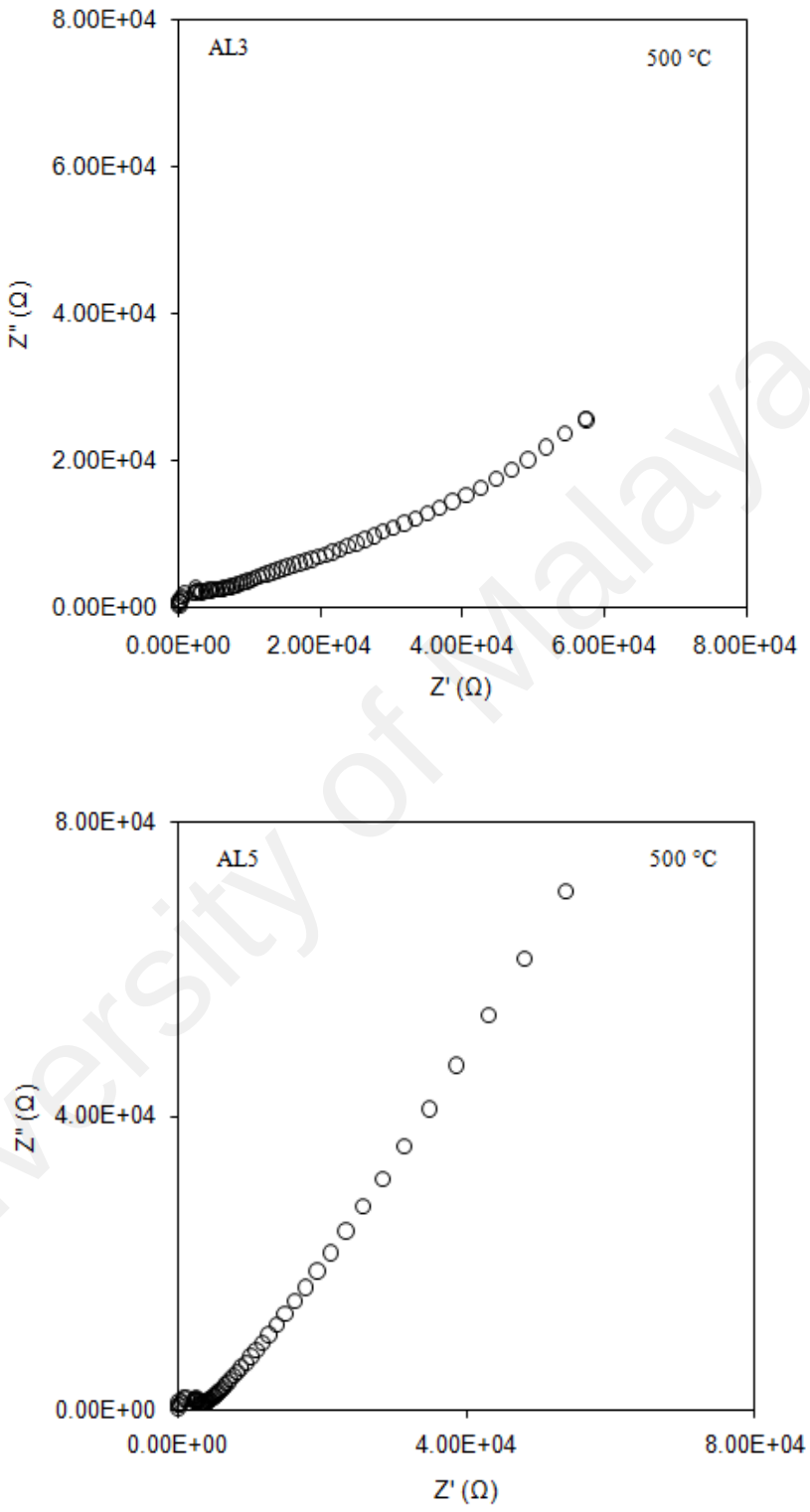

Figure 5.11: Complex impedance plots of $Li_{1+x}Al_xSn_{2-x}P_3O_{12}$ samples at 500 °C

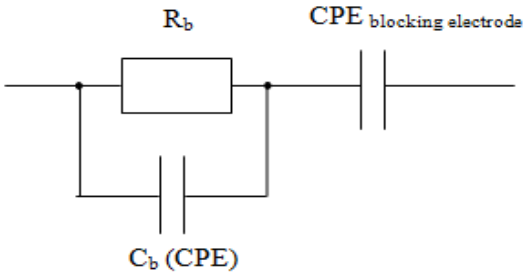

Figure 5.12: Equivalent circuit of $Li_{1+x}Al_xSn_{2-x}P_3O_{12}$ samples based on the impedance analysis at 500°C

Bulk and grain boundary conductivities, ζ_b and ζ_{gb} are then evaluated using R_b and R_{gb} values obtained from the impedance plots. The values of bulk, grain boundary and total conductivities for $Li_{1+x}Al_xSn_{2-x}P_3O_{12}$ samples are listed in Table 5.4. The bulk, grain boundary and total conductivities of $Li_{1+x}Al_xSn_{2-x}P_3O_{12}$ system increase as the value of x increases. Sample with $x = 0.5$ that is sample AL5 showed the highest total conductivity value of 1.02×10^{-6} S cm^{-1} at room temperature which is one order of magnitude greater compared to that of the $LiSn_2P_3O_{12}$ parent compound. This is attributable to the rise of one order of magnitude of the grain boundary conductivity in the Al^{3+} substituted samples. When the temperature rises to 500 °C, the ionic conductivity also rises to 8.18×10^{-5} S cm^{-1}.

Therefore it can be inferred that the rise of the total ionic conductivity in the samples with excess Li chiefly is contributed by grain boundary conductivity, not from bulk conductivity. This might be due to the ionic conductivity across grain boundaries correlates with the increased density of the pellets that takes place upon Al^{3+} substitution (Pérez-Estébanez et al., 2013) and a rise in the amount of interstitial Li^+ ions. The increase of the grain boundary conductivity may originate from segregation of

Li to the grain boundary to form Li-rich structures which may reduce the activation energy and increase the concentration of charge carriers, thereby increasing grain boundary conductivity (Chung & Kang, 2014).

Besides that, conductivity enhancement also come from the maximum Li^+–Li^+ interaction observed at M1 sites may be due to formation of newer channels at higher temperatures in the bottlenecks (Kothari & Kanchan, 2016). Furthermore, as temperature increases, the Li^+ ions populate intermediate sites like $M_{1/2}$, M3, M3" (Arbi et al., 2013) and at the intersection points within the bottleneck instead of the network M1 sites (Arbi et al., 2015). As such, creation of vacancies at M1 sites increases Li^+ mobility thus increases the conductivity of the sample (Arbi et al., 2007).

Table 5.4: Ionic conductivity values for $Li_{1+x}Al_xSn_{2-x}P_3O_{12}$ system at 30 °C

Sample	$\zeta_{b,30}$ (S cm^{-1})	$\zeta_{gb,30}$ (S cm^{-1})	$\zeta_{t,30}$ (S cm^{-1})
AL1	$(2.75 \pm 0.07) \times 10^{-6}$	$(1.13 \pm 0.05) \times 10^{-7}$	$(1.08 \pm 0.06) \times 10^{-7}$
AL3	$(4.27 \pm 0.06) \times 10^{-6}$	$(2.62 \pm 0.05) \times 10^{-7}$	$(2.47 \pm 0.05) \times 10^{-7}$
AL5	$(8.71 \pm 0.03) \times 10^{-6}$	$(1.16 \pm 0.03) \times 10^{-6}$	$(1.02 \pm 0.02) \times 10^{-6}$

Table 5.5: Ionic conductivity values for $Li_{1+x}Al_xSn_{2-x}P_3O_{12}$ system at 500 °C

Sample	$\zeta_{b,500}$ (S cm^{-1})	$\zeta_{t,500}$ (S cm^{-1})
AL1	$(7.18 \pm 0.05) \times 10^{-6}$	$(7.18 \pm 0.05) \times 10^{-6}$
AL3	$(6.55 \pm 0.04) \times 10^{-5}$	$(6.55 \pm 0.04) \times 10^{-5}$
AL5	$(8.18 \pm 0.04) \times 10^{-5}$	$(8.18 \pm 0.04) \times 10^{-5}$

Presented in Figure 5.13 is the variation of bulk conductivity with 1000/T of $Li_{1+x}Al_xSn_{2-x}P_3O_{12}$ samples. The activation energy, E_a for the Li^+ migration was established from the Arrhenius as in Equation 4.2. From the graph, it can be observed that the conductivity increases linearly with temperature implying that conduction is a thermally activated process. The regression value, R for all samples are found to be 0.9. Similar to the parent compound, two areas can be seen in the plots for sample AL1, AL3 and AL5. The first area is the low temperature region while area II is the high temperature region. As the value of x increases from 0.1 to 0.5, the bulk and grain boundary activation energy value decreases as listed in Table 5.4 and Table 5.5.

Sample AL5 which is the highest conducting sample possesses the lowest bulk activation energy at low and high temperature, 0.004 eV and 0.138eV respectively. This can be correlated with the conductivity value. Additionally, the activation energy value stated here is much lower than those reported by other groups of researchers (Cui et al., 2012; Norhaniza et al., 2010) . This low value of activation energy is typical of a fast ion conductor, and a result from the regularity of the diffusion channels in the NASICON structure. This fact favours lithium mobility in the $Li_{1+x}Al_xSn_{2-x}P_3O_{12}$ samples (Jonscher, 1983).

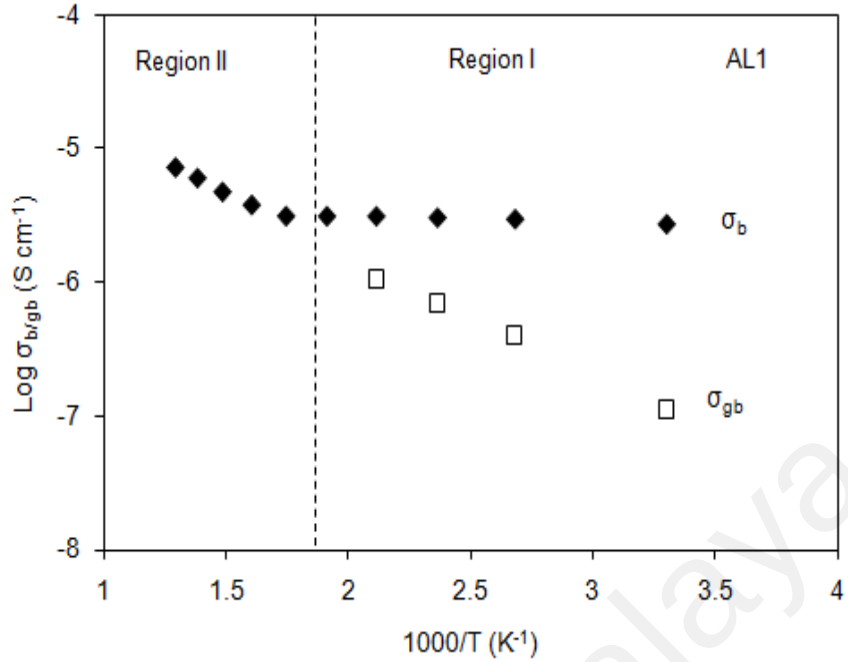

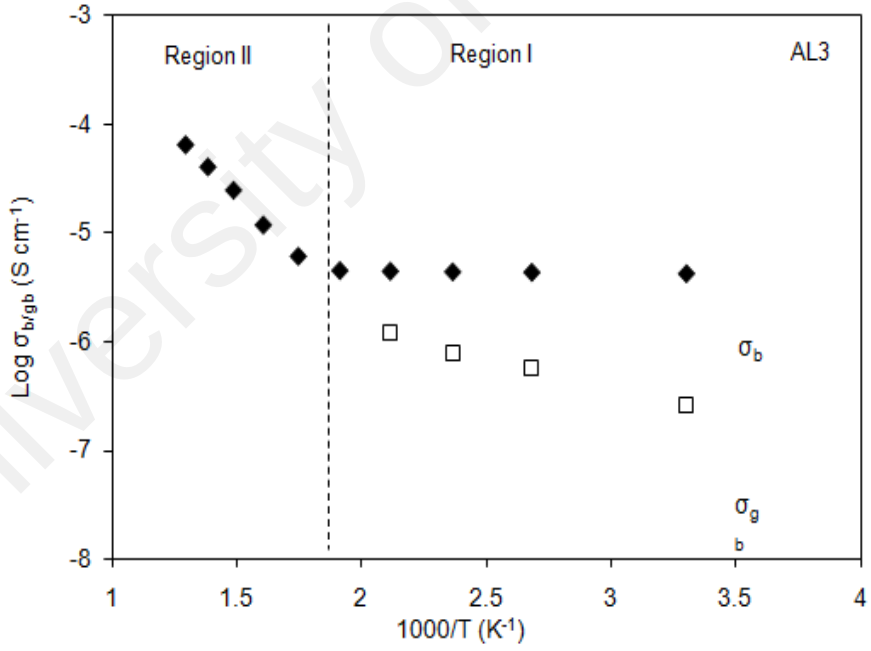

Figure 5.13, continued....

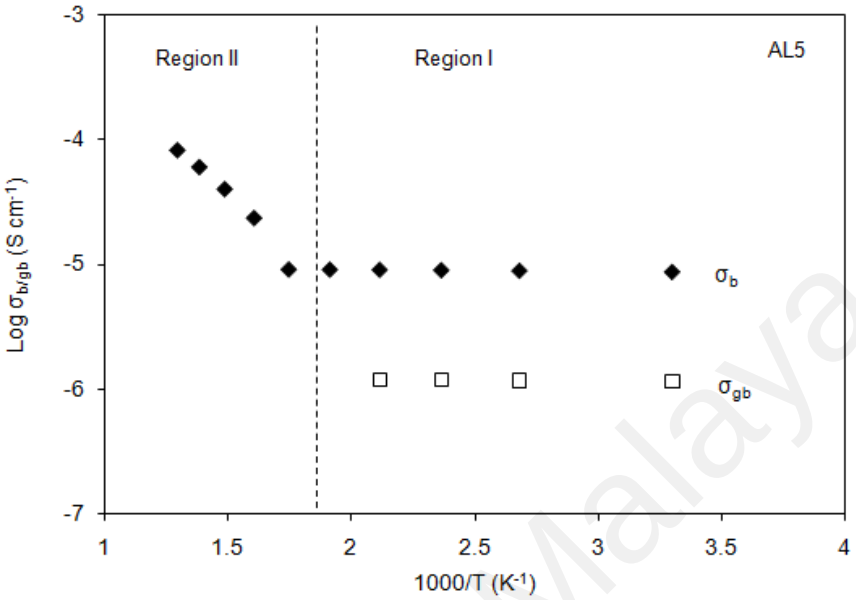

Figure 5.13: Log σ versus 1000/*T* plots of bulk and grain boundary conductivities of $Li_{1+x}Al_xSn_{2-x}P_3O_{12}$ samples

Table 5.6: Bulk and grain boundary activation energies for $Li_{1+x}Al_xSn_{2-x}P_3O_{12}$ system

Sample	$E_{a,b}$ (eV)		$E_{a,\ gb}$ (eV)	
	Region I (Low T)	Region II (High T)	Region I (Low T)	Region II (High T)
AL1	0.008	0.558	0.163	-
AL3	0.005	0.455	0.109	-
AL5	0.003	0.413	0.003	-

5.4.4.2 AC conductivity of $Li_{1+x}Al_xSn_{2-x}P_3O_{12}$ system

Figure 5.14 depicts log ζ_{ac} vs. log ω plots of the highest conducting sample that is sample AL5 at different temperatures. The plot contains a plateau in the middle frequency area and high frequency dispersion. The middle frequency plateau is due to a frequency independence of the conductivity corresponding to the DC conductivity. The transition from the DC plateau to AC conductivity dispersion area shifted towards a greater frequency range when the temperature increases. At high frequencies, the power law feature was detected in the form of Equation 4.3 (Jonscher, 1983):

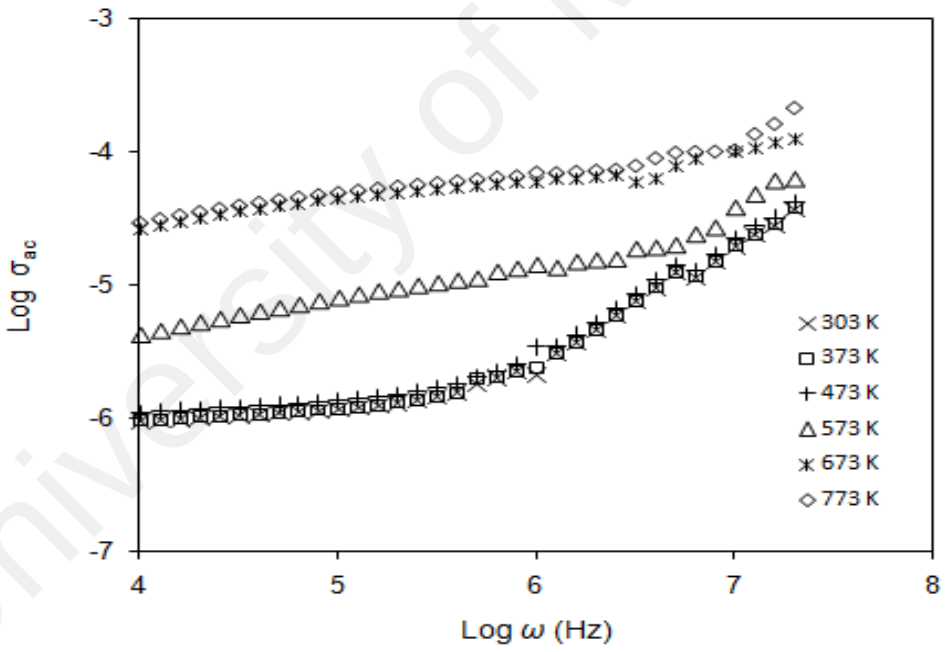

Figure 5.14: AC conductivity spectra of sample AL5 at various temperatures

Table 5.7 presents the values of ω_p, K, n,and μ, at all temperatures for sample AL5. The values of ω_p, K, n, and μ, rise with the increase of temperature. This means that conductivity enhancement in the samples is attributable to the increase in ionic mobility and density of mobile ions (Teo et al., 2012; Vijayakumar et al., 2003) . This is consistent with the results from impedance analysis which reveals that sample AL5 displays the highest ionic conductivity value. Sample AL5 also possesses the highest μ of 2.42×10^{-10} cm^2 V^{-1} s^{-1} and the highest n of 1.62×10^{24} cm^{-3}.

Table 5.7: Parameters of ω_p, K, n and μ for sample AL5 at various temperatures

T (K)	ω_p (Hz)	K (S cm^{-1} K Hz^{-1})	n (cm^{-3})	μ (cm^2 V^{-1} s^{-1})
303	1.12×10^6	3.38×10^{-10}	1.27×10^{23}	6.17×10^{-11}
373	1.58×10^6	3.66×10^{-10}	1.37×10^{23}	7.08×10^{-11}
473	1.77×10^6	4.52×10^{-10}	1.69×10^{23}	6.25×10^{-11}
573	7.94×10^6	9.74×10^{-10}	3.64×10^{23}	2.31×10^{-10}
673	9.55×10^6	4.14×10^{-9}	1.55×10^{24}	2.37×10^{-10}
773	1.12×10^7	4.34×10^{-9}	1.62×10^{24}	2.42×10^{-10}

Furthermore, AC conduction mechanism for sample AL5 was done by determining the temperature dependence of s. Figure 5.15 shows the variation of the exponent s with temperature. The evaluated value of s reduces from 0.99 to 0.22. The reducing value of s with temperature suggests that the CBH is the most suitable model to describe the AC conduction mechanism in the sample. This model assumes that the hopping of carriers between two sites over a barrier separating them and the hopping of carriers are thermally activated (Elliott, 1977).

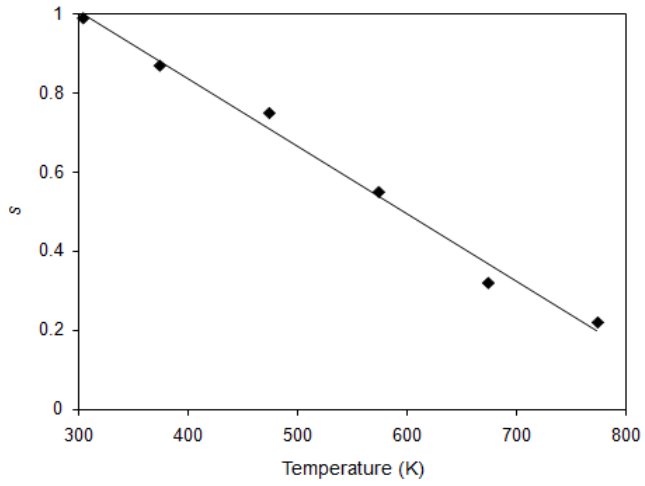

Figure 5.15: Variation of *s* with temperature for sample AL5

5.4.4.3 Transference number measurement analysis

The transference number of the highest conducting sample, sample AL5 for $Li_{1+x}Al_xSn_{2-x}P_3O_{12}$ system was determined using Wagner‟s polarization method. The direct current was recorded as a function of time upon application of a fixed DC voltage across SS/ sample AL5 solid electrolytes/SS. After polarization, the graph of normalized current versus time for the sample is displayed in Figure 5.16. From the figure, it can be seen that the current decreases exponentially with time and finally saturates after about 500 s. The value of ionic transference number is close to unity that is 0.99. This implies that the conductivity of the sample AL5 is mainly due to ions (Yadav & Bhatnagar, 2013) since the value were more than 0.5 and is anticipated to be that of Li^+ ions.

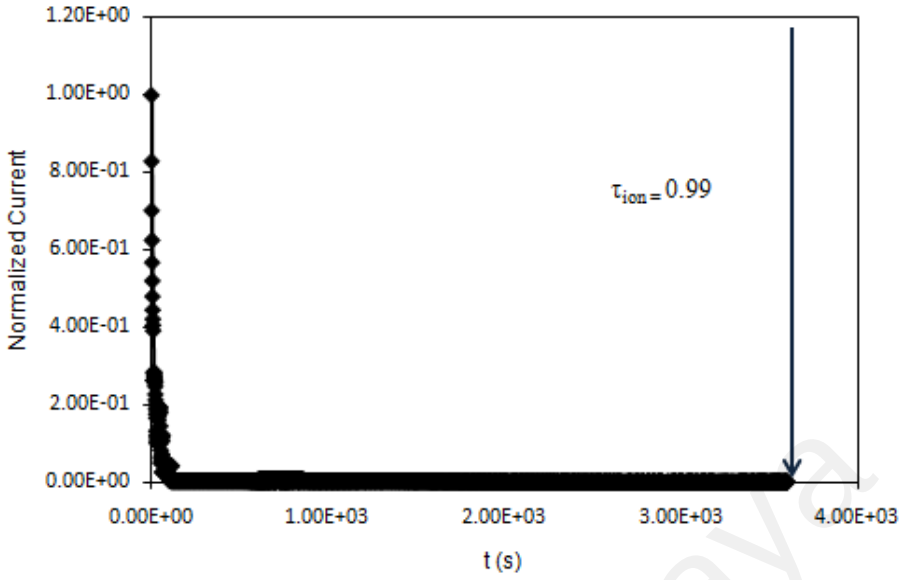

Figure 5.16: Typical plot of normalized polarization current versus time of sample AL5

5.5 Electrochemical stability of $Li_{1+x}Al_xSn_{2-x}P_3O_{12}$ system

The electrochemical stability window of electrolyte is a crucial parameter to be assessed for their application point of view in electrochemical devices. LSV was utilized in order to determine the decomposition voltage of the highest conducting sample, sample AL5. Figure 5.17 illustrates linear sweep voltammogram of the sample at room temperature. From the diagram, the voltage stability window for AL5 sample at room temperature is up to 5.1 V which is greater than that of the unsubstituted sample. This observation reveals that the substitution of Al^{3+} improved the electrochemical stability window by 6.3 % compared to the parent compound as a result of the shrinkage of the unit cell volume that improves the stability of the NASICON structure. As such, the electrochemical stability window of Al^{3+} substituted sample is wide enough to be applied as solid electrolytes in electrochemical devices.

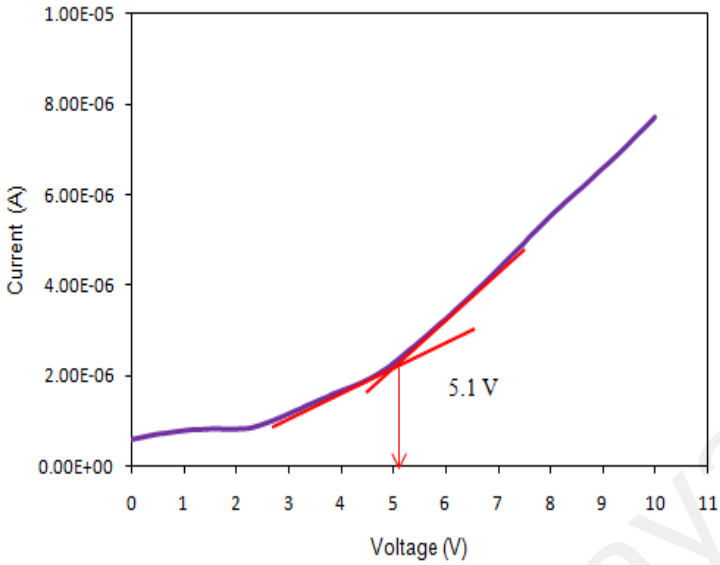

Figure 5.17: Linear sweep voltammogram of sample AL5

CHAPTER 6: TETRAVALENT SUBTITUTION OF Zr^{4+} AND Si^{4+} AT P^{5+} SITE: $Li_{1+y}Sn_2P_{3-y}Zr_yO_{12}$ AND $Li_{1+y}Sn_2P_{3-y}Si_yO_{12}$ SYSTEMS

6.1 Introduction

Besides substitution at Sn^{4+} site, conductivity enhancement can also be done by partial substitution at P^{5+} site with tetravalent ions; for example, Zr^{4+}. In this study, this partial substitution was carried out with the goal of creating Li^+ interstitial ions where $P^{5+} \rightarrow Li^+ + Zr^{4+}$. Therefore, we replaced greater ionic radius of Zr^{4+} ion (r_{ion} = 0.72 Å) and Si^{4+} ion (r_{ion} = 0.40 Å) when comparing to P^{5+} ion (r_{ion} = 0.38 Å) as the research on Zr^{4+} substituted into $LiSn_2P_3O_{12}$ has never been reported in the literature so far. This substitution is also anticipated to enlarge the size of the Li^+ ion migration channel, thus leading to a rise in ion mobility.

In this work, a simple and economical water based sol-gel technique was utilized to synthesize Zr^{4+} substituted at P^{5+} site producing compounds with general formula of $Li_{1+y}Sn_2P_{3-y}Zr_yO_{12}$ with y = 0.1, 0.3, 0.5, 0.7 and 0.9 as System V. In system VI, Si^{4+} ion was substituted at P^{5+} site in order to obtain compounds with general formula of $Li_{1+y}Sn_2P_{3-y}Si_yO_{12}$ with y = 0.1, 0.3, 0.5, 0.7 and 0.9 with the goal of creating Li^+ interstitial ions where $P^{5+} \rightarrow Li^+ + Si^{4+}$. Similar to the System V, the substitution of P^{5+} with Si^{4+} is expected to enlarge the migration channel of Li^+ ions. For both systems, all the samples were characterized in the aspects of structural, morphological, elemental, and electrical and also voltage stability window.

6.2 Classification of the samples

As mentioned in section 6.1, this chapter consists of two systems, $Li_{1+y}Sn_2P_{3-y}Zr_yO_{12}$ and $Li_{1+y}Sn_2P_{3-y}Si_yO_{12}$ with y = 0.1, 0.3, 0.5, 0.7 and 0.9. Table 6.1 below summarizes the designation of the studied samples based on the value of y for both systems.

Table 6.1: The classification of the samples in $Li_{1+y}Sn_2P_{3-y}Zr_yO_{12}$ and $Li_{1+y}Sn_2P_{3-y}Si_yO_{12}$ systems

System	*y*	Sample
V $Li_{1+y}Sn_2P_{3-y}Zr_yO_{12}$	0.1	ZR1
	0.3	ZR3
	0.5	ZR5
	0.7	ZR7
	0.9	ZR9
VI $Li_{1+y}Sn_2P_{3-y}Si_yO_{12}$	0.1	SI1
	0.3	SI3
	0.5	SI5
	0.7	SI7
	0.9	SI9

6.3 $Li_{1+y}Sn_2P_{3-y}Zr_yO_{12}$ System

6.3.1 XRD analysis

Presented in Figure 6.1 are the XRD patterns of the studied $Li_{1+y}Sn_2P_{3-y}Zr_yO_{12}$ system. All the samples in the system are indexed to rhombohedral ($R\bar{3}c$) $LiSn_2P_3O_{12}$ crystalline phase with the existence of unreacted cassiterite SnO_2 (Cui et al., 2012). However, the maximum substitution value of y is only up to 0.5. When y exceeded 0.5, certain peaks disappear and SnO_2 peaks become dominant. As such, further analysis is only done on the sample with $0 < y < 0.5$ and no further characterization was proceeded for the sample with y = 0.7 and 0.9. Furthermore, all peaks for sample ZR1, ZR3 and ZR5 are sharp and well defined. Therefore, it can be deduced that the compounds are generally well crystallized (Kubanska et al., 2014). The intensity of the peaks also increases with the increment of y.

In order to confirm that Zr^{4+} ion is in the $LiSn_2P_3O_{12}$ structure, the peaks in 2θ range 23.0°- 25.0° were carefully analyzed. Figure 6.2 shows the magnified XRD patterns in this 2θ range for sample ZR1, ZR3 and ZR5. As seen in this figure, the peak shifts to higher diffraction angle upon Zr^{4+} ion substitution indicating that Zr^{4+} ion is in the $LiSn_2P_3O_{12}$ structure. Nevertheless, no peak attributed to zirconium and the related compound is detected, indicating that Zr^{4+} is successfully placed into the $LiSn_2P_3O_{12}$ structure instead of forming impurities.

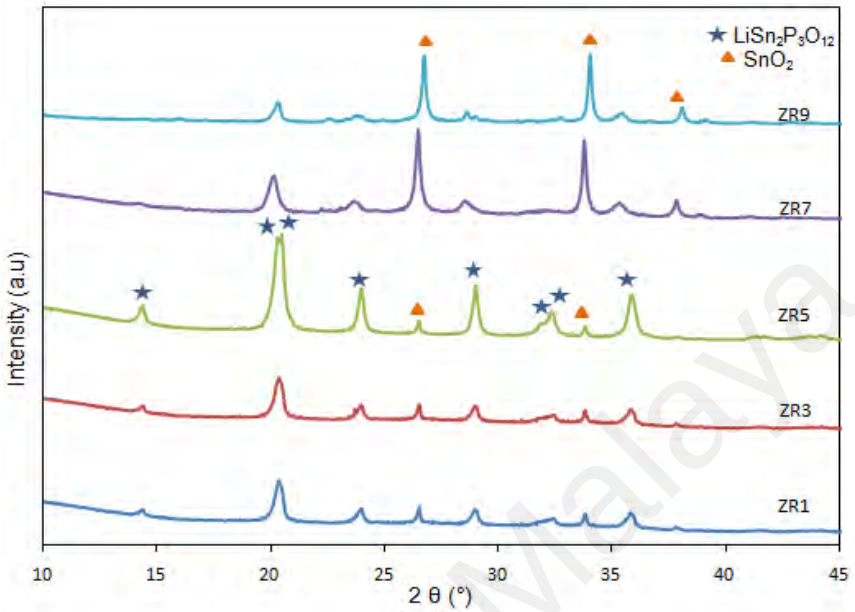

Figure 6.1: X-ray diffraction patterns of $Li_{1+y}Sn_2P_{3-y}Zr_yO_{12}$ system

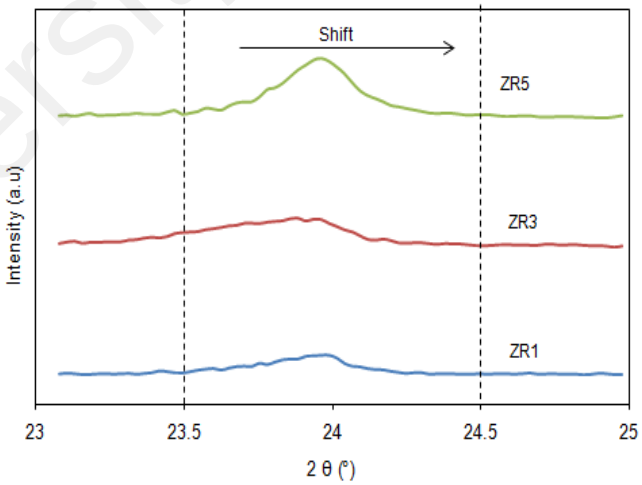

Figure 6.2: X-ray diffraction patterns of $Li_{1+y}Sn_2P_{3-y}Zr_yO_{12}$ system in 2θ range from 23.0° to 25.0°

Table 6.2 shows the variations of lattice parameters and crystallite size for the $Li_{1+y}Sn_2P_{3-y}Zr_yO_{12}$ system. The values of *a*, *c* and *V* in Zr substituted system increase as the value of *y* increases. Nevertheless, the increase in the unit cell volume compared to the unsubstituted parent compound is mostly related to the substitutions of greater ionic radius of Zr^{4+} ion (r_{ion} = 0.72 Å) compared to the P^{5+} ion (r_{ion} = 0.38 Å) (Rao et al., 2014). The crystallite size of the $Li_{1+y}Sn_2P_{3-y}Zr_yO_{12}$ system is bigger than that of the parent compound (137.4 Å). Furthermore, the density of the prepared pellet was established from the physical dimensions and the weight of the pellet compared to the theoretical density of 3.79 g cm^{-3}. The density was found to rise to 91% after zirconium was substituted to the parent compound.

Table 6.2: Lattice parameters and unit cell volume of $Li_{1+y}Sn_2P_{3-y}Zr_yO_{12}$ system

Sample	a [Å]	c [Å]	V [Å^3]	Crystallite size [Å]
ZR1	8.3895	22.0252	1343.41	140.51
ZR3	8.3941	22.0355	1344.58	143.56
ZR5	8.3968	22.0520	1346.46	146.23

6.3.2 FTIR analysis

FTIR spectra of various functional groups in $Li_{1+y}Sn_2P_{3-y}Zr_yO_{12}$ system in the region from 550 to 1400 cm^{-1} are displayed in Figure 6.3. All samples, sample ZR1, ZR3 and ZR5 shows the same stretching vibration modes. However, vibrations of PO_4 tetrahedral are found to be dominant in all the samples besides the asymmetric bending vibration modes of O-P-O units and the stretching vibrations of P-O-P unit. The bands in the region of 560 to 670 cm^{-1} are attributed to the asymmetric bending vibration modes of O-P-O units (Dayanand et al., 1996). Stretching vibrations of P-O-P are identified in the region of 700 to 800 cm^{-1} (Mariappan & Govindaraj, 2005). Asymmetric stretching vibrations of PO_4^{3-} ions can be seen in the bands in the region of 1000 to 1280 cm^{-1} while bands in the region of 900 to 980 cm^{-1} correspond to the symmetric stretching vibrations of the PO_4^{3-} ions (Ejehi et al., 2012; Kosova et al., 2008; Mariappan & Govindaraj, 2005). In all samples, ZRI, ZR3 and ZR5, as *y* increases, the two absorption bands of O-P-O and PO_4^{3-} are shifted to the lower wave number direction as the results of the improvement of the crystallanity of the sample as confirmed by XRD analysis.

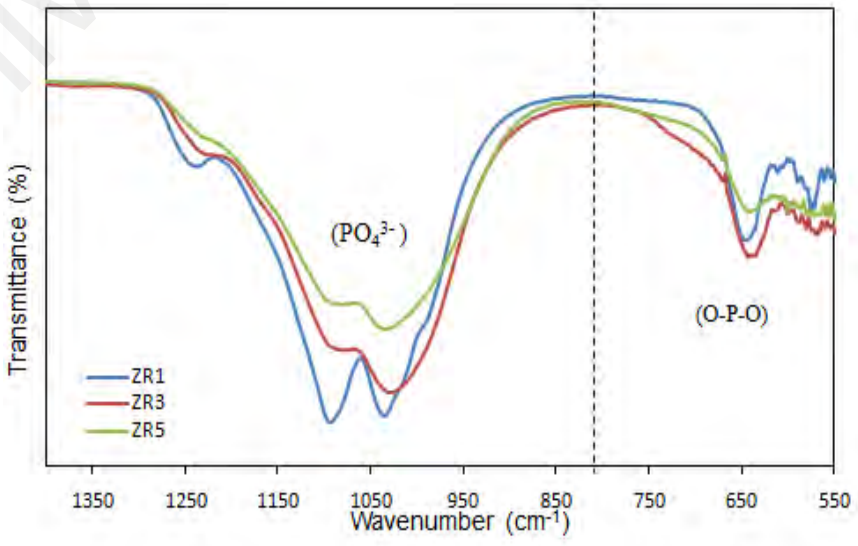

Figure 6.3: FTIR spectra of various functional groups in $Li_{1+y}Sn_2P_{3-y}Zr_yO_{12}$ system

6.3.3 SEM, EDX and particle size distribution analyses

Figure 6.4 displays the SEM micrographs of $Li_{1+y}Sn_2P_{3-y}Zr_yO_{12}$ system. In all samples, it is clear that the particles in the samples are agglomerated and increases when the value of *y* increases. These results can be correlated with the analysis of the particle size distribution as shown in Figure 6.5. The average particle size for sample ZR1 was 24.0 µm and increases to 60.50 µm for sample ZR5 and the value is larger compared to that of $LiSn_2P_3O_{12}$, which was 22.8 µm. This is due to the substitutions of greater ionic radius of Zr^{4+} ion (r_{ion} = 0.72 Å) compared to the P^{5+} ion (r_{ion} = 0.38 Å), which raised the particle"s size in the ZR5 sample.

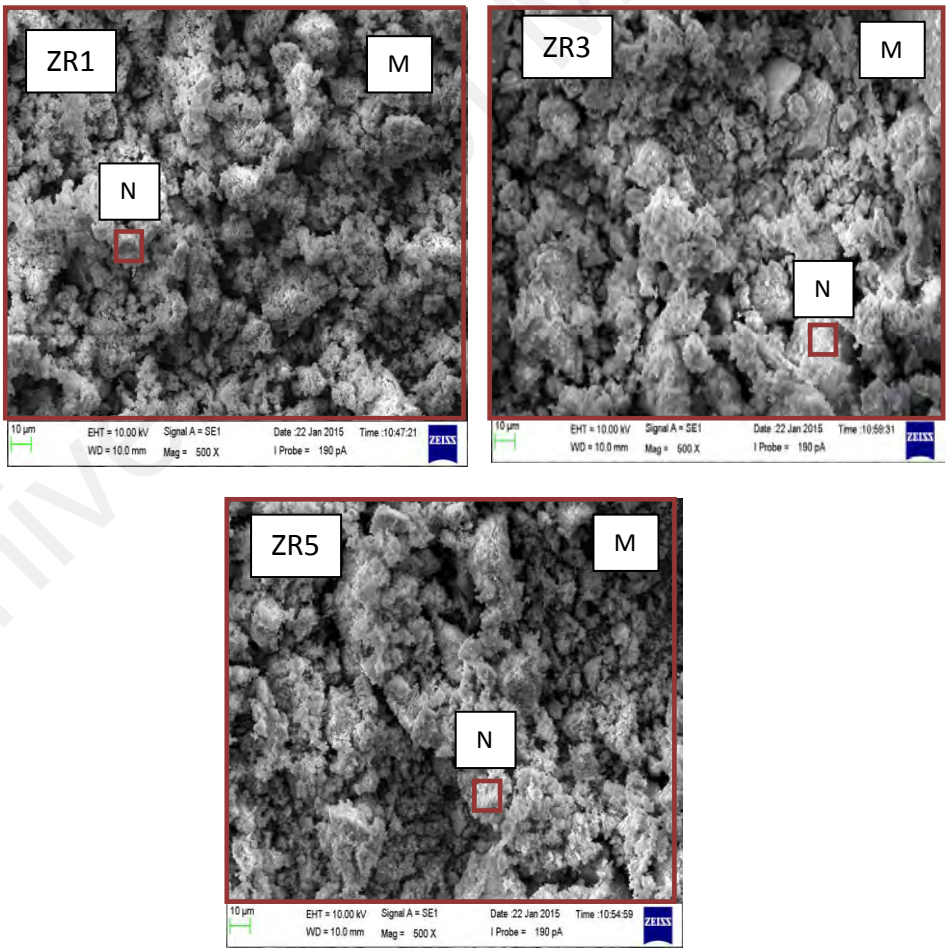

Figure 6.4: SEM micrographs of $Li_{1+y}Sn_2P_{3-y}Zr_yO_{12}$ system

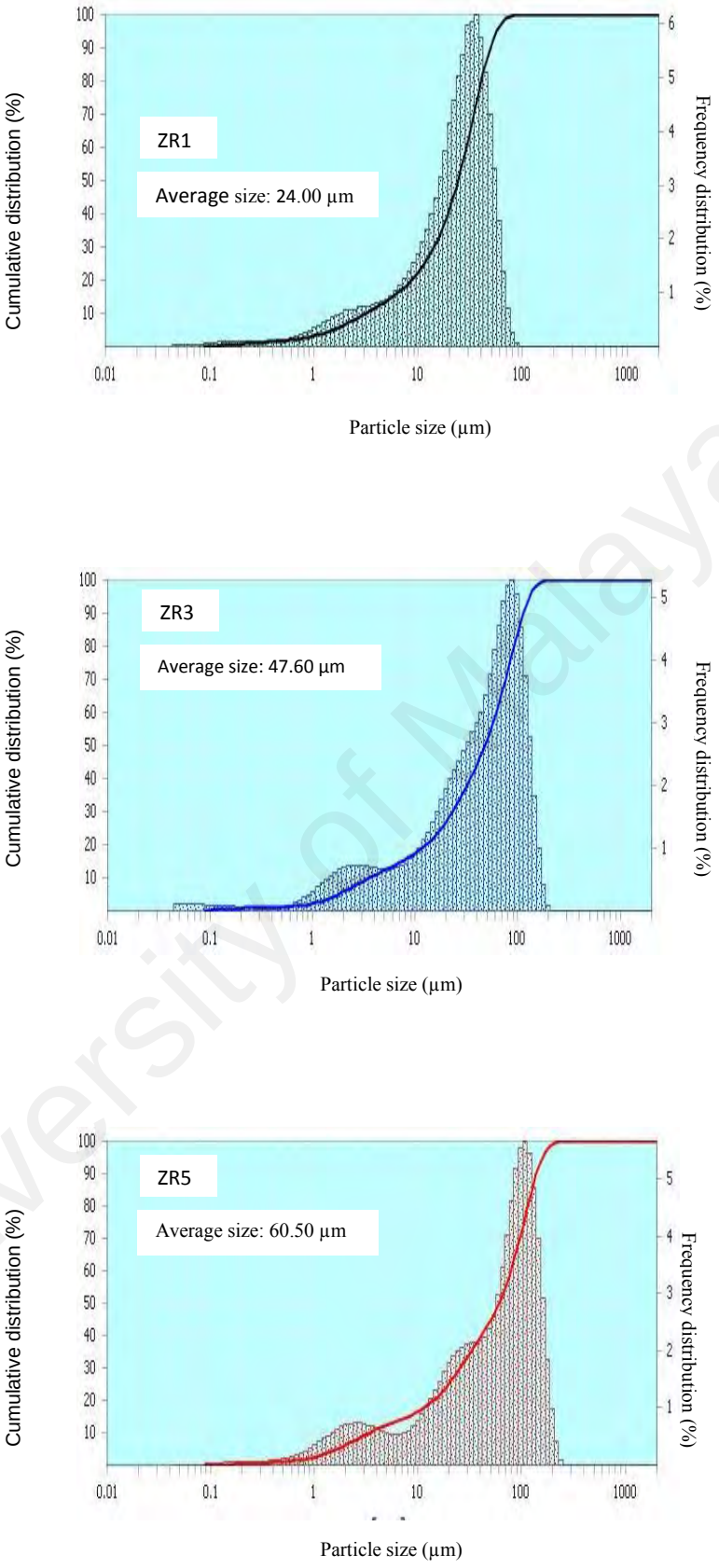

Figure 6.5: Particle size distribution of $Li_{1+y}Sn_2P_{3-y}Zr_yO_{12}$ system

EDX analysis was carried out in order to confirm the stoichiometric proportions and elemental analysis of the $Li_{1+y}Sn_2P_{3-y}Zr_yO_{12}$ system. The results of the EDX analysis are shown in Table 6.3. In this Zr^{4+} substituted system, the EDX analysis was carried out in tow region; larger region marked as M and smaller region marked as N. From the table, the atomic ratio of Sn : Zr: P: O for all samples are very near to the anticipated composition in both region M and N; thus verifying that the Zr^{4+} was successfully inserted into the $LiSn_2P_3O_{12}$ structure forming $Li_{1+y}Sn_2P_{3-y}Zr_yO_{12}$ compound. However the EDX of the samples couldn"t show the existence of lithium due to its light atomic and therefore, the concept of charge neutrality was applied for this case (Narváez-Semanate & Rodrigues, 2010; Norhaniza et al., 2011).

Table 6.3: The EDX stoichiometric atomic ratio of $Li_{1+y}Sn_2P_{3-y}Zr_yO_{12}$ system

Sample	Composition		Stoichiometric atomic ratio			
			Sn	Zr	P	O
ZR1	Starting mixture		2.00	0.10	2.90	12.00
	EDX analysis	M	2.00	0.11	2.89	11.98
		N	2.00	0.10	2.90	11.99
ZR3	Starting mixture		2.00	0.30	2.70	12.00
	EDX analysis	M	2.00	0.29	2.71	12.01
		N	2.00	0.29	2.69	11.99
ZR5	Starting mixture		2.00	0.50	2.50	12.00
	EDX analysis	M	2.00	0.51	2.51	12.00
		N	2.00	0.49	2.50	12.00

6.3.4 Electrical properties of $Li_{1+y}Sn_2P_{3-y}Zr_yO_{12}$ System

6.3.4.1 DC conductivity of $Li_{1+y}Sn_2P_{3-y}Zr_yO_{12}$ System

The complex impedance plots at room temperature obtained for ZR1, ZR3 and ZR5 samples are presented in Figure 6.6. As can be seen from the figure, the plots are made of two depressed semicircles in high and middle frequency area with an electrode spike at low frequency area. The high frequency semicircle is allocated to bulk response with its intercept at the *x*-axis allocated to bulk resistance, R_b, while the middle frequency semicircle is ascribed to grain boundary response with its intercept at the *x*-axis corresponds to grain boundary resistance, R_{gb}. The R_b and R_{gb} values decrease with *y* value indicating an increase in conductivity with increase of Zr^{4+} content.

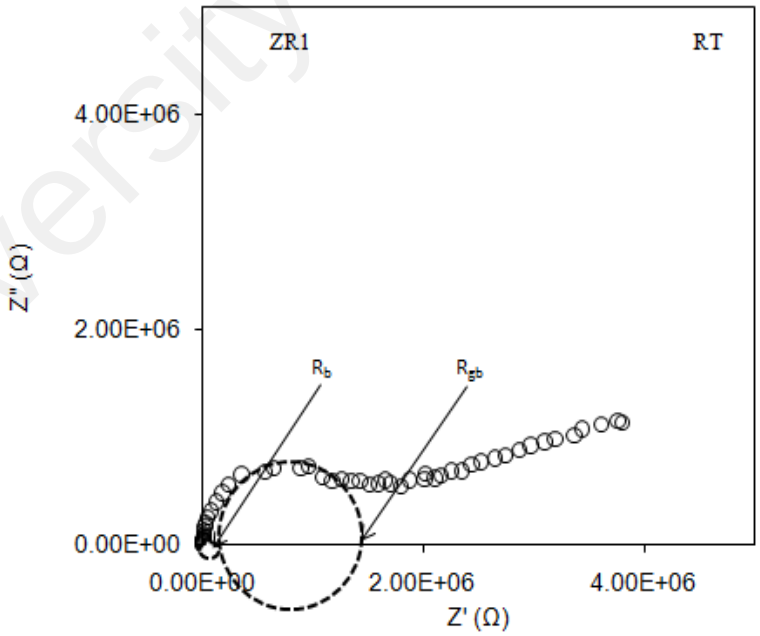

Figure 6.6, continued....

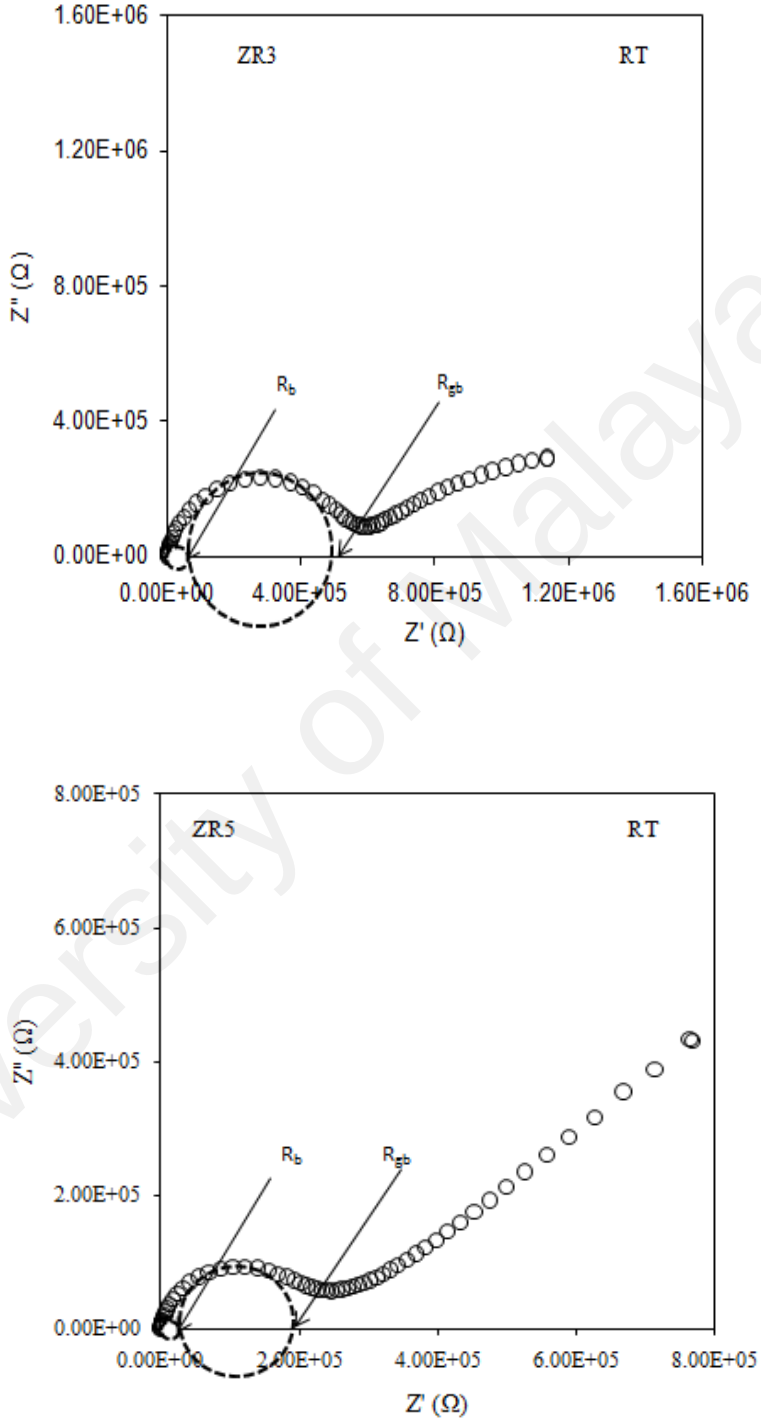

Figure 6.6: Complex impedance plots of $Li_{1+y}Sn_2P_{3-y}Zr_yO_{12}$ samples at room temperature

The complex impedance data shown in Figure 6.6 can be modelled by an equivalent circuit made up of bulk and grain boundary resistance, R_b and R_{gb} and bulk and grain boundary capacitance, C_b (CPE), C_{gb} (CPE) and $CPE_{blocking\ electrode}$ with constant phase element (CPE) behaviour as in Figure 6.7 (Kubanska et al., 2014).

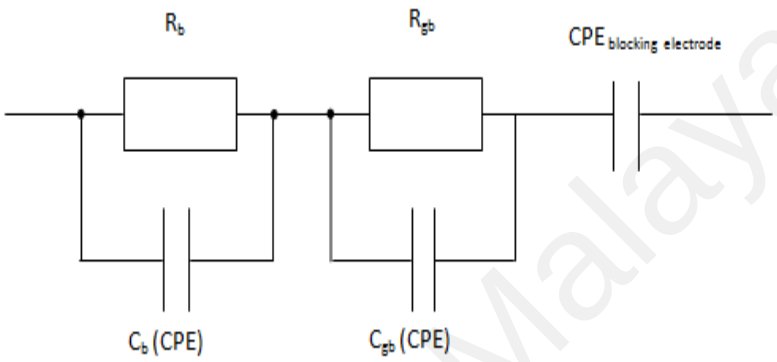

Figure 6.7: Equivalent circuit of $Li_{1+y}Sn_2P_{3-y}Zr_yO_{12}$ samples based on the impedance analysis at room temperature

Only one semicircle is detected corresponding to bulk resistance, R_b together with an electrode spike at low frequency area for ZR1, ZR3 and ZR5 samples when the temperature rises from 300 to 500 °C as shown in Figure 6.8 and 6.9. The experimental complex impedance data might be approximated by a circuit only containing bulk resistance, R_b and bulk capacitance, C_b (CPE) and $CPE_{blocking\ electrode}$ with constant phase element (CPE) behaviour as shown in Figure 6.10.

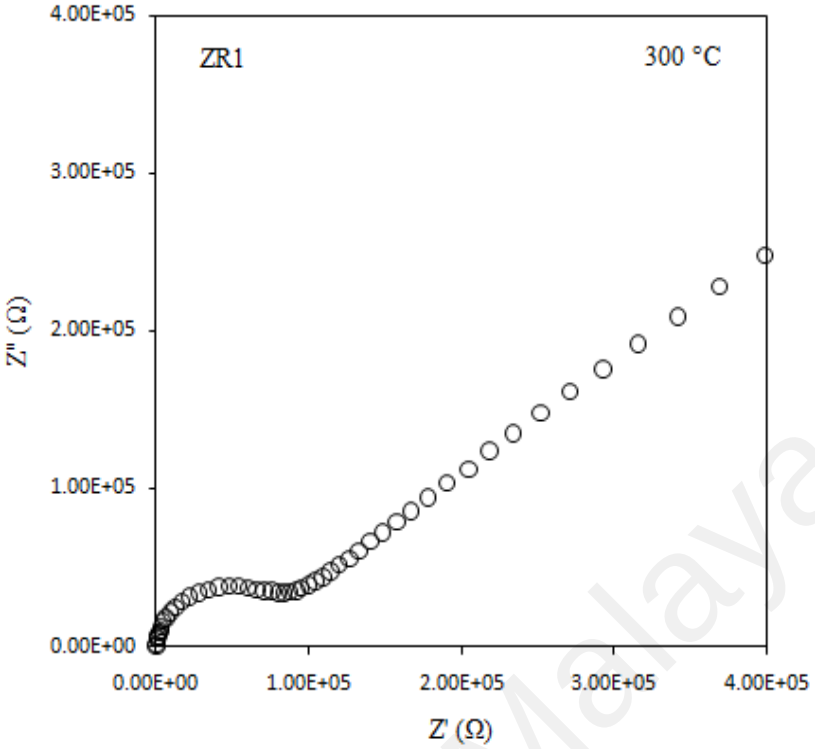

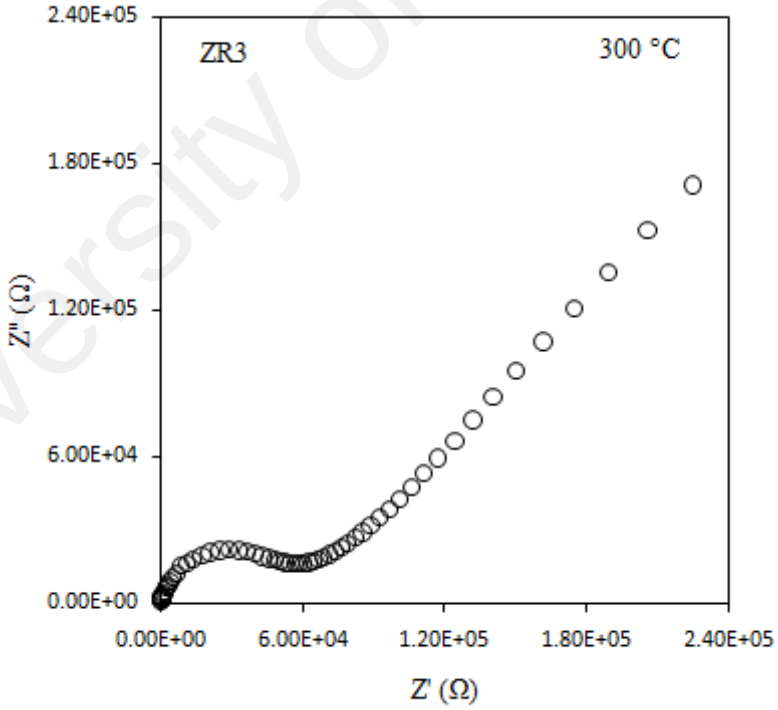

Figure 6.8, continued....

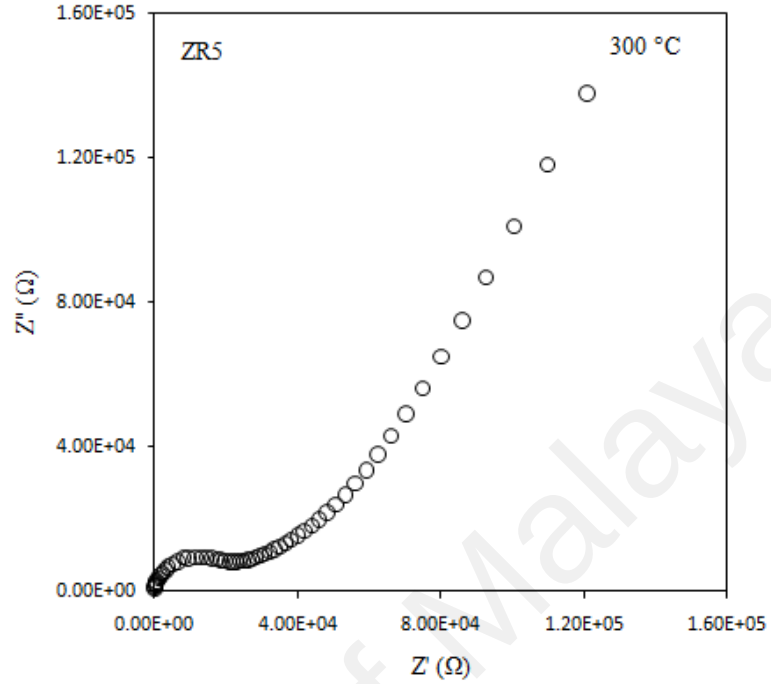

Figure 6. 8: Complex impedance plots of $Li_{1+y}Sn_2P_{3-y}Zr_yO_{12}$ samples at 300 °C

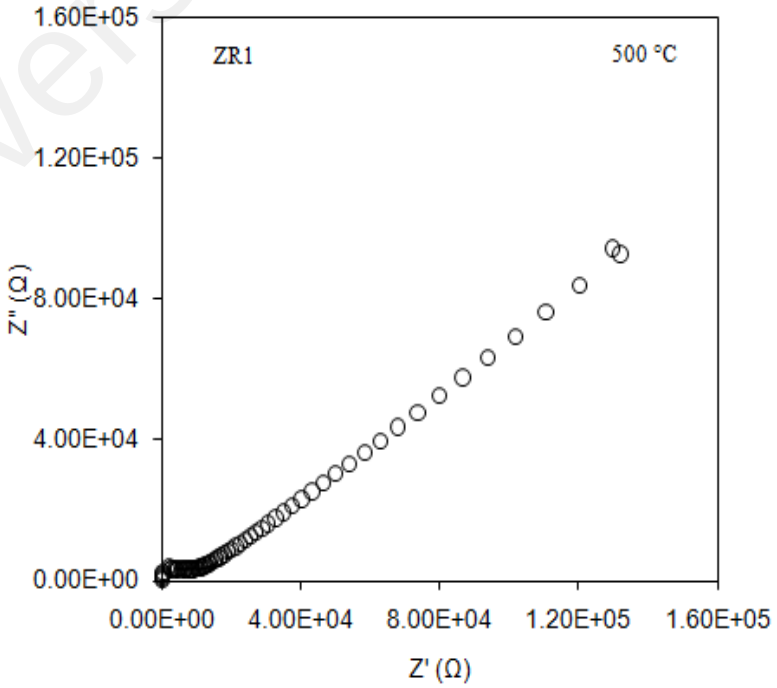

Figure 6.9, continued....

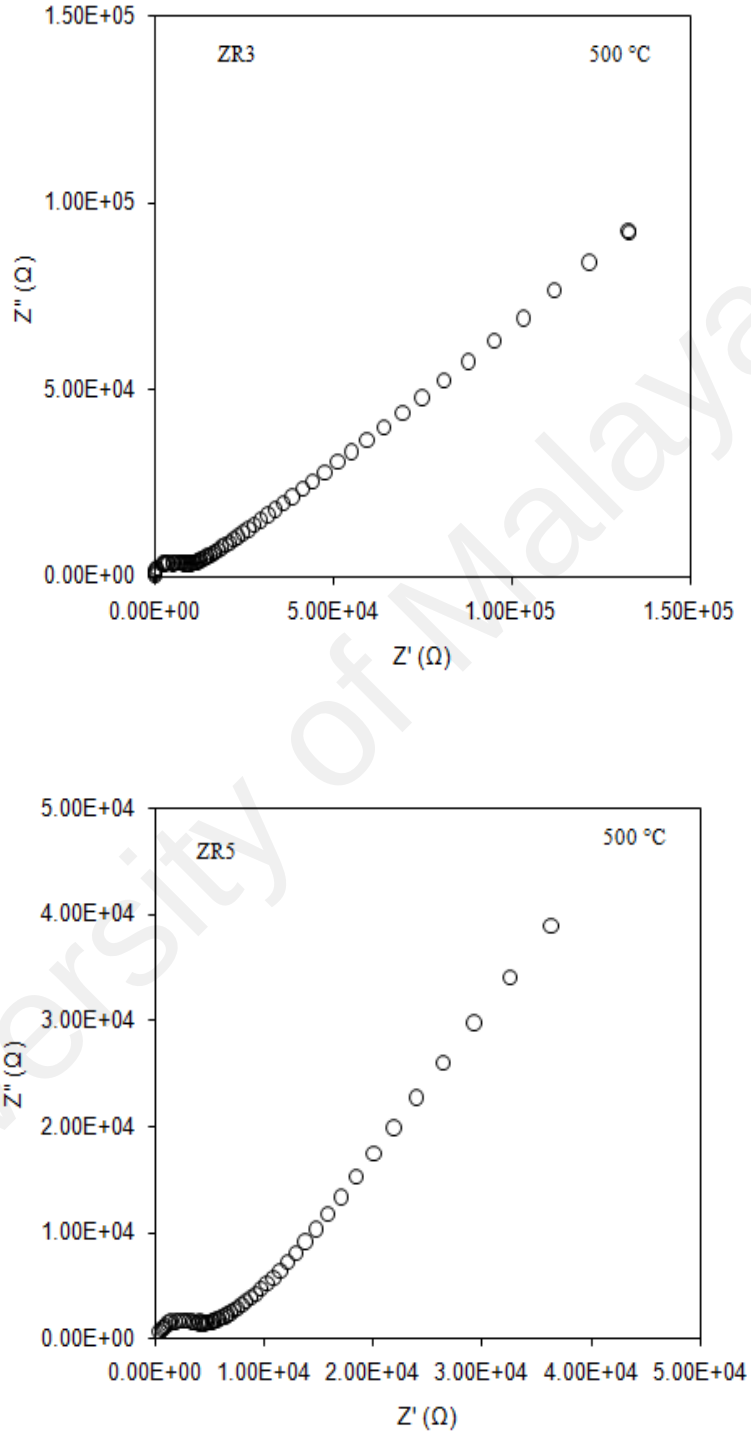

Figure 6.9: Complex impedance plots of $Li_{1+y}Sn_2P_{3-y}Zr_yO_{12}$ samples at 500 °C

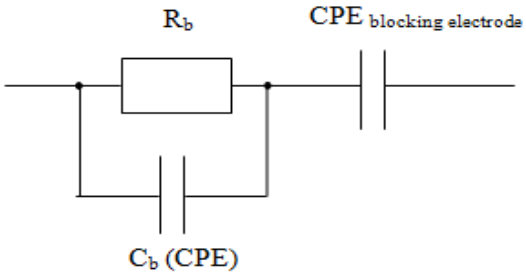

Figure 6.10: Equivalent circuit of $Li_{1+y}Sn_2P_{3-y}Zr_yO_{12}$ samples based on the impedance analysis at 500°C

Tables 6.4 and 6.5 shows the values of bulk, ζ_b, grain boundary, ζ_{gb} and total conductivities, ζ_t for $Li_{1+y}Sn_2P_{3-y}Zr_yO_{12}$ system. The values of bulk and grain boundary conductivities, ζ_b and ζ_{gb} are calculated using R_b and R_{gb} values obtained from the impedance plots. The bulk conductivity, ζ_b of all the samples in $Li_{1+y}Sn_2P_{3-y}Zr_yO_{12}$ system increases with the increment of y. Similar behaviour is observed for the grain boundary, ζ_{gb} and total conductivity value, ζ_t. Sample with $y = 0.5$ that is sample ZR5 showed the highest conducting total conductivity value at room temperature, 1.32×10^{-6} S cm^{-1} which is one order of magnitude greater compared to that of $LiSn_2P_3O_{12}$ parent compound. This is due to the rise of one order of magnitude of the grain boundary conductivity in the Zr^{4+} substituted sample as compared to the parent compound. As the temperature rises to 500 °C, the ionic conductivity increases to 5.77×10^{-5} S cm^{-1}. Thus, this improvement of conductivity is significantly contributed by the grain boundary conductivity.

Another factor that contributed to bulk conductivity improvements was the rise in crystallinity in the system (Xu et al., 2004). According to (Fu, 1997) and (Chowdari et al., 2000), the improvement in crystalline phase favours high ion conduction due to the

existence of greater conduction pathways for Li^+ ions migration. The change in lattice parameter can also contribute to conductivity improvement since it changes the bottleneck size and outcome in easy mobility of ion thus raises the ionic conductivity of the system (Chang et al., 2005). Apart of the bigger size than $P^{5+,}$ lower electronegativity in Zr^{4+} (1.72) as compared to P^{5+} (2.19) is anticipated to raise the average free path migration of lithium ions due to its lower attraction to lithium ion (Burmakin & Shekhtman, 2010).

Table 6.4: Ionic conductivity values for $Li_{1+y}Sn_2P_{3-y}Zr_yO_{12}$ system at 30 °C

Sample	$\zeta_{b,30}$ (S cm^{-1})	$\zeta_{gb,30}$ (S cm^{-1})	$\zeta_{t,30}$ (S cm^{-1})
ZR1	$(2.22 \pm 0.05) \times 10^{-6}$	$(1.72 \pm 0.07) \times 10^{-7}$	$(1.59 \pm 0.07) \times 10^{-7}$
ZR3	$(3.48 \pm 0.04) \times 10^{-6}$	$(4.50 \pm 0.06) \times 10^{-7}$	$(3.99 \pm 0.06) \times 10^{-7}$
ZR5	$(8.50 \pm 0.05) \times 10^{-6}$	$(1.57 \pm 0.07) \times 10^{-6}$	$(1.32 \pm 0.06) \times 10^{-6}$

Table 6.5: Ionic conductivity values for $Li_{1+y}Sn_2P_{3-y}Zr_yO_{12}$ system at 500 °C

Sample	$\zeta_{b,500}$ (S cm^{-1})	$\zeta_{t,500}$ (S cm^{-1})
ZR1	$(2.81 \pm 0.05) \times 10^{-5}$	$(2.81 \pm 0.05) \times 10^{-5}$
ZR3	$(3.07 \pm 0.04) \times 10^{-5}$	$(3.07 \pm 0.04) \times 10^{-5}$
ZR5	$(5.77 \pm 0.01) \times 10^{-5}$	$(5.77 \pm 0.01) \times 10^{-5}$

Figure 6.11 shows the variation of bulk conductivity with 1000/T of $Li_{1+y}Sn_2P_{3-y}Zr_yO_{12}$ system for ZR1, ZR3 and ZR5 samples. The activation energy, E_a for the Li^+ migration was calculated from the Arrhenius as in Equation 4.2. Similar to the spectra of bulk conductivity with 1000/T of the parent compound and Al^{3+} substituted compounds, two regions can be seen in the plots. The first region is the low temperature region while the second region is the high temperature region. The value of the activation energy, E_a is tabulated in Table 6.6. The bulk and grain boundary activation energy decreases with the increment of the value of y.

From the graph, it can be observed that the conductivity increases linearly with temperature implying that conduction is a thermally activated process. The regression value, R for all samples are found to be 0.9. Sample ZR5 which is the highest conducting sample showed the lowest bulk activation energy at low and high temperature, 0.003 eV and 0.360 eV respectively. This low value of activation energy is typical of a fast ion conductor, and a result from the regularity of the diffusion channels in the NASICON structure. The low E_a is favourable for ion conduction in the $Li_{1+y}Sn_2P_{3-y}Zr_yO_{12}$ samples (Jonscher, 1983). Additionally, the substitution of P^{5+} by Zr^{4+} expands the unit cell volume as shown by the XRD data. This increases triangular windows that relate M1 and $M_{1/2}$ sites which helps ion mobility in the $Li_{1.5}Sn_2P_{2.5}Zr_{0.5}O_{12}$ compound (Arbi et al., 2007).

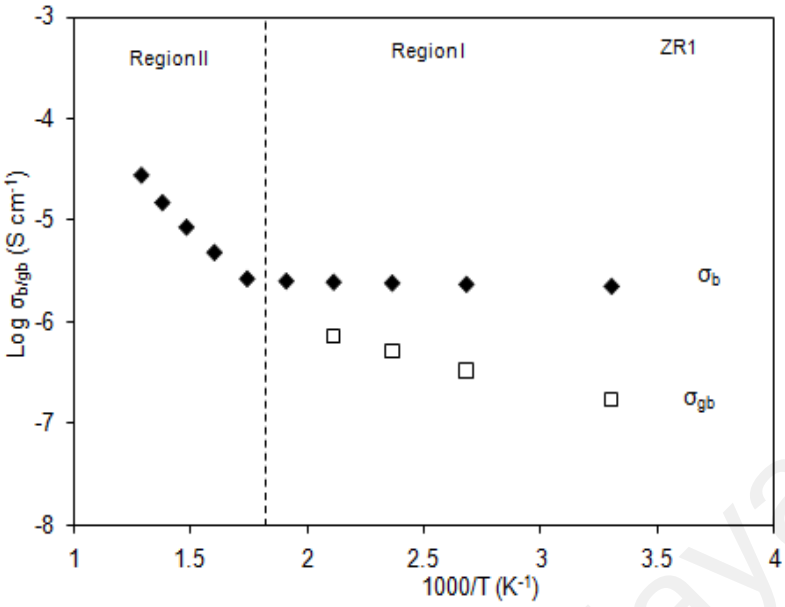

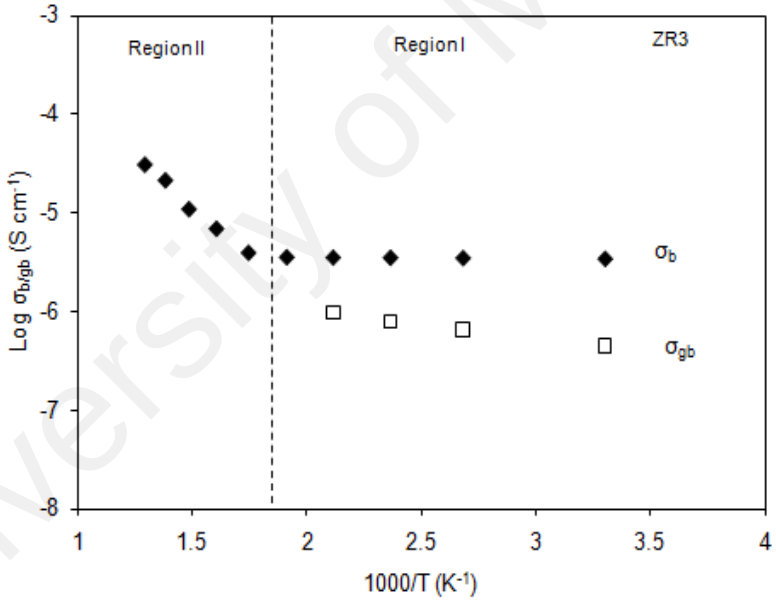

Figure 6.11, continued....

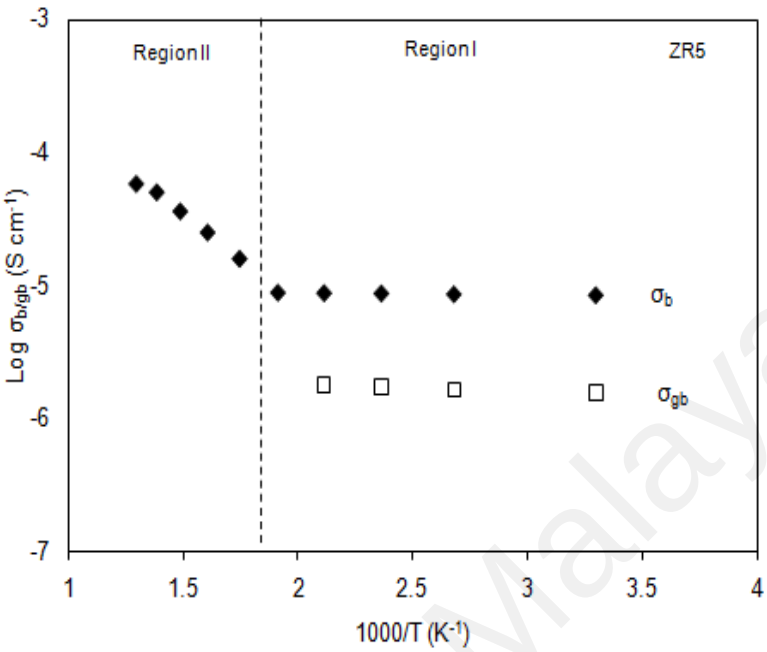

Figure 6.11: Log ζ versus 1000/T plots of bulk and grain boundary conductivities of $Li_{1+y}Sn_2P_{3-y}Zr_yO_{12}$ samples

Table 6.6: Bulk and grain boundary activation energies for $Li_{1+y}Sn_2P_{3-y}Zr_yO_{12}$ system

Sample	$E_{a,b}$ (eV)		$E_{a,\ gb}$ (eV)	
	Region I (Low T)	Region II (High T)	Region I (Low T)	Region II (High T)
ZR1	0.007	0.445	0.105	-
ZR3	0.003	0.395	0.055	-
ZR5	0.002	0.252	0.010	-

6.3.4.2 AC conductivity of $Li_{1+y}Sn_2P_{3-y}Zr_yO_{12}$ system

Figure 6.12 shows log ζ_{ac} versus log ω curves of the highest conducting sample that is sample ZR5 at different temperatures. Generally, the graph consists of intermediate frequency plateau and high frequency dispersion. At the plateau region, the conductivity is frequency independent and corresponds to the DC conductivity. The transition from the DC plateau to AC conductivity dispersion area shifted towards a greater frequency range when the temperature increases. At high frequencies, the power law feature was detected as in Equation 4.3 (Jonscher, 1983).

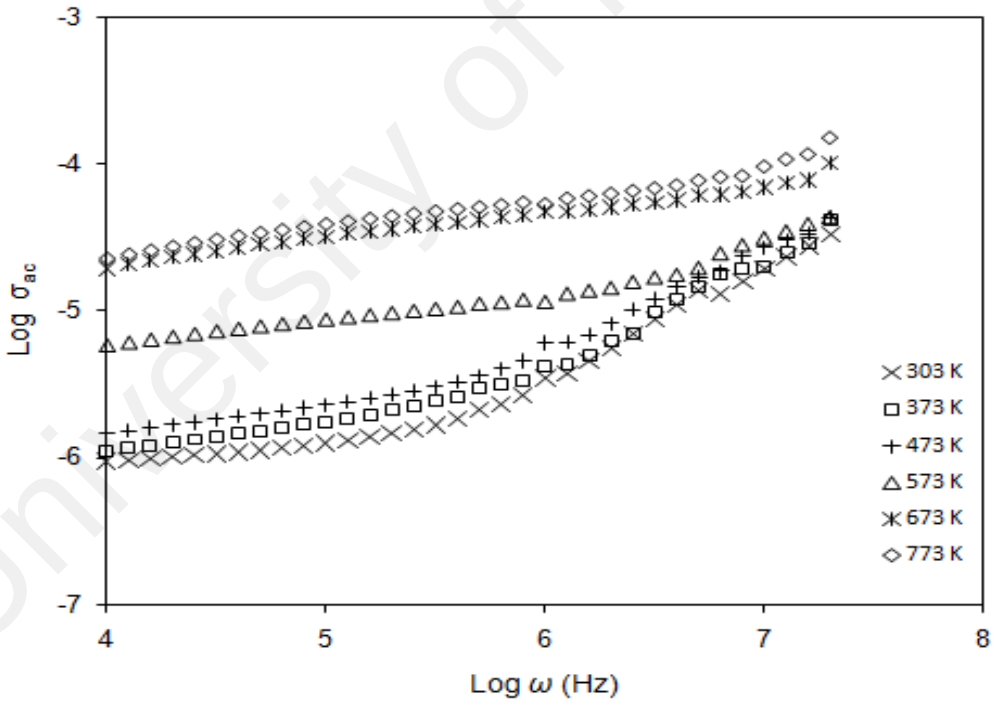

Figure 6.12: AC conductivity spectra for sample ZR5 at various temperatures

Table 6.7 shows the values of ζ, ω_p, K, n,and μ at all temperatures studied for ZR5 sample. From the table, it can be seen that the values ω_p, K, n, and μ, increase with temperature. As the temperature increases, the ions gains sufficient energy and thus the number of ions that hop from one site to another site also increases. Thus the increment of the ionic mobility, μ as well as density of mobile ions, n contributed to the increment of the conductivity in ZR5 sample (Teo et al., 2012; Vijayakumar et al., 2003). As such, the higher conductivity observed for ZR5 sample is due to the high ionic mobility, μ that is 1.73 × 10^{-10} cm^2 V^{-1} s^{-1} and the high density of mobile ions, n that is 2.13 x 10^{24} cm^{-3}.

Table 6.7: Parameters of ω_p, K, n and μ for sample ZR5

T (K)	ω_p (Hz)	K (S cm^{-1} K Hz^{-1})	n (cm^{-3})	μ (cm^2 V^{-1} s^{-1})
303	6.31×10^5	7.59×10^{-10}	2.84×10^{23}	3.48×10^{-11}
373	7.82×10^5	8.06×10^{-10}	3.02×10^{23}	3.50×10^{-11}
473	1.00×10^6	8.99×10^{-10}	3.36×10^{23}	3.53×10^{-11}
573	3.98×10^6	1.31×10^{-9}	4.91×10^{23}	1.16×10^{-10}
673	6.31×10^6	4.24×10^{-9}	1.59×10^{24}	1.57×10^{-10}
773	1.58×10^7	5.68×10^{-9}	2.13×10^{24}	1.73×10^{-10}

Besides that, the values of the frequency exponent s at different temperature were calculated from the slopes of linear part of the high frequency area of log ζ_{ac} versus log ω presented in Figure 6.12. The variation of s with temperature for the investigated sample is shown in Figure 6.13. It is observed from this figure that the frequency exponent s decreases with increasing temperature. The calculated value of s is found to decrease from 0.80 to 0.17. Such behavior suggests that the CBH conduction

mechanism is the predominant conduction mechanism. In CBH model, the conduction occurs via charge carriers hopping process over the Coulomb barrier separating them (Elliott, 1977). According to Elliott (1977), the hopping of the charge carriers are thermally activated (Elliott, 1977).

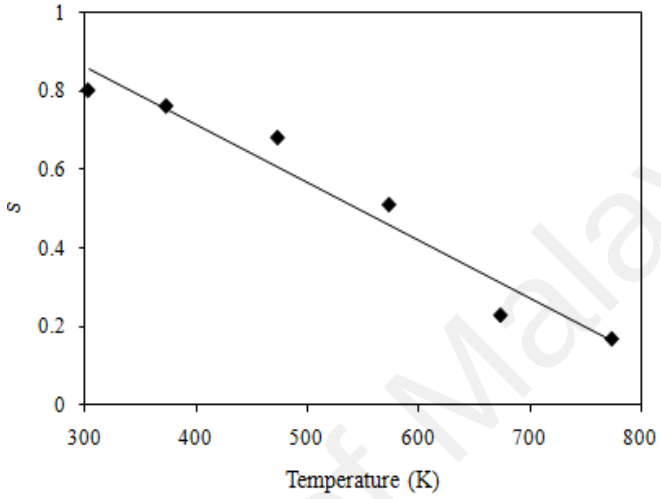

Figure 6.13: Variation of *s* with temperature for sample ZR5

6.3.4.2 Transference number measurement analysis

The η_{ion} for the highest conducting sample, sample ZR5 was evaluated using Wagner"s polarization method. In this technique, the direct current is monitored function of time of a fixed DC voltage of 0.5 V across SS/ sample ZR5 solid electrolytes/SS. Figure 6.14 shows the graph of normalized polarization current versus time. The transference number value is found to be 0.99 in sample ZR5. This value demonstrates that the majority of the charge carrier in the sample is Li^+ ion (Wang et al., 2013).

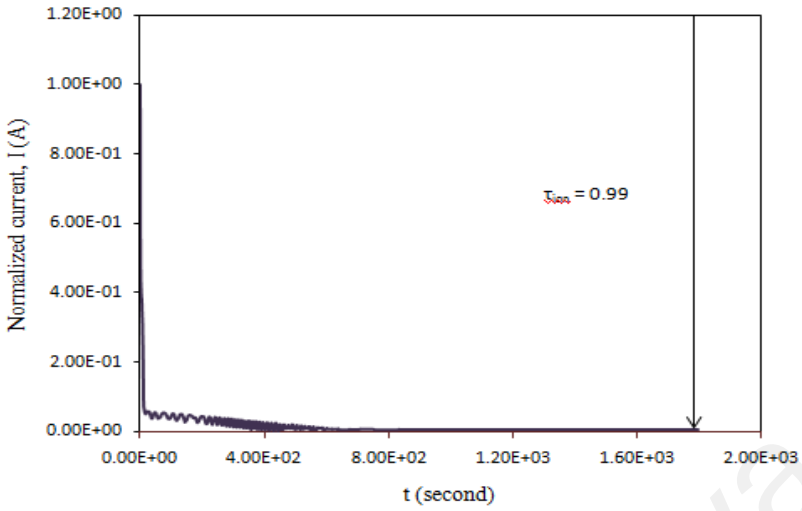

Figure 6.14: Typical plot of normalized polarisation current versus time of sample ZR5

6.3.5 Electrochemical stability of $Li_{1+y}Sn_2P_{3-y}Zr_yO_{12}$ System

Figure 6.15 displays the current-voltage response obtained for the highest conducting sample, sample ZR5 using stainless steel as the working electrode measured between the potential ranges from 0 to 10 V. According to Reddy et al. (2003), the onset of the current identifies the decomposition voltage of the sample (Reddy et al., 2003). From the figure, sample ZR5 is stable up to 5.2 V. This value is 8.3% greater than the unsubtituted sample. The current also starts to increase at potentials beyond this limit due to the decomposition of the electrolyte sample. This suggests that Zr^{4+} substitution increases the stability window of the electrolyte sample and indicates the suitability for electrochemical device applications.

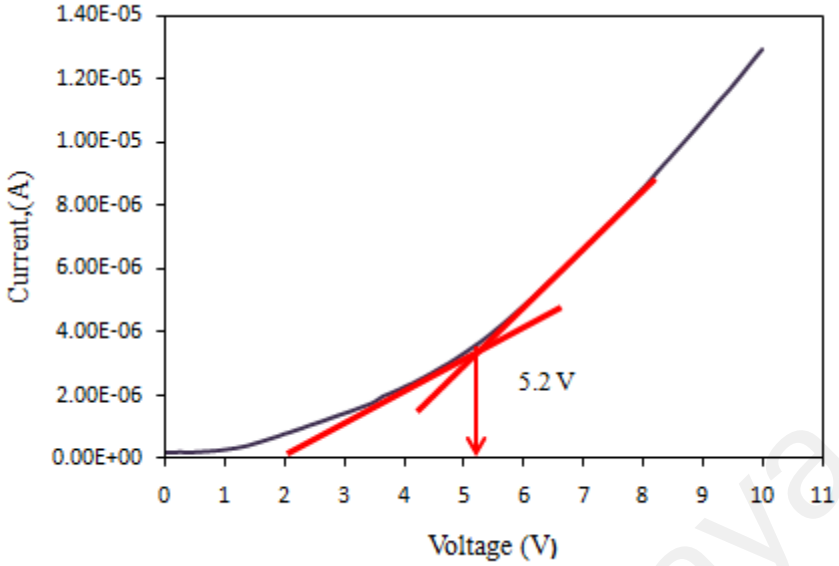

Figure 6.15: Linear sweep voltammogram of sample ZR5

6.4 $Li_{1+y}Sn_2P_{3-y}Si_yO_{12}$ System

6.4.1 XRD analysis

Figure 6.15 shows the XRD patterns of $Li_{1+y}Sn_2P_{3-y}Si_yO_{12}$ system. The XRD patterns clearly show that the peaks corresponding to NASICON material which are well matched with the peak positions assigned in standard JCPDS file. All the peaks are perfectly indexed on the rhombohedral ($R\bar{3}c$) $LiSn_2P_3O_{12}$ crystalline phase with the presence of unreacted cassiterite SnO_2 (Cui et al., 2012). However, the maximum value of substitution, *y* is only up to 0.5. When *y* exceeded 0.5, certain peaks disappeared and the samples become less crystalline with the existence of SnO_2 impurity peaks. As such further analysis was conducted only on SI1, SI3 and SI5 samples.

In SI1, SI3 and SI5 samples, the compound was well crystallized as all the peaks were sharp and well defined. The crystallinity also improves as *y* increases from 0.1 to 0.5. Besides that, the peaks in 2θ range 23.0°- 25.0° were carefully analyzed for the SI1, SI3 and SI5 samples in order to confirm that Si^{4+} has successfully substituted into the parent compound structure. The magnified XRD patterns in this 2θ range are shown in Figure 6.16. The diffraction peaks shifts to higher diffraction angle when Si^{4+} ion is substituted into the $LiSn_2P_3O_{12}$ structure showing that Si^{4+} ion is in the $LiSn_2P_3O_{12}$ structure. The absence of peaks attributed to any silicon related compound in the XRD spectra suggests that partial substitution has taken place.

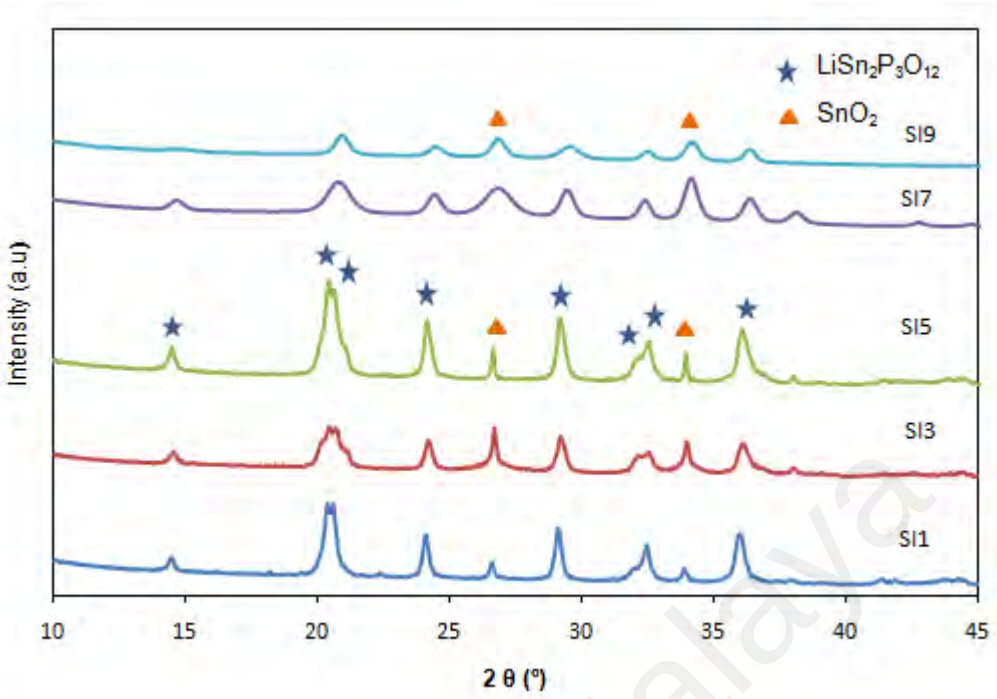

Figure 6.16: X-ray diffraction patterns of $Li_{1+y}Sn_2P_{3-y}Si_yO_{12}$ system

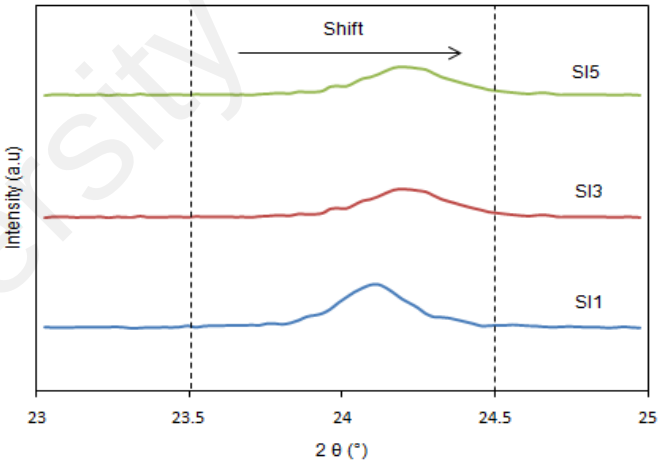

Figure 6.17: X-ray diffractograms of $Li_{1+y}Sn_2P_{3-y}Si_yO_{12}$ system in 2θ range from 23.0 to 25.0°

The values of the lattice parameters and crystallite size for the $Li_{1+y}Sn_2P_{3-y}Si_yO_{12}$ system are listed in Table 6.8. The values of *a*, *c* and *V* in Si^{4+} substituted system increases with the value of *y*. The increase in the unit cell volume compared to the unsubstituted parent compound is due to the substitutions of greater and almost similar ionic radius of Si^{4+} ion (r_{ion} = 0.40Å) compared to the P^{5+} ion (r_{ion} = 0.38 Å). The addition of Si^{5+} ions simultaneously produced additional Li^+ ions in order to balance the charge in the structure. Thus the adjustment in lattice parameters is due to accommodation of the structure to occupy the extra Li^+ ion (Berry et al., 2006).

In addition to this, the crystallite size of the $Li_{1+y}Sn_2P_{3-y}Si_yO_{12}$ system is also found to be smaller than the parent compound that is 137.4 Å. Furthermore, the density of the prepared $Li_{1+y}Sn_2P_{3-y}Si_yO_{12}$ system is found to rise to 92% of the theoretical value.

Table 6.8: Lattice parameters and unit cell volume of $Li_{1+y}Sn_2P_{3-y}Si_yO_{12}$ system

Sample	*a* [Å]	*c* [Å]	*V* [Å^3]	Crystallite size [Å]
SI1	8.4277	21.6033	1329.71	124.72
SI3	8.4351	21.6136	1332.68	128.89
SI5	8.4406	21.6753	1338.23	132.51

6.4.2 FTIR analysis

The NASICON-structured $Li_{1+y}Sn_2P_{3-y}Si_yO_{12}$ system was further investigated by FTIR analysis in the region from 550 to 1400 cm^{-1} as shown in Figure 6.17. The absorption bands corresponding to the vibrations of PO_4 tetrahedral are found to be active and dominant in all the samples. The absorption bands in the region of 560 to 670 cm^{-1} for all samples are caused by the asymmetric bending vibration modes of O-P-O units (Qiu et al., 2003). The bands observed in the region of 700 to 800 cm^{-1} are attributed to the stretching vibrations of P-O-P units (Kosova et al., 2008). Meanwhile, the bands in the region of 1000 to 1280 cm^{-1} for all samples indicated the presence of the asymmetric stretching vibrations while symmetric stretching vibrations of the PO_4^{3-} ions existed in bands in the region of 900 to 980 cm^{-1}(Savitha et al., 2006; Yamada & Takemoto, 2016). Comparing all the dominant absorption bands of O-P-O and PO_4^{3-} in all the samples, the two absorption bands are shifted to the lower wave number direction as the value of *y* increases from 0.1 to 0.5 suggesting that the crystallinity was intensified as *y* value increased in the system (Qiu et al., 2003).

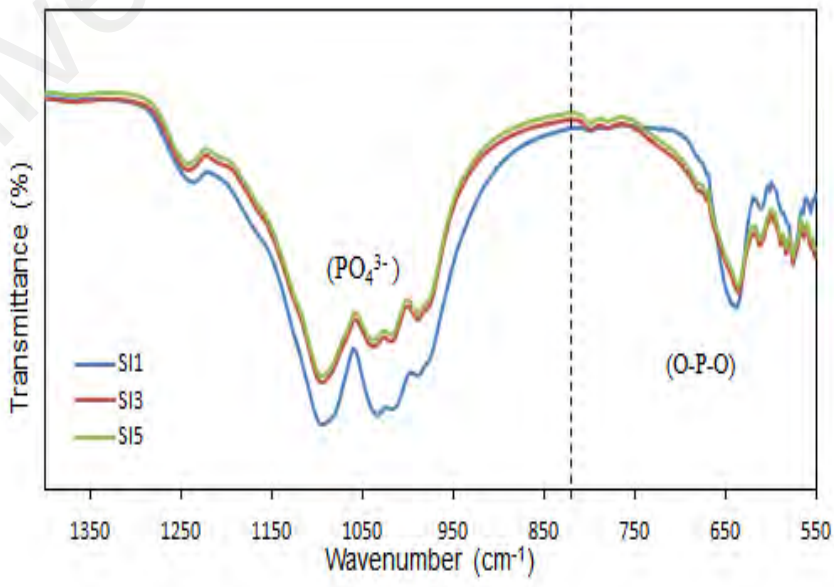

Figure 6.18: FTIR spectra of various functional groups in $Li_{1+y}Sn_2P_{3-y}Si_yO_{12}$ system

6.4.3 SEM, EDX and particle size distribution analyses

SEM was utilized to study the morphology of $Li_{1+y}Sn_2P_{3-y}Si_yO_{12}$ samples. Figure 6.18 illustrates SEM micrographs of SI1, SI3 and SI5 samples. These micrographs revelas that the particles in all the samples are agglomerated and increases with the increment of Si^{4+} content in the system. Increment of the particles size in all samples is confirmed by the analysis of the particle size distribution as shown in Figure 6.19. The average particle size increases from 25.10 µm in the SI1 sample to 26.0 µm in the SI3 sample while SI5 sample possessed particle size that is 30.70 µm. The average particle size for sample SI5 was higher compared to that of $LiSn_2P_3O_{12}$, which was only 22.8 µm as greater ioni radius of Si^{4+} ion (r_{ion} = 0.40 Å) compared to the P^{5+} ion (r_{ion} = 0.38 Å) has raised the particle"s size in the SI5 sample. This is attributed to the grain growth in all the samples as the effect of Si^{4+} substitutions (Adnan & Mohamed, 2014).

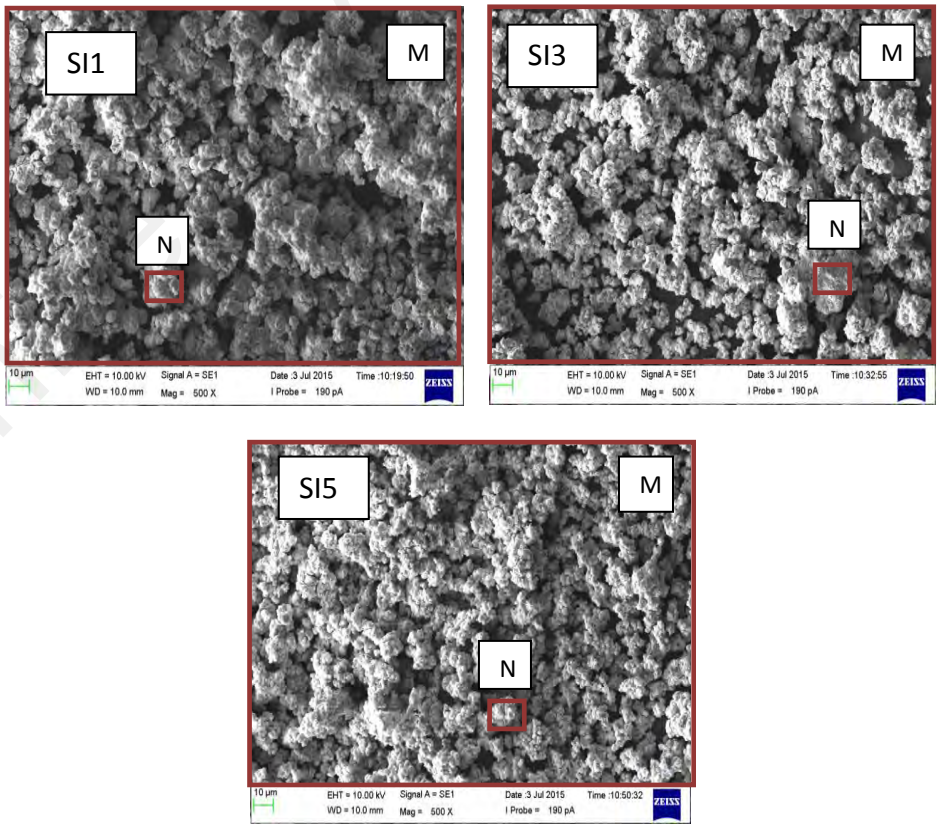

Figure 6.19: SEM micrographs of $Li_{1+y}Sn_2P_{3-y}Si_yO_{12}$ system

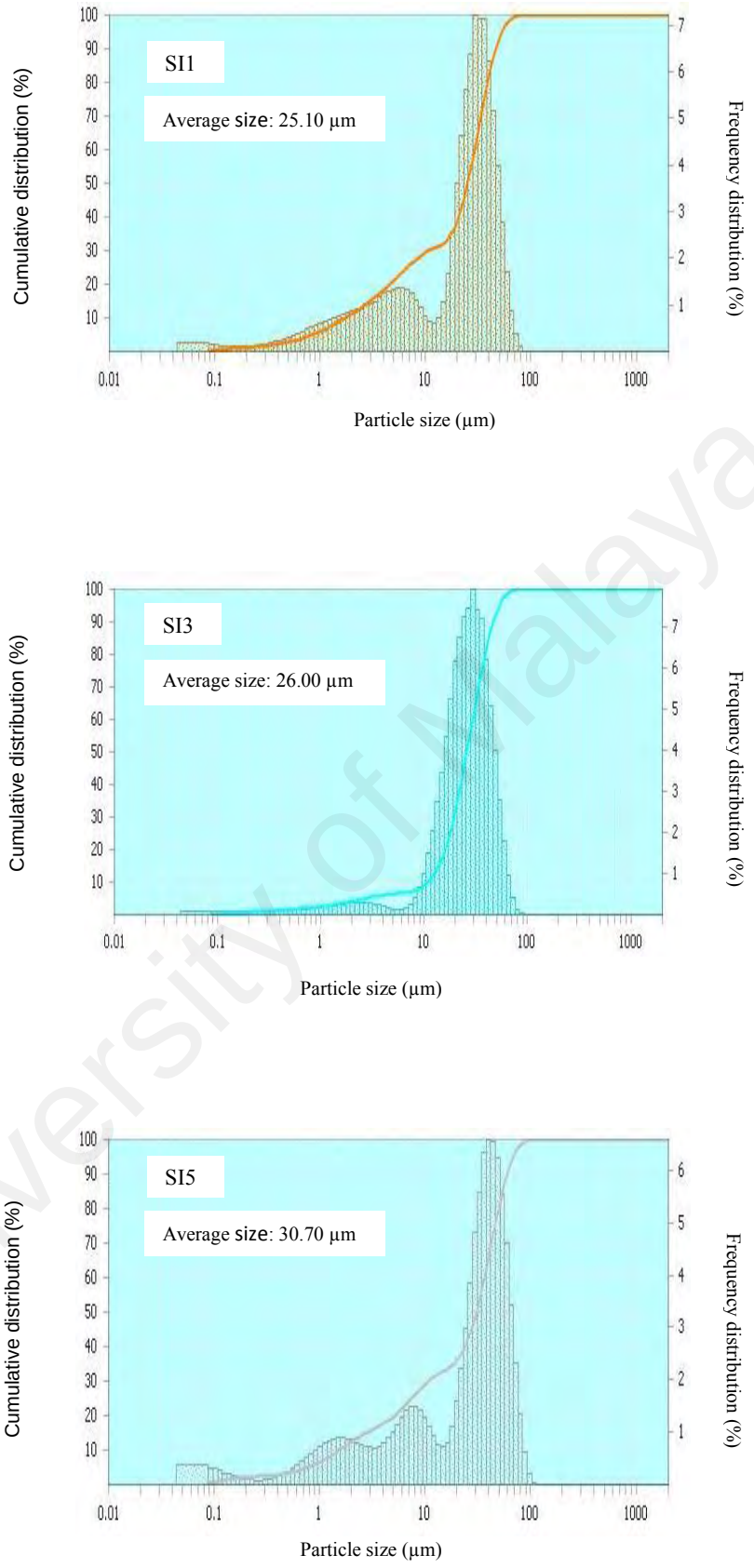

Figure 6.20: Particle size distributions of $Li_{1+y}Sn_2P_{3-y}Si_yO_{12}$ system

The stoichiometric of the elements in all the samples were analyzed using EDX analysis. The stoichiometric of the atomic ratios for Sn, Si, P and O are listed in Table 6.9 in two regions, marked as region M and N. Region M is the larger region while region N is the smaller region. However, the presence of lithium could not be detected by the EDX due to its light atomic weight. Therefore, by applying the concept of charge neutrality (Ramaraghavulu & Buddhudu, 2011; Wu et al., 2009), it is found that the atomic ratio of Sn : Si : P : O for all the samples at both regions, M and N are very close to the designated composition. This confirms that Si^{4+} is successfully substituted into the $LiSn_2P_3O_{12}$ structure leading to the formation of $Li_{1+y}Sn_2P_{3-y}Si_yO_{12}$ compound.

Table 6.9: The EDX stoichiometric atomic ratio of $Li_{1+y}Sn_2P_{3-y}Si_yO_{12}$ system

Sample	Composition		Stoichiometric atomic ratio			
			Sn	Si	P	O
SI1	Starting mixture		2.00	0.10	2.90	12.00
	EDX analysis	M	2.00	0.10	2.91	11.99
		N	2.00	0.11	2.90	11.99
SI3	Starting mixture		2.00	0.30	2.70	12.00
	EDX analysis	M	2.00	0.31	2.69	11.99
		N	2.00	0.30	2.71	12.00
SI5	Starting mixture		2.00	0.50	2.50	12.00
	EDX analysis	M	2.00	0.50	2.51	12.01
		N	2.00	0.50	2.49	12.00

6.4.4 Electrical properties of $Li_{1+y}Sn_2P_{3-y}Si_yO_{12}$ System

6.4.4.1 DC conductivity of $Li_{1+y}Sn_2P_{3-y}Si_yO_{12}$ System

Impedance spectroscopy is a useful method to resolve the contributions of various processes such as bulk, grain boundary, and electrode effect in the specified frequency domain. As such, the complex impedance plot of sample SI1, SI3 and SI5 at room temperature is shown in Figure 6.20. The plots consist of two overlapping semicircles with an electrode spike at low frequency area. The semicircle at the high frequency region is corresponding to bulk response with its intercept at the *x*-axis allocated to bulk resistance, R_b. Meanwhile the semicircle at the middle frequency is corresponding to grain boundary response. The intercept of the grain boundary response at the *x*-axis leads to grain boundary resistance, R_{gb}. Meanwhile, the spike in the low frequency is due to the processes occurring at the electrode and electrolyte interface (Irvine et al., 1990; Kumar & Balaya, 2016). As the value of *y* increases from 0.1 to 0.5 at room temperature, R_b and R_{gb} are shifts to lower impedance value suggesting an enhancement in ionic conductivity.

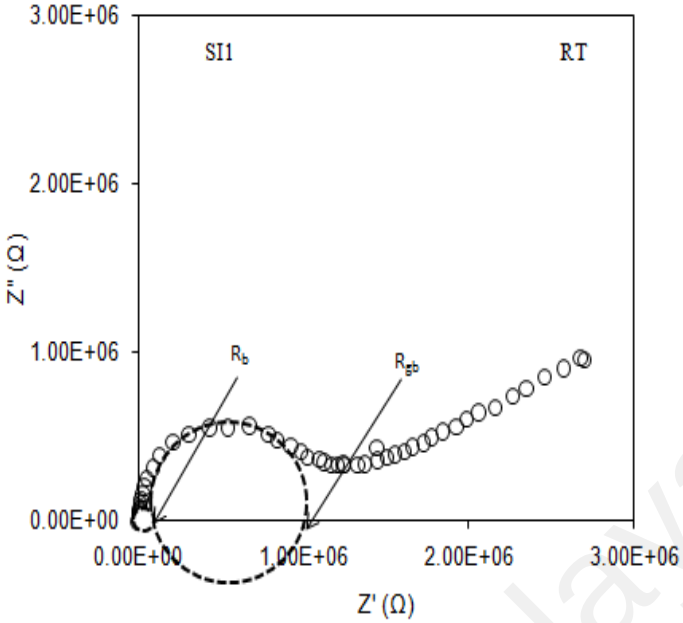

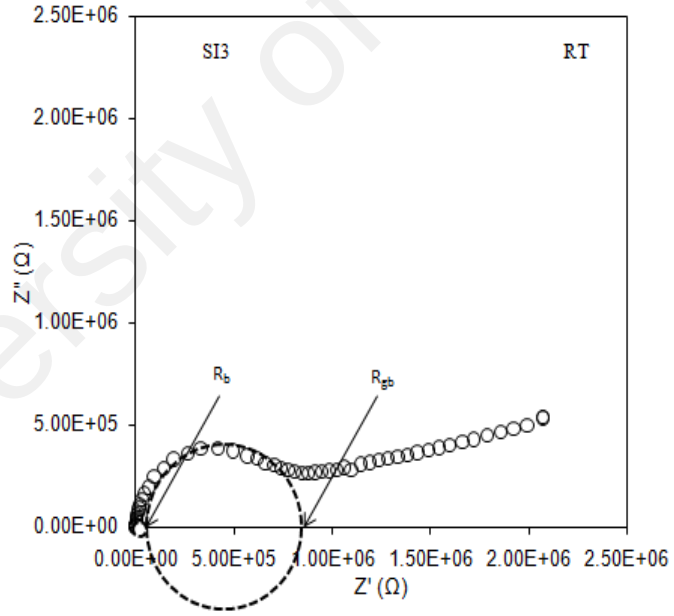

Figure 6.21, continued....

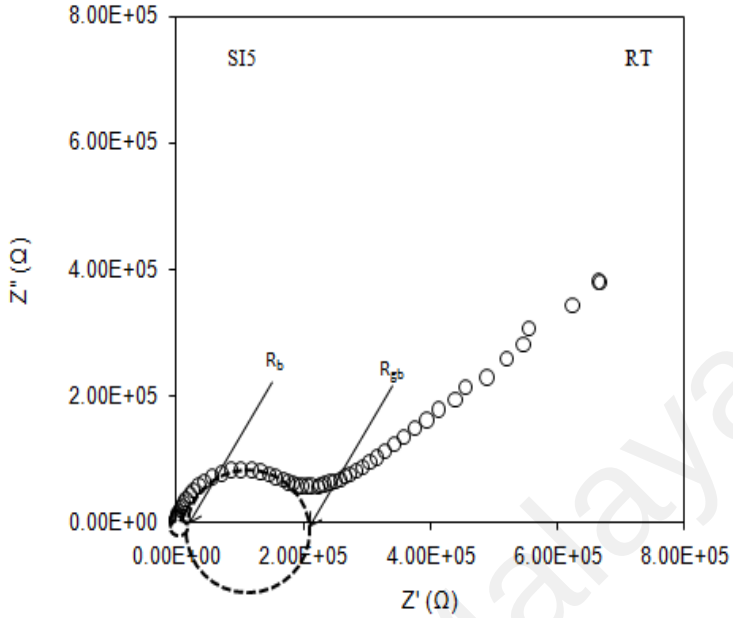

Figure 6.21: Complex impedance plots of $Li_{1+y}Sn_2P_{3-y}Si_yO_{12}$ samples at room temperature

The semicircle observed in the complex impedance plots can be represented by the impedance of an equivalent circuit made up of bulk and grain boundary resistance, R_b and R_{gb} and bulk and grain boundary capacitance, C_b (CPE), C_{gb} (CPE) and $CPE_{blocking\ electrode}$ with constant phase element (CPE) behaviour as in Figure 6.21 (Kubanska et al., 2014).

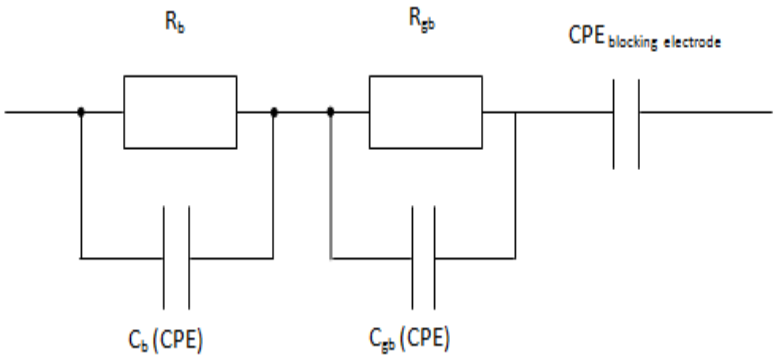

Figure 6.22: Equivalent circuit of $Li_{1+y}Sn_2P_{3-y}Si_yO_{12}$ samples based on the impedance analysis of the samples at room temperature

However, in all samples, only one semicircle is detected that represents bulk resistance, R_b and also an electrode spike at low frequency area as depicted in Figure 6.23 and 6.24 as the temperature increase from 300 to 500 °C. Experimental complex impedance data might now be represented by a circuit only containing bulk resistance, R_b and bulk capacitance, C_b (CPE) and $CPE_{blocking\ electrode}$ with constant phase element (CPE) behaviour as in Figure 6.25.

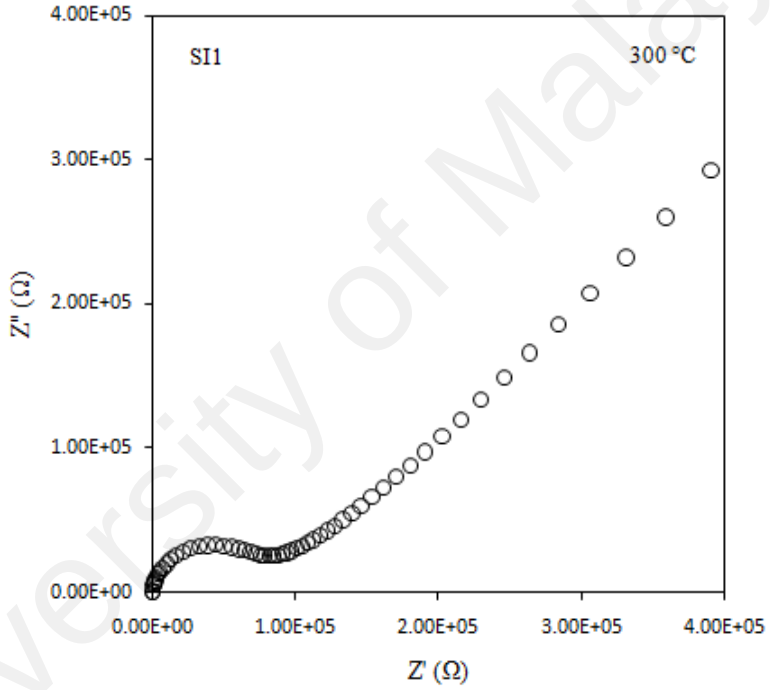

Figure 6.23, continued....

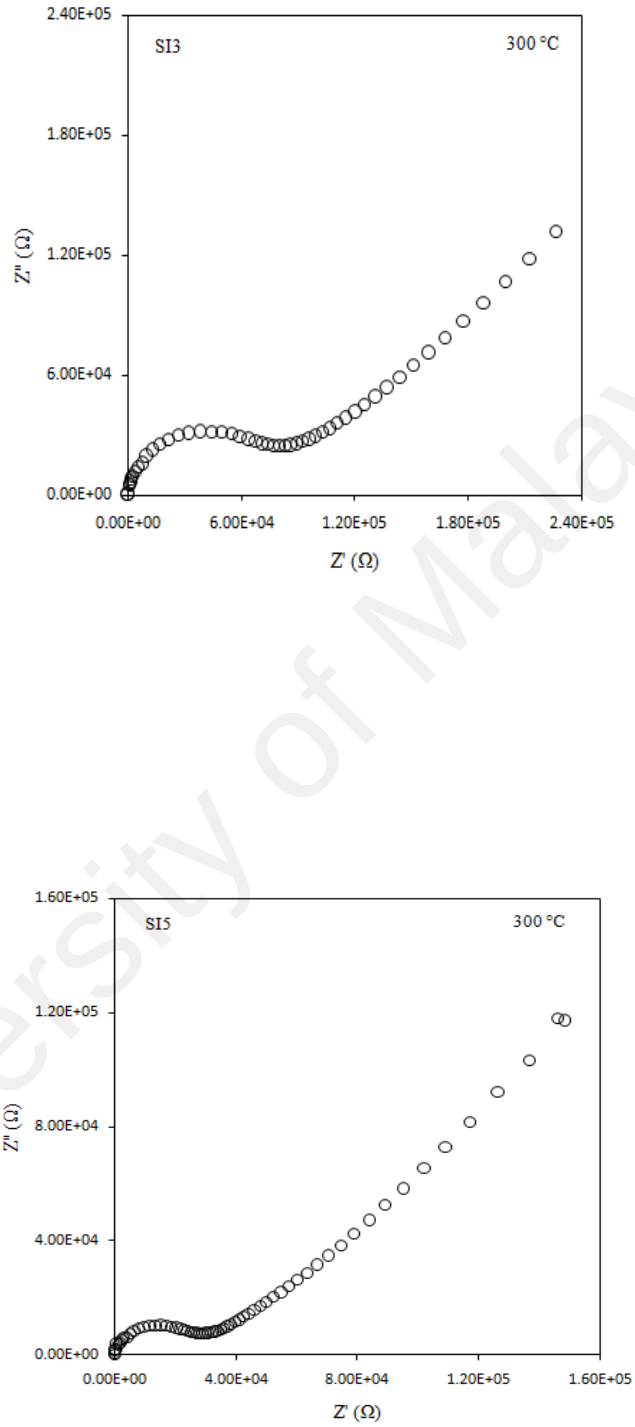

Figure 6.23: Complex impedance plots of $Li_{1+y}Sn_2P_{3-y}Si_yO_{12}$ samples at 300 °C

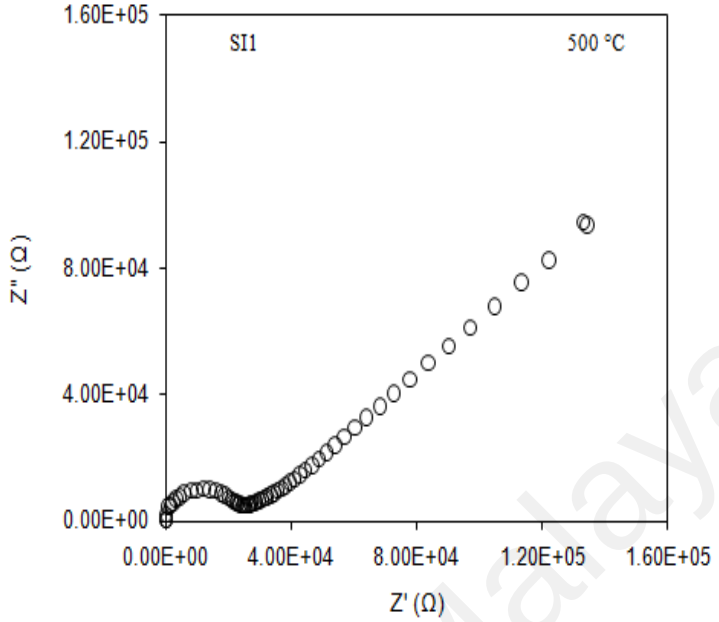

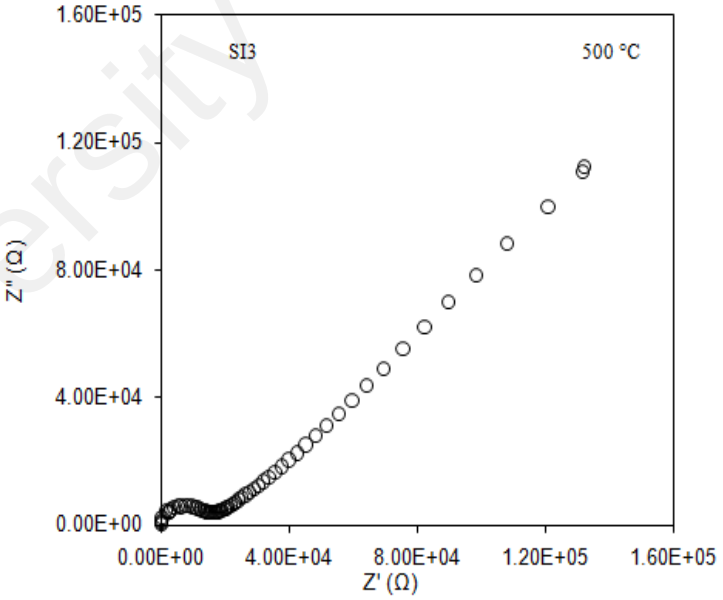

Figure 6.24, continued....

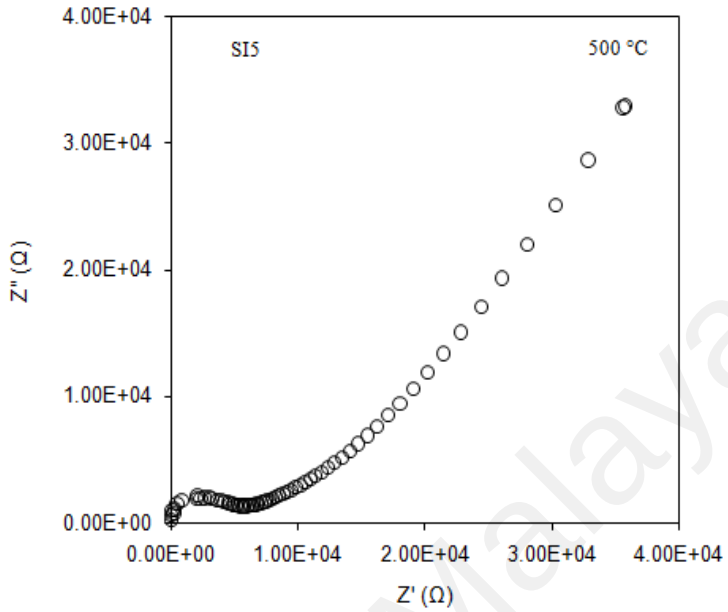

Figure 6.24: Complex impedance plots of $Li_{1+y}Sn_2P_{3-y}Si_yO_{12}$ samples at 500 °C

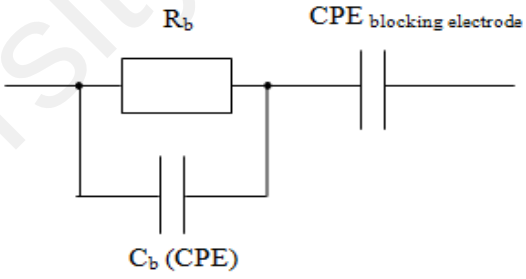

Figure 6.25: Equivalent circuit of $Li_{1+y}Sn_2P_{3-y}Si_yO_{12}$ samples based on the impedance analysis of the samples at 500°C

Then, the bulk and grain boundary conductivities, ζ_b and ζ_{gb} are calculated using R_b and R_{gb} values obtained from the previous impedance plots. Table 6.10 and 6.11 lists all the values of bulk, grain boundary and total conductivities for SI1, SI3 and SI5 samples. The bulk, grain boundary and total conductivities for all the samples show an increasing

trend as the value of y increases. Sample with y = 0.5 that is sample SI5 exhibited the highest conducting total conductivity value at room temperature of 1.05×10^{-6} S cm^{-1} which is one order of magnitude greater to that of $LiSn_2P_3O_{12}$ parent compound . When the temperature was increased to 500 °C, the ionic conductivity also increases to 6.05×10^{-5} S cm^{-1}. The conductivity value obtained at higher temperature for sample ZR5 is higher compared to V^{5+} substituted sample that is only 3.16×10^{-5} S cm^{-1} (Norhaniza et al., 2011).

Furthermore, the increment of the total ionic conductivity in the samples may be also attributed by the increment of the grain boundary conductivity as can be seen in Table 6.12. Besides that, additional Li^+ is introduced by substituting P^{5+} by Si^{4+} and located in an energetically favored site (M3). This occupation induces the nearest-neighboring M1 site to displace towards the next M3 site, which promotes an interstitial migration mechanism (Lang et al., 2015). On top of that, the increase in ζ_b can be most probably attributed to increasing amounts of Li^+ occupying the M_3 sites and displacing the Li^+ in M1 sites towards the nearest-neighboring M3 sites. Therefore, the additional Li content further promotes the Li^+ diffusion and increases the conductivity in the system (Rettenwander et al., 2016).

The enhancement in ionic conductivity ontained in this study was resulted from the framework distortion due to the replacement of the larger Si ion (r_{ion} = 0.40 Å) for the smaller P ion (r_{ion} = 0.38 Å). This distortion alters the local electron density of adjacent phosphorous atoms due to a lower electronegativity of Si (1.90) compared with P (2.19). It affects the lithium ion dynamics and consequently affects its bulk conductivity (Geng et al., 2015).

Table 6.10: Ionic conductivity values for $Li_{1+y}Sn_2P_{3-y}Si_yO_{12}$ system at 30 °C

Sample	$\zeta_{b,30}$ (S cm^{-1})	$\zeta_{gb,30}$ (S cm^{-1})	$\zeta_{t,30}$ (S cm^{-1})
SI1	$(2.17 \pm 0.04) \times 10^{-6}$	$(2.22 \pm 0.04) \times 10^{-7}$	$(2.01 \pm 0.04) \times 10^{-7}$
SI3	$(2.58 \pm 0.04) \times 10^{-6}$	$(3.02 \pm 0.02) \times 10^{-7}$	$(2.70 \pm 0.03) \times 10^{-7}$
SI5	$(8.09 \pm 0.03) \times 10^{-6}$	$(1.20 \pm 0.02) \times 10^{-6}$	$(1.05 \pm 0.02) \times 10^{-6}$

Table 6. 11: Ionic conductivity values for $Li_{1+y}Sn_2P_{3-y}Si_yO_{12}$ system at 500 °C

Sample	$\zeta_{b,500}$ (S cm^{-1})	$\zeta_{t,500}$ (S cm^{-1})
SI1	$(9.43 \pm 0.03) \times 10^{-6}$	$(9.43 \pm 0.03) \times 10^{-6}$
SI3	$(1.51 \pm 0.03) \times 10^{-5}$	$(1.51 \pm 0.03) \times 10^{-5}$
SI5	$(6.05 \pm 0.02) \times 10^{-5}$	$(6.05 \pm 0.02) \times 10^{-5}$

Figure 6.26 displays the plot of variation of bulk conductivity with 1000/T of $Li_{1+y}Sn_2P_{3-y}SI_yO_{12}$ samples. The activation energy, E_a for the Li^+ migration was established from the Arrhenius as in Equation 4.2. For all of the samples, two regions can be seen similarly with other systems discussed in previous chapter. The first region is assigned to low temperature region while region II can be associated with high temperature region. The activation energy for bulk, $E_{a,b}$ and grain boundary, $E_{a,gb}$ were extracted from the plot of variation of bulk conductivity with 1000/T and tabulated in Table 6.12. From the graph, it can be observed that the conductivity increases linearly with temperature implying that conduction is a thermally activated process. The regression value, R for all samples are found to be 0.9. Both $E_{a,b}$ and $E_{a,gb}$ are observed to decrease with the increment of the Si^{4+} ion content. Sample SI5 which is the highest conducting sample possessed the lowest $E_{a,b}$ and $E_{a,gb}$ which indicate two different

barriers of ion mobility. Lower $E_{a,b}$ and $E_{a,gb}$ values exhibits that Li^+ ions are easier to move in the structure which leads to the enhancement of the conductivity .

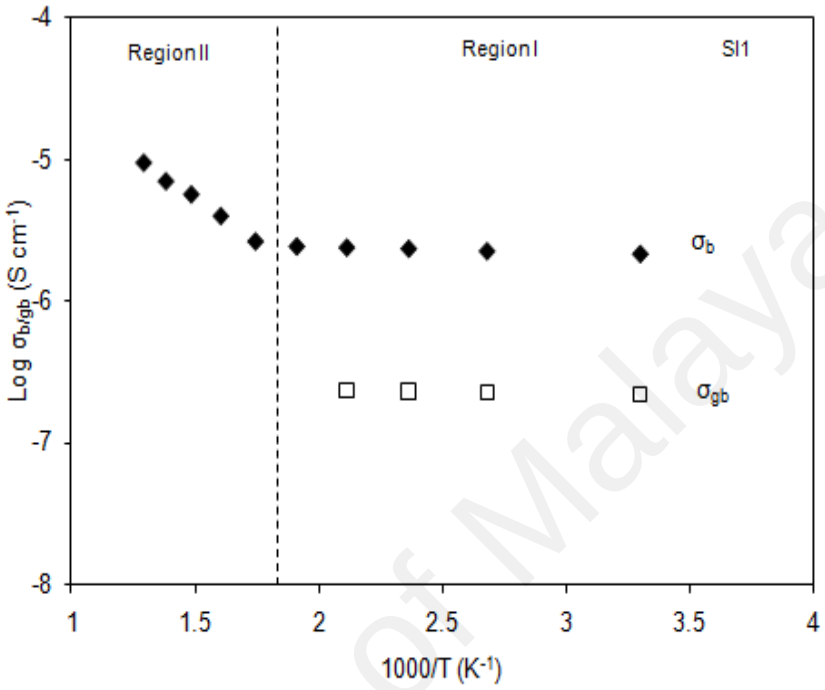

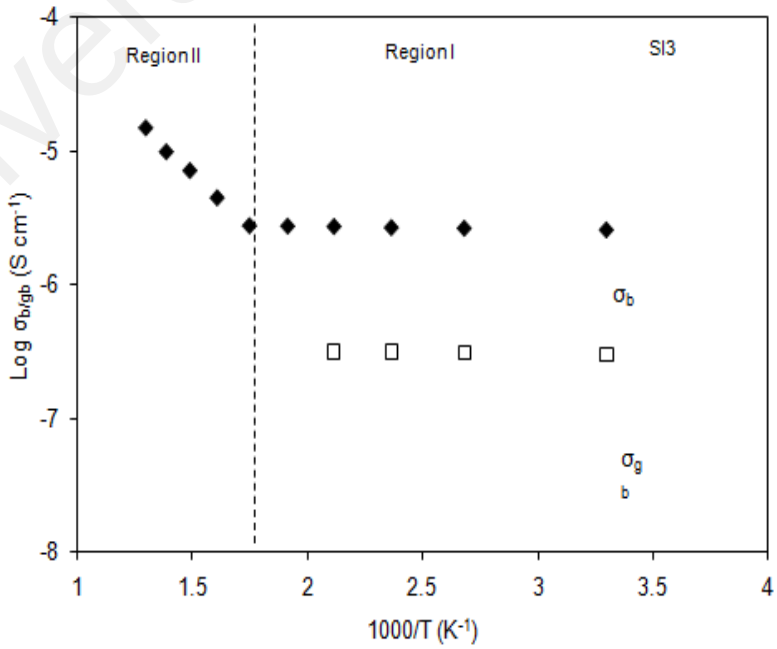

Figure 6.26, continued....

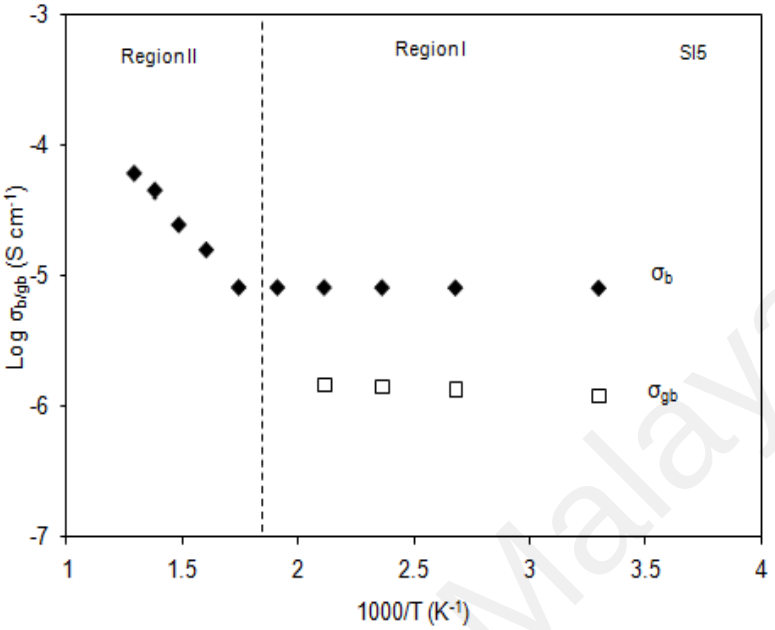

Figure 6.26: Log σ versus 1000/T plots of bulk and grain boundary conductivities of $Li_{1+y}Sn_2P_{3-y}Si_yO_{12}$ samples

Table 6.12: Bulk and grain boundary activation energies for $Li_{1+y}Sn_2P_{3-y}Si_yO_{12}$ system

Sample	$E_{a,b}$ (eV)		$E_{a,gb}$ (eV)	
	Region I (Low T)	Region II (High T)	Region I (Low T)	Region II (High T)
SI1	0.007	0.320	0.013	-
SI3	0.004	0.237	0.007	-
SI5	0.001	0.185	0.015	-

6.4.4.2 AC conductivity of $Li_{1+y}Sn_2P_{3-y}Si_yO_{12}$ System

Figure 6.27 shows log ζ_{ac} versus log ω plots of the highest conducting sample that is sample SI5 at various temperatures. It is clear that two different regions are observed in this figure. The middle frequency plateau was due to the frequency independence of the conductivity corresponding to the DC conductivity. The transition from the DC plateau to AC conductivity dispersion area shifted towards a greater frequency range when the temperature increases. At high frequencies, the power law dependence was detected in the form of Equation 4.3 (Jonscher, 1983).

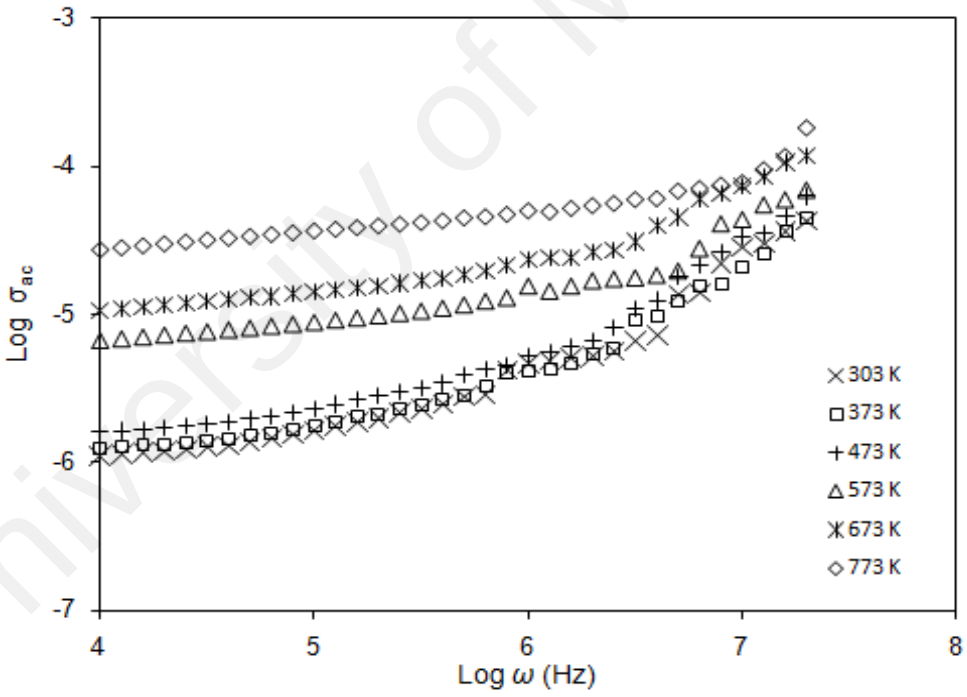

Figure 6.27: AC conductivity spectra for sample SI5 at various temperatues

The value of ω_p, K, n,and μ, at all temperatures of sample SI5 are shown in Table 6.13. All the values of ω_p, K, n, and μ, increase with the increment of temperature, showing the same trend with the previous systems. This suggests that the conductivity of the sample can be attributed by the increment of the ionic mobility, μ as well as density of mobile ions, n (Teo et al., 2012). The highest conducting sample, sample SI5 possessed the highest ionic mobility, μ that is 3.42×10^{-10} cm^2 V^{-1} s^{-1} and the highest density of mobile ions, n that is 1.00×10^{24} cm^{-3}.

Table 6.13: Parameters of ω_p, K, n and μ for sample SI5 in $Li_{1+y}Sn_2P_{3-y}Si_yO_{12}$ system

T (K)	ω_p (Hz)	K (S cm^{-1} K Hz^{-1})	n (cm^{-3})	μ (cm^2 V^{-1} s^{-1})
303	3.98×10^6	4.80×10^{-10}	1.80×10^{23}	2.19×10^{-10}
373	6.31×10^6	4.38×10^{-10}	1.64×10^{23}	2.83×10^{-10}
473	7.08×10^6	5.55×10^{-10}	2.08×10^{23}	2.50×10^{-10}
573	1.00×10^7	9.05×10^{-10}	3.39×10^{23}	2.92×10^{-10}
673	1.26×10^7	1.69×10^{-9}	6.32×10^{23}	3.13×10^{-10}
773	1.58×10^7	2.68×10^{-9}	1.00×10^{24}	3.42×10^{-10}

The behavior of the exponent factor s as a function of temperature can be used to predict the origin of the conduction mechanism in the system. Values of the frequency exponent s at different temperature were calculated from the slopes of the linear part in the high frequency area of log ζ_{ac} versus log ω presented in Figure 6.28. The variation of s with temperature for the investigated sample, SI5 is shown in Figure 6.26. It is

observed from this figure that the frequency exponent *s* decreases with increasing temperature.The evaluated value of *s* reduces from 0.92 to 0.46. According to the CBH model, the values of the frequency exponent *s* decrease with the increase in the temperature. This model is in good agreement with the experimental results, suggesting thus that the electrical AC conduction mechanism in the sample can be explained by charge carrier hops between sites over the potential barrier separating them (Said et al., 2016). Moreover, the hopping of the charge carriers are also thermally activated (Taher et al., 2015).

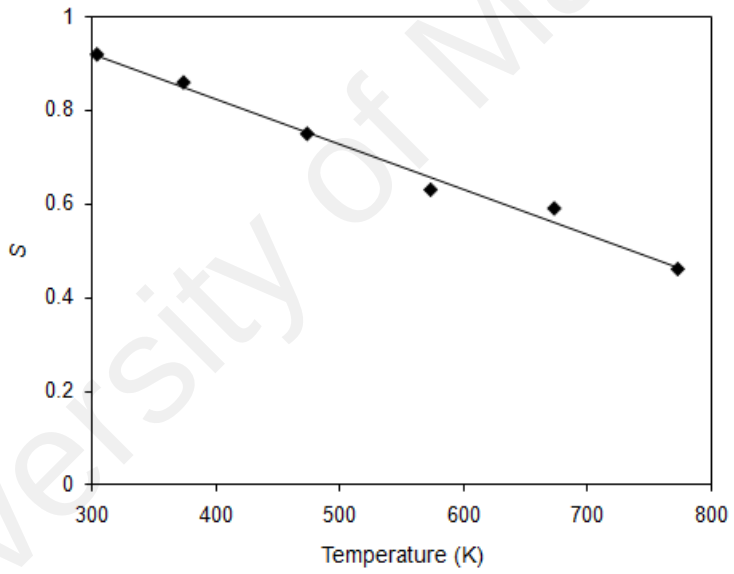

Figure 6.28: Variation of *s* with temperature for sample SI5

6.4.4.2 Transference number measurement analysis

Simple and useful technique to measure the ionic transference number is Wagner‟s polarization method (Lee et al., 2006). Using this method, NASICON samples were sandwiched between two stainless steel electrodes and 0.5 V DC voltage was applied across it. Figure 6.29 displays a typical plot of normalized polarization current versus time for the highest conducting sample that is sample SI5. The total ionic transference number value is close to unity that is 0.99 confirming that the conductivity is a result of ionic mobility rather than electronic mobility (Jolley et al., 2015).

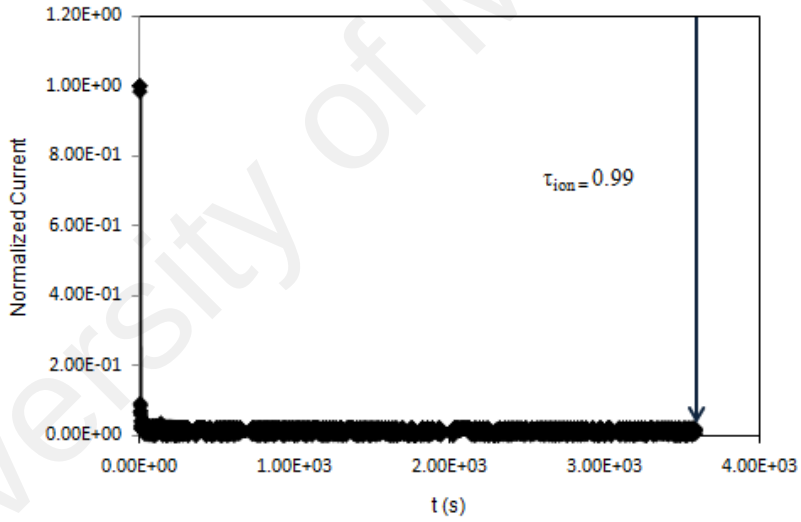

Figure 6.29: Typical plot of normalized polarisation current versus time of sample SI5

6.4.5 Electrochemical stability of $Li_{1+y}Sn_2P_{3-y}Si_yO_{12}$ System

Figure 6.30 shows linear sweep voltammogram of the highest conducting sample that is sample SI5. The figure shows that the current increases gradually with the increment of voltage above 5.1 V. This voltage is the decomposition voltage of the studied sample. This means that Si^{4+} substituted sample also possessed 6.3 % wider voltage stability window compared to the unsubstituted sample. The sample also exhibits electrochemical stability window more than 4.5 V (Robertson et al., 1997) and suggests that the sample is stable enough to be applied as solid electrolytes in electrochemical devices.

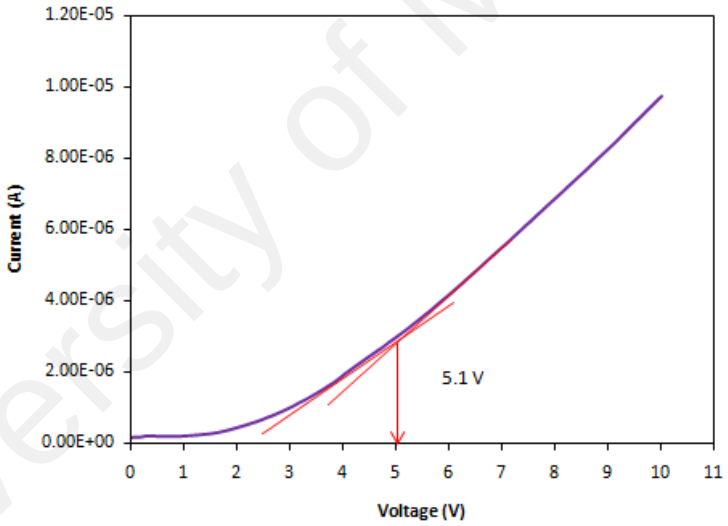

Figure 6.30: Linear sweep voltammogram of sample SI5

CHAPTER 7: CONCLUCIONS AND RECOMMEDATIONS FOR FUTURE WORKS

7.1 Conclusions

The NASICON-structured materials, $LiSn_2P_3O_{12}$ was successfully obtained by employing water based citric acid assisted sol-gel method. In the first stage, parameters of sol-gel method have been optimized in order to minimize the impurity in the $LiSn_2P_3O_{12}$ system. As such, $LiSn_2P_3O_{12}$ samples were sintered at two different sintering times; 24 and 48 hours and different sintering temperatures ranging from 550 – 650 °C. It was found that $LiSn_2P_3O_{12}$ samples were successfully synthesized with trace amount of unreacted SnO_2 impurity upon sintering at 600 and 650 °C for 48 hours. Then, structural modifications of the $LiSn_2P_3O_{12}$ parent compound were successfully done by trivalent ions (Cr^{3+} and Al^{3+}) substitutions at Sn^{4+} site and also by using tetravelant ions (Zr^{4+} and Si^{4+}) subtituitions at P^{5+} site. Furthermore, the effects of the structural modifications at Sn^{4+} and P^{5+} site on $LiSn_2P_3O_{12}$ to the electrical and electrochemical stability window were succesfully reported.

The formation of the rhombohedral NASICON-type symmetrical structure ($R\bar{3}c$) in the $LiSn_2P_3O_{12}$ compound was confirmed by XRD analysis. After substitutions of trivalent ions (Cr^{3+} and Al^{3+}) at Sn^{4+} site and tetravelant ions (Zr^{4+} and Si^{4+}) at P^{5+} site, all the prepared samples possessed rhombohedral NASICON-type symmetrical structure ($R\bar{3}c$). Besides that no peak associated with $Cr^{3+,}$ Al^{3+}, Zr^{4} and Si^{4+} were detected and indicated that they were successfully inserted into the $LiSn_2P_3O_{12}$ structure rather than forming impurities. In $Li_{1+x}Al_xSn_{2-x}P_3O_{12}$ system, values of a, c and V in Al substituted system decreased as the value of x increased. Nevertheless, the decrease in

the unit cell volume compared to the unsubstituted parent compound was mostly related to the substitutions of smaller ionic radius of Al^{3+} ion (r_{ion} = 0.53 Å) compared to the Sn^{4+} ion (r_{ion} = 0.69 Å). In $Li_{1+y}Sn_2P_{3-y}Zr_yO_{12}$ system, values of *a*, *c* and *V* in Zr substituted system increased with the value of *y*. However, the increase in the unit cell volume compared to that if the unsubstituted parent compound was mostly related to the substitutions of greater ionic radius of Zr^{4+} ion (r_{ion} = 0.72 Å) compared to the P^{5+} ion (r_{ion} = 0.38 Å). In $Li_{1+y}Sn_2P_{3-y}Si_yO_{12}$ system, the values of *a*, *c* and *V* in Si increased as the value of *y* increased. The increase in the unit cell volume compared to the unsubstituted parent compound was due to the substitutions of larger Si^{4+} ion (r_{ion} = 0.40 Å) compared to the P^{5+} ion (r_{ion} = 0.38 Å). In all the substituted systems; $Li_{1+x}Al_xSn_{2-x}P_3O_{12}$, $Li_{1+y}Sn_2P_{3-y}Zr_yO_{12}$ and $Li_{1+y}Sn_2P_{3-y}Si_yO_{12}$, the maximum value of substitutions of *x* and *y* was 0.5. When *x* or *y* exceeded 0.5, certain peaks corresponding to $LiSn_2P_3O_{12}$ disappeared and SnO_2 impurity peaks became dominant.

The effects of the structural modifications to the electrical properties were studied using impedance analysis and transference number measurements. Modifications of the structural properties at Sn^{4+} and P^{5+} site significantly enhanced the conductivity and electrochemical properties of the system. In $LiSn_2P_3O_{12}$ parent compound, samples sintered at 600°C for 48 hours (sample B1) with the volume of 1341. 38 Å showed that grain boundary conductivity; ζ_{gb} increased by an order of magnitude from 2.99 $\times 10^{-7}$ S cm^{-1} at 30 °C to 7.22 $\times 10^{-6}$ S cm^{-1} at 500 °C. Furthermore, bulk conductivity, ζ_b also increased by the same order of magnitude that was 7.22 $\times$ 10^{-6} S cm^{-1} at 30 °C to 1.38 $\times$ 10^{-5} S cm^{-1} at 500 °C. The highest total conductivity, ζ_t found was 1.38 $\times$ 10^{-5} Scm^{-1} at 500 °C for sample B1. The bulk ionic conductivity increased to 8.18 $\times 10^{-5}$ S cm^{-1} at 500 °C when trivalent Al^{3+} was substituted at Sn^{4+} site ($Li_{1.5}Al_{0.5}Sn_{1.5}P_3O_{12}$) with the volume of the sample was 1313.00 Å. Meanwhile, when

tetravalent (Si^{4+}, Zr^{4+}) ions were substituted at and P^{5+} site ($Li_{1.5}Sn_2P_{2.5}Zr_{0.5}O_{12}$ and $Li_{1.5}Sn_2P_{2.5}Si_{0.5}O_{12}$), the ionic conductivity increased to 5.77 $\times 10^{-5}$ S cm^{-1} (1346. 46 Å) and 6.05 $\times 10^{-5}$ S cm^{-1} (1338.23 Å) respectively. The highest bulk ionic conductivity obtained was for the $Li_{1.5}Al_{0.5}Sn_{1.5}P_3O_{12}$sample with a value of 8.18 $\times 10^{-5}$ S cm^{-1} at 500°C with the volume of the sample was 1313.00 Å. So, it was proven that Al^{3+} substitution yielded the most suitable volume of the NASICON structured that led to the enhancement of the ionic conductivity. Besides that, it can also be inferred that the rise of total ionic conductivity in the all the samples originated from grain boundary conductivity, not from the bulk conductivity. The increase in the ionic conductivity across grain boundaries was ascribed to the increased density of the samples upon Al^{3+}, Zr^{4+} and Si^{4+} substitutions as well as a rise in the amount of interstitial Li^+ ions.

The conductivity–temperature study showed that all the samples obey the Arrhenius behaviour implying that conduction was a thermally activated process. Besides that, the increment in the ionic conductivity in the samples can be attributed to the rise in ionic mobility as well as density of mobile ions. The trend of μ showed that the sample AL5 displayed the highest ionic conductivity value and also possessed the highest ionic mobility, μ that is 2.42 $\times$ 10^{-10} cm^2 V^{-1} s^{-1} and the highest density of mobile ions, *n* that is 1.62 x 10^{24} cm^{-3}.

AC conductivity analysis also revealed that, the temperature dependence of *s* in all systems decreased with an increase in temperature. The reducing value of *s* with temperature suggested that the Correlated Barrier Hopping model was the predominant AC conduction mechanism in the all the samples. This implied that the model considers

the hopping of carriers between two sites over a barrier separating them and the hopping of the charge carriers were thermally activated.

Besides that, transference number measurements of all the highest conducting sample in Al^{3+}, Zr^{4+} and Si^{4+} substituted systems revealed that all the samples possessed the total ionic transference number value that was close to unity. This indicated that the conductivity of the samples in all the systems were predominantly ionic and were anticipated to be that of Li^{+} ions.

In LSV analysis, $LiSn_2P_3O_{12}$ samples sintered at 600°C for 48 hours (sample B1) was electrochemically stable up to 4.8 V. However, when trivalent Al^{3+} was substituted at Sn^{4+} site, the sample possessed 6.3 % wider electrochemical stability window that was 5.1 V. Besides that, sample substituted with Zr^{4+} ion possessed the highest electrochemical stability window up to 5.2 V compared to sample substituted with Si^{4+} that was only stable up to 5.1 V. This suggests that Al^{3+}, Zr^{4+} and Si^{4+} substitutions increases the stability windows of the electrolytes. As such, the electrochemical stability windows of $LiSn_2P_3O_{12}$ sample and also the Al^{3+}, Zr^{4+} and Si^{4+} substituted samples are wide enough to be applied as solid electrolytes in electrochemical devices.

7.2 Recommendations for Future Works

As mentioned earlier, the solid electrolyte samples studied in this work have the potential for application in electrochemical devices. However, further work should be done for deeper understanding of the properties of these solid electrolyte systems. The structural, electrical and electrochemical properties of the electrolytes can further be improved by several approaches. The suggestions below may be considered for this purpose.

i. In order to obtain pure samples of $LiSn_2P_3O_{12}$, optimization of sol-gel method still need to be considered such as the starting materials used and also the pH of the mixed solutions.

ii. Structural studies of the samples should be further discussed by employing Rietveld method. The Rietveld method creates a virtual separation of the overlapping peaks in XRD analysis thereby allowing an accurate determination of the structure.

iii. In order to further increase the ionic conductivity of the system, multiple substitutions may be done at both Sn^{4+} and P^{5+} sites. The multiple substitutions are expected to optimize the bottleneck in the system and also increase the mobility of Li^+ ions. It is also expected to produce Li^+ interstitial ions and may result in enhancement of conductivity.

iv. Lithium transference number measurements should be done in order to determine the actual type of charge carriers in the systems.

References

Abrahams, I. , Bruce, P. G. , West, A. R. , & David, W. I. F. (1988). Structure determination of LISICON solid solutions by powder neutron diffraction. *Journal of Solid State Chemistry, 75*(2), 390-396.

Adnan, S. B. R. S, Mohamed, N. S, & Norwati, K. A. (2011). Li_4SiO_4 Prepared by Sol-gel Method as Potential Host for LISICON Structured Solid Electrolytes. *World Academy of Science, Engineering and Technology, International Journal of Mathematical, Computational, Physical, Electrical and Computer Engineering, 5*(2), 183-186.

Adnan, S. B. R. S, & Mohamed, N. S. (2014). Structural, electrical and electrochemical properties of novel $Li_{4+\ 2x+\ y}Zn_xM_y\ Si_{1-xy}O_{\ 4}$ (where x= 0.04, y= 0.03; M= Al, Cr) ceramic electrolytes. *Electrochimica Acta, 146*, 598-610.

Adnan , S. B. R. S. , & Mohamed, N. S. (2012). Conductivity and dielectric Studies of Li_2ZnSiO_4 Ceramic Electrolyte Synthesized via Citrate Sol gel Method. *International Journal of Electrochemical Science, 7*, 9844-9858.

Adnan , S. B. R. S. , & Mohamed, N. S. (2014). Effects of Sn substitution on the properties of Li_4SiO_4 ceramic electrolyte. *Solid State Ionics, 262*, 559-562.

Agrawal, R. C. , & Gupta, R. K. (1999). Superionic solid: composite electrolyte phase–an overview. *Journal of materials science, 34*(6), 1131-1162.

Alami, M. , Brochu, R. , Soubeyroux, J. L. , Gravereau, P. , Le Flem, G. , & Hagenmuller, P. (1991). Structure and thermal expansion of $LiGe_2(PO_4)_3$. *Journal of Solid State Chemistry, 90*(2), 185-193.

Alamo, J. (1993). Chemistry and properties of solids with the [NZP] skeleton. *Solid State Ionics, 63*, 547-561.

Alamo, J. , & Rodrigo, J. L. (1989). Thermal expansion of $LiZr_2(PO_4)_3$: Water inclusion influence. *Solid State Ionics, 32*, 70-76.

Allen, T. (2013). *Particle size measurement*: Springer.

Almond, D. P. , Duncan, G. K. , & West, A. R. (1983). The determination of hopping rates and carrier concentrations in ionic conductors by a new analysis of ac conductivity. *Solid State Ionics, 8*(2), 159-164.

Anantharamulu, N. , Rao, K. K. , Rambabu, G. , Kumar, B. V. , Radha, V. , & Vithal, M. (2011). A wide-ranging review on Nasicon type materials. *Journal of materials science, 46*(9), 2821-2837.

Antony, C. J., Aatiq, A., Panicker, C. Y., Bushiri, M. J., Varghese, H. T., & Manojkumar, T. K. (2011). FT-IR and FT-Raman study of Nasicon type phosphates, $ASnFe(PO_4)_3$ [A= Na 2, Ca, Cd]. *Spectrochimica Acta Part A: Molecular and Biomolecular Spectroscopy, 78*(1), 415-419.

Aono, H. , Sugimoto, E. , Sadaoka, Y. , Imanaka, N. , & Adachi, G. (1990a). Electrical properties of sintered lithium titanium phosphate ceramics ($Li_{1+x}M_xTi_{2-x}(PO_4)_3$, $M^{3+}= Al^{3+}$, Sc^{3+}, or Y^{3+}). *Chemistry Letters*(10), 1825-1828.

Aono, H. , Sugimoto, E. , Sadaoka, Y. , Imanaka, N. , & Adachi, G. (1990b). Ionic conductivity and sinterability of lithium titanium phosphate system. *Solid State Ionics, 40*, 38-42.

Aono, H. , Sugimoto, E. , Sadaoka, Y. , Imanaka, N. , & Adachi, G. (1991). Electrical property and sinterability of $LiTi_2(PO_4)_3$ mixed with lithium salt (Li_3PO_4 or Li_3BO_3). *Solid State Ionics, 47*(3-4), 257-264.

Aono, H. , Sugimoto, E. , Sadaoka, Y. , Imanaka, N. , & Adachi, G. (1993). Electrical properties and crystal structure of solid electrolyte based on lithium hafnium phosphate $LiHf_2(PO_4)_3$. *Solid State Ionics, 62*(3-4), 309-316.

Arbi , K, Bucheli , W, Jiménez , R, & Sanz , J. (2015). High lithium ion conducting solid electrolytes based on NASICON $Li_{1+x}Al_xM_{2-x}(PO_4)_3$ materials (M = Ti, Ge and $0 \leq x \leq 0.5$). *Journal of the European Ceramic Society, 35*(5), 1477-1484.

Arbi, K. , Ayadi-Trabelsi, M. , & Sanz, J. (2002). Li mobility in triclinic and rhombohedral phases of the Nasicon-type compound $LiZr_2(PO_4)_3$ as deduced from NMR spectroscopy. *Journal of Materials Chemistry, 12*(10), 2985-2990.

Arbi, K. , Hoelzel, M. , Kuhn, A. , García-Alvarado, F. , & Sanz, J. (2013). Structural Factors That Enhance Lithium Mobility in Fast-Ion $Li_{1+x}Ti_{2-x}Al_x(PO_4)_3$ ($0 \leq x \leq 0.4$) Conductors Investigated by Neutron Diffraction in the Temperature Range 100–500 K. *Inorganic chemistry, 52*(16), 9290-9296.

Arbi, K. , Jimenez, R. , Šalkus, T. , Orliukas, A. F., & Sanz, J. (2015). On the influence of the cation vacancy on lithium conductivity of $Li_{1+x}R_xTi_{2-x}(PO_4)_3$ Nasicon type materials. *Solid State Ionics, 271*, 28-33.

Arbi, K. , Rojo, J. M. , & Sanz, J. (2007). Lithium mobility in titanium based Nasicon $Li_{1+x}Ti_{2-x}Al_x(PO_4)_3$ and $LiTi_{2-x}Zr_x(PO_4)_3$ materials followed by NMR and impedance spectroscopy. *Journal of the European Ceramic Society, 27*(13), 4215-4218.

Arbi, K. , Tabellout, M. , Lazarraga, M. G. , Rojo, J. M., & Sanz, J. (2005). Non-Arrhenius conductivity in the fast lithium conductor $Li_{1.2}Ti_{1.8}Al_{0.2}(PO_4)_3$: A Li 7 NMR and electric impedance study. *Physical Review B, 72*(9), 094302.

Armand, M. B. (1986). Polymer electrolytes. *Annual Review of Materials Science, 16*(1), 245-261.

Armand, M. B. , Chabagno, J. M., Duclot, N. J., & Vashishta, P. (1979). Mundy, Shenoy (Eds.), Fast Ion Transport in Solids: North-Holland, Amsterdam.

Bard, A. J., Faulkner, L. R., Leddy, J., & Zoski, C. G. (1980). *Electrochemical methods: fundamentals and applications* (Vol. 2): Wiley New York.

Barsoukov, E., & Macdonald, J. R. (2005). *Impedance spectroscopy: theory, experiment, and applications*: John Wiley & Sons.

Berry, F. J, Costantini, N., & Smart, L. E. (2006). Synthesis and characterisation of Cr^{3+}-containing NASICON-related phases. *Solid State Ionics, 177*(33), 2889-2896.

Best , A. S. , Forsyth , M. , & MacFarlane , D. R. . (2000). Stoichiometric changes in lithium conducting materials based on $Li_{1+x}Al_xTi_{2-x}(PO_4)_3$: impedance, X-ray and NMR studies. *Solid State Ionics, 136–137*, 339-344.

Best, A. S., Newman, P. J., MacFarlane, D. R., Nairn, K. M., Wong, S., & Forsyth, M. (1999). Characterisation and impedance spectroscopy of substituted $Li_{1.3}Al_{0.3}Ti_{1.7}(PO_4)_{3-x}(ZO_4)_x$ (Z= V, Nb) ceramics. *Solid State Ionics, 126*(1), 191-196.

Bhargav, P. B., Mohan, V. M., Sharma, A., & Rao, V. V. R. N. (2007). Structural, electrical and optical characterization of pure and doped poly (vinyl alcohol)(PVA) polymer electrolyte films. *International Journal of Polymeric Materials, 56*(6), 579-591.

Bohre, A., Avasthi, K., Singh, B., & Shrivastava, O. P. (2014). Crystallographic evaluation of titanate ceramics as a host structure for immobilization of samarium. *Radiochemistry, 56*(1), 92-97.

Bohre, A., & Shrivastava, O. P. (2013). Crystal chemistry of immobilization of divalent Sr in ceramic matrix of sodium zirconium phosphates. *Journal of Nuclear Materials, 433*(1), 486-493.

Bradley, J. N., & Greene, P. D. (1967). Solids with high ionic conductivity in group 1 halide systems. *Transactions of the Faraday Society, 63*, 424-430.

Bruce, P. G., & West, A. R. (1980). Phase diagram of the LISICON, solid electrolyte system, Li_4GeO_4 · Zn_2GeO_4. *Materials Research Bulletin, 15*(3), 379-385.

Bruce, P. G., & West, A. R. (1982). Ionic conductivity of LISICON solid solutions, $Li_{2+2x}Zn_{1-x}GeO_4$. *Journal of Solid State Chemistry, 44*(3), 354-365.

Burmakin, E. I. , & Shekhtman, G. S. (2010). Lithium-conducting solid electrolytes of Li_4GeO_4-Li_3PO_4 system with additions of zirconium ions. *Russian Journal of Electrochemistry, 46*(2), 243-246.

Casciola, M., Costantino, U., Merlini, L., Andersen, I. G. K., & Andersen, E. K. (1988). Preparation, structural characterization and conductivity of $LiZr_2(PO_4)_3$. *Solid State Ionics, 26*(3), 229-235.

Catti, M., & Stramare, S. (2000). Lithium location in NASICON-type Li^+ conductors by neutron diffraction: II. Rhombohedral α-$LiZr_2(PO_4)_3$ at T= 423 K. *Solid State Ionics, 136*, 489-494.

Catti, M., Stramare, S., & Ibberson, R. (1999). Lithium location in NASICON-type Li^+ conductors by neutron diffraction. I. Triclinic α′-$LiZr_2(PO_4)_3$. *Solid State Ionics, 123*(1), 173-180.

Chandra , A. , Bhatt , A. , & Chandra , A. (2013). Ion Conduction in Superionic Glassy Electrolytes: An Overview. *Journal of Materials Science & Technology, 29*(3), 193-208.

Chandra, S., & Laskar, A. L. (1989). *Superionic Solids and Solid Electrolytes: Recent Trends*: Academic Press.

Chang, C-M. , Hong, S-H. , & Park, H-M. (2005). Spark plasma sintering of Al substituted $LiHf_2(PO_4)_3$ solid electrolytes. *Solid State Ionics, 176*(35), 2583-2587.

Chang, C-M. , Lee, Y. I. , Hong, S-H. , & Park, H-M. (2005). Spark Plasma Sintering of $LiTi_2(PO_4)_3$-Based Solid Electrolytes. *Journal of the American Ceramic Society, 88*(7), 1803-1807.

Chourashiya, M. G. (2013). *Studies on synthesis and characterizations of gadolinium doped ceria solid electrolyte.* (Doctoral Dissertation), Shivaji University.

Chowdari, B. V. R. , Rao, G. V. S., & Lee, G. Y. H. (2000). XPS and ionic conductivity studies on Li_2O–Al_2O_3–(TiO_2 or GeO_2)–P_2O_5 glass–ceramics. *Solid State Ionics, 136*, 1067-1075.

Chung, H. , & Kang, B. (2014). Increase in grain boundary ionic conductivity of $Li_{1.5}Al_{0.5}Ge_{1.5}(PO_4)_3$ by adding excess lithium. *Solid State Ionics, 263*, 125-130.

Cui, W-J. , Yi, J. , Chen, L. , Wang, C-X. , & Xia, Y-Y. (2012). Synthesis and electrochemical characteristics of NASICON-structured $LiSn_2(PO_4)_3$ anode material for lithium-ion batteries. *Journal of Power Sources, 217*, 77-84.

Dayanand, C. , Bhikshamaiah, G. , Tyagaraju, V. J., Salagram, M. , & Murthy, A. S. R. K. (1996). Structural investigations of phosphate glasses: a detailed infrared study of the x (PbO)-(1− x) P_2O_5 vitreous system. *Journal of Materials Science, 31*(8), 1945-1967.

Delmas, C. , Viala, J. C., Olazcuaga, R., Le Flem, G. , Hagenmuller, P. , Cherkaoui, F. , & Brochu, R. (1981). Conductivite ionique dans les systems $Na_{1+x}Zr_{2-x}L_x(PO_4)_3$ (L= Cr, Yb). *Materials Research Bulletin, 16*(1), 83-90.

Ding, F. , Xu, W. , Shao, Y. , Chen, X. , Wang, Z. , Gao, F. , . . . Zhang, J-G. (2012). H^+ diffusion and electrochemical stability of $Li_{1+x+y}Al_xTi_{2-x}Si_yP_{3-y}O_{12}$ glass in aqueous Li/air battery electrolytes. *Journal of Power Sources, 214*, 292-297.

Ejehi, F. , Marashi, S. P. H. , Ghaani, M. R. , & Haghshenas, D. F. (2012). The synthesis of NASICON-type $ZrNb(PO_4)_3$ structure by the use of Pechini method. *Ceramics International, 38*(8), 6857-6863.

Elliott, S. R. (1977). A theory of ac conduction in chalcogenide glasses. *Philosophical Magazine, 36*(6), 1291-1304.

Elliott, S. R. (1987). Ac conduction in amorphous chalcogenide and pnictide semiconductors. *Advances in Physics, 36*(2), 135-217.

Fenton, D. E., Parker, J. M. , & Wright, P. V. (1973). Complexes of alkali metal ions with poly (ethylene oxide). *polymer, 14*(11), 589.

Fergus, J. W. (2012). Ion transport in sodium ion conducting solid electrolytes. *Solid State Ionics, 227*, 102-112.

Fu, J. (1997). Fast Li^+ Ion Conduction in Li_2O-Al_2O_3-TiO_2-SiO_2-P_2O_2 Glass-Ceramics. *Journal of the American Ceramic Society, 80*(7), 1901-1903.

Gaber, A. , Abdel-Rahim, M. A. , Abdel-Latief, A. Y. , & Abdel-Salam, M. N. (2014). Influence of calcination temperature on the structure and porosity of nanocrystalline SnO_2 synthesized by a conventional precipitation method. *J Electrochemistry Sci, 9*, 81-95.

Galasso, F. S. (2013). *Structure, Properties and Preparation of Perovskite-Type Compounds: International Series of Monographs in Solid State Physics* (Vol. 5): Elsevier.

Geng, S. , Yang, Y. , Zhang, Y. , Ding, W. , Wang, X. , Peng, H. , & Bakenov, Z. (2015). Effect of VO_4^{3-} Substitution for PO_4^{3-} on Electrical Conductivity in the Nasicon $Li_3Sc_2(PO_4)_3$ Compound. *Electrochimica Acta, 176*, 327-333.

Ghosh, A. (1990). Frequency-dependent conductivity in bismuth-vanadate glassy semiconductors. *Physical Review B, 41*(3), 1479.

Goldstein, J. , Newbury, D. E., Echlin, P. , Joy, D. C., Romig Jr, A. D., Lyman, C. E., . . . Lifshin, E. (2012). *Scanning electron microscopy and X-ray microanalysis: a text for biologists, materials scientists, and geologists*: Springer Science & Business Media.

Goodenough, J. B. , Hong, H. Y-P. , & Kafalas, J. A. (1976). Fast Na^+-ion transport in skeleton structures. *Materials Research Bulletin, 11*(2), 203-220.

Guin, M. , & Tietz, F. (2015). Survey of the transport properties of sodium superionic conductor materials for use in sodium batteries. *Journal of Power Sources, 273*, 1056-1064.

Harada, Y. , Hirakoso, Y. , Kawai, H. , & Kuwano, J. (1999). Order–disorder of the A-site ions and lithium ion conductivity in the perovskite solid solution $La_{0.67-x}Li_{3x}TiO_3$(x= 0.11). *Solid State Ionics, 121*(1), 245-251.

Hong, H. Y-P. (1976). Crystal structures and crystal chemistry in the system $Na_{1+x}Zr_2Si_xP_{3-x}O_{12}$. *Materials Research Bulletin, 11*(2), 173-182.

Hong, H. Y-P. (1978). Crystal structure and ionic conductivity of $Li_{14}Zn(GeO_4)_4$ and other new Li^+ superionic conductors. *Materials Research Bulletin, 13*(2), 117-124.

Iglesias, J. E. , Sanz, J. , Martínez-Juárez, A. , & Rojo, J. M. (1997). Low-temperature triclinic distortion in NASICON-type $LiSn_2(PO_4)_3$. *Journal of Solid State Chemistry, 130*(2), 322-326.

Illbeigi, M. , Fazlali, A. , Kazazi, M. , & Mohammadi, A. H. (2016). Effect of simultaneous addition of aluminum and chromium on the lithium ionic conductivity of $LiGe_2(PO_4)_3$ NASICON-type glass–ceramics. *Solid State Ionics, 289*, 180-187.

Inada, R. , Ishida, K-i. , Tojo, M. , Okada, T. , Tojo, T. , & Sakurai, Y. (2015). Properties of aerosol deposited NASICON-type $Li_{1.5}Al_{0.5}Ge_{1.5}(PO_4)_3$ solid electrolyte thin films. *Ceramics International, 41*(9, Part A), 11136-11142.

Irvine, J. T. S., Sinclair, D. C., & West, A. R. (1990). Electroceramics : Characterization by impedance spectroscopy. *Advanced Materials, 2*(3), 132-138.

Jackman, S. D., & Cutler, R. A. (2013). Stability of NASICON-type $Li_{1.3}Al_{0.3}Ti_{1.7}P_3O_{12}$ in aqueous solutions. *Journal of Power Sources, 230*, 251-260.

Jenkins, R. (2000). *X-Ray Techniques: Overview, Encyclopedia of analytical chemistry*: Wiley Online Library.

Jenkins, R. , & Snyder, R. L. (1996). Diffraction theory. *Introduction to X-ray Powder Diffractometry, Volume 138*, 47-95.

Jiao, L. F. , Zhang, M. , Yuan, H. T. , Zhao, M. , Guo, J. , Wang, W. , . . . Wang, Y. M. (2007). Effect of Cr doping on the structural, electrochemical properties of Li $[Li_{0.2}Ni_{0.2-x/2}Mn_{0.6-x/2}Cr_x]O_2$ (x= 0, 0.02, 0.04, 0.06, 0.08) as cathode materials for lithium secondary batteries. *Journal of Power Sources, 167*(1), 178-184.

Jolley, A. G., Cohn, G., Hitz, G. T., & Wachsman, E. D. (2015). Improving the ionic conductivity of NASICON through aliovalent cation substitution of $Na_3Zr_2Si_2PO_{12}$. *Ionics, 21*(11), 3031-3038.

Jonscher, A. K. (1983). Chelsea Dielectric Press: London.

Kahn, F. J. , Pershan, P. S. , & Remeika, J. P. (1969). Ultraviolet magneto-optical properties of single-crystal orthoferrites, garnets, and other ferric oxide compounds. *Physical review, 186*(3), 891.

Kamaya, N. , Homma, K., Yamakawa, Y. , Hirayama, M. , Kanno, R. , Yonemura, M. , . . . Kawamoto, K. (2011). A lithium superionic conductor. *Nature Materials, 10*(9), 682-686.

Khorassani, A. , & West, A. R. (1984). Li^+ ion conductivity in the system Li_4SiO_4 · Li_3VO_4. *Journal of Solid State Chemistry, 53*(3), 369-375.

Knauth, P. (2009). Inorganic solid Li ion conductors: An overview. *Solid State Ionics, 180*(14), 911-916.

Kosova, N. V., Devyatkina, E. T., Stepanov, A. P., & Buzlukov, A. L. (2008). Lithium conductivity and lithium diffusion in NASICON-type $Li_{1+x}Ti_{2-x}Al_x(PO_4)_3$ (x= 0; 0.3) prepared by mechanical activation. *Ionics, 14*(4), 303-311.

Kothari, D. H. , & Kanchan, D. K. (2016). Study of Li^+ conduction in $Li_{1.3}Al_{0.3-x}Sc_xTi_{1.7}(PO_4)_3$ (x= 0.01, 0.03, 0.05 and 0.07) NASICON ceramic compound. *Physica B: Condensed Matter, 494*, 20-25.

Kotobuki, M. , & Koishi, M. (2013). Preparation of $Li_{1.5}Al_{0.5}Ti_{1.5}(PO_4)_3$ solid electrolyte via a sol–gel route using various Al sources. *Ceramics International, 39*(4), 4645-4649.

Kotobuki, M. , & Koishi, M. (2015). Sol–gel synthesis of $Li_{1.5}Al_{0.5}Ge_{1.5}(PO_4)_3$ solid electrolyte. *Ceramics International, 41*(7), 8562-8567.

Krok, F. (1987). Influence of sintering conditions on chemical composition of NASICON. *Solid State Ionics, 24*(1), 21-28.

Kubanska, A. , Castro, L. , Tortet, L. , Schäf, O. , Dollé, M. , & Bouchet, R. (2014). Elaboration of controlled size $Li_{1.5}Al_{0.5}Ge_{1.5}(PO_4)_3$ crystallites from glass-ceramics. *Solid State Ionics, 266*, 44-50.

Kudo, T., & Fueki, K. (1990). *Solid State Ionics*: VCH, Berlin.

Kumar, P. P, & Yashonath, S. (2006). Ionic conduction in the solid state. *Journal of Chemical Sciences, 118*(1), 135-154.

Kumar, S. , & Balaya, P. . (2016). Improved ionic conductivity in NASICON-type Sr^{2+} doped $LiZr_2(PO_4)_3$. *Solid State Ionics, 296*, 1-6.

Kunze, D. , & Van Gool, W. (1973). Fast ion transport in solids. *North Holland, Amsterdam*, 495.

Kurazhkovskaya, V. S. , Bykov , D. M., Borovikova , E. Y. , Boldyrev , N. Y., Mikhalitsyn , L. , & Orlova, A. I. (2010). Vibrational spectra and factor group analysis of lanthanide and zirconium phosphates $M_{III0.33}Zr_2(PO_4)_3$, where M_{III}= Y, La–Lu. *Vibrational Spectroscopy, 52*(2), 137-143.

Kuwano, J. , Sato, N. , Kato, M. , & Takano, K. (1994). Ionic conductivity of $LiM_2(PO_4)_3$ (M= Ti, Zr, Hf) and related compositions. *Solid State Ionics, 70*, 332-336.

Kuwano, J. , & West, A. R. (1980). New Li^+ ion conductors in the system, Li_4GeO_4-Li_3VO_4. *Materials Research Bulletin, 15*(11), 1661-1667.

Lang, B. , Ziebarth, B. , & Elsässer, C. (2015). Lithium Ion Conduction in $LiTi_2(PO_4)_3$ and Related Compounds Based on the NASICON Structure: A First-Principles Study. *Chemistry of Materials, 27*(14), 5040-5048.

Latie, L. , Villeneuve, G. , Conte, D. , & Le Flem, G. (1984). Ionic conductivity of oxides with general formula $Li_xLn_{1/3}Nb_{1-x}Ti_xO_3$ (Ln= La, Nd). *Journal of Solid State Chemistry, 51*(3), 293-299.

Lazarraga, M. G. , Ibañez, J. , Tabellout, M. , & Rojo, J. M. (2004). On the aggregation process of ceramic $LiSn_2P_3O_{12}$ particles embedded in Teflon matrix. *Composites science and technology, 64*(5), 759-765.

Lee, C. , Dutta, P. K., Ramamoorthy, R. , & Akbar, S. A. (2006). Mixed ionic and electronic conduction in Li_3PO4 electrolyte for a CO_2 gas sensor. *Journal of The Electrochemical Society, 153*(1), H4-H14.

Liang, C. C. (1973). Conduction characteristics of the lithium iodide-aluminum oxide solid electrolytes. *Journal of the Electrochemical Society, 120*(10), 1289-1292.

Liang, C. C. , Joshi, A. V. , & Hamilton, N. E. (1978). Solid-state storage batteries. *Journal of Applied Electrochemistry, 8*(5), 445-454.

Lin, Z-X. , Yu, H-J. , Li, S-C. , & Tian, S-B. (1988). Lithium ion conductors based on $LiTi_2P_3O_{12}$ compound. *Solid State Ionics, 31*(2), 91-94.

Losilla, E. R. , Aranda, M. A. G. , Martínez-Lara, M. , & Bruque, S. (1997). Reversible triclinic-rhombohedral phase transition in $LiHf_2(PO_4)_3$: Crystal structures from neutron powder diffraction. *Chemistry of materials, 9*(7), 1678-1685.

MacDonald, J. R. (1987). Impedence Spectroscopy--Emphasizing Solid Materials and Systems. *Wiley-Interscience, John Wiley and Sons*, 1-346.

Marcinek, M., Syzdek, J., Marczewski, M., Piszcz, M., Niedzicki, L., Kalita, M., . . . Wieczorek, W. (2015). Electrolytes for Li-ion transport – Review. *Solid State Ionics, 276*, 107-126.

Mariappan, C. R. , & Govindaraj, G. (2005). Conductivity and ion dynamic studies in the $Na_{4.7+x}Ti_{1.3-x}(PO_4)_{3.3-x}$ ($0 \leq x \leq 0.6$) NASICON material. *Solid state ionics, 176*(13), 1311-1318.

Martínez-Juárez, A. , Amarilla, J. M. , Iglesias, J. E. , & Rojo, J. M. (1997). Ionic conductivity of $LiHf_2(PO_4)_3$ with NASICON-type structure and its possible application as electrolyte in lithium batteries. *Journal of the Brazilian Chemical Society, 8*(3), 261-264.

Martínez-Juárez, A. , Iglesias, J. E. , & Rojo, J. M. (1996). Ionic conductivity of NASICON-type $LiHf_2(PO_4)_3$: a reexamination. *Solid State Ionics, 91*(3), 295-301.

Martinez-Juarez, A. , Jimenez, R. , Duran-Martin, P. , Ibañez, J. , & Rojo, J. M. (1997). Effect of the phase transition of on the ion conduction in-Teflon composites. *Journal of Physics: Condensed Matter, 9*(20), 4119.

Martinez-Juarez, A. , Rojo, J. M., Iglesias, J. E., & Sanz, J. (1995). Reversible monoclinic-rhombohedral transformation in $LiSn_2(PO_4)_3$ with NASICON-type structure. *Chemistry of Materials, 7*(10), 1857-1862. doi: 10.1021/cm00058a016

Martinez, A. , Rojo, J. M. , Iglesias, J. E. , Sanz, J. , & Rojas, R. M. (1994). Formation process of $LiSn_2(PO_4)_3$, a monoclinically distorted NASICON-type structure. *Chemistry of materials, 6*(10), 1790-1795.

Minami, T. (1985). Fast ion conducting glasses. *Journal of Non-Crystalline Solids, 73*(1-3), 273-284.

Minami, T. , Tatsumisago, M. , Wakihara, M. , Iwakura, C. , Kohjiya, S. , & Tanaka, I. (2006). *Solid state ionics for batteries*: Springer Science & Business Media.

Moffatt, W. G., Pearsall, G. W., & Wulff, J. (1964). *The Structure and Properties of Materials*. John Wiley & Sons Inc.

Morimoto, H. , Awano, H. , Terashima, J. , Shindo, Y. , Nakanishi, S. , Ito, N. , . . . Tobishima, S. (2013). Preparation of lithium ion conducting solid electrolyte of NASICON-type $Li_{1+x}Al_xTi_{2-x}(PO_4)_3$ ($x = 0.3$) obtained by using the mechanochemical method and its application as surface modification materials of $LiCoO_2$ cathode for lithium cell. *Journal of Power Sources, 240*, 636-643.

Murugavel, S. , & Upadhyay, M. (2012). AC conduction in amorphous semiconductors. *Journal of the Indian Institute of Science, 91*(2), 303-318.

Narváez-Semanate, J. L. , & Rodrigues, A. C. M. (2010). Microstructure and ionic conductivity of $Li_{1+x}Al_xTi_{2-x}(PO_4)_3$ NASICON glass-ceramics. *Solid State Ionics, 181*(25), 1197-1204.

Norhaniza, R. , Subban, R. H. Y. , & Mohamed, N. S. (2010). Effects of sintering temperature on the structure and conductivity of $LiSn_2P_3O_{12}$ prepared by mechanical milling method. *Advanced Materials Research, 129*, 338-342.

Norhaniza, R. , Subban, R. H. Y. , & Mohamed, N. S. (2013). Cr and V substituted $LiSn_2P_3O_{12}$ solid electrolyte materials. *Journal of Power Sources, 244*, 300-305.

Norhaniza, R. , Subban, R. H. Y. , Mohamed, N. S. , & Ahmad, A. (2012). Chromium substituted $LiSn_2P_3O_{12}$ solid electrolyte. *International Journal of Electrochemical Science, 7*, 10254.

Norhaniza, R. , Subban, R. H. Y., & Mohamed, N. S. (2011). Ion conduction in vanadium-substituted $LiSn_2P_3O_{12}$ electrolyte nanomaterials. *Journal of Materials Science, 46*(24), 7815-7821.

Notten, P. H. L. , Roozeboom, F. , Niessen, R. A. H. , & Baggetto, L. (2007). 3-D integrated all-solid-state rechargeable batteries. *Advanced Materials, 19*(24), 4564-4567.

Ortiz, G. F. , López, M. C. , Lavela, P. , Vidal-Abarca, C. , & Tirado, J. L. (2014). Improved lithium-ion transport in NASICON-type lithium titanium phosphate by calcium and iron doping. *Solid State Ionics, 262*, 573-577.

París, M. A. , & Sanz, J. (2000). Structural changes at the triclinic-rhombohedral transition and their influence on the Li mobility of the fast-ion conductor $LiHf_2(PO_4)_3$. *Physical Review B, 62*(2), 810.

Park, M. , Zhang, X. , Chung, M. , Less, G. B. , & Sastry, A. M. (2010). A review of conduction phenomena in Li-ion batteries. *Journal of Power Sources, 195*(24), 7904-7929.

Pendry, J. B. (1990). Low-energy electron diffraction *Interaction of Atoms and Molecules with Solid Surfaces* (pp. 201-211): Springer.

Pérez-Estébanez, M. , Isasi-Marín, J. , Díaz-Guerra, C. , Rivera-Calzada, A. , León, C. , & Santamaría, J. (2013). Influence of chromium content on the optical and electrical properties of $Li_{1+x}Cr_xTi_{2-x}(PO_4)_3$. *Solid State Ionics, 241*, 36-45.

Pérez-Estébanez, M., Isasi-Marín, J., Többens, D. M., Rivera-Calzada, A., & León, C. (2014). A systematic study of Nasicon-type $Li_{1+x}M_xTi_{2-x}(PO_4)_3$ (M: Cr, Al, Fe) by neutron diffraction and impedance spectroscopy. *Solid State Ionics, 266*, 1-8.

Petit, D. , Colomban, P. , Collin, G. , & Boilot, J. P. (1986). Fast ion transport in $LiZr_2(PO_4)_3$: Structure and conductivity. *Materials Research Bulletin, 21*(3), 365-371.

Pike, G. E. (1972). AC conductivity of scandium oxide and a new hopping model for conductivity. *Physical Review B, 6*(4), 1572.

Pinus, I. Y. , Khoroshilov, A. V. , Gavrichev, K. S. , Tarasov, V. P. , & Yaroslavtsev, A. B. (2012). On cationic mobility in Nasicon phosphates $LiTi_2(PO_4)_3$ and $Li_{0.9}Ti_{1.9}Nb_{0.1}(PO_4)_3$. *Solid State Ionics, 212*, 112-116.

Qiu, F. , Zhu, Q. , Yang, X. , Quan, Y. , & Sun, L. (2003). Investigation of CO_2 sensor based on NASICON synthesized by a new sol–gel process. *Sensors and Actuators B: Chemical, 93*(1), 237-242.

Ramaraghavulu, R, & Buddhudu, S. (2011). Analysis of structural, thermal and dielectric properties of $LiTi_2(PO_4)_3$ ceramic powders. *Ceramics International, 37*(8), 3651-3656.

Rao, A. V. , Veeraiah, V. , Rao, A. V. P. , Babu, B. K. , & Kumar, K. V. (2014). Influence of Zr^{4+} doping on structural, spectroscopic and conductivity studies of lithium titanium phosphate. *Ceramics International, 40*(9), 13911-13916.

Reddy, C. V. S., Sharma, A. K. , & Rao, V. V. R. N. (2003). Conductivity and discharge characteristics of polyblend (PVP+ PVA+ KIO_3) electrolyte. *Journal of Power Sources, 114*(2), 338-345.

Rettenwander, D. , Welzl, A. , Pristat, S. , Tietz, F. , Taibl, S. , Redhammer, G. J. , & Fleig, J. (2016). A microcontact impedance study on NASICON-type $Li_{1+x}Al_xTi_{2-x}(PO_4)_3$ ($0 \leq x \leq 0.5$) single crystals. *Journal of Materials Chemistry A, 4*(4), 1506-1513.

Robertson, A. D. , West, A. R. , & Ritchie, A. G. (1997). Review of crystalline lithium-ion conductors suitable for high temperature battery applications. *Solid State Ionics, 104*(1), 1-11.

Said, R. B., Louati, B., & Guidara, K. (2016). Conductivity behavior of the new pyrophosphate $NaNi_{1.5}P_2O_7$. *Ionics, 22*(2), 241-249.

Sanz, J. , Rojo, J. M. , Jimenez, R. , Iglesias, J. E. , & Alamo, J. (1993). Stabilization of the rhombohedral phase in $LiZr_2(PO_4)_3$ by thermal quenching. *Solid State Ionics, 62*(3-4), 287-292.

Sarıboğa, V. , Özdemir, H. , & Öksüzömer, M. A. F. (2013). Cellulose templating method for the preparation of $La_{0.8}Sr_{0.2}Ga_{0.83}Mg_{0.17}O_{2.815}$ (LSGM) solid oxide electrolyte. *Journal of the European Ceramic Society, 33*(8), 1435-1446.

Savitha, T. , Selvasekarapandian, S. , Ramya, C. S. , Bhuvaneswari, M. S. , Hirankumar, G. , Baskaran, R. , & Angelo, P. C. (2006). Structural and ionic transport properties of $Li_2AlZr[PO_4]_3$. *Journal of Power Sources, 157*(1), 533-536.

Schrader, B. (2008). *Infrared and Raman spectroscopy: methods and applications*: John Wiley & Sons.

Schroeder, M. , Glatthaar, S. , & Binder, J. R. (2011). Influence of spray granulation on the properties of wet chemically synthesized $Li_{1.3}Ti_{1.7}Al_{0.3}(PO_4)_3$ (LATP) powders. *Solid State Ionics, 201*(1), 49-53.

Scrosati, B. (2000). Recent advances in lithium ion battery materials. *Electrochimica Acta, 45*(15), 2461-2466.

Scrosati, B. , & Vincent, C. A. (2000). Polymer electrolytes: the key to lithium polymer batteries. *Mrs Bulletin, 25*(03), 28-30.

Sebastian , L. , & Gopalakrishnan , J. (2003). Lithium ion mobility in metal oxides: a materials chemistry perspective. *Journal of Materials Chemistry, 13*(3), 433-441.

Shindo, D. , & Oikawa, T. (2002). Energy Dispersive X-ray Spectroscopy *Analytical Electron Microscopy for Materials Science* (pp. 81-102): Springer.

Song, W. , Ji, X. , Wu, Z. , Zhu, Y. , Yang, Y. , Chen, J. , . . . Banks, C. E. (2014). First exploration of Na-ion migration pathways in the NASICON structure $Na_3V_2(PO_4)_3$. *Journal of Materials Chemistry A, 2*(15), 5358-5362.

Souquet, J. L. (1981). Ionic transport in amorphous solid electrolytes. *Annual Review of Materials Science, 11*(1), 211-231.

Stuart, B. (2005). *Infrared spectroscopy*: Wiley Online Library.

Sudreau, F. , Petit, D. , & Boilot, J. P. (1989). Dimorphism, phase transitions, and transport properties in $LiZr_2(PO_4)_3$. *Journal of Solid State Chemistry, 83*(1), 78-90.

Suryanarayana, C. , & Norton, M. G. (2013). *X-ray diffraction: a practical approach*: Springer Science & Business Media.

Syvitski, J. P. M. (2007). *Principles, methods and application of particle size analysis*: Cambridge University Press.

Taher, Y. B., Moutia, N. , Oueslati, A. , & Gargouri, M. (2016). Electrical properties, conduction mechanism and modulus of diphosphate compounds. *RSC Advances, 6*(46), 39750-39757.

Taher, Y. B., Oueslati, A., Maaloul, N. K., Khirouni, K., & Gargouri, M. (2015). Conductivity study and correlated barrier hopping (CBH) conduction mechanism in diphosphate compound. *Applied Physics A, 120*(4), 1537-1543.

Takada, K. , Inada, T. , Kajiyama, A. , Kouguchi, M. , Sasaki, H. , Kondo, S. , . . . Watanabe, M. (2004). Solid state batteries with sulfide-based solid electrolytes. *Solid State Ionics, 172*(1), 25-30.

Takada, K. , Tansho, M. , Yanase, I. , Inada, T. , Kajiyama, A. , Kouguchi, M. , . . . Watanabe, M. . (2001). Lithium ion conduction in $LiTi_2(PO_4)_3$. *Solid State Ionics, 139*(3), 241-247.

Tan, G. , Wu, F. , Li, L. , Liu, Y. , & Chen, R (2012). Magnetron sputtering preparation of nitrogen-incorporated lithium–aluminum–titanium phosphate based thin film electrolytes for all-solid-state lithium ion batteries. *The Journal of Physical Chemistry C, 116*(5), 3817-3826.

Tatsumisago, M. , Nagao, M. , & Hayashi, A. (2013). Recent development of sulfide solid electrolytes and interfacial modification for all-solid-state rechargeable lithium batteries. *Journal of Asian Ceramic Societies, 1*(1), 17-25.

Tatsumisago, M. , Shinkuma, Y. , & Minami, T. (1991). Stabilization of superionic α-Agl at room temperature in a glass matrix. *Nature 354*, 217 - 218.

Teo, L. P. , Buraidah, M. H. , Nor, A. F. M. , & Majid, S. R. (2012). Conductivity and dielectric studies of Li_2SnO_3. *Ionics, 18*(7), 655-665.

Thangadurai, V. , Kaack, H. , & Weppner, W. J. (2003). Novel Fast Lithium Ion Conduction in Garnet-Type $Li_5La_3M_2O_{12}$ (M= Nb, Ta). *Journal of the American Ceramic Society, 86*(3), 437-440.

Thangadurai, V. , Narayanan, S. , & Pinzaru, D. (2014). Garnet-type solid-state fast Li ion conductors for Li batteries: critical review. *Chemical Society Reviews, 43*(13), 4714-4727.

Thangadurai, V. , & Weppner, W. (2005). $Li_6ALa_2Ta_2O_{12}$ (A= Sr, Ba): Novel Garnet-Like Oxides for Fast Lithium Ion Conduction. *Advanced Functional Materials, 15*(1), 107-112.

Thangadurai, V. , & Weppner, W. (2006). Recent progress in solid oxide and lithium ion conducting electrolytes research. *Ionics, 12*(1), 81-92.

Traversa, E. , Aono, H. , Sadaoka, Y. , & Montanaro, L. (2000). Electrical properties of sol–gel processed NASICON having new compositions. *Sensors and Actuators B: Chemical, 65*(1), 204-208.

Van Grieken, R. , & Markowicz, A. (2001). *Handbook of X-ray Spectrometry*: CRC Press.

Vijayakumar, M. , Hirankumar, G. , Bhuvaneswari, M. S, & Selvasekarapandian, S. (2003). Influence of B_2O_3 doping on conductivity of $LiTiO_2$ electrode material. *Journal of Power Sources, 117*(1), 143-147.

Vijayan, L. , & Govindaraj, G. (2011). Structural and electrical properties of high-energy ball-milled NASICON type $Li_{1.3}Ti_{1.7}Al_{0.3}(PO_4)_{2.9}(VO_4)_{0.1}$ ceramics. *Journal of Physics and Chemistry of Solids, 72*(6), 613-619.

Vijayan, L. , & Govindaraj, G. (2012). *NASICON materials: structure and electrical properties*: INTECH Open Access Publisher.

Wagner, J. B. (1980). Transport in compounds containing a dispersed second phase. *Materials Research Bulletin, 15*(12), 1691-1701.

Wagner , J. B , & Wagner, C. (1957). Electrical conductivity measurements on cuprous halides. *The Journal of Chemical Physics, 26*(6), 1597-1601.

Wang, G. X. , Bradhurst, D. H. , Dou, S. X. , & Liu, H. K. (2003). $LiTi_2(PO_4)_3$ with NASICON-type structure as lithium-storage materials. *Journal of Power Sources, 124*(1), 231-236.

Wang, J. (2006). *Analytical electrochemistry*: John Wiley & Sons.

Wang, Y, Liu, Z. , Zhu, X. , Tang, Y. , & Huang, F. (2013). Highly lithium-ion conductive thio-LISICON thin film processed by low-temperature solution method. *Journal of Power Sources, 224*, 225-229.

Wang , Y. , Liu, B. , Li, Q. , Cartmell, S. , Ferrara, S. , Deng, Z. D. , & Xiao, J. (2015). Lithium and lithium ion batteries for applications in microelectronic devices: A review. *Journal of Power Sources, 286*, 330-345.

Wolfenstine, J. , Allen, J. L. , Sumner, J. , & Sakamoto, J. (2009). Electrical and mechanical properties of hot-pressed versus sintered $LiTi_2(PO_4)_3$. *Solid State Ionics, 180*(14), 961-967.

Wong, S. , Newman, P. J., Best, A. S., Nairn, K. M., Macfarlane, D. R., & Forsyth, M. (1998). Towards elucidating microscopic structural changes in Li-ion conductors $Li_{1+y}Ti_{2-y}Al_y[PO_4]_3$ and $Li_{1+y}Ti_{2-y}Al_y[PO_4]_{3-x}[MO_4]_x$ (M= V and Nb): X-ray and 27 Al and 31 P NMR studies. *Journal of Materials Chemistry, 8*(10), 2199-2203.

Wu, F, Liu, Y. , Chen, R. , Chen, S. , & Wang, G. (2009). Preparation and performance of novel Li–Ti–Si–P–O–N thin-film electrolyte for thin-film lithium batteries. *Journal of Power Sources, 189*(1), 467-470.

Xu, X. , Wen, Z. , Gu, Z. , Xu, X. , & Lin, Z. (2004). Preparation and characterization of lithium ion-conducting glass-ceramics in the $Li_{1+x}Cr_xGe_{2-x}(PO_4)_3$ system. *Electrochemistry Communications, 6*(12), 1233-1237.

Yadav, P. , & Bhatnagar, M. C. (2012). Structural studies of NASICON material of different compositions by sol–gel method. *Ceramics International, 38*(2), 1731-1735.

Yadav, P. , & Bhatnagar, M. C. (2013). Preparation, structure and conductivity of Sn modified NASICON material. *Journal of Electroceramics, 30*(3), 145-151.

Yamada, H. , & Takemoto, K. (2016). Local structure and composition change at surface of lithium-ion conducting solid electrolyte. *Solid State Ionics, 285*, 41-46.

Yamamoto, H. , Tabuchi, M. , Takeuchi, T. , Kageyama, H. , & Nakamura, O. (1997). Ionic conductivity enhancement in $LiGe_2(PO_4)_3$ solid electrolyte. *Journal of Power Sources, 68*(2), 397-401.

Yang, B. , Li, X. , Guo, H. , Wang, Z. , & Xiao, W. (2015). Preparation and properties of $Li_{1.3}Al_{0.3}Ti_{1.7}(PO_4)_3$ by spray-drying and post-calcining method. *Journal of Alloys and Compounds, 643*, 181-185.

Yao, Y-F. Y. , & Kummer, J. T. (1967). Ion exchange properties of and rates of ionic diffusion in beta-alumina. *Journal of Inorganic and Nuclear Chemistry, 29*(9), 24662467-24662475.

Zhang , K. , Sunarso, J. , Shao, Z. , Zhou, W. , Sun, C. , Wang, S. , & Liu, S. (2011). Research progress and materials selection guidelines on mixed conducting perovskite-type ceramic membranes for oxygen production. *RSC advances, 1*(9), 1661-1676.

Zhang, P., Wang, H., Si, Q., Matsui, M., Takeda, Y., Yamamoto, O., & Imanishi, N. (2015). High lithium ion conductivity solid electrolyte of chromium and aluminum co-doped NASICON-type $LiTi_2(PO_4)_3$. *Solid State Ionics, 272*, 101-106.

Zhao, E. , Ma, F. , Jin, Y. , & Kanamura, K. (2016). Pechini synthesis of high ionic conductivity $Li_{1.3}Al_{0.3}Ti_{1.7}(PO_4)_3$ solid electrolytes: The effect of dispersant. *Journal of Alloys and Compounds, 680*, 646-653.

Zhou, D. F. , Xia, Y. J. , Zhu, J. X. , & Meng, J. (2009). Preparation and electrical properties of new oxide ion conductors $Ce_{6-x}Dy_xM_oO_{15-\delta}$ ($0.0 \leq x \leq 1.8$). *Solid State Sciences, 11*(9), 1587-1591.

LIST OF PUBLICATIONS, CONFERENCES ATTENDED AND AWARDS

Publications:

1. N. A. Mustaffa, S. B. R. S. Adnan, M. Sulaiman, N. S. Mohamed, Low-temperature sintering effects on NASICON-structured $LiSn_2P_3O_{12}$ solid electrolytes prepared via citric acid-assisted sol-gel method. Ionics 21 (2015) 955 – 965. (Published)
2. N. A. Mustaffa, N. S. Mohamed, Properties of Stannum-Based Li-NASICON-Structured Solid Electrolytes for Potential Application in Electrochemical Devices. Int. J. Electrochem. Sci. 10 (2015) 5382 – 5394. (Published)
3. N. A. Mustaffa, N. S. Mohamed, Zirconium-substituted $LiSn_2P_3O_{12}$ solid electrolyte prepared via sol-gel method. J. Sol-Gel Sci. Technol (2016) 585 - 593. (Published)
4. N. A. Mustaffa, N.S. Mohamed (2015). Lithium conducting NASICON Structured $Li_{1+x}Cr_xSn_{2-x}P_3O_{12}$ Solid Electrolytes Prepared via Citric Acid Assisted Sol-gel Method. (Submitted)
5. N. A. Mustaffa, N.S. Mohamed (2015). Effects of Cr^{3+} and Zr^{4+} Substitution on Stannum Based NASICON-Structured Ceramic Electrolytes. (Submitted)
6. N. A. Mustaffa & N.S. Mohamed (2016). Enhanced Conductivity and Electrochemical Stability of NASICON-Structured Lithium Stannum Phosphate Ceramic Electrolytes via Aluminium Substitution. (Submitted)
7. N. A. Mustaffa & N.S. Mohamed (2016). Silicon Substituted Lithium Stannum Phosphate Ceramic Electrolytes: Electrical and Electrochemical Properties. (Manuscript in preparation)

Conferences:

1. International Conference on Materials Challenges in Alternative & Renewable Energy 2015 Conference (MCARE 2015), 24 – 27 February 2015, Lotte Hotel Jeju, Jeju, South Korea. (Poster presenter)
2. 5th International Conference on Solid State Science and Technology (ICSSST 2015), 13 – 15 December 2015, The Bayview Hotel Langkawi, Langkawi. (Poster presenter)
3. 4th International Conference on Nano and Materials Engineering (ICNME 2016), 7 – 8 April 2016, Kuta Central Park Hotel, Bali, Indonesia. (Oral presenter)

Awards:

1. Bronze Medal
   Invention, Innovation & Design Exposition (IIDEX) 2015, 27 – 30 April 2015, UiTM Shah Alam, Shah Alam.
2. Best Poster Awards
   5th International Conference on Solid State Science and Technology, 13 – 15 December 2015, The Bayview Hotel Langkawi, Langkawi.
3. 1st Place, University of Malaya Three Minute Thesis Competition (UM3MT) 2016, Faculty Level.
4. 1st Runner-up, University of Malaya Three Minute Thesis Competition (UM3MT) 2016, University Level.